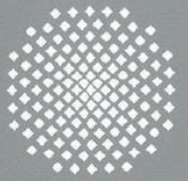
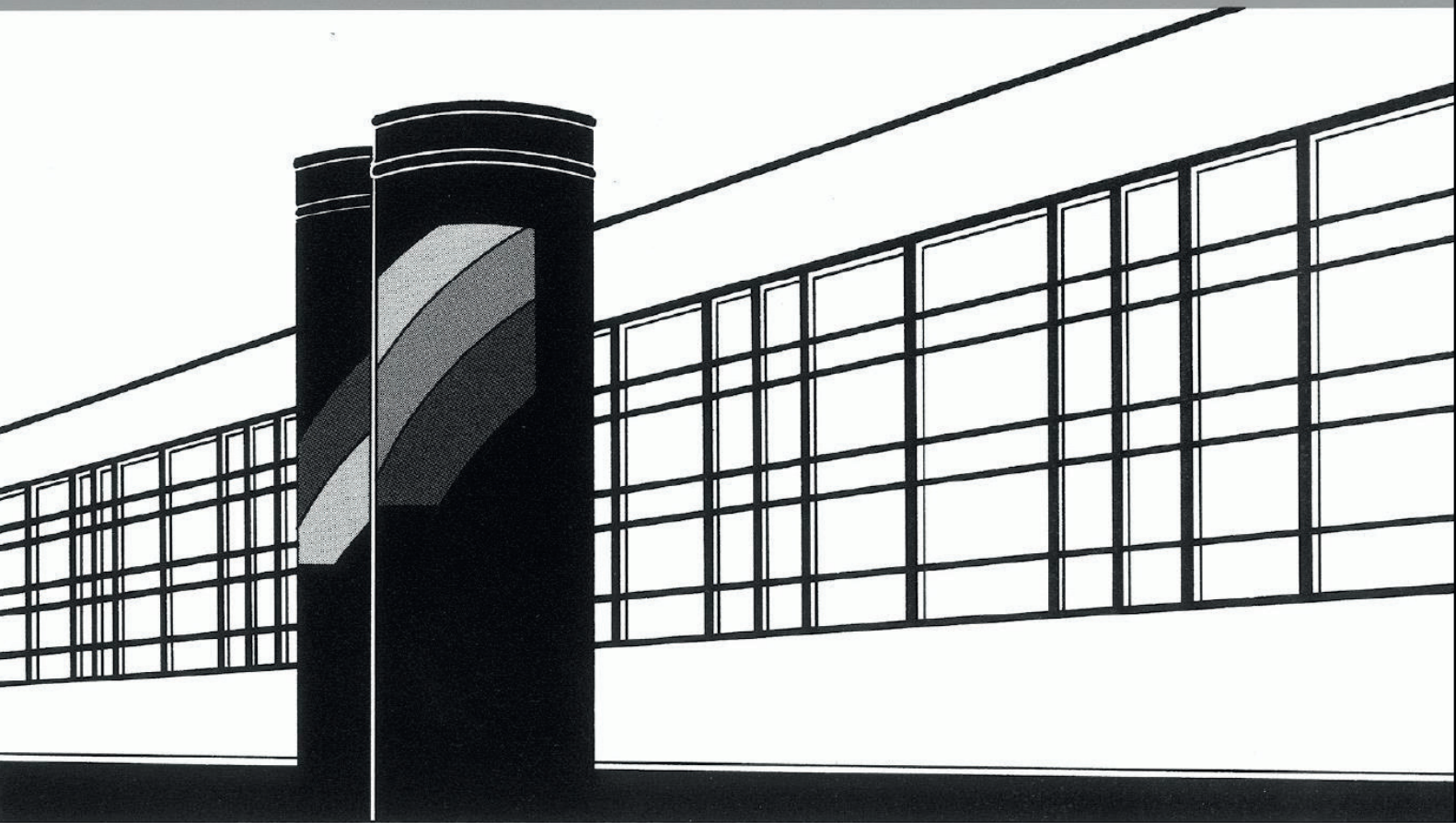


Universität Stuttgart



Institut für Wasser- und Umweltsystemmodellierung

# *Mitteilungen*



Heft 236 Katherina Inés Baber

Coupling free flow and flow in porous media in biological and technical applications: From a simple to a complex interface description



# **Coupling free flow and flow in porous media in biological and technical applications: From a simple to a complex interface description**

von der Fakultät Bau- und Umweltingenieurwissenschaften der  
Universität Stuttgart zur Erlangung der Würde eines  
Doktor-Ingenieurs (Dr.-Ing.) genehmigte Abhandlung

vorgelegt von

**Katherina Inés Baber**  
aus Neustadt am Rübenberge

Hauptberichter: Prof. Dr.-Ing. Rainer Helmig  
Mitberichter: Prof. Dr.-Ir. Majid Hassanizadeh  
Prof. Dr.-Ing. Wolfgang Ehlers

Tag der mündlichen Prüfung: 15. Juli 2014

Institut für Wasser- und Umweltsystemmodellierung  
der Universität Stuttgart  
2014



Heft 236    Coupling free flow and flow in  
porous media in biological and  
technical applications: From a  
simple to a complex interface  
description

von  
Dr.-Ing. Katherina Inés Baber

**D93 Coupling free flow and flow in porous media in biological and technical applications: From a simple to a complex interface description**

**Bibliografische Information der Deutschen Nationalbibliothek**

Die Deutsche Nationalbibliothek verzeichnet diese Publikation in der Deutschen Nationalbibliografie; detaillierte bibliografische Daten sind im Internet über <http://www.d-nb.de> abrufbar

**Baber, Katherina Inés:**

Coupling free flow and flow in porous media in biological and technical applications: From a simple to a complex interface description, Universität Stuttgart. - Stuttgart: Institut für Wasser- und Umweltsystemmodellierung, 2014

(Mitteilungen Institut für Wasser- und Umweltsystemmodellierung, Universität Stuttgart: H. 236)

Zugl.: Stuttgart, Univ., Diss., 2014  
ISBN 978-3-942036-40-5

NE: Institut für Wasser- und Umweltsystemmodellierung <Stuttgart>: Mitteilungen

Gegen Vervielfältigung und Übersetzung bestehen keine Einwände, es wird lediglich um Quellenangabe gebeten.

Herausgegeben 2014 vom Eigenverlag des Instituts für Wasser- und Umweltsystemmodellierung

Druck: Document Center S. Kästl, Ostfildern

## Danksagung

An dieser Stelle möchte ich all denen danken, die zum Gelingen dieser Arbeit beigetragen und mich in ihrem Entstehen unterstützt haben.

Zuerst möchte ich Philipp Nuske für die vielen guten Einfälle, für seine Rückendeckung und Unerschütterlichkeit danken. Mein Dank gilt auch meinen Eltern, die immer ein offenes Ohr für mich haben und mich immer mit allen Kräften unterstützen. Außerdem möchte ich mich bei Nicolas Schwenck bedanken. Denn er war der beste Büro-Mitbewohner den man sich wünschen konnte und hat mit guter Laune und fachlichem Rat wesentlich zu dieser Arbeit beigetragen.

Bernd Flemisch danke ich dafür, dass er immer Licht ins mathematische und numerische Dunkel gebracht hat. Mein Dank gilt auch der gesamten Gruppe des LH<sup>2</sup> für die entspannte, lustige Arbeitsatmosphäre und den großen Teamgeist. Diese Stimmung wäre nicht möglich ohne Rainer Helmig, denn er sorgt dafür, dass nicht jeder still in seinem Kämmerchen hockt. Ich danke Rainer Helmig außerdem für seine Unterstützung und Diskussionsbereitschaft in den letzten fünf Jahren sowie für all die Möglichkeiten, die er mir geboten hat. Letztendlich gilt mein Dank Prudence Lawday und Maria Costa, die immer wissen, wo es lang geht, immer ein offenes Ohr haben und oft für einen Plausch zu haben sind.

Vielen Dank auch an Timo Koch, Dominik Riesterer, Felix Ischinger und Sina Ackermann für ihre fleißige Unterstützung.

Majid Hassanizadeh und Wolfgang Ehlers danke ich für die Übernahme der Mitberichte. Majid Hassanizadeh danke ich außerdem für die produktive Zeit, die ich im wunderschönen Utrecht verbringen durfte.

Außerdem danke ich der DFG für die Finanzierung der Arbeit und des dreimonatigen Forschungsaufenthalts an der Utrecht University im Rahmen des Exzellenzclusters Simulation Technology (SimTech).



# Contents

<b>Nomenclature and Abbreviations</b>	<b>III</b>
<b>List of Figures</b>	<b>XVII</b>
<b>List of Tables</b>	<b>XXV</b>
<b>Abstract</b>	<b>i</b>
<b>Zusammenfassung</b>	<b>iii</b>
<b>1 Introduction</b>	<b>1</b>
<b>2 Theoretical background</b>	<b>5</b>
2.1 Coupling free flow and flow in porous media . . . . .	6
2.1.1 Coupling free flow and flow in porous media: One-phase flow . .	8
2.1.2 Coupling free flow and flow in porous media: Component and energy transport . . . . .	10
2.1.3 Coupling free flow and flow in porous media: Numerical approaches	11
2.2 Describing thin porous media . . . . .	13
2.3 Example applications . . . . .	15
2.3.1 Modelling transvascular exchange . . . . .	15
2.3.2 Modelling water management in PEM fuel cells . . . . .	17
2.4 Properties of droplets . . . . .	22
<b>3 Coupling concept for a simple interface</b>	<b>33</b>
3.1 Structures and scales: The continuum approach . . . . .	33
3.2 Subdomain model: Porous medium . . . . .	37
3.3 Subdomain model: Free flow . . . . .	41

3.4	Coupling concept: Simple interface . . . . .	42
3.4.1	Mechanical equilibrium . . . . .	45
3.4.2	Thermal equilibrium . . . . .	49
3.4.3	Chemical equilibrium . . . . .	49
<b>4</b>	<b>Coupling concepts for a complex interface</b>	<b>53</b>
4.1	Complex interface: Bundle-of-tubes model . . . . .	54
4.2	Complex interface: Drop concept . . . . .	60
4.2.1	REV drop concept . . . . .	63
4.2.2	Drop formation . . . . .	64
4.2.3	Coupling conditions for the drop-covered interface . . . . .	67
4.2.4	Combined coupling conditions for the drop-covered and drop-free interface . . . . .	71
4.2.5	Pore-velocity approach . . . . .	74
4.2.6	Drop detachment . . . . .	75
4.2.7	Influence of drops on the free gas flow . . . . .	76
4.3	Discussion of the pressure condition . . . . .	77
4.3.1	Discussion of the mechanical-equilibrium condition . . . . .	79
4.3.2	Discussion of the Young-Laplace condition . . . . .	83
<b>5</b>	<b>Numerical model</b>	<b>85</b>
5.1	Discretisation . . . . .	86
5.2	The mortar method . . . . .	89
5.2.1	Model assumptions required for the implementation . . . . .	95
5.3	Droplet-specific implementation . . . . .	97
<b>6</b>	<b>Application and results: Transvascular exchange</b>	<b>101</b>
6.1	Physiological background . . . . .	102
6.2	Coupled model for transvascular exchange: Assumptions . . . . .	108
6.3	Results . . . . .	111
6.3.1	The reference case . . . . .	111
6.3.2	Parameter study and sensitivity analysis . . . . .	117
6.3.3	Influence of lymph drainage, degradation and adsorption . . . . .	119
6.4	Discussion . . . . .	121

<b>7</b>	<b>Application and results: Water management in PEM fuel cells</b>	<b>123</b>
7.1	Technical background . . . . .	124
7.1.1	Gas channel . . . . .	126
7.1.2	Gas-diffusion layer . . . . .	127
7.1.3	Catalyst layer and membrane . . . . .	131
7.1.4	Electro-chemistry . . . . .	131
7.2	Coupled model for water management in fuel cells: Assumptions . . . .	135
7.3	Results . . . . .	137
7.3.1	Simple interface model with electro-chemistry . . . . .	138
7.3.2	Coupled model with drop formation: The reference case . . . . .	144
7.3.3	Influence of the choice of $\Omega_{\text{drop}}$ . . . . .	149
7.3.4	Parameter study with a simplified model . . . . .	153
7.3.5	Pore-velocity approach . . . . .	160
7.4	Discussion . . . . .	161
<b>8</b>	<b>Final remarks</b>	<b>163</b>
8.1	Summary and conclusions . . . . .	163
8.2	Outlook . . . . .	168
	<b>Bibliography</b>	<b>171</b>
<b>A</b>	<b>Drop details</b>	<b>189</b>
A.1	Capillary pressure exerted by the curved drop surface . . . . .	189
A.2	Evaporation from drops . . . . .	190
<b>B</b>	<b>Software revisions</b>	<b>195</b>



# Nomenclature

## Greek letters

$\alpha$	-	charge-transfer coefficient
$\alpha_{BJ}$	-	Beavers-Joseph coefficient
$\beta$	rad	azimuthal angle in the contact area
$\delta$	m	thickness of the bundle-of-tubes model
$\delta_{mem}$	m	thickness of the membrane
$\delta_{shoulder}$	m	thickness of the fuel-cell shoulder
$\varepsilon$	-	normalized sensitivity coefficient
$\eta_{act}$	V	activation losses
$\eta_{conc}$	V	concentration losses
$\eta_{ohmic}$	V	ohmic losses
$\gamma_{gs}$	N/m	interfacial tension of gas in contact with the solid phase
$\gamma_{lg}$	N/m	interfacial tension of liquid in contact with the gas phase
$\gamma_{ls}$	N/m	interfacial tension of liquid in contact with the solid phase
$\Gamma$		the interface
$\lambda_g$	J/m s K	heat conductivity of the gas phase
$\lambda_l$	J/m s K	heat conductivity of the water phase
$\lambda_{mem}$	J/m s K	effective heat conductivity of the membrane
$\lambda_{pm}$	J/m s K	effective heat conductivity of the porous medium
$\lambda_s$	J/m s K	heat conductivity of the solid phase of a porous medium

$\lambda_{\text{shoulder}}$	$\text{J/m s K}$	effective heat conductivity of the fuel-cell shoulder
$\lambda_{\text{void}}$	$\text{J/m s K}$	effective heat conductivity of the pore space of a porous medium
$\lambda$		Lagrange multiplier
$\lambda_p$	Pa	Lagrange multiplier for the normal forces at the interface
$\lambda_{p_{\text{drop}}}$	Pa	Lagrange multiplier for the internal drop pressure
$\lambda_T$	$\text{J/m}^2 \text{ s}$	Lagrange multiplier for the energy flux at the interface
$\lambda_{V_{\text{drop}}}$	mol	Lagrange multiplier for the storage of the water component inside the drop $\lambda_{V_{\text{drop}}} = \varrho_{l,\text{drop}} x_{l,\text{drop}}^w V_{\text{drop}}$
$\lambda_{v_x}$	$\text{m/s}$	Lagrange multiplier for the horizontal velocity at the interface
$\lambda_{v_y}$	$\text{mol/m}^2 \text{ s}$	Lagrange multiplier for the vertical mass flux at the interface
$\lambda_x$	$\text{mol/m}^2 \text{ s}$	Lagrange multiplier for the component flux at the interface
$\mu_\alpha$	Pa s	dynamic viscosity of phase $\alpha$
$\mu^\kappa$	Pa s	dynamic viscosity of component $\kappa$
$\omega$		test function
$\Omega$		model domain
$\Omega_{\text{drop}}$	$\text{m}^2$	drop-REV or area of influence of one drop at the interface
$\Phi$	-	porosity
$\pi$	Pa	osmotic pressure
$\psi$	$\text{J/mol}$	chemical potential
$\psi_\alpha^\kappa$	$\text{J/mol}$	chemical potential of component $\kappa$ in phase $\alpha$
$\varrho_\alpha$	$\text{mol/m}^3$	molar density of phase $\alpha$
$\varrho_\alpha^m$	$\text{kg/m}^3$	mass density of phase $\alpha$

$\varrho^\kappa$	mol/m <sup>3</sup>	molar density of component $\kappa$
$\sigma_d$	-	osmotic reflection coefficient
$\sigma_f$	-	reflection coefficient
$\boldsymbol{\sigma}$	Pa	stress tensor
$\tau$	-	tortuosity
$\boldsymbol{\tau}$	Pa	$\boldsymbol{\tau} = \tau_{ij}$ shear stress
$\theta$	rad	contact angle
$\theta_a$	rad	advancing contact angle
$\theta_r$	rad	receding contact angle
$\theta^*$	rad	static contact angle
$\xi$		Lagrange-multiplier test function
$\chi_{\text{tiss}}^\kappa$	kg/kg	integrated mass fraction of component $\kappa$ in the tissue
$v$	-	load transfer number
<b>Roman letters</b>		
a	-	activity
$a_{\text{drop}}$	-	ratio of the area covered by a drop to the area of influence $\Omega_{\text{drop}}$
$a_{\text{drop}}^o$	-	ratio of the drop surface area to the area of influence $\Omega_{\text{drop}}$
$a_{\text{fc}}$	-	surface increasing factor
$a_g$	-	ratio of the area in contact with the free gas flow
A	m <sup>2</sup>	area
$A_{\text{drop}}^{\text{CA}}$	m <sup>2</sup>	area covered by a drop / drop contact area
$A_{\text{drop}}^o$	m <sup>2</sup>	drop surface area
$A_{\text{drop}}^{o*}$	m <sup>2</sup>	surface area of the cap of a drop
$A_{\text{free}}$	m <sup>2</sup>	area where porous medium and free flow are in direct contact
$A_g$	m <sup>2</sup>	contact area of free and porous-medium gas phase at the interface
$A_\Gamma$	m <sup>2</sup>	area of the interface $\Gamma$
$A_{\Gamma\alpha}$	m <sup>2</sup>	area of the interface $\Gamma$ taken up by phase $\alpha$

$A_{GC}$	$m^2$	cross-section of the gas channel
$A_l$	$m^2$	contact area of free gas and porous-medium liquid phase at the interface
$A_{pore}$	$m^2$	cross-section of a pore
$A_{lymph}$	$m^2$	surface area of the lymphatic vessels
$b$	$m$	depth
$B_i$	$m^3$	box $i$ in the discretisation scheme
$c_s$	$J/mol\ K$	specific heat capacity of the solid phase
$c_w$	-	drag coefficient
$c_0^\kappa$	$mol/cm^2$	concentration of component $\kappa$ at the reaction surface at reference conditions
$c^\kappa$	$mol/cm^2$	concentration of component $\kappa$ at the reaction surface
$d_{drop}$	$m$	drop diameter
$D_{cap}^\kappa$	$m^2/s$	diffusion coefficient of component $\kappa$ in the capillary
$D_{wall}^\kappa$	$m/s$	diffusion coefficient of component $\kappa$ in the capillary wall
$D_\alpha^\kappa$	$m^2/s$	diffusion coefficient of component $\kappa$ in phase $\alpha$
$D_\alpha^{\kappa,pm}$	$m^2/s$	porous-medium diffusion coefficient of component $\kappa$ in phase $\alpha$
$D_{tiss}^\kappa$	$m^2/s$	diffusion coefficient of component $\kappa$ in the tissue
$E$		element of the finite-element approximation
$E$	$V$	fuel-cell voltage
$E_0$	$V$	ideal, reversible fuel-cell voltage under standard conditions
$E_{th}$	$V$	thermo-neutral fuel-cell voltage
$f_{evap}^\kappa$	$mol/m^2\ s$	evaporation flux of component $\kappa$ from the drop surface
$f_N$		Neumann boundary flux
$f_{\bar{r}_{pore}}$	$\%$	percentage per pore-size class

$F$	C/mol	Faraday constant: 96 485.3365 C/mol
$F_{\text{drag}}$	N	drag force
$F_{p\mathbf{v}^2}$	N	force caused by the dynamic pressure
$F_{\gamma l g}^{\text{max}}$	N	maximum retention force of the drop
$F_{\text{lift}}$	N	lifting force
$F_p$	N	pressure force
$F_{gs}$	N	surface-tension force between solid $s$ and gas $g$ phase
$F_{lg}$	N	surface-tension force between liquid $l$ and gas $g$ phase
$F_{sl}$	N	surface-tension force between solid $s$ and liquid $l$ phase
$F_{\tau}$	N	shear force
$\mathbf{f}$	mol/m <sup>2</sup> s	flux term
$\mathbf{f}^{\text{ff}}$	mol/s	flux term in the free-flow region
$\mathbf{f}^{\kappa}$	mol/m <sup>2</sup> s	component flux term
$\mathbf{f}_m$	mol/m <sup>2</sup> s	mass flux term
$\mathbf{f}_v$	N/m <sup>2</sup>	momentum flux term
$\mathbf{f}^{\text{pm}}$	mol/s	flux term in the porous medium
$\mathbf{f}_{\text{pore}}$	mol/s	flux term in a pore
$\mathbf{f}_T$	J/m <sup>2</sup> s	energy flux term
$g$	J/mol	specific Gibbs free energy
$\Delta g_0$	J/mol	free activation enthalpy
$\mathbf{g}$	m/s <sup>2</sup>	gravity vector
$h^{\kappa}$	J/mol	specific enthalpy of component $\kappa$
$h_{\alpha}$	J/mol	specific enthalpy of phase $\alpha$
$h_{\text{vap}}$	J/mol	specific enthalpy of vaporisation
$h$	m	height
$\bar{h}_{\text{drop}}$	m	average drop height
$H_{gl}^a$	-	Henry coefficient for the component air
$i$	A/m <sup>2</sup>	current density
$i_0$	A/m <sup>2</sup>	exchange current density
$\mathbf{I}$		unit matrix

<b>J</b>		the jacobian
$k$	1/s	first-order rate constant
$k_{r\alpha}$	-	relative permeability of phase $\alpha$
$k_{\text{off}}$	1/s	kinetic constant (backward reaction)
$k_{\text{on}}$	$\text{m}^3/\text{mol s}$	kinetic constant (forward reaction)
$K_i$	$\text{m}^2$	component of the porous-medium permeability
$K_{\text{lymph}}$	$\text{m}/\text{Pa s}$	hydraulic conductivity of the lymphatic-vessel wall
$K_{\text{wall}}$	$\text{m}/\text{Pa s}$	hydraulic conductivity of the capillary-vessel wall
$K_{\text{xx}}$	$\text{m}^2$	intrinsic permeability in x direction
$K_{\text{yy}}$	$\text{m}^2$	intrinsic permeability in y direction
<b>K</b>	$\text{m}^2$	intrinsic permeability
$L_{\text{drop}}$	m	length of the contact line of a sessile drop
$M$	$\text{mol}/\text{m}^3$	storage term
$M^\kappa$	$\text{mol}/\text{kg}$	molar mass of component $\kappa$
$n_{e^-}$	-	number of electrons
$n_{\text{it}}$	-	number of Newton steps
$n_{\text{max}}$	-	maximum number of Newton steps
$n_{\bar{i}\text{pore}}$	-	number of pores per class of the pore distribution
$n_{\text{target}}$	-	target number of Newton steps
$n_{H_2O}$	-	water-transport number in the membrane
$N$		ansatz function of the finite-element approximation
<b>n</b>	-	normal vector
<b>n<sub>f</sub></b>	$\text{m}^2$	normal vector of the sub-control volume face
$p_0$	Pa	reference pressure
$p$	Pa	pressure
$p_\alpha$	Pa	pressure of phase $\alpha$
$p_c$	Pa	capillary pressure
$p_{\text{drop}}$	Pa	pressure inside a drop

$p_g^{\text{O}_2}$	Pa	partial pressure of oxygen in the gas phase $g$
$p_g^{\text{O}_2,\text{in}}$	Pa	partial pressure of oxygen in the gas phase $g$ at the inlet
$p_g^{\text{O}_2,\text{ref}}$	Pa	partial pressure of oxygen in the gas phase $g$ at reference conditions
$p_{\text{pore}}$	Pa	pressure inside a pore
$p$		parameter
$p_{\text{sat}}^w$	Pa	water vapour pressure
$p_{\text{sat,Kelvin}}^w$	Pa	water vapour pressure determined with the Kelvin equation
$p^{\text{eff}}$	Pa	effective pressure
$q$	mol/m <sup>3</sup> s	source/sink term
$q_\alpha$	mol/m <sup>3</sup> s	source/sink term of phase $\alpha$
$q_{\text{ads}}^\kappa$	mol/m <sup>3</sup> s	sink term for component $\kappa$ due to adsorption
$q_\alpha^\kappa$	mol/m <sup>3</sup> s	source/sink term of component $\kappa$ in phase $\alpha$
$q_{\text{deg}}^\kappa$	mol/m <sup>3</sup> s	sink term due to degradation
$q_{\text{lymph}}^\kappa$	mol/m <sup>3</sup> s	sink term for component $\kappa$ due to lymph drainage
$q_{\text{lymph}}$	mol/m <sup>3</sup> s	sink term due to lymph drainage
$qT$	J/m <sup>3</sup> s	energy source/sink term
$r$	m	radius
$r_{\text{drop}}^{\text{CA}}$	m	radius of the contact area
$r_{\text{drop}}$	m	drop radius
$\bar{r}_{\text{pore}}$	m	average pore radius
$R$	m	mean curvature
$R_{\text{ohm}}$	$\Omega/\text{cm}^2$	specific ohmic resistance
$R_0$	mol/m <sup>3</sup>	receptor-ligand concentration
$\mathbf{R}$	-	the residual
$\mathfrak{R}$	J/mol K	ideal gas constant: 8.314 J/mol K
$s$	J/mol K	specific entropy
$S_f$		sub-control volume face

$S$	-	saturation
$S_\alpha$	-	saturation of phase $\alpha$
$S_\alpha^R$	-	residual saturation of phase $\alpha$
$t_{1/2}$	s	half-life
$t$	s	time
$T$	K	temperature
$T_c$	K	critical temperature
$T_\alpha$	K	temperature of phase $\alpha$
$T_{\text{ref}}$	K	reference temperature
$\mathbf{t}$		tangential vector
$\mathbf{t}_i$	-	basis of the tangent plane of the interface
$u_\alpha$	J/mol	specific internal energy of phase $\alpha$
$u$		unknown
$\hat{u}$		unknown at the node
$\tilde{u}$		finite-element approximation of the unknown
$\mathbf{u}$		vector of unknowns
$v_{\text{cap}}$	m/s	velocity inside a capillary blood vessel
$v_{\text{pore}}$	m/s	pore velocity
$v_i^k$	m <sup>3</sup>	sub-control volume $k$ in box $i$
$V_{\text{tiss}}$	m <sup>3</sup>	volume of the tissue space
$V$	m <sup>3</sup>	volume
$V_{\text{cap}}$	m <sup>3</sup>	drop-cap volume
$V_{\text{drop}}$	m <sup>3</sup>	drop volume
$V^n$	m <sup>3</sup> /mol	molar volume
$V_{\text{pores}}$	m <sup>3</sup>	volume of the pore space
$\mathbf{v}_\alpha$	m/s	$\mathbf{v}_\alpha = v_{\alpha,i}$ velocity vector of phase $\alpha$
$W$	N m	Work
$\mathbf{x}_f$		integration point in the discretisation scheme
$x_{l,\text{drop}}^\kappa$	mol/mol	mole fraction of component $\kappa$ in the drop
$x_\alpha^\kappa$	mol/mol	mole fraction of component $\kappa$ in phase $\alpha$
$X_\alpha^\kappa$	kg/kg	mass fraction of component $\kappa$ in phase $\alpha$

<b>x</b>	$\mathbf{x} = x_i = (x, y, z)$ coordinate
<b>Superscripts and Subscripts</b>	
$\alpha$	phase $\alpha \in l$ (liquid), $g$ (gas), blood (blood), if (interstitial fluid), lymph (lymph fluid)
bottom	bottom of pores
CA	contact area
cap	capillary blood vessel
$D$	Dirichlet boundary condition
drop	drop properties
forward	forward reaction
$\Gamma$	the interface
$i, j, k, l, m, n$	indices
in	inside properties
$\kappa$	component $\kappa \in w$ (water), $a$ (air), $H_2O$ , $O_2$
lymph	lymphatic space
$m$	mass
micro	quantities on the micro or pore scale
$m_i$	number of moles of species $i$ transferred dur- ing the reaction, stoichiometric ratio
$N$	Neumann boundary condition
pore	pore properties
products	products of the reaction
reactants	reactants
reverse	reverse reaction
$s$	solid phase
$T$	energy
tiss	tissue space
top	top of pores
<b>Symbols</b>	
dim	dimensions of the system
$\Delta\theta^{\max}$	rad contact-angle hysteresis $\theta_a - \theta_r$



# Abbreviations

1D	one-dimensional
2D	two-dimensional
3D	three-dimensional
Bo	Bond number: $Bo = \frac{\rho_g g d_{\text{drop}}^2}{\gamma_{lg}}$
CL	Catalyst Layer
DG	Discontinuous Galerkin
DUNE	Distributed and Unified Numerics Environment
FE	Finite Element
FV	Finite Volume
GC	Gas Channel
GDL	Gas-Diffusion Layer
MPL	Micro-Porous Layer
MRI	Magnetic-Resonance Imaging
PEM	Polymer-Electrolyte Membrane
PTFE	Polytetrafluoroethylene
Re	Reynolds number: $Re = \frac{\rho v d}{\mu}$
REA	Representative-Elementary Area
REV	Representative-Elementary Volume
VOF	Volume-Of-Fluid method



# List of Figures

1.1	Possible descriptions for the interface between free-flow and porous-medium region: A simple interface devoid of thermodynamic properties, a bundle-of-tubes approximation and a concept accounting for drop formation, growth and detachment. . . . .	2
2.1	Thin porous media can either be interface layers between free flow and porous-medium (left) or independent domains (right). . . . .	5
2.2	Coupling concepts for a single-phase flow system (reproduced from Mosthaf et al., 2011). . . . .	6
2.3	On the pore scale (left), the distribution of all phases and pore sizes is resolved. On the Representative-Elementary Volume (REV)-scale (middle), the velocity profile for coupled free flow (single-phase Stokes equations) and porous-medium flow (multi-phase Darcy’s law) is continuous and the interface can be described either as a transition zone with continuously varying parameters or as a sharp interface (partly after Chandesris and Jamet (2009))(reproduced from Mosthaf et al., 2011). . . . .	8
2.4	Drops form in the gas channel of Polymer-Electrolyte Membrane (PEM) fuel cells (reproduced from Eller et al., 2011, by permission from ECS – The Electrochemical Society). . . . .	17
2.5	Liquid water distribution (blue) in the Gas-Diffusion Layer (GDL) fibre structure and drop formation (reproduced with permission from Suresh and Jayanti, 2010, copyright 2010, The International Association of Hydrogen Energy). . . . .	21

2.6	Drop constitutions showing the static contact angle $\theta^*$ , the drop height $h$ , the curvature radius $r_{\text{drop}}$ and the radius of the contact surface $r_{\text{drop}}^{\text{CA}}$ for: a) a wetting drop, b) a non-wetting drop and c) a drop influenced by flow forces developing contact-angle hysteresis between advancing $\theta_a$ and receding $\theta_r$ contact angle. . . . .	23
2.7	a) Force balance at the contact line, where $F_{lg}$ , $F_{gs}$ , $F_{sl}$ are the surface-tension forces between the solid, liquid and gas phases, b) in total, the horizontal components of the surface-tension forces cancel out. . . . .	24
2.8	Deformed drop. . . . .	25
2.9	Contact line movement with time for different static contact angles (top: $\theta^* = 110^\circ$ , bottom: $\theta^* = 170^\circ$ ). (reproduced from Qin et al., 2012d, by permission from ECS – The Electrochemical Society). . . . .	28
3.1	Definition of the REV (adapted from Helmig, 1997). . . . .	34
3.2	Van-Genuchten parametrisation of the macroscopic capillary-pressure–saturation relationship (after Gostick et al., 2006). . . . .	36
3.3	A simple interface devoid of thermodynamic properties couples free-flow and porous-medium region. . . . .	43
3.4	Transition from pore-scale to a volume-averaged description: a) on the pore-scale shear stresses occur due to interactions between the gas phase in the free-flow region and the gas, fluid and solid phases in the porous medium, b) a volume-averaged description has to account for all these contributions while the different phases of the porous medium are not locally resolved any more, c) exchange processes also occur between the two mobile phases of the porous medium and the free gas phase (pore-scale description), d) on the REV-scale, coupling conditions account for these processes without resolving them locally (reproduced from Mosthaf et al., 2011). . . . .	44

3.5	Mechanical equilibrium at the pore scale and at the REV-scale (normal component). The coupling conditions on the REV scale have to account for the traction between the gas phase in the free-flow region and the gas, solid and water phase in the porous medium. Capillarity effects occur at the interface between the fluid phases in the porous medium as well as at the interface to the gaseous free-flow region. On the REV-scale capillary pressure is a function of the water saturation (reproduced from Mosthaf et al., 2011). . . . .	46
3.6	Mechanical equilibrium at the pore-scale and at the REV-scale (tangential component). The coupling conditions on the REV-scale have to account for the traction between the gas phase in the free-flow region and the gas, solid and water phase in the porous medium (reproduced from Mosthaf et al., 2011). . . . .	48
3.7	Chemical equilibrium at the pore-scale and at the REV-scale. On the micro-scale, equilibrium conditions between the gas phase in the free-flow region and the two phases in the porous medium have to be formulated, consisting of continuity of chemical potential. On the REV-scale, continuity of chemical potential between the phases inside the porous medium is assumed and continuity of mole fractions is applied as coupling condition between the gas phase in the free flow and porous medium (reproduced from Mosthaf et al., 2011). . . . .	50
4.1	A pore-scale bundle-of-tubes approach couples free-flow and porous-medium region. . . . .	55
4.2	Pore-size distribution at the interface which is sorted into classes of tubes with mean radius $\bar{r}_{\text{pore}}$ with $f_{\bar{r}_{\text{pore}}}$ percent of pores and $n_{\bar{r}_{\text{pore}}}$ pores per class.	55
4.3	Force and flux balance for one pore. . . . .	56
4.4	The interface concept accounts for drop formation, growth and detachment. The coupling conditions account for the mass and energy of the drop. . . . .	61
4.5	Simplified spherical drop. . . . .	62
4.6	Conceptual model: The interface $\Gamma$ between free flow and porous medium is divided into an integral number of areas of influence $\Omega_{\text{drop}}$ . There is one drop per area of influence. The area of influence is partly covered by the drop $\Omega_{\text{drop}} = A_{\text{free}} + A_{\text{drop}}^{\text{CA}}$ . . . . .	64

4.7	A bundle-of-tubes model describes the interface region between porous medium and free flow representing pores ending in the free-flow region. Possible pore constitutions are: a) gas flux through pore, b) water meniscus in pores with direct evaporation, c) spherical caps with a diameter equal to the pore diameter, d) a drop fed by the porous medium, evaporating into the free-flow region. . . . .	65
4.8	Force balance with drop: internal and external pressure forces related through capillary pressure. . . . .	69
4.9	Internal force balance on a drop. . . . .	69
4.10	Free flow influenced by drops. . . . .	76
4.11	a) pressure equilibrium determining whether a meniscus will move inside a pore, b) mechanical equilibrium on top of a water-filled pore. . . . .	78
4.12	The free-flow normal force, the porous-medium phase pressures $p_g^{\text{pm}}$ and $p_l^{\text{pm}}$ and the internal drop pressure $\lambda_{\text{drop}}$ are related by microscopic and macroscopic capillary-pressure formulations. . . . .	83
5.1	Schematic description of the spatial discretisation (box scheme). . . . .	87
5.2	Mortar elements between free-flow and porous-medium compartment: Introducing Lagrange multipliers as new unknowns at the interface. . . . .	89
5.3	Visualisation of the REV drop concept: instead of one small drop per grid cell, the volumes are assembled to form one large drop per drop REV. Drop radius and the area weighting $a_g$ and $a_{\text{drop}}$ are calculated from the large drop and are valid for all contributing cells. . . . .	96
5.4	Visualisation of the implementation: Before each Newton step, the formation of new drops is checked and calculated. Then the drop grows and the new drop properties are calculated. At the end of a time step, the detachment condition is evaluated. . . . .	99
6.1	Structure of the capillary wall showing a variety of para- and transcellular pathways. 1+2) Intercellular clefts of different diameter, 3+4) open and closed fenestrations, 5) pores of fused vesicles, 6) vesicles, 7+8) transcellular transport mechanisms. The exact structure is strongly dependent on anatomic location and physiological/pathological conditions (Baber, 2009). . . . .	104

6.2	Capillary types (R. Krstic (1991) Human Microscopic Anatomy, in Junqueira et al. (2002), with kind permission of Springer, Heidelberg). . . . .	104
6.3	Pressure significantly decreases along the capillary. In combination with osmotic pressure, this leads to inward and outward flow. . . . .	106
6.4	Numerical setup of the model for transvascular exchange: the top region corresponds to half of the capillary blood vessel, symmetry conditions are assumed on the top boundary, blood and therapeutic agent enter from the left. The bottom region corresponds to the tissue space, the interstitial pressure is fixed at the bottom boundary, all other boundaries are outflow conditions. The two regions are separated by the thin porous medium representing the capillary wall. . . . .	112
6.5	Isobars (grey) and stream lines (orange) in the tissue compartment. The grey line depicts the border stream line: left of the black line fluid is reabsorbed coming from the bottom of the tissue. Therapeutic agent reaches the right part only by diffusion. (with kind permission of Ischinger (2013)) . . . . .	112
6.6	Interstitial pressure: the grey plane represents the size of the tissue compartment, above is the capillary wall. There is a strong pressure gradient across the capillary wall. Pressure significantly decreases from the arterial to the venous end. (with kind permission of Ackermann (2013))	114
6.7	Distribution of therapeutic agent (red) within the two-dimensional model domain in healthy tissue. (with kind permission of Ackermann (2013))	115
6.8	Surface plot of the mass fraction of therapeutic agent in the tissue compartment. The line plot of the mass fraction just below the capillary wall has a local maximum due to the reflection coefficient. (with kind permission of Ischinger (2013)) . . . . .	116
6.9	Line plots of mass fraction in the tissue parallel to the capillary wall for different diffusion coefficients (left) and reflection coefficients (right). The values are taken from the literature review and the variation of $\pm 5\%$ refers to the reference value given in table 6.1. Higher diffusion and reflection coefficients cause a more even distribution of the therapeutic agent. (with kind permission of Ischinger (2013)) . . . . .	116

6.10	Results of the sensitivity analysis: the normalized sensitivity coefficient $\varepsilon$ is shown for each varied parameter. Red illustrates a high influence ( $\varepsilon \geq 0.5$ ), yellow illustrates medium influence ( $\varepsilon = 0.25$ ), green means no influence ( $\varepsilon = 0.0$ ). In between the color scale is linear. (with kind permission of Ischinger (2013)) . . . . .	118
7.1	Schematic of a fuel cell. Oxygen and hydrogen are supplied through the gas channels (Gas Channel (GC)), diffuse through the gas-diffusion layers (GDL) and react in the catalyst layer (CL). Water is produced. Anode and cathode are separated by a proton-conducting membrane (PEM). .	125
7.2	Schematic of voltage-current diagram for a PEM fuel cell under current load (after Ochs, 2008). . . . .	133
7.3	The capillary-pressure-saturation and the relative-permeability-saturation curve measured by Acosta et al. (2006). . . . .	139
7.4	Numerical setup of the fuel-cell model: the top region corresponds to the gas channel where a parabolic velocity profile is specified with no slip on the top boundary. The gas phase flows from left to right. At the inlet, the mole fraction of water is set to $0.02 \text{ mol/mol}$ . The bottom regions correspond to the gas-diffusion layer and catalyst layer. Neumann no-flow conditions are specified at all porous-medium boundaries. The water saturation is set to 0.1 initially. At the bottom, source and sink terms for water, oxygen and energy represent the catalyst layer and the current density is calculated. . . . .	140
7.5	Distribution of the mole fraction of water in the gas phase $x_g^{\text{H}_2\text{O}}$ in the free-flow region and of the water saturation $S_l$ in the porous medium. The arrows indicate the free-flow velocity. . . . .	141
7.6	Distribution of the mole fraction of oxygen in the gas phase $x_g^{\text{O}_2}$ in the free-flow region and the porous medium. The arrows indicate the free-flow velocity. . . . .	142
7.7	Distribution of the gas-phase pressure $p_g$ in the free-flow region and the porous medium. The arrows indicate the free-flow velocity. . . . .	142
7.8	Distribution of the temperature $T$ in the gas-phase in the free-flow region and the porous medium scaled to the porous medium. The arrows indicate the free-flow velocity. . . . .	142
7.9	Current density $i$ in the catalyst layer at the bottom of the domain. . .	143

7.10	Pressure field and water distribution after 305 s: The inertial term in the Navier-Stokes equations causes oscillations in the pressure field in the free-flow region, which extend into the porous medium. The water distribution is not affected. . . . .	144
7.11	Numerical setup of the fuel-cell model: the top region corresponds to the gas channel where a parabolic velocity profile is specified with a no-slip condition on the top and bottom boundary. The gas phase flows from left to right. The bottom region corresponds to the gas-diffusion layer. Neumann no-flow conditions are specified at the left and right boundaries. At the bottom, Neumann fluxes for water and air represent the catalyst layer. . . . .	145
7.12	Water distribution and temperature field after 293 s without drops. The arrows indicate the free-flow velocity. . . . .	145
7.13	Drop volume $V_{\text{drop}}$ over time showing cyclical drop formation and detachment and the influence of evaporation from the drop surface. The corresponding maximal drop height is approximately 0.7 mm. . . . .	147
7.14	Distribution of the mass fraction of water in the gas phase $X_g^w$ in the free-flow region and of the water saturation $S_l$ in the porous medium with drop evaporation. At a later point in time, oscillations occur at the interface. . . . .	148
7.15	Distribution of the mass fraction of water in the gas phase $X_g^w$ in the free-flow region and of the water saturation $S_l$ in the porous medium without drop evaporation. The arrows indicate the free-flow velocity. . . . .	148
7.16	Velocity field of water and gas phase in the porous medium at $t = 294$ s	148
7.17	Pressure $p$ at the interface at $t = 294$ s. . . . .	149
7.18	Total mass fluxes $\mathbf{f}_m$ across the interface plotted over time. The fluxes from the free-flow $\mathbf{f}_m^{\text{ff}}$ and the porous-medium $\mathbf{f}_m^{\text{pm}}$ region are discontinuous due to the storage in the drop. . . . .	150
7.19	Drop volume $V_{\text{drop}}$ over time showing the first and second drop for a simulation with two drops forming at the interface ( $\Omega_{\text{drop}} = 0.5A_\Gamma$ ). . . . .	151
7.20	Drop volume $V_{\text{drop}}$ over time showing for a simulation with four drops forming at the interface ( $\Omega_{\text{drop}} = 0.25A_\Gamma$ ). . . . .	152
7.21	Distribution of the mass fraction of water in the gas-phase $X_g^w$ in the free-flow region and of the water saturation $S_l$ in the porous medium for a different number of drops. . . . .	152

7.22	Total mass fluxes $\mathbf{f}_m$ across the interface plotted over time. The fluxes from the free-flow into the porous-medium region are discontinuous due to the storage in the drop. . . . .	153
7.23	Drop volume $V_{\text{drop}}$ over time showing that drops do not form until the drop-formation condition is fulfilled. Evaporation still shows a stagnation of the growth process. The corresponding maximal drop height is approximately 0.95 mm. . . . .	154
7.24	Drop volume $V_{\text{drop}}$ over time showing the influence of a variation in contact angle. . . . .	155
7.25	Drop volume $V_{\text{drop}}$ over time showing the influence of the maximally sustained contact-angle hysteresis. . . . .	156
7.26	The different capillary-pressure–saturation curves. . . . .	157
7.27	Drop volume $V_{\text{drop}}$ over time showing the influence of the variation of the capillary-pressure–saturation curve. . . . .	158
7.28	Drop volume $V_{\text{drop}}$ over time showing the influence of the variation of the maximal free-flow velocity. . . . .	159
7.29	Drop volume $V_{\text{drop}}$ over time showing the influence of the drag-force calculation. . . . .	159
7.30	Drop volume $V_{\text{drop}}$ over time calculated with the pore-velocity approach. . . . .	160
8.1	Graphical abstract: the left column illustrates the coupling concepts developed in this work, the centre column shows the example applications and the right column illustrates possibilities for further research. . . . .	164
A.2.1	Drop. . . . .	191

# List of Tables

3.1	Porous-medium equations and associated primary variables. . . . .	39
3.2	Material laws and equations of state dependent on primary variables. .	40
3.3	Free-flow equations and associated primary variables. . . . .	41
3.4	Summary of the balance equations describing the different submodels and listing of the according primary variables. . . . .	43
6.1	Parameter values for simulations with healthy tissue. The symbols listed under “Sink terms” are explained in section 6.2. . . . .	113
6.2	Parameter values for simulations with tumour tissue differing from the healthy case shown in table 6.1. The symbols listed under “Sink terms” are explained in section 6.2. . . . .	120
7.1	Exponents for the empirical definitions of the diffusion coefficient (see equations (7.4) and (7.5)). . . . .	129
7.2	Parameter values used in the fuel-cell simulations. . . . .	138
7.3	Initial and boundary conditions. . . . .	139
7.4	Parameter values of the electro-chemistry model based on Acosta et al. (2006). . . . .	141
7.5	Pore distribution of the gas-diffusion layer after Acosta et al. (2006). . .	146
7.6	Interface coverage ratio $a_{\text{drop}}$ . . . . .	151
A.1.1	The magnitude of the geometric factor in the $p_c$ calculation for a range of static contact angles relevant for PEM fuel cells. . . . .	190
B.0.1	Software revisions used for the simulations of transvascular exchange (chapter 6, Ischinger (2013) and Ackermann (2013)) and drop dynamics in PEM fuel cells (chapter 7). . . . .	196



# Abstract

The objective of this work is the development of model concepts and methods for the coupling of free flow and flow in porous media. Coupling concepts of varying complexity ranging from a simple to a pore-scale to a complex interface approach are derived. The main focus is the development and testing of an REV-scale coupling concept that accounts for drop dynamics at the interface. The developed coupling concepts are based on the assumption of thermodynamic equilibrium and on flux balances. The formulation of mechanical equilibrium in the pore-scale and complex interface concept is challenging due to the scale-dependent definition of pressure. The combination of microscopic and macroscopic pressure formulations causes pressure jumps at the interface and non-physical pressure gradients. Hence, an extensive discussion of the pressure conditions is given.

The coupled model is implemented in the C++ simulator DuMu<sup>x</sup> (Flemisch et al., 2011) using the mortar method. The applicability of the developed concepts is assessed on the basis of two applications: transvascular exchange and drop dynamics in PEM fuel cells.

**The simple interface concept** In Mosthaf et al. (2011) and Baber et al. (2012), we develop a concept for coupling non-isothermal compositional two-phase flow in the porous-medium with a non-isothermal compositional single-phase system in the free-flow region. The concept is based on the two-domain approach with a simple interface devoid of thermodynamic properties.

In this work, the simple interface concept is applied to model transvascular exchange. The simulations reproduce filtration and reabsorption and reveal the influence of wall and tissue parameters on the final distribution of therapeutic agents. However, the complex structure of the micro-vascular wall and the influence of the different pathways cannot be resolved by the presented approach.

**The bundle-of-tubes concept** In some applications, the complex structure of the interface and the processes happening therein cannot be described by a simple interface devoid of thermodynamic properties. In such cases, it might be beneficial to resolve the interface layer or interface region on the pore-scale. We present a first step towards a resulting coupled pore-/REV-scale model where the interface is described by a bundle-of-tubes approach. The coupling concept between the one-phase free-flow, the pore-scale

and the two-phase porous-medium model is based on flux continuity and the assumption that pore- and REV-scale pressure are equal.

**The complex interface concept** We develop an REV-scale interface concept that describes drop formation, growth and detachment on a hydrophobic interface between free and porous-medium flow. The interface stores the mass and energy of the drops without resolving them. The direct exchange between free-flow and porous-medium region next to the drop is also part of the coupling concept since it preserves the exchange processes described by the simple interface concept. The fraction of the interface which is covered by drops is used to obtain an area-weighted average of the coupling conditions with and without drop so that coupling conditions for the whole interface are obtained.

The complex interface concept captures drop formation, growth and detachment. These processes are influenced by the conditions of both the free-flow and porous-medium region. The temporal evolution of the drop volume is an outcome of the model. The number of drops that can form on the interface is defined a priori by choosing the size of a drop REV. Neither the influence of the drops on the free-flow conditions nor film flow or sliding and merging of drops is included since the focus is on the interface description.

The model is applied to simulate drop formation in the cathode of PEM fuel cells. In fuel cells, water is generated by the electro-chemical reaction in the catalyst layer and flows through the hydrophobic porous fibre structure of the GDL. Reaching the GC, water forms drops on the hydrophobic interface between GC and GDL. The drops significantly influence the water management in fuel cells which must be optimised to achieve good performance and durability.

The numerical results show that it is possible to include drop dynamics in the REV-scale coupling conditions between free and porous-medium flow. Drop formation, growth and detachment are represented correctly, if the evaporation from the drop surface is neglected. The interface-coverage ratio, which is an indicator for the quality of the water management, can be predicted. The simulations for a higher number of drops suggest that the interface conditions dominate the system. A parameter study shows that interface wettability and free-flow velocity have a significant influence on the drop growth and detachment.

In summary, this work reveals the potential of the developed coupling concepts to deal with realistic problems and exposes the need for further improvement and development.

# Zusammenfassung

Das Ziel dieser Arbeit ist die Weiterentwicklung von Modellkonzepten und Methoden zur Beschreibung von Strömungs- und Transportprozessen in gekoppelten Systemen aus freier Strömung und porösem Medium. Dabei können sich diese beiden Strömungsgebiete entweder in direktem Kontakt befinden oder durch eine dünne Zwischenschicht voneinander getrennt sein. Das Hauptaugenmerk liegt auf der Entwicklung eines Modellkonzepts zur Beschreibung von Tropfenbildung, -wachstum und -ablösung an der Grenzfläche der beiden Gebiete. Eine derartige Tropfendynamik beeinflusst zum Beispiel das Wassermanagement in Polymer-Elektrolyt-Membran(PEM)-Brennstoffzellen.

Die entwickelten Kopplungsbedingungen basieren auf der Bilanzierung von Massen-, Impuls- und Energieflüssen sowie der Annahme von thermodynamischem Gleichgewicht an der Grenzfläche. Dabei ist die Definition des mechanischen Gleichgewichts aufgrund der skalenabhängigen Definition des Drucks konzeptionell schwierig. Die Kombination aus Porendruck und gemitteltem Druck kann zu Drucksprüngen und unphysikalischen Druckgradienten an der Grenzfläche führen. Daher beinhaltet die Arbeit eine ausführliche Diskussion der auftretenden Probleme und der gewählten Lösungsansätze.

Im Rahmen der Arbeit wurden drei Ansätze mit unterschiedlichem Komplexitätsgrad entwickelt und in die C++-Simulationsumgebung DuMu<sup>x</sup> implementiert. Die Anwendbarkeit der entwickelten mathematischen Modellkonzepte wird anhand zweier Beispiele gezeigt. Neben der bereits genannten Tropfendynamik in PEM-Brennstoffzellen, werden die Austauschprozesse zwischen kapillaren Blutgefäßen und umliegendem Gewebe untersucht.

**Das Konzept der *simplen* Grenzfläche** Zunächst werden der Grenzfläche keine thermodynamischen Eigenschaften zugewiesen. Sie kann weder Masse noch Impuls noch Energie speichern. Dieses Konzept wurde in Mosthaf et al. (2011) und Baber et al. (2012) für nicht-isotherme Mehrkomponentensysteme mit einer Phase in der freien Strömung und zwei Phasen im porösen Medium entwickelt und in Mosthaf et al. (2014) zur Beschreibung von Verdunstungsprozessen aus feuchten Böden herangezogen.

Im Rahmen dieser Arbeit wird der entwickelte Ansatz zur Modellierung von Austauschprozessen zwischen Blutgefäß und Gewebe verwendet. Medikamente werden häufig

direkt über die Blutbahn verabreicht. Sie breiten sich über das Blutgefäßsystem im Körper aus und können in den kleinsten Blutgefäßen, den Kapillaren, in das umliegende Gewebe übergehen. Der Austausch wird durch die äußerst dünne Kapillarwand reguliert. Um die Austauschprozesse im Modell abzubilden, wird ein System bestehend aus einer Kapillare (freie Strömung), der Kapillarwand und dem umliegenden Gewebe (poröses Medium) betrachtet. Die Kapillarwand ist als eine Zwischenschicht zu sehen, die freie Strömung und poröses Medium voneinander trennt. Sie wird hier als eine dünne, poröse Schicht mit einem Kontinuumsansatz modelliert.

Die Simulationsergebnisse zeigen, dass sich die grundlegenden Prozesse, wie Filtration und Reabsorption, reproduzieren lassen. Im Rahmen einer Parameterstudie kann der Einfluss von Wand- und Gewebeeigenschaften auf die Medikamentenverteilung gezeigt werden. Auch der Einfluss von Abbau im Blut, Lymphdrainage und Reaktionen mit den Gewebezellen wird mit einfachen Ansätzen untersucht. Aufgrund prinzipiell mangelnder Informationen über die tatsächlich dominierenden Prozesse und Transportwege ist die Aussagekraft des Modells jedoch gering.

Vor allem die Beschreibung der Kapillarwand bietet Potential für Verbesserung. Die Anwendbarkeit des Kontinuumsansatzes im Falle der dünnen, heterogenen Kapillarwand ist fragwürdig. Alternativ könnte in Zukunft ein Ansatz basierend auf zweidimensionalen Kontinua, wie er in Qin and Hassanizadeh (2014) vorgestellt wurde, angewendet werden.

Um einen tatsächlichen Beitrag zu einem besseren Verständnis der Austauschprozesse und zur Verbesserung von Therapien leisten zu können, wäre außerdem ein detailliertes Modell der Kapillarwand nötig. Dafür könnte diese auf der Porenskala aufgelöst werden.

**Das Röhrenmodell** Motiviert durch die zuvor genannte begrenzte Anwendbarkeit des Modells in Bezug auf transvaskuläre Austauschprozesse, wird im Rahmen dieser Arbeit ein theoretischer Entwurf für einen Kopplungsansatz auf der Porenskala erarbeitet. Die Schicht zwischen freier Strömung und porösem Medium wird dabei durch ein Röhrenmodell beschrieben. Die Kopplungsbedingungen basieren auf analytischen Lösungen für eindimensionale Strömungen in Rohren und auf der Kontinuität der Flüsse. Des Weiteren wird angenommen, dass Porendruck und gemittelter Druck gleichgesetzt werden können. Der Modellansatz kann die Grundlage für die Kopplung von Kontinuums- und Porennetzwerkmodellen bilden.

**Das Konzept der komplexen Grenzfläche** Um Tropfenbildung-, wachstum und -ablösung beschreiben zu können, wurde das bestehende Kopplungskonzept erweitert, sodass die Masse und Energie der Tropfen von den Kopplungsbedingungen erfasst wird, ohne die Tropfenform und -verteilung aufzulösen. Das Kopplungskonzept folgt dem Kontinuumsansatz. Die exakte Position der Tropfen ist nicht bekannt; nur der Anteil der Grenzfläche, der mit Tropfen bedeckt ist, wird ermittelt. Das flächengewichtete Mittel aus Kopplungsbedingungen mit und ohne Tropfen liefert die Bedingungen für die gesamte Grenzfläche. Diese speichert nun die Masse und Energie der Tropfen und hat daher den Charakter einer *komplexen* Grenzfläche.

Die mögliche Anzahl von Tropfen wird vor Simulationsbeginn festgelegt und sollte durch experimentelle Untersuchungen gestützt sein. Die zeitliche Entwicklung der Tropfenvolumina sowie der Anteil der Grenzfläche, der mit Tropfen bedeckt ist, können durch das Modell vorhergesagt werden.

PEM Brennstoffzellen sind eine vielversprechende innovative Technologie, die in Kombination mit dem Ausbau erneuerbarer Energien das wachsende Mobilitätsbedürfnis der Gesellschaft effizient und emissionsarm befriedigen könnte. In Brennstoffzellen reagieren Wasserstoff und Sauerstoff zu Wasser. Die Wassermenge und -verteilung hat einen großen Einfluss auf die Leistung und Lebensdauer der Zelle. Zur Verbesserung des Wassermanagements ist ein fundiertes Wissen über die Strömungsvorgänge nötig. Wasser wird in der Katalysatorschicht gebildet und strömt durch die hydrophobe Fasermatrix der Gasdiffusionsschicht in Richtung Gaskanal. An der Grenzfläche zwischen Gaskanal und poröser Diffusionsschicht bilden sich Tropfen, die einerseits die Strömung im Kanal und andererseits die Bedingungen in der Diffusionsschicht signifikant beeinflussen.

Die Simulationsergebnisse zeigen, dass das entwickelte Modell in der Lage ist, Tropfenbildung-, wachstum und -ablösung abzubilden, wenn die Verdunstung der Wassertropfen vernachlässigt wird. Eine Parameterstudie verdeutlicht den Einfluss der Tropfenzahl, der Strömungsgeschwindigkeit im Gaskanal und der Benetzungseigenschaften der Gasdiffusionsschicht.

Die durchgeführten Simulationen sind ein Machbarkeitsnachweis, erlauben aber nur vage Vorhersagen für realistische Systeme. Bisher können der Einfluss der Tropfen auf die freie Strömung sowie das Schicksal der sich ablösenden Tropfen nicht abgebildet werden. Tropfen können auf der Grenzfläche entlang rutschen, sich vereinen, von der Strömung

transportiert werden oder einen Wasserfilm in den hydrophilen Ecken des Gaskanals bilden. Außerdem verursachen sie einen signifikanten Druckabfall im Gaskanal, der die Effizienz der Brennstoffzelle in der Praxis stark beeinflusst.

Zusammenfassend verdeutlicht diese Arbeit das Potential der entwickelten Kopplungskonzepte zur Beantwortung realistischer Fragestellungen und zeigt Möglichkeiten für die Weiterentwicklung und Verbesserung der Modelle auf.

# 1 Introduction

The interaction of free and porous-medium flow is dominated by interface processes. The quantification of transfer fluxes of mass, momentum and energy is crucial for applications like evaporation from soil, water management in fuel cells or transport of therapeutic agents in the human body.

The suitability of a mathematical description of the interface structure and interface processes depends on the characteristics and complexity of the considered application. The free-flow and porous-medium domains can be either separated by an interface layer or be in direct contact. Such different interface structures can be described by different conceptual models. If the free-flow and porous-medium region touch, the system can either be described based on a transition zone with continuously varying properties (one-domain approach) or with a sharp interface and appropriate coupling conditions (two-domain approach). A sharp interface devoid of thermodynamic properties is referred to as *simple interface* in the following (Hassanizadeh and Gray, 1989). In case of an interface layer between free and porous-medium flow, a structure much thinner than the surrounding regions strongly influences the behaviour of the whole system. Hence, an adequate description for these possibly complex, heterogeneous, thin structures has to be found. In any case, the challenge is the correct and efficient description of the governing forces, conditions and exchange processes at the interface which are influenced by the non-isothermal, compositional, multi-phase nature of the surrounding systems. This can be particularly demanding due the thin heterogeneous porous structures or due to complex processes like film flow, pooling and drop formation or electro-chemical processes.

In the scope of this work, three different interface concepts are derived which are illustrated in figure 1.1. The concept of a **simple interface** with coupling conditions based on thermodynamic equilibrium and flux continuity is the starting point. Based

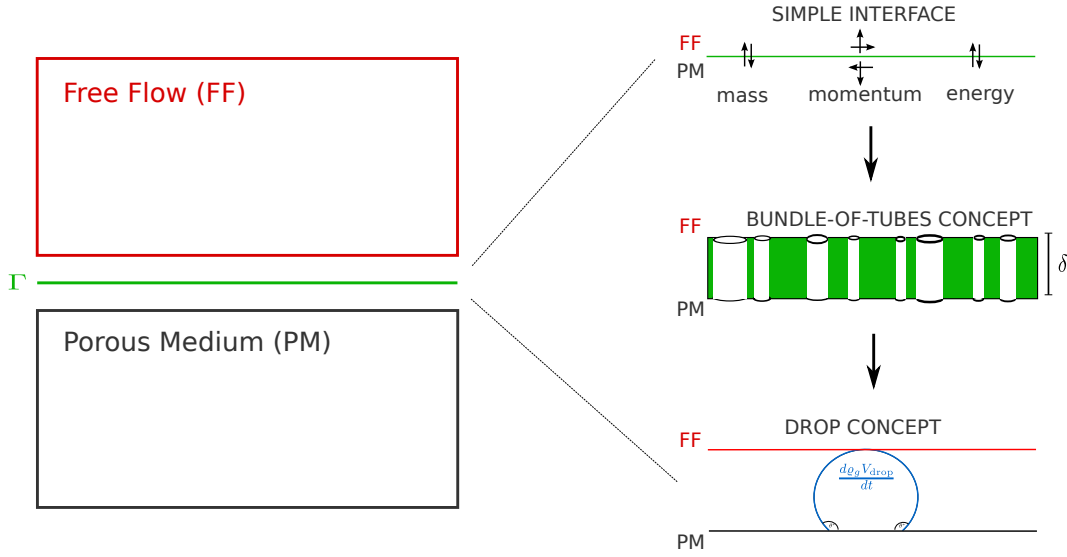


**Figure 1.1:** Possible descriptions for the interface between free-flow and porous-medium region: A simple interface devoid of thermodynamic properties, a bundle-of-tubes approximation and a concept accounting for drop formation, growth and detachment.

on its assumptions and requirements, a pore-scale interface concept is developed using a **bundle-of-tubes** approximation for the interface. The final model includes both the simple and the pore-scale approach and accounts for **drop** formation, growth and detachment at a hydrophobic interface between free-flow and porous-medium region.

The simple interface concept proved to be feasible for the description of evaporation processes from soil, for example (Mosthaf et al., 2011, Baber et al., 2012). However, features like boundary layers and local variations of the water content significantly influence the evaporation rate and can hardly be captured by this approach (Mosthaf et al., 2014). The formation of drops or films on the porous surface are other features with a significant influence which had not been considered in the Representative-Elementary Volume (REV)-scale coupling approaches until now. One solution for capturing more complex interface processes is to resolve the interface region on the pore-scale (in the following also referred to as micro-scale) and to couple it to the surrounding REV-scale (or macro-scale) models. A first step in this direction is the application of a bundle-of-tubes concept. Based on the two previous concepts, drop dynamics are integrated into the REV-scale coupling concept. Consequently, the interface can store the mass, momentum and energy of the drops, causing discontinuities of thermodynamic quantities at the interface and accounting for the complex interface dynamics in an averaged manner. Such an interface is called *complex interface* in the following.

The objective of this thesis is the extension of the existing coupling concept, which couples REV-scale models for free and porous-medium flow by a simple interface, towards a coupled micro-/macro model and a complex interface. The focus is on the extension of the REV-scale coupling concept to account for drop formation, growth and detachment - processes that occur in Polymer-Electrolyte Membrane (PEM) fuel cells, for example. The derivation of this complex interface description is based on phenomenological considerations and not derived rigorously by homogenisation. The most appropriate interface concept is applied to the physiological and technical problems of transvascular exchange and water management in fuel cells, respectively. All models are based on the assumption of thermodynamic equilibrium and on the balance of mass and energy fluxes. Processes like turbulent free flow, boundary layer effects, radiation and pore-scale features as discussed in Mosthaf et al. (2014) are not considered in the scope of this work.

The thesis is structured as follows: Chapter 2 provides the necessary context and background, summarising the existing modelling approaches for coupled systems (see section 2.1). Recent ideas for an alternative description of so-called *thin porous media* as two-dimensional (2D) continua are presented in section 2.2. Such approaches might be interesting for modelling fuel-cell diffusion media or interface layers like the micro-vascular wall. A review of the state-of-the-art models for transvascular exchange and water management in fuel cells is given in sections 2.3.1 and 2.3.2. Furthermore, the basic physics and principles of droplets are explained in section 2.4 to facilitate the understanding of the drop concept.

The consistent, general coupling concept which is published in Mosthaf et al. (2011) and Baber et al. (2012) is summarised in chapter 3. The coupled model for non-isothermal compositional one-phase free flow and non-isothermal compositional two-phase porous-medium flow is explained. Its applicability, limitations and extensions are discussed in Mosthaf et al. (2014) but are not part of this work.

The new concepts for a more complex interface are explained in detail in chapter 4. A first step towards a coupled micro-/macro-model is the approximation of the interface region or interface layer by a bundle-of-tubes concept (see section 4.1). The mathematical coupling concept is general enough to be extended to couple REV-scale models with a real pore-network model. In section 4.2, drop dynamics are integrated into the REV-scale

coupling concept yielding a complex interface which stores mass and energy of droplets without resolving them.

In chapter 5, the numerical implementation, which is based on the mortar method, is delineated. All models are implemented in the open-source C++ simulator DuMu<sup>x</sup> (Flemisch et al., 2011).

The adaptation of the general coupling concepts to the needs of actual applications is shown in chapters 6 and 7. There, the systems are simplified to 2D problems. Transvascular exchange between blood vessels and porous tissue happens across the micro-vascular wall. The latter can be seen as an interface layer between free flow and porous medium. In the scope of this work, its structure and pathways are not resolved on the pore-scale but described as another REV-scale structure. The coupling concept of a simple interface is employed. The complex interface concept is applied to the coupled system of gas channel and fibrous gas-diffusion layer in the cathode of PEM fuel cells. A parameter study is presented investigating the influence of flow conditions, material properties and model assumptions on drop formation, growth and detachment.

Chapter 8 concludes with a summary and outlook. The model which is based on the simple interface concept reproduces the basic processes of transvascular exchange, but the results motivate a more detailed resolution of the transvascular pathways. In a pore-scale interface model, the paracellular pathways could be represented by non-intersecting, circular pores yielding a bundle-of-tubes description. The complex interface concept captures drop formation, growth and detachment. These processes are influenced by the conditions of both the free-flow and porous-medium region. To describe the pressure loss in the gas channel and the fate of the drops after detachment, the free flow model needs to be extended.

## 2 Theoretical background

Based on an extensive literature review, the theoretical background of this thesis is given in this chapter. First, the fundamentals of coupling free and porous-medium flow are summarised. Until recently, the coupling concepts were limited to one-phase systems and based on a simple interface concept. The existing approaches describing flow, component transport and energy distribution are reviewed in section 2.1 and their strengths and limitations are evaluated.

In coupled systems, thin porous structures, which have a very small thickness compared to their width, might play an important role. Such structures are called *thin porous media*. On the one hand, the interface itself can be such a thin porous medium, if it is made up of an individual layer with specific material properties (left in figure 2.1). The wall of capillary blood vessels is such an interface layer which separates the blood flow from the porous tissue. On the other hand, the domains involved in coupled free and porous-medium flow can be thin porous media themselves (right in figure 2.1), like the porous gas-diffusion layer in PEM fuel cells. When dealing with such thin porous media, both REV-scale and pore-scale descriptions might eventually meet their limits, either due to a lack of resolution or a lack of efficiency. The 2D-continua approach presented by Qin and Hassanizadeh (2014) offers a promising alternative. It is discussed in section 2.2 to give a broader perspective, but is not applied in the scope of this work.

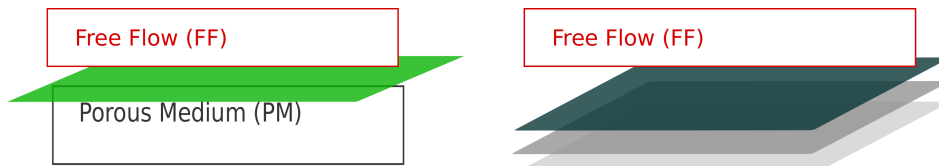


**Figure 2.1:** Thin porous media can either be interface layers between free flow and porous-medium (left) or independent domains (right).

The focus of this thesis is on the development of coupling concepts with varying complexity. Their applicability is assessed with the help of two applications. The exchange between blood vessels and surrounding tissue is governed by the permeability of the capillary wall. In polymer-electrolyte fuel cells, drops form at the interface between porous diffusion layer and gas channel. Drop formation, growth and detachment significantly influence the mass, momentum and energy transfer across the interface. A literature review of the existing approaches for modelling transvascular exchange as well as water management and drop formation in fuel cells can be found in sections 2.3.1 and 2.3.2. The required basic knowledge about droplets is also provided (see section 2.4).

## 2.1 Coupling free flow and flow in porous media

When coupling free and porous-medium flow, the challenge is to derive a general, efficient model that accounts for the physics at the interface. Moreover, systems of equations of different order have to be coupled. The coupling concepts presented in the literature differ mostly in the description of the interface which can either be described as a transition zone (one-domain approach, see figure 2.2a) or as a sharp interface (two-domain approach, see figure 2.2b).

In a special issue, Shavit (2009) summarises the efforts that have been made to derive consistent coupling approaches. Until then, all approaches were limited to single-phase systems in both domains. Since many applications involve multi-phase flow, we developed

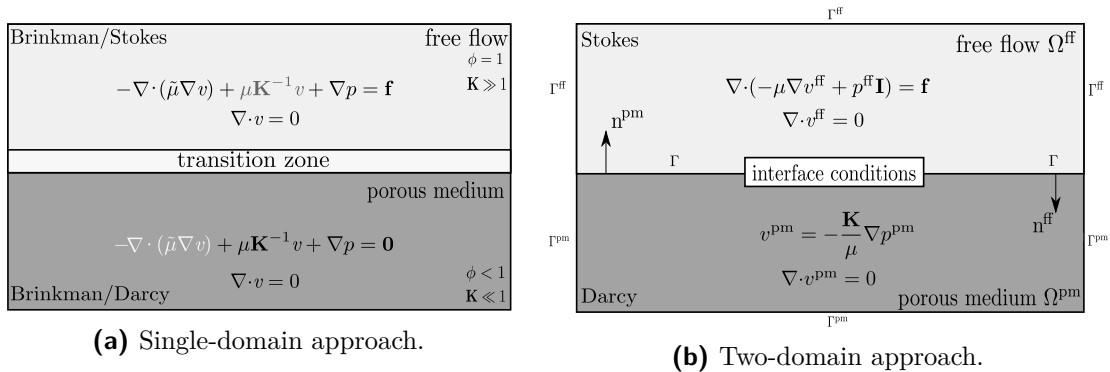


**Figure 2.2:** Coupling concepts for a single-phase flow system (reproduced from Mosthaf et al., 2011).

---

a concept for coupling non-isothermal, compositional two-phase flow in the porous-medium with a non-isothermal compositional single-phase system in the free-flow region in Mosthaf et al. (2011) and Baber et al. (2012). The concept is based on the two-domain approach with a simple interface devoid of thermodynamic properties and is explained in detail in section 3.4. A similar approach is used by Chen et al. (2014) and Brenner et al. (2014). The latter apply it to the interface between a nuclear-waste geological repository and the ventilation gallery.

Mosthaf et al. (2014) assess the model's capability to predict evaporative drying rates from hydrophilic soil influenced by flow through a wind tunnel. They find that the model can predict the behaviour during and the transition between the different stages of evaporation theoretically. A comparison with experiments clearly shows the achievements and limitations of the model. A laminar free-flow model underestimates the evaporation rate significantly. The implementation of algebraic turbulence models (Fetzer, 2012) yields a match of the initial rate, but cannot predict the course of the drying curve over time. Mosthaf et al. (2014) find that the influence of pore-scale processes, surface water content, boundary-layer thickness and porous-medium properties is significant and needs to be included in the REV-scale model. They include a simple boundary-layer model approximating the diffusion from the interface into the free-flow region by a solution-dependent condition dependent on the boundary-layer thickness. The effect of the variation in surface water content is included through a mass-transfer coefficient according to Schlünder (1988) and Haghighi et al. (2013). Furthermore, the capillary-pressure–saturation relation has a strong impact on the transition between the different stages of evaporation.

In the following, coupling concepts and possible numerical implementations for non-isothermal compositional single-phase systems which can be found in the literature are summarised.

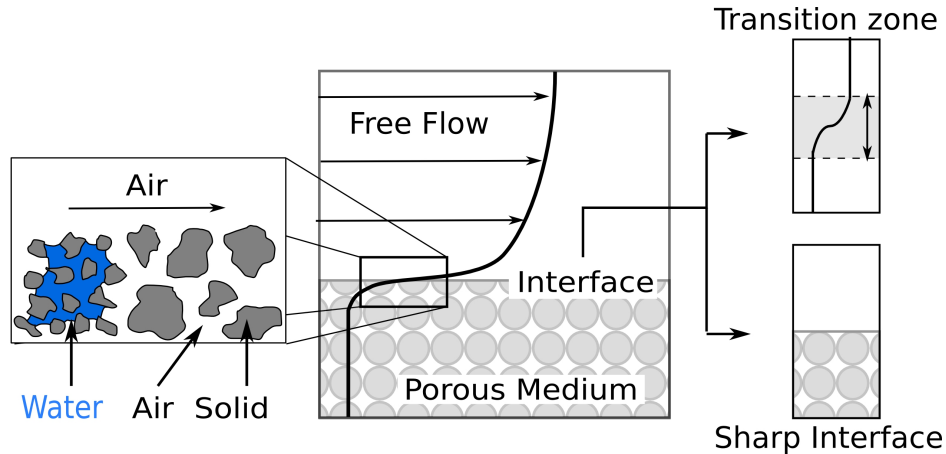


**Figure 2.3:** On the pore scale (left), the distribution of all phases and pore sizes is resolved. On the REV-scale (middle), the velocity profile for coupled free flow (single-phase Stokes equations) and porous-medium flow (multi-phase Darcy’s law) is continuous and the interface can be described either as a transition zone with continuously varying parameters or as a sharp interface (partly after Chandesris and Jamet (2009))(reproduced from Mosthaf et al., 2011).

### 2.1.1 Coupling free flow and flow in porous media: One-phase flow<sup>1</sup>

On the pore-scale, the pore structure is resolved and the same type of equations, the Navier-Stokes equations, are used to describe the flow in the free-flow region and within the pores. On the REV-scale, however, the potential theory is applied in the porous medium using Darcy’s law and coupling strategies have to be found to couple the two domains. Two basic strategies for the description of mass and momentum transfer in coupled free and porous-medium flow on the Darcy-scale can be identified (Jamet et al., 2009, Shavit, 2009) and are illustrated in figure 2.3. In the single-domain approach, one set of equations is assumed to be valid in the whole domain and the coupling is realised via a transition zone where the material parameters are varied. In the two-domain approach, two sets of equations are used for the subdomains which are coupled in terms of suitable transfer conditions at the interface.

The single-domain approach (figure 2.2a) usually involves the solution of the Brinkman equation in the entire domain (Brinkman, 1947). This model results from a superposition of the Stokes equations and Darcy’s law, requiring the introduction of an apparent

<sup>1</sup>This section is published in Mosthaf, K., Baber, K., Flemisch, B., Helmig, R., Leijnse, A., Rybak, I., and Wohlmuth, B. (2011). A coupling concept for two-phase compositional porous media and single-phase compositional free flow. *Water Resources Research*, 47:W10522556.

---

viscosity inside the porous medium. There is no need to specify coupling conditions between the free-flow region and the porous medium since velocity and stress continuity are automatically satisfied. The transition between the two regions is achieved either by specifying the continuous spatial variation of physical properties such as permeability and porosity within an equi-dimensional transition zone or by admitting a discontinuous variation across a lower-dimensional interface. The physical transition zone is usually only a few grain diameters thick (Jamet et al., 2009). The choice of the parameters in this zone may decisively influence the results and, generally, it is hardly possible to determine them (Goyeau et al., 2003, Rosenzweig and Shavit, 2007).

The two-domain approach (figure 2.2b) is based on different models in the two subdomains: the Navier-Stokes equations, which in case of very low Reynolds numbers (Reynolds number:  $Re = \frac{\rho v d}{\mu}$  (Re)) can be simplified to the Stokes equations, are applied in the free-flow region and Darcy's law is used in the porous medium. In addition to the subdomain models, suitable coupling conditions have to be specified at the interface. Realistically, processes between free-flow and porous-medium regions are not only interface-driven but the two regions interact via a transition zone where changes in fluid properties and strong gradients in the driving forces may occur. According to Hassanizadeh and Gray (1989), this transition zone can either be approximated by a simple interface devoid of thermodynamic properties or by an interface that can store and transport mass and other thermodynamic quantities. The simple interface corresponds to continuity of thermodynamic properties at the interface, whereas an interface with thermodynamic properties leads to discontinuities which are then characterised by appropriate conditions involving jump coefficients (Ochoa-Tapia and Whitaker, 1995, Chandesris and Jamet, 2009). One way to derive the coupling conditions is to apply the volume-averaging technique (Gray et al., 1993, Whitaker, 1999). The resulting conditions include excess surface terms to account for the transition between the free-flow and the porous-medium region (Ochoa-Tapia and Whitaker, 1995, Chandesris and Jamet, 2009). Based on these excess terms, the jump coefficients can be derived (Valdes-Parada et al., 2009a). However, the coupling conditions are often simplified by neglecting the contribution of these terms and assuming continuity, since the characteristics of these surface excess terms at the interface are hard to determine (Valdes-Parada et al., 2007). The decision of continuity or discontinuity has to be made for mass and momentum respectively. One approach is to guarantee the continuity of normal forces and mass conservation across the interface (Layton et al., 2002). Alternatively, Ochoa-Tapia and

Whitaker (1995) proposed a stress-jump condition obtained by volume averaging. A two-step upscaling approach and the method of matched asymptotic expansions is used by Chandesris and Jamet (2006, 2007) for the derivation of a velocity-jump and a stress-jump condition at the interface. Moreover, the Beavers-Joseph velocity-jump condition (Beavers and Joseph, 1967) is often used to provide a connection between the tangential free-flow velocity and the seepage velocity in the porous medium. It is required as an additional boundary condition for the Stokes domain, because the equations in the two domains are of different order. The relation between velocities and shear stress is given in terms of an additional parameter, the Beavers-Joseph coefficient. This parameter depends on the properties of the fluid and the permeable material and can be determined experimentally or by numerical simulation. Saffman (1971) shows that the filtration velocity (porous medium) in the Beavers-Joseph condition is negligible in comparison to the free-flow velocity. Hence, the Beaver-Joseph condition becomes a Robin boundary condition for the tangential free-flow velocity as it contains the derivative of the velocity as well as the velocity itself. The Beavers-Joseph-Saffman condition has been mathematically justified by Jäger and Mikelić (2000, 2009) by means of homogenisation. There exist several alternatives to the Beavers-Joseph condition, (Levy and Sanchez-Palencia, 1975, Alazmi and Vafai, 2001, Goyeau et al., 2003).

Summing up, the challenge of the one-domain approach is the description of the spatial variation of the parameters in the transition zone, whereas in case of the two-domain approach, the definition of coupling conditions that represent the transfer processes at the interface is the challenging task. Valdes-Parada et al. (2007) analyse the one- and the two-domain approach and point out that both can be derived by volume averaging.

### **2.1.2 Coupling free flow and flow in porous media: Component and energy transport<sup>2</sup>**

The concepts presented above have been developed for single-phase single-component systems describing the coupling for mass and momentum. However, in many applications compositional multi-phase flow occurs, and there is an urgent need for a more general model.

---

<sup>2</sup>This section is published in Mosthaf, K., Baber, K., Flemisch, B., Helmig, R., Leijnse, A., Rybak, I., and Wohlmuth, B. (2011). A coupling concept for two-phase compositional porous media and single-phase compositional free flow. *Water Resources Research*, 47:W10522556.

For an extension to a non-isothermal system, coupling approaches for the energy balance at the interface have to be found. Prat (1990) uses the method of volume-averaging to analyse the one- and two-domain approach for conductive heat transfer between free-flow and porous medium. Jamet et al. (2009) show the equivalence of the discontinuous one- and two-domain approach for a heat-conduction problem, provided that the one-domain approach is mathematically interpreted in the sense of distributions. Alazmi and Vafai (2001) review coupling conditions for conductive and convective heat transfer and find that both continuity and discontinuity of temperature and heat flux have been applied in various combinations showing only minor differences.

For the description of transport processes in compositional single-phase flow, it is again possible to use either the one- or the two-domain approach. Valdes-Parada et al. (2006, 2007), for example, show the coupling of diffusive mass flux across the interface using both approaches. In Valdes-Parada et al. (2006), they describe diffusive mass transport between micro- and macro pores in packed-bed reactors and derive a jump condition for the two-domain approach from volume-averaging. Neglecting surface accumulation and surface transport excess, the jump in the diffusive flux is determined by a jump coefficient that accounts for the reaction rate at the fluid-porous interface. This jump condition is supplemented by a continuity assumption for the concentrations at the interface. In case of a non-reactive medium, this leads to continuity of the diffusive mass flux and the concentration. Valdes-Parada et al. (2009b) extend the concept to convective transport along with adsorption and reaction in the porous medium.

In summary, the concepts explained above allow the description of compositional non-isothermal systems and need to be extended in order to be applicable to multi-phase systems.

### 2.1.3 Coupling free flow and flow in porous media: Numerical approaches<sup>3</sup>

Various discretisation techniques, such as finite elements, mixed methods, control-volume techniques, and Discontinuous Galerkin (DG) approaches have been developed and

---

<sup>3</sup>This section is published in Baber, K., Mosthaf, K., Flemisch, B., Helmig, R., Müthing, S., and Wohlmuth, B. (2012). Numerical scheme for coupling two-phase compositional porous-media flow and one-phase compositional free flow. *IMA Journal of Applied Mathematics*, 77(6):887–909. first published online July 26, 2012.

analysed for coupled single-phase single-component systems. In Discacciati et al. (2002, 2007), a formulation based on the Beavers-Joseph-Saffman interface condition (Beavers and Joseph, 1967, Saffman, 1971) is studied, continuous finite elements are used in both regions and subdomain-iterative methods for solving coupled problems are developed. Cao et al. (2010) apply the Beavers-Joseph condition without the Saffman simplification. The application of the continuous Finite Element (FE) method for the Stokes problem with a mixed FE method for the Darcy problem is considered in Layton et al. (2002) where the coupling conditions are imposed with the help of Lagrange multipliers. The existence and uniqueness of a weak solution of the coupled system is proved. Discontinuous-Galerkin methods for the coupled system are proposed in Rivière (2005) and Girault and Rivière (2009), and the existence of a weak solution with some a-priori estimates is shown. Discacciati and Quarteroni (2004) use a Galerkin-Finite-Element approximation in both domains and propose iterative subdomain methods based on either a Dirichlet-Neumann method or a Conjugate Gradient method for the solution of the Steklov-Poincaré interface problem. In Rivière and Yotov (2005) the DG method is used in the Stokes region and coupled to a mixed FE method in the Darcy region. Mixed FE methods are developed and analysed for coupled systems with large cavities in the porous medium by Arbogast and Brunson (2007). Quite recently, new types of mixed DG techniques are successfully applied to the Stokes-Darcy coupling (Rivière and Kanschat, 2010). Chidyagwai and Rivière (2010) compare different combinations of DG and FE methods with respect to accuracy, robustness and mass conservation. However, all these techniques have been developed for a single-phase single-component system.

For the discretisation of the present compositional coupled model, the implicit Euler time-integration and a vertex-centred control-volume finite-element method (also called box method, Huber and Helmig (2000)) in space is used. In the free-flow domain, a stabilisation technique similar to Franca et al. (1993) is generalised and implemented for the Stokes equations. Special care at the interface is required to avoid spurious oscillations. The arising non-linear system is solved fully implicitly applying a Newton solver (see section 5).

## 2.2 Describing thin porous media

As mentioned above, thin porous media can occur as individual domains (right in figure 2.1) or as interface layers (left in figure 2.1). Systems like paper printers, filters, hygiene products and fuel cells involve thin, heterogeneous porous structures. The endothelium of the capillary blood vessels is a thin porous interface layer. The thickness of these media, which is of the same order of magnitude as the pore diameter, is very small compared to the other dimensions. The description and coupling of such thin porous layers cannot be done with the models collected in the previous sections. On the one hand, the applicability of the REV-continuum concept - and the use of Darcy's law - is highly questionable since the existence of an REV is not necessarily given. According to Qin and Hassanizadeh (2014), an REV "must be much larger than the pore-scale dimensions but much smaller than the modelling domain". Even if the existence of an REV is assumed, a three-dimensional (3D) description of such a thin porous medium requires a very fine grid resolution causing high computational demands and grid cells of the size of a pore. On the other hand, the description of systems of several thin porous media is challenging since the dimension of the interfaces is of the same order of magnitude as the thin porous medium itself. Furthermore, all processes might be strongly influenced by these interfaces. Hence, new concepts are required for the description of a thin porous medium itself, for the coupling to other thin porous media, and for the coupling to surrounding regions.

Qin and Hassanizadeh (2014) suggest to define an REV of which the vertical extent corresponds to the height of the porous layer and apply a thermodynamic volume-averaging approach. Consequently, the thin porous-medium layers are treated as 2D continua described by planar balance equations and macroscopic thickness-averaged properties. In a layered system, the thin porous media interact by source and sink terms. Thus, lateral processes can be described and vertical processes are included by interaction with adjacent layers.

Roth et al. (2013) support the approach by experimental results. The Gas-Diffusion Layer (GDL) of PEM fuel cells is a thin porous medium with a large aspect ratio (thickness with respect to lateral extent) and the definition of a 3D REV and the application of classical averaged continuum models has been questioned. Roth et al. (2013) obtain x-ray tomographic images of running fuel cells. They average the obtained information

over the GDL thickness, reducing the data sets from 3D to 2D. The analysis of the thickness-averaged data yields values for Representative-Elementary Area (REA)s for porosity and saturation. Roth et al. (2013) find that the REA for the water distribution depends on the water saturation and is not equal to the structural REA for porosity obtained from a dry GDL. The saturation-dependence of the REA can be explained with the process of water filling the pores of a hydrophobic porous medium. Large pores are filled first but might be far apart, causing an increase in the REA-size. Note that the REA can be transformed to the REV for thin porous media by multiplication with the layer thickness.

Qin and Hassanizadeh (2014) develop the general theoretical framework for non-isothermal multi-phase flow and transport including phase change in a deformable thin porous medium. Interfaces between fluid phases or porous layers cannot store thermodynamic properties or sustain stress. The system of equations is developed for two interacting continua, but can be extended to an arbitrary number of layers as long as the interaction is only affected by the two adjacent layers. To derive the constitutive relations needed to close the system and to specify the exchange terms, the system is simplified to an immiscible two-phase system without phase change. Then, constitutive relationships describing the interaction of the 2D continua are postulated exploiting the entropy inequality. The authors conclude that Darcy's law may be used within the 2D layers if the system is close to equilibrium and if fluid motion due to thermal effects, the variation of the layer thickness and the effects of variations in the saturation are neglected. The pressure gradient is the main driving force for the mass exchange between layers. The effect of imperfect boundaries between layers has to be included in material coefficients which need to be determined experimentally.

In the future, this new concept should be used to describe thin porous layers like the GDL in fuel cells or the micro-vascular wall. An appropriate coupling concept for the coupling to surrounding macro-models needs to be developed. The coupling of a bundle-of-tubes model to surrounding 3D-REV-scale models is a first step in this direction (see section 4.1). A pore-network description of the thin interface layer would increase the understanding and facilitate the final step where 2D continua describing the interface layer are coupled to 3D porous-medium and free-flow regions. This is beyond the scope of this work.

## 2.3 Example applications

The interface concepts developed in the scope of this work are employed to model transvascular exchange and drop dynamics in fuel cells. In the following two sections, conceptual models and numerical approaches employed in the literature to describe these systems are collected.

### 2.3.1 Modelling transvascular exchange

The efficient and uniform systemic delivery of therapeutic agents to the target cells is crucial for all therapies. From the point of entry to the target cells, many different barriers have to be overcome. Therapeutic agents distribute in the circulatory system of the body and are delivered to the organ level. In the smallest blood vessels, the therapeutic substances cross the blood-vessel walls and enter the surrounding interstitial space. This process is called *transvascular exchange*. It occurs through a variety of para- and transcellular pathways like pores of different size or vesicles. Finally, the agent distributes in the tissue and interacts with the target cells. Chauhan et al. (2011) discuss the influence of tumour properties and the tumour micro-environment on the distribution of therapeutic agents. They conclude that tumours impede all steps of the distribution process reducing the blood flow, increasing the interstitial pressure and the interstitial resistance, and reducing transvascular exchange to diffusion. Erbertseder et al. (2012) model the whole distribution process. Flow and transport in the blood vessels is described with a vascular-graph model (Reichold, 2011). The vascular graph model is coupled sequentially to a double-continuum model describing the interaction between vascular and tissue compartment. The resulting distribution of the therapeutic agent in the tissue space is fed to a cell-population model predicting apoptotic cell death (Hasenauer et al., 2010b).

Transvascular exchange determines the amount of therapeutic agent which reaches the tissue space. Motivated by the complexity of transvascular pathways, efforts have been made to develop simplified models in order to explain capillary permeability. Generally, the Starling law (see equation (6.1)) and the Staverman-Kedem-Katchalsky (see equation (6.2)) equation are employed which describe transvascular solvent and solute flow dependent on gradients in pressure, osmotic pressure and concentration.

Zhao et al. (2007) use these equations to determine source terms for a 3D computational model of the interstitial tumour space. They analyse the influence of heterogeneous transvascular hydraulic and diffusive permeability based on the measured filtration rate obtained from Magnetic-Resonance Imaging (MRI) of a mouse sarcoma. Smith and Humphrey (2007) also account for transvascular exchange by including a source term based on Starling's law in a model for convection-enhanced drug delivery in brain tissue. They assume a uniform effective vascular pressure and conclude that transvascular exchange significantly alters the interstitial fluid pressure. Pishko et al. (2011) and Magdoom et al. (2014) present an MRI-imaged-based tumour model accounting for heterogeneous vascular and tissue properties for predicting tracer distributions in different tissues. Similar to Smith and Humphrey (2007), they implement source and sink terms for transvascular and lymphatic flow in a porous-medium model assuming the vascular and osmotic pressures to be constant. Curry (1984) derives the Starling and Staverman-Kedem-Katchalsky equations based on thermodynamic principles and obtains concentration-dependent expressions for the diffusive permeability and the reflection coefficient. Moreover, he discusses model concepts like the pore theory or the fibre-matrix model and presents a mathematical model for vesicular transport based on the diffusive motion of the vesicles.

In the pore theory, the capillary wall is described as an ensemble of cylindrical pores and slits of different diameter. Michel and Curry (1999) find that the measured permeability of a continuous capillary can be reproduced by roughly 10 000 small pores with a diameter of 5 nm and less than ten large pores with a diameter of 30 nm. Formaggia et al. (2009) use a similar pore system composed of small (pore radius  $r = 4\text{-}5$  nm) and large pores (pore radius  $r = 25\text{-}30$  nm or larger). The models assume blood to be a Newtonian fluid and viscous Poiseuille flow inside the pores, and include restricted diffusion and solute exclusion at the pore entrance (Michel and Curry, 1999). The transvascular hydraulic and diffusive permeability can be calculated based on the pore geometry (Sugihara-Seki and Fu, 2005).

In the fibre-matrix model, the fibre length and size determine transvascular permeability. The fibre model is often used to describe the properties of the glycocalyx, a layer of macro-molecules and plasma proteins adsorbed to the luminal side of the capillary wall. Michel and Curry (1999) choose a fibre spacing of 7 nm. The electro-chemical processes induced by the negatively charged glycocalyx influence transvascular exchange of charged

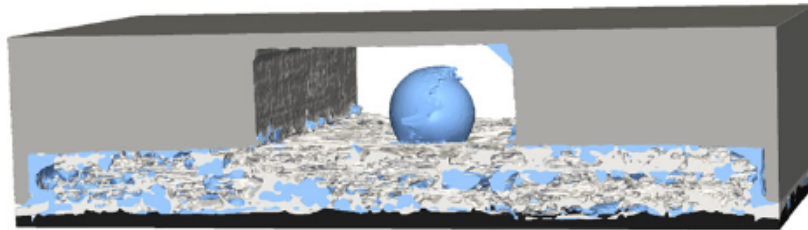


**Figure 2.4:** Drops form in the gas channel of PEM fuel cells (reproduced from Eller et al., 2011, by permission from ECS – The Electrochemical Society).

macro-molecules significantly and are explained in detail in Stace and Damiano (2001). Under equilibrium conditions, the negative charge of the glycocalyx is balanced by the salt-ion distribution in the blood, leading to concentration gradients in the mobile ion distribution. The resulting electrical field determines diffusion of charged molecules and leads to exclusion of macro-molecules from the glycocalyx. Hence, the glycocalyx is the first barrier to substance exchange and determines the number of macro-molecules that are able to enter the paracellular pores. Curry (1984) and Stace and Damiano (2001) combine Fick's law with the Nernst-Planck equation to describe transport of charged molecules influenced by an electric field.

Sugihara-Seki and Fu (2005) review models for transvascular permeability of water and solutes and mention a combination of fibre-matrix and cleft model. It consists of a finite fibre-matrix region at the entrance of clefts and pores, a small number of large 150x20 nm pores and a large number of small slits (2 nm) and pores (3 nm).

A model for transvascular exchange which couples the free blood flow to the porous wall and tissue is presented in chapter 6.

### 2.3.2 Modelling water management in PEM fuel cells<sup>4</sup>

Water management in PEM fuel cells significantly influences performance and durability. The water management is strongly influenced by the mass and energy transfer between the free flow in the Gas Channel (GC) and the two-phase flow in the porous gas-diffusion

<sup>4</sup>This section is published in Baber, K., Flemisch, B., and Helmig, R. (2014). Modelling drop dynamics at the interface between free and porous-medium flow using the mortar method. submitted to International Journal of Heat and Mass Transfer.

layer. Modelling the coupled system of GC and GDL is challenging since drops form on the hydrophobic interface (see figure 2.4).

The water distribution in the different fuel-cell components has been analysed experimentally and numerically ranging from molecular- to pore- to REV-scale investigations. Current modelling approaches for the different fuel-cell components and present research requirements are summarised in Gurau and Mann (2009), Wu et al. (2009) and Wang et al. (2011). Wang et al. (2011) stress the need for numerical models which lead to a better understanding of the highly coupled, non-linear, multi-physics processes in fuel cells. The knowledge gained will be used to increase durability and to reduce costs.

Gurau and Mann (2009, 2010) state that the water distribution in PEM fuel cells is strongly impacted by the macroscopic interfaces. Kandlikar et al. (2014) and Wang et al. (2011) stress the need for a mathematical model that can describe the transport processes across the gas-channel–gas-diffusion-layer interface. At this interface at the cathode side, evaporation occurs and sessile drops form (Gurau and Mann, 2009, 2010, Cho et al., 2012a). Once detached due to drag forces, the drops are either transported with the GC flow field or wick into the hydrophilic GC corners (Herescu and Allen, 2012). The drops influence the water distribution inside the GDL fibre structure as well as the gas flow and pressure field in the channel. Kandlikar et al. (2014) analyse the mutual interaction of drops, gas-channel walls, pressure drop in the gas channel and transport limitations across the GDL-GC interface. They analyse each process individually and provide a detailed literature review. They find that the ratio of the GDL surface covered by drops or slugs significantly influences oxygen transport and that the variation of the contact angle determines the removal of drops and slugs from the gas channel.

The processes occurring in the cathode side of fuel cells have been analysed on different scales. In the following, we will first summarise investigations of drops influenced by a flow field. Then, pore- and REV-scale approaches for the coupled system of GC, GDL and drop dynamics are reviewed.

**Investigations of drops** Chen et al. (2005) and Kumbur et al. (2006) develop analytical models for the instability of spherical drops influenced by flow at low Reynolds numbers based on a force-balance approach. Model predictions are compared with experimental data for different flow conditions and material properties. Zhang et al. (2006) observe the

water distribution in the GDL and drop formation as well as detachment due to shear forces or due to wicking into the gas-channel corners in transparent fuel cells. They find a relation between gas-flow velocity, detachment mechanism and radius. Theodorakakos et al. (2006) perform a numerical and experimental analysis of the detachment behaviour and give a comprehensive literature review of fuel-cell and drop models. They determine values for the static, advancing and receding contact angle experimentally and model the dynamic deformation and detachment process using the Navier-Stokes equations and the Volume-Of-Fluid method (VOF). Cho et al. (2012a,b) find analytical expressions for drop deformation and detachment and compare them with numerical simulations and experiments. They conclude that deformation is negligible under most operating conditions (gas-phase velocity  $\mathbf{v}_g \leq 2 \text{ m/s}$ ) and that viscous drag dominates for small drops whereas the pressure force becomes more dominant for larger drops.

These studies neglect the influence of the gas-channel geometry assuming that the drop does not touch the gas-channel walls. Gopalan and Kandlikar (2014) perform ex-situ experiments, investigating the detachment time and the required pressure drop in trapezoidal gas channels for different GC corner angles and gas velocities. They find that at low velocities (gas-phase velocity  $\mathbf{v}_g \leq 4 \text{ m/s}$ ) drops grow larger and interact with the hydrophilic channel walls, but that the drops are detached before interaction with the wall happens for larger velocities. Qin et al. (2012d) use the VOF method to describe drop and film dynamics in the gas channel. They observe a significant elongation of the contact line and a significant influence of the wettability of the gas-channel walls on the drop behaviour and film-flow development. Carton et al. (2012) analyse the coalescence of drops and slug movement comparing VOF simulations and experiments.

**Pore-scale approaches** Most of the above mentioned studies focus on drop behaviour and the interaction with the gas flow. Pore-scale simulations are used to determine effective properties and to simulate the mutual interaction of GC, GDL and drops.

Rosén et al. (2012) perform experiments with X-ray tomographic microscopy and Lattice-Boltzmann simulations in realistic GDL geometries to obtain porosity, permeability, capillary pressure, relative permeability and diffusivity from the water-saturation profiles. Luo et al. (2010) employ a pore-scale model topologically equivalent to the GDL structure. They compare non-woven paper material and woven cloth, and link water-transport characteristics to micro-structural features. Furthermore, they compute macroscopic

properties like capillary-pressure–saturation and relative-permeability–saturation relations. In Qin (2012) (Chapter 3) the GDL is described by an anisotropic, stochastically generated fibre structure. In- and through-plane permeability are calculated. Using an isothermal one-phase model, the slip velocity at the GDL-GC interface is predicted. Gostick (2013) develop a 3D pore-network model with a random architecture for the fibrous gas-diffusion layer, accounting for anisotropy and using non-cylindrical pore throats. They obtain an effective diffusivity tensor and capillary-pressure–saturation relationships.

Kuttanikkad et al. (2011) analyse the influence of wettability changes on capillary-pressure or relative-permeability–saturation relations and diffusivity using a pore-network model. They conclude that the macroscopic properties are not affected by mixed wettability as long as the fraction of hydrophilic pores is below the percolation threshold<sup>5</sup>. Above the threshold, mixed wettability has a significant influence, yielding higher relative permeabilities for the gas phase, for example. Sinha and Wang (2008) explain the behaviour of water on a mixed-wet GDL-GC interface theoretically. Water emerging from the GDL at the interface will form a film on the hydrophilic parts of the surface. When it reaches hydrophobic parts, pinning of the contact line occurs and drops form. The drops grow with increasing contact angle until a threshold contact angle is reached and the contact line unpins to let the drop grow further. They analyse the effect of mixed wettability on the water distribution inside the GDL using a pore-network model with cubic pore-bodies and pore-throats with a square cross-section. They reveal the role of capillary fingering with respect to the water-distribution process (supported by Kuttanikkad et al. (2011)) and discuss the applicability of the two-phase Darcy law. An optimal hydrophilic fraction leading to minimal transport losses is found. Based on fluorescence microscopy and pore-network modelling, Shahraeeni and Hoorfar (2013) claim that hydrophobic media lead to higher local but lower overall water saturations in the GDL.

Suresh and Jayanti (2010) perform pore-scale VOF simulations in a 2D segment of GDL and GC, investigating the influence of the GC-flow conditions on the water transport in the GDL and on the drop formation. The GDL is represented by 10 layers of cylindrical fibres. Suresh and Jayanti (2010) observe fingering and channelling within

---

<sup>5</sup>Above the percolation threshold, the connected fluid phase forms a cluster spanning the entire system (Škvor and Nezbeda, 2009).

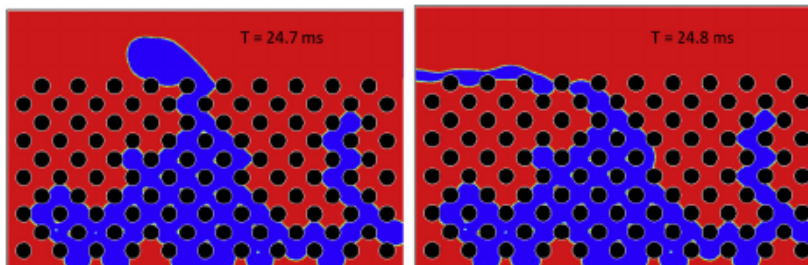


**Figure 2.5:** Liquid water distribution (blue) in the GDL fibre structure and drop formation (reproduced with permission from Suresh and Jayanti, 2010, copyright 2010, The International Association of Hydrogen Energy).

the hydrophobic fibre structure and drop formation, growth and detachment on the interface (see figure 2.5).

**REV-scale approaches** In Qin et al. (2012b,a), a macroscopic one-dimensional model for water flooding in the gas-channel is proposed. It includes the description of film flow in the gas-channel corners and of drops on the GDL surface. The drop radius is assumed to be directly dependent on a given local water flux from the GDL, gas flow velocity, GC geometry and an empirical parameter. Qin et al. (2012b) find that film flow has a negligible influence on the pressure drop, whereas the pressure drop increases significantly in the presence of droplets. Qin et al. (2012a) stress the importance of a more comprehensive droplet model.

The occurrence of sessile drops makes it hard to find realistic boundary conditions at the GDL-surface, if a coupled system of GC and GDL is considered. Often, a value for the saturation or capillary pressure is specified at the interface (Natarajan and Nguyen, 2001, Berning and Djilali, 2003). Like many others before them, Qin et al. (2012c) employ the two-phase Darcy approach in both the GDL and the GC, assuming the GC to be a structured porous medium with a porosity of one. This avoids coupling of the two domains, but is a poor description of the gas-channel dynamics and does not account for drop dynamics.

Gurau et al. (2008) and Gurau and Mann (2010) include drop formation and detachment into a 3D model of the cathode side. They employ a multi-phase multi-fluid REV-scale model in both the porous GDL and the free-flow GC domain. At the interface, they assume a saturation equilibrium based on the description of sessile drops. The water pressure  $p_i^{\text{pm}}$  is set equal to the internal drop pressure  $p_{\text{drop}}$  which in turn depends

on the drop radius. This leads to a jump in saturation and a discontinuity in the capillary-pressure gradient at the interface. Drop formation depends on the pore-size distribution at the interface and the porous-medium water pressure. Drops grow until they are detached due to gravity and shear forces. Gurau et al. (2008) and Gurau and Mann (2010) find cyclic variations of the water saturation in areas feeding the drops. The main limitations of this approach are that one drop per pore is assumed and that drops do not merge. This yields several small drops per REV.

Berning et al. (2009) also focus on the interface treatment using a stationary 3D multi-fluid model of the PEM fuel-cell cathode. They derive an interface condition for the capillary pressure based on the water flux inside the porous medium and the number of drops at the interface which is assumed to be constant during the simulations. The interaction of drops and gas flow is not included in the model. They find that the interface condition has only limited influence on the water saturation within the GDL. In Berning et al. (2010) the multi-fluid model is extended by a kinetic phase-change approach. It is used to analyse the effect of an interdigitated flow field in the gas channel. A more effective water transport is observed. The occurring pressure drop is predicted to be between 0.3 kPa and 3 kPa in dependence of current density and stoichiometric ratio. In Berning et al. (2011), the model is extended to account for the polymer-electrolyte membrane and the anode side. The focus is on a better understanding of the transfer mechanisms of water through the membrane which are found to depend strongly on the surface area of the electrolyte in the catalyst layer.

Wang et al. (2011) see the combination of drop dynamics at the GC-GDL interface, transport processes in all fuel-cell compartments and chemical reactions as a current research request.

A model coupling free flow in the gas channel to the porous gas-diffusion layer and accounting for drop dynamics at the interface is presented in section 4.2. The obtained numerical results are shown in chapter 7.

## **2.4 Properties of droplets**

Drops form within another fluid phase or on solid surfaces due to surface-tension effects. Drops in a fluid phase are mostly spherical and might deform due to gravity

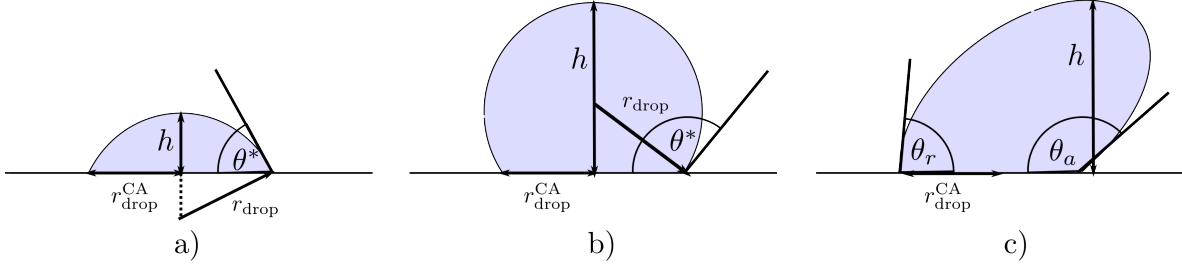


**Figure 2.6:** Drop constitutions showing the static contact angle  $\theta^*$ , the drop height  $h$ , the curvature radius  $r_{\text{drop}}$  and the radius of the contact surface  $r_{\text{drop}}^{\text{CA}}$  for: a) a wetting drop, b) a non-wetting drop and c) a drop influenced by flow forces developing contact-angle hysteresis between advancing  $\theta_a$  and receding  $\theta_r$  contact angle.

effects and flow forces (e.g. rain drops). The shape of a sessile drop depends on the wettability. On ideal (flat, homogeneous, smooth, rigid and isotropic) surfaces, a static or equilibrium contact angle  $\theta^*$  establishes (Erbil et al., 2002). The static contact angle can be determined experimentally by either the sessile-drop, captive-bubble or Wilhelmy-plate method (Butt et al., 2003).

A completely wetting fluid with respect to the solid surface forms a continuous film instead of a drop. A wetting fluid forms a drop with a static contact angle  $\theta^* < 90^\circ$  (see a) in figure 2.6). A non-wetting fluid forms a drop with a static contact angle  $\theta^* > 90^\circ$  (see b) in figure 2.6). Based on the contact angle  $\theta^*$ , the geometric information of the drop can be obtained. With the drop height  $h$ , the curvature radius  $r_{\text{drop}}$  and the radius of the contact area  $r_{\text{drop}}^{\text{CA}}$ , the drop volume, surface area, contact area and contact line of a spherical cap are:

$$V_{\text{drop}} = \frac{\pi}{3}h^2(3r_{\text{drop}} - h) \quad \text{with} \quad r_{\text{drop}} = \frac{h}{1 - \cos \theta^*}, \quad (2.1)$$

$$A_{\text{drop}}^o = 2\pi r_{\text{drop}} h, \quad (2.2)$$

$$A_{\text{drop}}^{\text{CA}} = \pi(r_{\text{drop}}^{\text{CA}})^2 \quad \text{with} \quad r_{\text{drop}}^{\text{CA}} = r \sin \theta^*, \quad (2.3)$$

$$L_{\text{drop}} = 2\pi r_{\text{drop}}^{\text{CA}}. \quad (2.4)$$

At the beginning of the nineteenth century, Thomas Young studied the cohesion of fluids and capillarity effects in tubes (Young, 1804). Young's equation (2.5) relates the static contact angle to the surface tensions of the phases:

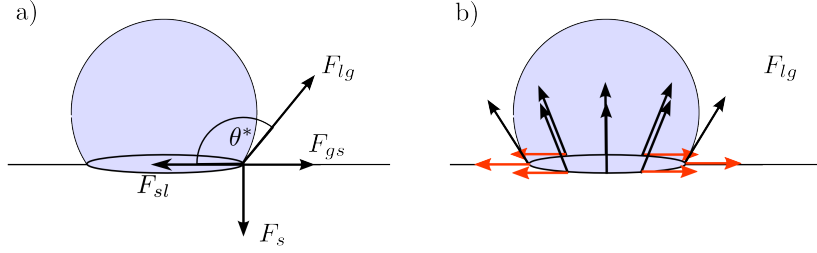


**Figure 2.7:** a) Force balance at the contact line, where  $F_{lg}$ ,  $F_{gs}$ ,  $F_{sl}$  are the surface-tension forces between the solid, liquid and gas phases, b) in total, the horizontal components of the surface-tension forces cancel out.

$$\gamma_{lg} \cos \theta^* = \gamma_{gs} - \gamma_{ls}. \quad (2.5)$$

Until today, Young's equation is employed as quantitative description of wetting phenomena. It describes optically observable phenomena (Butt et al., 2003) and is valid on the pore-scale at equilibrium conditions. For a sessile drop at equilibrium conditions, it can be derived based on thermodynamics by setting the change in Gibbs free energy to zero and neglecting gravitational forces. Alternatively, it can be obtained from a momentum balance at the contact line (see figure 2.7 a) and Hassanizadeh and Gray (1993)). Butt et al. (2007) discuss the limits of the assumption of equilibrium. They conclude that drops will evaporate in an open system making a thermodynamic derivation of Young's equation impossible. However, they do not question its validity. The influence of gravity is negligible for small drops where the height is smaller than the capillary constant:  $h < \sqrt{\frac{2\gamma_{lg}}{\rho l}}$  (Butt et al., 2007) or where the Bond number:  $Bo = \frac{\rho g d_{\text{drop}}^2}{\gamma_{lg}}$  ( $Bo$ ) is smaller than 0.1 (Gopalan and Kandlikar, 2014).

Under equilibrium conditions, the surface tension gives the drop its spherical shape and leads to a circular contact line. Surface tension causes a pressure of curvature or capillary pressure:

$$p_c = \frac{2\gamma_{lg}}{r_{\text{drop}}}. \quad (2.6)$$

Equation (2.6) is valid for spherical drops surrounded by another fluid (e.g. gas). It is derived by balancing the surface-tension and volume-changing work (see appendix A.1). The capillary pressure caused by the curved drop surface (see equation (2.6)) is

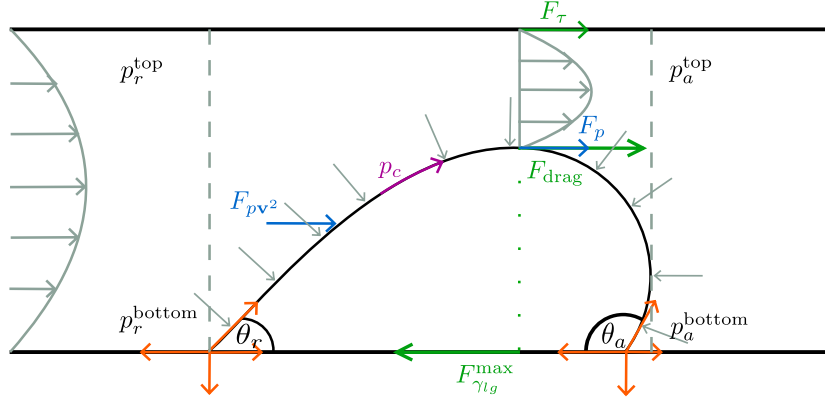


**Figure 2.8:** Deformed drop.

not constant if the drop deforms. For sessile drops, a geometric factor occurs which accounts for the form of a spherical cap and surface-tension effects in the contact line at the bottom of the drop (see appendix A.1):

$$p_c = \frac{2\gamma_{lg}}{r_{\text{drop}}} \frac{2(1 - \cos \theta^*) + \cos \theta^* \sin \theta^{*2}}{(1 - \cos \theta^*)^2(2 + \cos \theta^*)}. \quad (2.7)$$

For the contact angles in hydrophobic media, like the GDL, this factor is close to 1.0 (see table A.1.1 in appendix A.1). It does not account for deformed drop geometries which yield a varying curvature radius and a varying capillary pressure across the drop surface. Chen et al. (2005), Cho et al. (2012a,b) and Gurau and Mann (2010) use  $p_c = \frac{2\gamma_{lg}}{r_{\text{drop}}}$  and we will do the same in the course of this work.

The ideal case of a static drop, meaning a drop that does not grow or shrink, is very unlikely, since a drop tends to evaporate (Butt et al., 2007). Growing or shrinking causes a movement of the contact line. Consequently, most experiments can only provide a range for the static contact angle  $\theta^*$  given by the advancing  $\theta_a$  and receding  $\theta_r$  contact angles (see figure 2.6 c)). The advancing contact angle  $\theta_a$  is observed when the contact area grows and more solid surface is covered. The receding contact angle  $\theta_r$  is observed in the opposite case. The difference between these angles is called contact-angle hysteresis  $\Delta\theta^{\text{max}} = \theta_a - \theta_r$ . Contact-angle hysteresis occurs due to surface roughness, chemical surface heterogeneities or adsorbed substances. Moreover, a drop subjected to a surrounding flow field will deform due to the exerted drag force and contact-angle hysteresis occurs (see figure 2.8).

Figure 2.8 shows the situation of a sessile drop subjected to forces from an external flow field inside a gas channel. For a spherical drop at equilibrium, the integral of the horizontal force contributions along the contact line is zero (see figure 2.7 b)). Hence, drops are not able to take up force, e.g. drag forces, in any other way but by deformation.

The flow field exerts pressure  $F_p$  and shear  $F_\tau$  forces as well as a force caused by the dynamic pressure  $F_{p\mathbf{v}^2}$  on the drop (see figure 2.8). These forces form the drag force  $F_{\text{drag}}$ . To calculate the drag force exerted on a drop by fluid flow, different approaches are possible. Based on principles from fluid mechanics, the following formula can be used (Zhang et al., 2006, Cho et al., 2012a,b):

$$F_{\text{drag}} = \frac{1}{2} \rho_g^m |\mathbf{v}_g|^2 c_w(Re) A, \quad (2.8)$$

where  $A$  is the projected area of the drop normal to the principal flow direction. The drag coefficient  $c_w$  depends on the size of the drop and on the Reynolds number (Zhang et al., 2006):

$$c_w = \frac{24}{Re} (1 + 0.1925 Re^{0.63}). \quad (2.9)$$

Zhang et al. (2006) point out that equation (2.8) is only valid for full spheres (non-deformed sessile drops are spherical caps) subjected to a uniform velocity field. Cho et al. (2012a,b) propose an empirical expression for  $c_w$ , stating that it might be impossible to describe the drag force for all possible channel dimensions (channel height  $h_{GC}$ ), drop geometries and flow conditions with only one formula:

$$c_w = 46.247 \left( \frac{d_{\text{drop}}}{h_{GC}} \right)^{0.1757} Re^{(0.2158 \frac{d_{\text{drop}}}{h_{GC}} - 0.6384)} \quad \text{with} \quad Re = \frac{\rho_g |\mathbf{v}_g| h_{GC}}{\mu_g}. \quad (2.10)$$

It is also possible to derive the drag force from a force balance:

$$F_{\text{drag}} = F_\tau + F_p + F_{p\mathbf{v}^2}, \quad (2.11)$$

where  $F_\tau$  is the friction force on the top wall above the drop,  $F_p$  is the pressure force acting across the drop and  $F_{pv^2}$  is the force exerted by the dynamic pressure at the front of the drop (Chen et al., 2006, Cho et al., 2012a,b). The friction force at the top wall  $F_{\tau i} = \tau_{ij} A_j$  is the shear stress acting on the projected area  $A_j$ . Given a Newtonian fluid and laminar flow, the shear stress is given as:

$$\tau_{ij} = \mu_\alpha \left( \frac{\partial v_{\alpha i}}{\partial x_j} + \frac{\partial v_{\alpha j}}{\partial x_i} \right).$$

The dynamic-pressure force is given as  $F_{pv^2} = \frac{1}{2} \rho_g^m |\mathbf{v}_g|^2 A$ . The pressure force  $F_p$  is calculated from the pressure difference across the drop  $F_p = \Delta p A$ . The pressure force acting on the drop surface is not constant around the drop, but varies due to the variation of the flow field. The non-symmetrical shape of the drop complicates the calculation of the force balance. Schillberg and Kandlikar (2007) stress the importance of a correct description of the drop geometry for the estimation of the drag force. Gopalan and Kandlikar (2014) develop a correlation between pressure drop, gas velocity and GC corner angle in trapezoidal fuel-cell GCs to predict the minimum pressure drop required for drop detachment.

A retention force  $F_{\gamma_{lg}}^{\max}$  works against  $F_{\text{drag}}$  (see figure 2.8). The drop detaches from the surface once the drag force exceeds the surface-tension force which is caused by contact-angle hysteresis  $\Delta\theta^{\max}$  and elongation of the contact area. A geometric description for the contact area and the drop volume is needed for the estimation of this retention force. Extrand and Gent (1990) showed in experiments that drops elongate. Qin et al. (2012d) performed direct simulations of drops emerging from pipes subjected to gas drag. The resulting contact lines are shown in figure 2.9. Qin et al. (2012d) concluded that the deformation of the contact line is smaller for hydrophobic surfaces and detachment occurs faster.

Schillberg and Kandlikar (2007) give a comprehensive overview of existing drop models and their respective assumptions. Often, a circular contact line is assumed, neglecting deformation of the contact area and assuming contact-angle hysteresis to be the only cause for the retention force. Common assumptions for the contact line are:

- two semi-circles with constant contact angles  $\theta_a$  and  $\theta_r$  respectively (Chen et al., 2005),

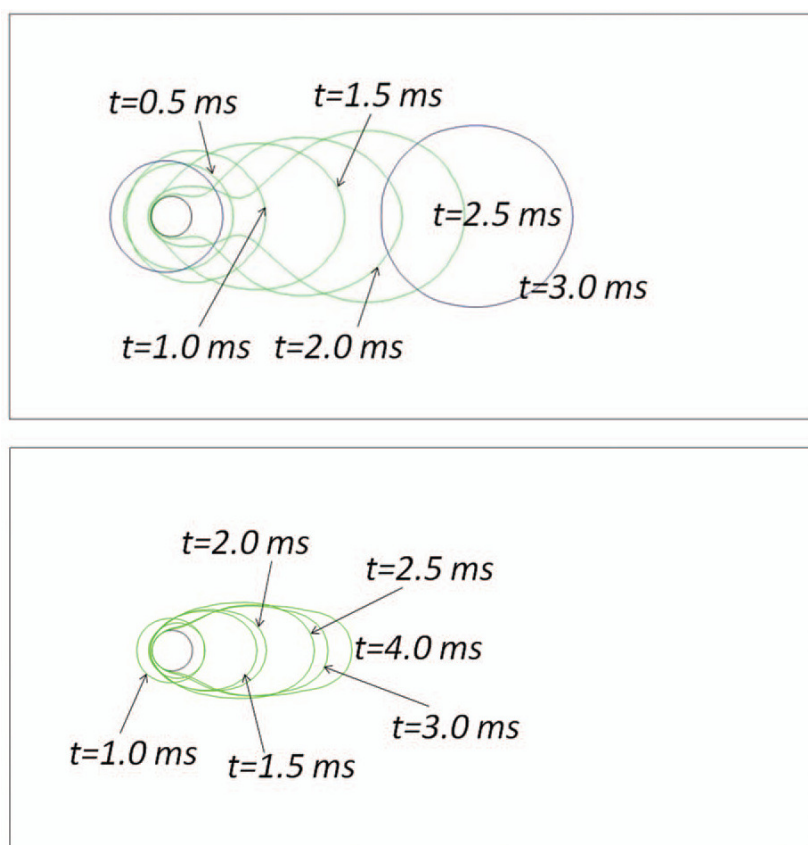


**Figure 2.9:** Contact line movement with time for different static contact angles (top:  $\theta^* = 110^\circ$ , bottom:  $\theta^* = 170^\circ$ ). (reproduced from Qin et al., 2012d, by permission from ECS – The Electrochemical Society.).

- a linear variation of the contact angle along the circular contact line between  $\theta_a$  and  $\theta_r$  (Kumbur et al., 2006):

$$\theta(\beta) = -\frac{\Delta\theta^{\max}}{\pi}\beta + \theta_a, \quad (2.12)$$

- a constant contact angle in the front semi-circle and a linear variation in the tail half (Basu et al., 1997):

$$\theta(\beta) = -\frac{2\beta}{\pi}\theta_r + \left(1 - \frac{2\beta}{\pi}\right)\theta_a. \quad (2.13)$$

This yields different possible expressions for the horizontal surface-tension force:

- Chen et al. (2005):

$$F_{\gamma_{lg}}^{\max} = \pi(r_{\text{drop}} \sin \theta_a)\gamma_{lg} \cos(180 - \theta_a) + \pi(r_{\text{drop}} \sin \theta_r)\gamma_{lg} \cos \theta_r, \quad (2.14)$$

- Kumbur et al. (2006):

$$F_{\gamma_{lg}}^{\max} = \gamma_{lg}r_{\text{drop}}^{\text{CA}}\pi \left[ \frac{\sin(\Delta\theta^{\max} - \theta^*) - \sin \theta^*}{\Delta\theta^{\max} - \pi} + \frac{\sin(\Delta\theta^{\max} - \theta^*) - \sin \theta^*}{\Delta\theta^{\max} + \pi} \right], \quad (2.15)$$

- Cho et al. (2012a):

$$F_{\gamma_{lg}}^{\max} = 4\gamma_{lg}\pi r_{\text{drop}} \sin^2 \theta^* \sin \frac{\Delta\theta^{\max}}{2}. \quad (2.16)$$

Equations (2.14) to (2.16) show that the surface-tension force is proportional to the radius of the contact area  $r_{\text{drop}}^{\text{CA}}$  and related to the difference in advancing and receding contact angle  $\Delta\theta^{\max}$ . According to experiments from Extrand and Gent (1990), a greater force is required to detach a drop with increasing volume. In agreement with equation (2.15), the critical force per radius is constant for each liquid-solid combination (Extrand and Gent, 1990). The maximum retention force is given for the maximally sustained difference in contact angles which can be determined experimentally. Once the maximally sustained difference in contact angles is reached for a given drop volume, the drop will detach.

Drops detach due to a drag force  $F_{\text{drag}}$  in horizontal direction or a lifting force  $F_{\text{lift}}$  in vertical direction. Basu et al. (1997) consider the vertical force balance to determine if or when lifting of the drop occurs. According to Cho et al. (2012a), the drag force overcomes the retention force more easily. Consequently, the maximum horizontal retention force is usually used to estimate the critical drag force for detachment. Note that calculating the drag force and comparing it with the retention force does not allow any conclusion about the drop's exact behaviour. Once detached from its initial position, the drop will either slide or roll on the porous surface, lift into the gas flow or wick into the corners of the gas-flow channel. Experiments from Eller et al. (2011) show that not only the drop volume is removed from the surface but drop detachment sucks water from a thin porous body like a fuel-cell GDL and drains it down to the bottom. In fuel cells, water removal is influenced by the gas-flow velocity, material properties of GC and GDL, contact-angle hysteresis and GC cross-section geometry (Gopalan and Kandlikar, 2014).

As mentioned above, evaporation significantly influences drop dynamics. The phase equilibrium between the liquid drop and the surrounding vapour determines the evaporation rate. The curved surface of the drop leads to a higher saturated vapour pressure causing increased evaporation rates compared to flat surfaces (Butt et al., 2007). This is described by the Kelvin equation, which describes the dependence of the vapour pressure  $p_{\text{sat,Kelvin}}^w$  on the drop radius (Galvin, 2005):

$$p_{\text{sat,Kelvin}}^w = p_{\text{sat}}^w(T) e^{\left(\frac{M^\kappa}{\rho^\kappa RT} p_c\right)} \quad \text{with} \quad p_c = \frac{2\gamma_{lg}}{r_{\text{drop}}} \quad \text{for drops}, \quad (2.17)$$

where  $p_{\text{sat}}^w$  is the vapour pressure over a flat surface,  $M^\kappa$  is the molar mass of the component  $\kappa$ ,  $\rho^\kappa$  is the liquid density of component  $\kappa$ ,  $\gamma_{lg}$  is the surface tension and  $r_{\text{drop}}$  is the drop radius. Concave surfaces (like in hydrophilic pores, for example) lead to a decreased vapour pressure (Mitropoulos, 2008), while convex surfaces (of e.g. drops) yield higher vapour pressures compared to the reference state. Depending on the curvature, the sign of the exponent in equation (2.17) has to be chosen. The Kelvin equation is based on the assumptions that the vapour behaves like an ideal gas, the liquid phase is incompressible, the pressure is constant inside the drop and the surface tension is independent of the curvature of the interface. It can be derived based on thermodynamic principles or on hydrostatic considerations (Galvin, 2005).

In still air, the water vapour diffuses outward towards the unsaturated regions. Hence, the evaporative flux is defined by Fick's law (Song et al., 2011):

$$\dot{m}_{\text{evap}}^{\kappa} = -D_g^w \rho_g \frac{dx_g^w}{dx} A, \quad (2.18)$$

where  $D_g^w$  is the diffusion coefficient of water in the gas phase,  $x_g^w$  is the mole fraction of water in the gas phase,  $x$  is the radial distance and  $A$  is the area across which evaporation occurs. Integrating equation (2.18) from the drop surface to infinity yields the mass change over time (Erbil et al., 2002, Song et al., 2011):

$$\frac{d\rho_l V_{\text{drop}}}{dt} = -4\pi D_g^w r_{\text{drop}} (x_{g,\text{drop}}^w - x_{g,\infty}^w) \rho_g f(\theta). \quad (2.19)$$

$f(\theta)$  represents the dependence of the evaporation rate on the contact angle. Picknett and Bexon (1977) derived an expression for  $f(\theta)$  valid for  $10^\circ \leq \theta < 180^\circ$ :

$$f(\theta) = 0.5 \cdot (0.00008957 + 0.6333\theta + 0.116\theta^2 - 0.08878\theta^3 + 0.01033\theta^4). \quad (2.20)$$

Bourges-Monnier and Shanahan (1995) assumed purely radial evaporation through the surface of the spherical-drop cap and proposed the following expression:

$$f(\theta) = -\frac{\cos(\theta)}{2 \ln(1 - \cos(\theta))}. \quad (2.21)$$

Picknett and Bexon (1977) found two main modes of evaporation of droplets: evaporation at constant contact angle and decreasing contact area, and evaporation at constant contact area and decreasing contact angle. According to Erbil et al. (2002) the dominating mode for water (contact angle below  $90^\circ$ ) is that of constant contact angle. They also report that this mode was observed for water droplets on poly-tetrafluorethylene surfaces (contact angle above  $90^\circ$ ). An estimate of the evaporative flux for a two-dimensional setting considering advective transport is given in appendix A.2.

The basic concepts for the description of sessile drops given in this section form the basis for the coupling concept presented in section 4.2 which accounts for drop dynamics at the interface between free and porous-medium flow.

The literature review shows that various coupling concepts for free flow and flow in porous media exist and that efforts have been made to describe transvascular exchange and drop dynamics in fuel cells. The models range from pore-scale to REV-scale descriptions and the coupling concepts mostly rely on a simple interface concept. However, a consistent interface description for processes of varying complexity is still missing. Concerning drop dynamics in fuel cells, the literature review reveals a need for realistic boundary conditions between GDL and GC and for the prediction of the drop distribution at the interface. To fill this gap, we develop an efficient REV-scale approach in the following chapters that covers coupling approaches ranging from a simple, to a pore-scale and a complex interface description. The latter accounts for drop formation, growth and detachment influenced by free gas and two-phase porous-medium flow.

# 3 Conceptual and mathematical model: Coupling concept for a simple interface

The focus of this work is on the description of the interface between porous-medium and free-flow region. A continuum approach is applied to all compartments. Its basic assumptions and challenges occurring when bridging scales are laid out in section 3.1. In this chapter, the conceptual and mathematical basics of the multi-phase compositional non-isothermal submodels are explained (see sections 3.2 and 3.3).

In Mosthaf et al. (2011) and Baber et al. (2012), we develop a concept to model evaporation from soil based on the two-domain approach with a simple interface devoid of thermodynamic properties. The coupling concept is explained in detail in section 3.4 and is extended towards a more complex interface description in chapter 4. All balance equations and coupling conditions are developed for non-isothermal two-phase two-component porous-medium flow in contact with a non-isothermal one-phase two-component Navier-Stokes flow.

## 3.1 Structures and scales: The continuum approach<sup>6</sup>

Depending on the level of abstraction, systems can be described on different scales inducing respective parameters. Volume averaging over an REV<sup>7</sup> leads to an averaged

---

<sup>6</sup>Parts of this section are taken from Baber, K. (2009). Modeling the transfer of therapeutic agents from the vascular space to the tissue compartment (A continuum approach). Master's thesis, Dep. of Hydromechanics and Modeling of Hydrosystems, IWS, University of Stuttgart.

<sup>7</sup>Representative volume over which an average is performed to pass from a microscopic to a macroscopic description (Bear, 1972).

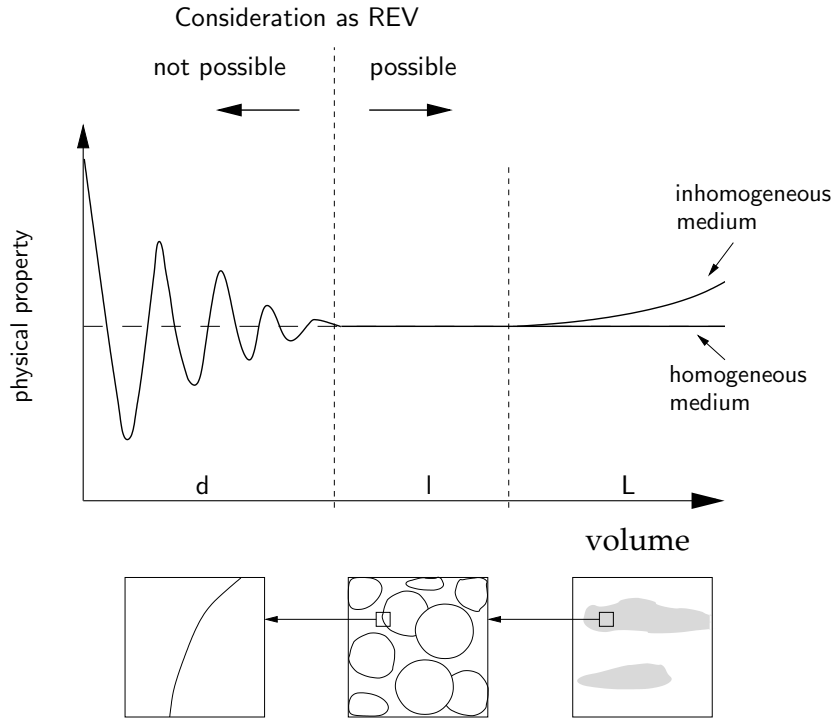


**Figure 3.1:** Definition of the REV (adapted from Helmig, 1997).

description of the system with effective parameters (Bear, 1972). For the process of volume averaging the range of the REV-size is crucial as the averaged quantities have to be independent of the REV-size within that range. As figure 3.1 shows, the REV must be neither too small, as inhomogeneities on the micro-scale cause oscillations, nor too large, as heterogeneities within the domain would be included. Effects that occur due to heterogeneities on a scale smaller than the chosen one are taken into account by the effective parameters. Heterogeneities on a larger scale can be considered by spatial variation of the effective properties. In case of very thin heterogeneous structures, the definition of the REV is challenging. Alternatively, a thin-porous-medium approach where the REV-height corresponds the thickness of the porous-medium structure can be applied (see section 2.2 and Qin and Hassanizadeh (2014)).

The averaging process involves different scales. The finest scale is the molecular scale. Averaging over a large number of molecules and describing a substance with continuous average properties and continuous differentiable functions is called continuum approach. This is the fundamental approach of fluid mechanics (Helmig, 1997, Class, 2001). Water, for example, is considered as continuous fluid phase with average fluid properties like density  $\rho_l$  and viscosity  $\mu_l$ . The overall fluid-flow behaviour is examined instead of

looking at the movement of single molecules.

In the next instance, the continuum approach leads to the micro-scale or pore-scale on which the individual pore spaces are resolved. On the micro-scale, the structure and geometry of the pore network has to be known in order to model fluid flow. Within the pores fluid flow can be described by the Navier-Stokes equations or with the help of pore-network models (Blunt, 2000, Blunt et al., 2002, Joekar-Niasar, 2010). Pore-network models can be quasi-static (Joekar-Niasar et al., 2008) or dynamic (Joekar-Niasar et al., 2010).

Further averaging yields a macro- or REV-scale description. Instead of resolving the spatial distribution of solid and fluid phase, volume fractions are considered and effective parameters like porosity<sup>8</sup>  $\Phi$  or intrinsic permeability<sup>9</sup>  $\mathbf{K}$  are obtained. On the macro-scale, Darcy's law is used to describe fluid flow (see section 3.2). For some microscopic properties, the transition to the macro-scale is not straight forward. Especially the definition of the macroscopic phase and capillary pressure<sup>10</sup> is challenging. Korteland et al. (2010) discuss averaging procedures for pressure and support the centroid-corrected averaging operator presented by Nordbotten et al. (2008) as improvement to the usually applied intrinsic phase average. At equilibrium conditions on the micro-scale, capillary pressure in a hydrophobic porous medium is defined as:

$$p_c^{\text{micro}} = \frac{2\gamma_{lg}}{R} = p_l^{\text{micro}} - p_g^{\text{micro}}, \quad (3.1)$$

where  $R = \frac{\bar{r}_{\text{pore}}}{\cos \theta}$  is the mean curvature of the interface meniscus in the pore and  $p_l^{\text{micro}}$  and  $p_g^{\text{micro}}$  are the microscopic phase pressures. Often, this expression is transferred directly to the macro-scale, even though a rigorous derivation based on a volumetric average is not possible since equation (3.1) is valid on the interface only (Hassanizadeh and Gray, 1993).

---

<sup>8</sup>A macroscopic porous-medium property defined as the ratio of void space to bulk volume  $\Phi = \frac{V_{\text{pores}}}{V}$  (Bear, 1972).

<sup>9</sup>Intrinsic permeability solely depends on the properties of the porous medium like pore-size and pore-shape distribution, tortuosity and porosity. Bear (1972) lists various formulations that relate  $\mathbf{K}$  to the matrix properties.

<sup>10</sup>The pressure difference between two fluid phases across a curved interface. On the micro-scale, it is given by the Young-Laplace equation. On the macro-scale, Brooks and Corey (1964) and van Genuchten (1980) provide correlations dependent on the water saturation  $p_c(S_l)$ .

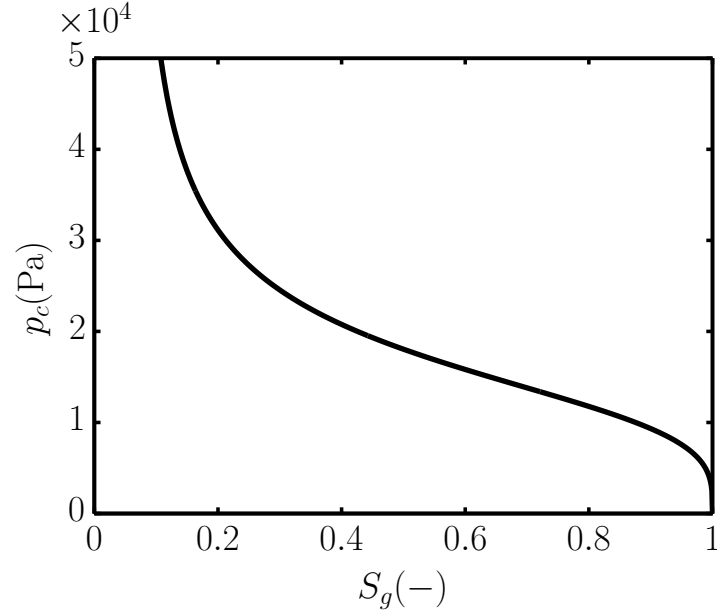


**Figure 3.2:** Van-Genuchten parametrization of the macroscopic capillary-pressure-saturation relationship (after Gostick et al., 2006).

Hassanizadeh and Gray (1993) also claim that the application of equation (3.1) on the macro-scale cannot explain the behaviour of measured macroscopic capillary-pressure-saturation relationships (see figure 3.2). The macroscopic capillary pressure

$$p_c = p_l - p_g = p_c(S_l) \quad (3.2)$$

must be understood as some function that relates the macroscopic phase pressures and not as a result of a balance of forces (Hassanizadeh and Gray, 1993). An empirical or experimentally obtained relation between capillary pressure and saturation (see figure 3.2) is generally applied on the macro-scale to define the relation between the phase pressures (Brooks and Corey, 1964, van Genuchten, 1980). Hassanizadeh and Gray (1993) derive an expression for the macroscopic capillary pressure based on rational thermodynamics, relating  $p_c$  to a change in free energy of the fluid phases and all existing interfaces caused by a change in saturation.

In the scope of this work, the subdomains are described on the REV-scale with a classical continuum approach. In the following sections (3.2 and 3.3), the mathematical models for the porous and free-flow subdomains are explained.

## 3.2 Subdomain model: Porous medium<sup>11</sup>

The porous-medium model in  $\Omega^{\text{pm}}$  is based on the following assumptions:

- local thermodynamic (mechanical, thermal and chemical) equilibrium,
- a rigid solid phase (subscript  $s$ ),
- two-phase flow consisting of a liquid phase (subscript  $l$ ) and a gas phase (subscript  $g$ ),
- Newtonian fluids,
- two components being present in each phase: water (superscript  $w$ ) and air (superscript  $a$ ),
- air is considered to be an ideal gas,
- slow flow velocities ( $\text{Re} \ll 1$ ) allow the application of the multi-phase Darcy's law for the phase velocities,
- binary diffusion and a negligible influence of dispersion due to slow flow velocities and comparatively high diffusion coefficients in the gas phase.

The model allows the transfer of components from one phase to another and is able to describe vaporisation and condensation as well as dissolution and degassing within the porous medium. The validity of the assumption of local thermodynamic equilibrium is investigated in Nuske et al. (2014) who compare the equilibrium model to a model based on kinetic phase exchange. A similar approach is shown in Berning et al. (2010) and Wu et al. (2009) where the model is adapted to hydrophobic media and fast free-flow velocities. Berning et al. (2010) find almost 100% relative humidity in the gas phase for the given assumptions and constitutive relations supporting the validity of the local-equilibrium assumption. The non-isothermal model presented here comprises two mass-balance equations and one energy balance. Table 3.1 summarises the employed

---

<sup>11</sup>This section is published in Baber, K., Mosthaf, K., Flemisch, B., Helmig, R., Mütting, S., and Wohlmuth, B. (2012). Numerical scheme for coupling two-phase compositional porous-media flow and one-phase compositional free flow. *IMA Journal of Applied Mathematics*, 77(6):887–909. first published online July 26, 2012.

balance equations and chosen primary variables. The definitions of the respective parameters, material laws and equations of state are listed in table 3.2.

The mass conservation in  $\Omega^{\text{pm}}$  is expressed by one mass-balance equation for each component  $\kappa \in \{w, a\}$ , where  $\Phi$  is the porosity,  $S_\alpha$  is the saturation<sup>12</sup> of the phase  $\alpha$ ,  $x_\alpha^\kappa$  stands for the mole fraction of the component  $\kappa$  in the phase  $\alpha$ ,  $\rho_\alpha$  is the molar phase density (see table 3.2),  $D_\alpha^{\kappa, \text{pm}}$  is the diffusion coefficient in phase  $\alpha$  in the porous medium (see table 3.2) and  $q_\alpha^\kappa$  are given source or sink terms. Different expressions for the effective diffusion coefficients in hydrophobic porous-media exist and are discussed in section 7.1.2. The Darcy velocity  $\mathbf{v}_\alpha$  is calculated using the multi-phase Darcy law (Helmig, 1997) with the relative permeability<sup>13</sup>  $k_{r\alpha}$  of phase  $\alpha$ , the dynamic viscosity  $\mu_\alpha$  of phase  $\alpha$ , the tensor of intrinsic permeability  $\mathbf{K}$  and the gradient of the phase pressure  $\nabla p_\alpha$ . Summing up the mass-balance equations for the two components, with  $x_\alpha^w + x_\alpha^a = 1$ , and assuming binary diffusion, we obtain the total mass-balance equation. In this case, the source and sink terms are also summed up for the components,  $q_\alpha = q_\alpha^w + q_\alpha^a$ . It is now possible to choose equivalently two of the three balance equations for a complete model description.

Under the assumption of local thermal equilibrium ( $T_l = T_g = T_s = T$ ), justified by slow flow conditions, one single energy-balance equation that accounts for convective and conductive heat fluxes, the heat sources  $q_T$  within the domain and the storage of heat in the fluid phases and the porous material can be applied. In the energy equation,  $u_\alpha$  is the specific internal energy of the phase  $\alpha$ ,  $\rho_s$  and  $c_s$  are the density and specific heat capacity of the porous medium,  $h_\alpha$  is the specific enthalpy and  $\lambda_{\text{pm}}$  is the effective heat conductivity of the porous medium which depends on the liquid saturation  $S_l$ , the porosity and the heat conductivities of the gas  $\lambda_g$ , water  $\lambda_l$  and solid  $\lambda_s$  phase (see table 3.2). Note, that the energy flux due to diffusive mass transfer is neglected. A detailed explanation of the model concept applied in the porous medium and of the underlying assumptions can be found in Class et al. (2002).

<sup>12</sup>"The fraction of the void volume of the porous medium occupied by phase  $\alpha$  within an REV":  
 $S_\alpha = \frac{V_\alpha}{V_{\text{REV}}}$  (Bear, 1972).

<sup>13</sup>The saturation-dependent quantity  $k_{r\alpha}(S)$  describes the influence of the presence of one phase on the flow behaviour of the other phase and vice versa (Helmig, 1997). Classical examples for relative-permeability–saturation relations are those after Brooks and Corey (1964) and van Genuchten (1980).

**Table 3.1:** Porous-medium equations and associated primary variables.

Balance equations	Primary variable
Mass balance for component $\kappa \in \{w, a\}$ : $\sum_{\alpha \in \{l, g\}} \Phi \frac{\partial(\varrho_\alpha x_\alpha^\kappa S_\alpha)}{\partial t} + \nabla \cdot \mathbf{f}^\kappa - \sum_{\alpha \in \{l, g\}} q_\alpha^\kappa = 0 \quad (3.3)$ $\mathbf{f}^\kappa = \sum_{\alpha \in \{l, g\}} (\varrho_\alpha \mathbf{v}_\alpha x_\alpha^\kappa - D_\alpha^{\kappa, \text{pm}} \varrho_\alpha \nabla x_\alpha^\kappa)$	$S_l$ or $x_\alpha^\kappa$
Total mass balance: $\sum_{\alpha \in \{l, g\}} \Phi \frac{\partial(\varrho_\alpha S_\alpha)}{\partial t} + \nabla \cdot \mathbf{f}_m - \sum_{\alpha \in \{l, g\}} q_\alpha = 0 \quad (3.4)$ $\mathbf{f}_m = \sum_{\alpha \in \{l, g\}} (\varrho_\alpha \mathbf{v}_\alpha)$	$p_g$
Darcy's law: $\mathbf{v}_\alpha = -\frac{k_{r\alpha}}{\mu_\alpha} \mathbf{K} (\nabla p_\alpha - \varrho_\alpha^m \mathbf{g}), \quad \alpha \in \{l, g\}$	
Energy balance: $\sum_{\alpha \in \{l, g\}} \Phi \frac{\partial(\varrho_\alpha u_\alpha S_\alpha)}{\partial t} + (1 - \Phi) \frac{\partial(\varrho_s c_s T)}{\partial t} + \nabla \cdot \mathbf{f}_T - q_T = 0 \quad (3.5)$ $\mathbf{f}_T = \sum_{\alpha \in \{l, g\}} (\varrho_\alpha h_\alpha \mathbf{v}_\alpha - \lambda_{\text{pm}} \nabla T)$	$T$

Depending on the local phase state, primary variables have to be chosen and the secondary variables have to be expressed as functions of the primary variables. Here, the gas-phase pressure  $p_g$ , the saturation of the liquid phase  $S_l$  and the temperature  $T$  are chosen as primary variables for the two-phase system. Based on this, the secondary variables can be calculated, using the relations in table 3.2. If one phase disappears locally, the system of equations is significantly simplified. The saturation cannot be used as a primary variable any more. Possible choices for the numerical algorithm are then a primary-variable switch (Class et al., 2002) or the introduction of additional primary variables and additional constraints in the form of non-linear complementarity functions as proposed in Lauser et al. (2011). We use the former approach here.

**Table 3.2:** Material laws and equations of state dependent on primary variables.

	Equations of state	References
<b>Secondary variables:</b>		
Saturation $S_g$	$S_g = 1 - S_l$	
Liquid-phase pressure $p_l$	$p_c = p_l - p_g$	Helmig (1997)
Air in water phase $x_l^a$	Henry's law: $x_l^a = p_g^a / H_{gl}^a$	
Vapour in gas phase $x_g^w$	$x_g^w = p_{\text{sat,Kelvin}}^w / p_g$	
Kelvin equation	$p_{\text{sat,Kelvin}}^w = p_{\text{sat}}^w \exp\left(-\frac{p_c}{\rho_l \mathcal{R}T}\right)$	Galvin (2005) Butt et al. (2007)
Mass/mole fractions	$X_\alpha^w + X_\alpha^a = x_\alpha^w + x_\alpha^a = 1$ $X_\alpha^\kappa = x_\alpha^\kappa M^\kappa / (x_\alpha^w M^w + x_\alpha^a M^a)$	
<b>Parameters:</b>		
Density $\rho_\alpha$	$\rho_\alpha = f(\rho^\kappa, x_\alpha^\kappa, p_\alpha, T)$	IAPWS (2009)
Component density $\rho^\kappa$	incompressible fluid, ideal gas	Reid et al. (1987)
Viscosity $\mu_\alpha$	$\mu_l = \mu^w, \mu_g$ (Wilke method)	Poling et al. (2001)
Surface tension $\gamma_{lg}$	$\gamma_{lg} = 0.2358 \left(1 - \frac{T}{T_c}\right)^{1.256}$ $\left(1 - 0.625 \left(1 - \frac{T}{T_c}\right)\right)$	IAPWS (1994)
Diffusion coefficient $D_\alpha^{\kappa,\text{pm}}$	$D_\alpha^{\kappa,\text{pm}} = \tau \Phi S_\alpha D_\alpha^\kappa$	Millington&Quirk (1961) Acosta et al. (2006)
Tortuosity $\tau$	$\tau = \frac{(\Phi S_\alpha)^{7/3}}{\Phi^2}$	Millington&Quirk (1961)
Capillary pressure $p_c$	$p_c = f(S_l)$	van Genuchten (1980) Acosta et al. (2006)
Relative permeability $k_{r\alpha}$	$k_{r\alpha} = f(S_l)$	van Genuchten (1980) Acosta et al. (2006)
Eff. heat conductivity $\lambda_{\text{pm}}$	$\lambda_{\text{pm}} = f(\Phi, S_l, \lambda_g, \lambda_l, \lambda_s)$	
Internal energy $u_\alpha$	$u_\alpha = h_\alpha - p_\alpha / \rho_\alpha$	
Enthalpy $h$		
- gas phase	$h_g = x_g^w h^w + x_g^a h^a$	
- water phase	$h_l = h^w$	
- component air	$h^a = 1005(T - 273.15 \text{ K})$	Kays et al. (2005)
- component water	$h^w = f(p_\alpha, T)$	IAPWS (2009)

**Table 3.3:** Free-flow equations and associated primary variables.

Balance equations	Primary variable
Mass balance for component $\kappa$ : $\frac{\partial(\varrho_g x_g^\kappa)}{\partial t} + \nabla \cdot \mathbf{f}^\kappa - q_g^\kappa = 0, \quad \mathbf{f}^\kappa = (\varrho_g \mathbf{v}_g x_g^\kappa - D_g^\kappa \varrho_g \nabla x_g^\kappa) \quad (3.6)$	$x_g^\kappa$
Total mass balance: $\frac{\partial \varrho_g}{\partial t} + \nabla \cdot \mathbf{f}_m - q_g = 0, \quad \mathbf{f}_m = (\varrho_g \mathbf{v}_g) \quad (3.7)$	$p_g$
Momentum balance (Navier-Stokes equations): $\frac{\partial(\varrho_g^m \mathbf{v}_g)}{\partial t} + \nabla \cdot (\varrho_g^m \mathbf{v}_g \otimes \mathbf{v}_g) + \nabla \cdot \mathbf{f}_v - \varrho_g^m \mathbf{g} = 0, \quad (3.8)$ $\mathbf{f}_v = p_g \mathbf{I} - \boldsymbol{\tau} = p_g \mathbf{I} - \mu_g (\nabla \mathbf{v}_g + \nabla \mathbf{v}_g^T)$	$\mathbf{v}_g$
Energy balance: $\frac{\partial(\varrho_g u_g)}{\partial t} + \nabla \cdot \mathbf{f}_T - q_T = 0, \quad \mathbf{f}_T = (\varrho_g h_g \mathbf{v}_g - \lambda_g \nabla T) \quad (3.9)$	$T$

### 3.3 Subdomain model: Free flow<sup>14</sup>

The model in the free-flow domain  $\Omega^{\text{ff}}$  is based on the following setup:

- a laminar fully developed flow field,
- binary diffusion,
- single-phase flow of a Newtonian fluid (here a gas phase is considered:  $\alpha = g$ ),
- two components in the gas phase: water ( $w$ ) and air ( $a$ ).

The four equations which are solved in the free-flow domain are shown in table 3.3: two scalar mass-balance equations (one for the water component and one for the total mass), one vector-valued momentum-balance equation and one scalar energy-balance equation. The same notation as in the porous-medium region is used and a compressible gas phase, which behaves like an ideal gas, is considered. In Fetzer (2012) different analytical turbulence models are tested and in Mosthaf et al. (2014) the significant influence of the thickness of boundary layers is stressed. A combination of the newly

<sup>14</sup>Parts of this section are published in Baber, K., Mosthaf, K., Flemisch, B., Helmig, R., Müthing, S., and Wohlmuth, B. (2012). Numerical scheme for coupling two-phase compositional porous-media flow and one-phase compositional free flow. *IMA Journal of Applied Mathematics*, 77(6):887–909. first published online July 26, 2012.

developed interface descriptions with these relatively new research results is postponed to future research. Turbulence and boundary-layer effects are not considered in the scope of this work, but a fully developed laminar flow field is assumed (see chapters 6 and 7 for respective Reynolds numbers). By assuming gravity to be the only external force, the Navier-Stokes equations result as momentum-balance equations (Oertel jr., 2012). The unsteady Navier-Stokes equations shown in table 3.3 are based on Newton's law and include the symmetrised gradient of the velocity and the tensor product  $\mathbf{v}_g \otimes \mathbf{v}_g = \mathbf{v}_g \mathbf{v}_g^T$ . The equations of state shown in table 3.2 are again used to calculate enthalpy and internal energy.

As primary variables, the pressure of the gas phase  $p_g$ , the mole fraction of water in the gas phase  $x_g^k$ , the velocity of the gas phase  $\mathbf{v}_g$  and the temperature  $T$  are chosen.

### 3.4 Coupling concept: Simple interface<sup>15</sup>

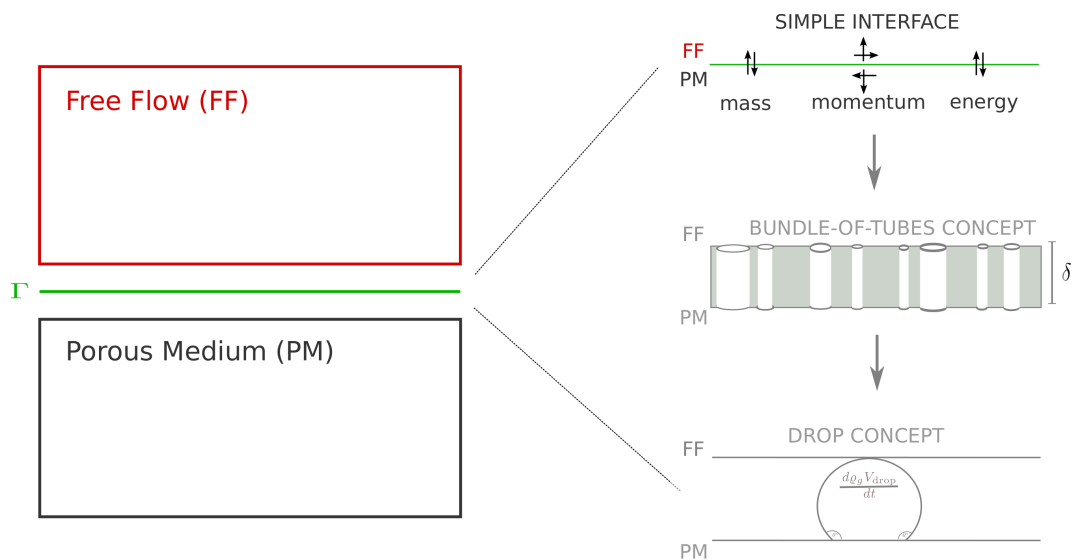
Suitable conditions need to be posed at the interface in order to couple the two domains explained in the previous sections properly. These conditions are based on the balance equations and primary variables of the subdomain models shown in table 3.4. The system is described with a sharp interface and appropriate coupling conditions (two-domain approach). We make assumptions based on phenomenological explanations to simplify the description of the interface and get as close as possible to a so-called simple interface (see figure 3.3).

Figure 3.4 illustrates the processes on the pore-scale: mass, momentum and energy exchange between the phases of the porous medium and the gas phase in the free-flow domain takes place. Coupling conditions in form of volume-averaged quantities have to be found which still account for the pore-scale processes. These conditions are integrated into the REV-scale models explained in sections 3.2 and 3.3. The coupling is motivated by the assumption of thermodynamic equilibrium. However, due to the different model concepts applied in the two subdomains, rigorous thermodynamic equilibrium consisting of mechanical, thermal and chemical equilibrium cannot be completely achieved. Based on phenomenological explanations, assumptions are made that result in conditions that

<sup>15</sup>This section is published in Mosthaf, K., Baber, K., Flemisch, B., Helmig, R., Leijnse, A., Rybak, I., and Wohlmuth, B. (2011). A coupling concept for two-phase compositional porous media and single-phase compositional free flow. *Water Resources Research*, 47:W10522556.

**Table 3.4:** Summary of the balance equations describing the different submodels and listing of the according primary variables.

Balance equations	Primary variables
<b>Free-flow region:</b>	
mass balance (3.7)	$p_g$
component mass balance (3.6)	$x_g^w$
momentum balances (3.8)	$\mathbf{v}_g$
energy balance (3.9)	$T$
<b>Porous-medium region:</b>	
mass balance (3.4)	$p_g$
component mass balance for $\kappa = w$ (3.3)	$S_l$ or $x_\alpha^\kappa$
energy balance (3.5)	$T$

**Figure 3.3:** A simple interface devoid of thermodynamic properties couples free-flow and porous-medium region.

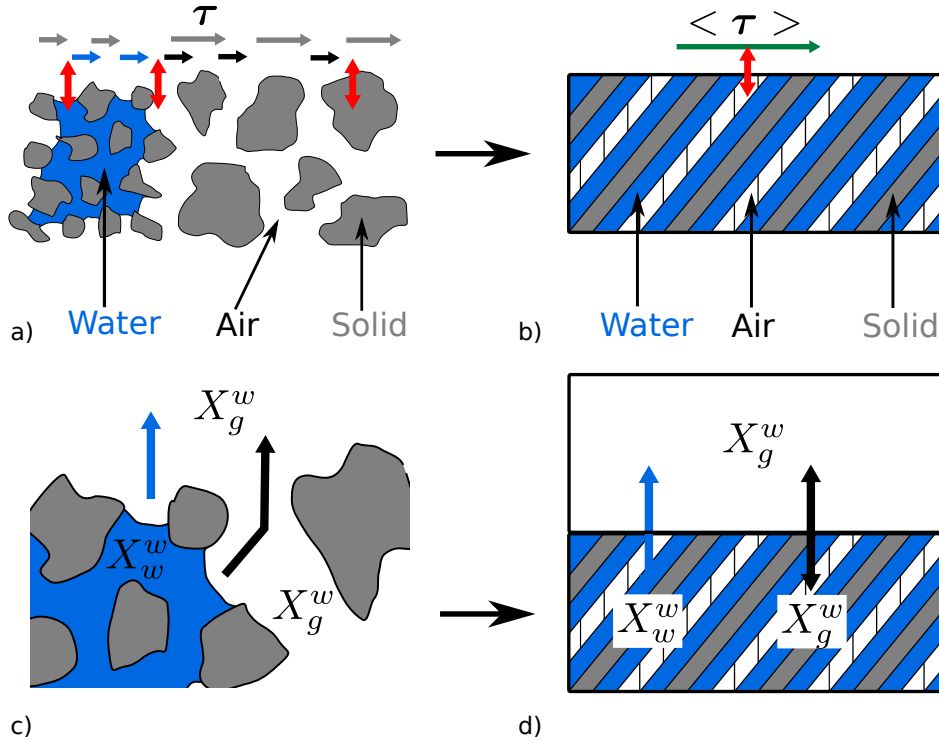


**Figure 3.4:** Transition from pore-scale to a volume-averaged description: a) on the pore-scale shear stresses occur due to interactions between the gas phase in the free-flow region and the gas, fluid and solid phases in the porous medium, b) a volume-averaged description has to account for all these contributions while the different phases of the porous medium are not locally resolved any more, c) exchange processes also occur between the two mobile phases of the porous medium and the free gas phase (pore-scale description), d) on the REV-scale, coupling conditions account for these processes without resolving them locally (reproduced from Mosthaf et al., 2011).

are physically meaningful and as close to thermodynamic equilibrium as possible. This leads to a solvable but still simple model that accounts for the physics at the interface.

The mechanical equilibrium (equilibrium of forces) is given by

1. the continuity of the normal stresses (3.11c) resulting in a possible jump in the gas-phase pressure,
2. the continuity of the normal mass fluxes (3.13),
3. a condition for the tangential component of the free-flow velocity. Here, the Beavers-Joseph-Saffman condition (3.12) is used, despite its theoretical limitations to single-phase parallel flow, its empirical character and the difficulty of determining the Beavers-Joseph coefficient.

The thermal equilibrium is given by

1. the continuity of the temperature (3.14),
2. the continuity of the normal heat fluxes (3.15).

The chemical equilibrium is defined through the continuity of the chemical potential in the gas phase. In the case of continuous pressure, this results in the continuity of the mole fractions at the interface. However, due to the pressure jump arising from the continuity of normal stresses, continuity of chemical potential cannot be presumed. Nevertheless, we assume continuity of mole fractions, see coupling condition (3.18), and note that this results in a possible discontinuity of the chemical potential. Furthermore, we require continuity of the component fluxes (3.19) across the interface.

Based on the physical equilibrium equations, we work out our mathematical and physical interface model in the following subsections. Figures 3.5 to 3.7 illustrate the conditions of thermodynamic equilibrium on the pore and REV-scale. The pore-scale processes are simplified and shown for illustrative reasons only. Their purpose is to help to understand the phenomenological explanations for the presented coupling conditions.

### 3.4.1 Mechanical equilibrium

On the pore-scale, the mechanical equilibrium at the interface has to be formulated between the gas phase in the free-flow region and the gas, solid and water phase in the porous medium (see figure 3.5). On the REV-scale, one condition has to be found that accounts for the equilibrium between the gas phase in the free-flow region and all three phases in the porous medium, since the distribution of phases is not resolved any more.

Therefore, the interface traction is decomposed into its normal and tangential contribution. The normal component of the traction tensor of a Newtonian fluid at the interface is given by:

$$\boldsymbol{\sigma} \mathbf{n} = (-p_g \mathbf{I} + \boldsymbol{\tau}) \mathbf{n} = \left[ -p_g \mathbf{I} + \mu_g \nabla (\mathbf{v}_g + \mathbf{v}_g^T) \right] \mathbf{n}. \quad (3.10)$$

It acts as a surface load on the fluid volume inside  $\Omega^{\text{ff}}$ . Thus, the force on the interface  $\Gamma$  is equal to  $-\boldsymbol{\sigma} \mathbf{n}$ . Additionally, the inertia forces  $(-\rho_g^m \mathbf{v}_g \otimes \mathbf{v}_g) \mathbf{n}$  have to be considered.

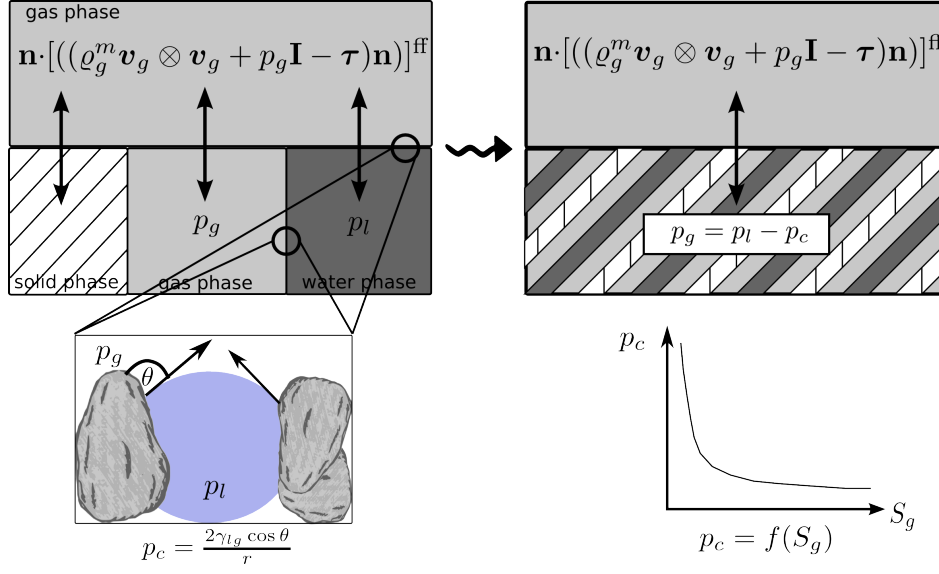


**Figure 3.5:** Mechanical equilibrium at the pore scale and at the REV-scale (normal component). The coupling conditions on the REV scale have to account for the traction between the gas phase in the free-flow region and the gas, solid and water phase in the porous medium. Capillarity effects occur at the interface between the fluid phases in the porous medium as well as at the interface to the gaseous free-flow region. On the REV-scale capillary pressure is a function of the water saturation (reproduced from Mosthaf et al., 2011).

At the porous-medium side of the interface, slow flow velocities are assumed and Darcy's law is used. Viscous stresses  $\boldsymbol{\tau}$  have not to be treated explicitly since they are already accounted for in the permeability, see e.g. Whitaker (1999). Consequently, only the pressure forces acting on  $\Gamma$  have to be taken into account in  $\Omega^{\text{pm}}$ .

Under the assumption of a rigid solid phase and no-slip at the solid-phase surface, no interface condition between gas phase and solid phase needs to be formulated. Mechanical equilibrium between the gas phases in the two domains is represented by the continuity of momentum fluxes shown in equation (3.11a). There,  $A_g$  denotes the contact area between free gas phase and the gas phase in the porous medium. In order to identify the coupling conditions between the liquid and the gas phase across the interface, the pore scale processes must be considered. In the porous medium, capillarity effects occur at the gas-liquid interface (see figure 3.5) due to interfacial tension. The result is a pressure discontinuity across the interface of the two fluids which is defined as capillary pressure (see section 3.1). The pore-scale equation (3.1) is valid only for circular tubes and shows capillary pressure as a function of the surface tension  $\gamma_{lg}$ , contact angle  $\theta$  and pore radius  $\bar{r}_{\text{pore}}$ . The concept of pore-scale capillarity is transferred to the REV-scale by

considering macroscopic capillarity through the capillary-pressure–saturation relation (3.2). Note that capillarity effects occur at the interface of the gas and liquid phase in the porous medium as well as at the interface  $A_l$  of water filled pores and the gaseous free-flow region (see figure 3.5). Following the same reasoning as inside the porous medium, the gas phase at the free-flow side of the interface has to balance the sum of the water pressure and the macroscopic capillary pressure (see equations (3.2) and (3.11b)). By summing up equations (3.11a) and (3.11b), equation (3.11c) results as coupling condition representing the continuity of normal forces across the whole interface on the REV-scale.

$$\left[ A_g \mathbf{n} \cdot \left( (\rho_g^m \mathbf{v}_g \otimes \mathbf{v}_g + p_g \mathbf{I} - \boldsymbol{\tau}) \mathbf{n} \right) \right]^{\text{ff}} = [p_g A_g]^{\text{pm}} \quad (3.11a)$$

$$\left[ A_l \mathbf{n} \cdot \left( (\rho_g^m \mathbf{v}_g \otimes \mathbf{v}_g + p_g \mathbf{I} - \boldsymbol{\tau}) \mathbf{n} \right) \right]^{\text{ff}} = \underbrace{[(p_l - p_c(S_l)) A_l]^{\text{pm}}}_{p_g} \quad (3.11b)$$

---


$$(3.11a) + (3.11b) \quad \left[ \mathbf{n} \cdot \left( (\rho_g^m \mathbf{v}_g \otimes \mathbf{v}_g + p_g \mathbf{I} - \boldsymbol{\tau}) \mathbf{n} \right) \right]^{\text{ff}} = [p_g]^{\text{pm}} \quad (3.11c)$$

The capillary pressure at the interface in (3.11b) might be different from the capillary pressure inside the porous medium. This difference in the capillary pressure is assumed to be negligible and the same capillary-pressure–saturation relation as inside the first layer of the porous medium is applied. Due to condition (3.11c), the pressure is possibly discontinuous at the interface and a jump in the pressure-dependent variables, such as density and viscosity, can be expected. Pressure is usually a continuous thermodynamic property. The discontinuity arises from the use of different model concepts and causes a first perturbation of the thermodynamic equilibrium. We note that (3.11c) is exactly the pressure drop in the artificial boundary condition derived in Heywood et al. (1996).

Now, a condition for the tangential component of the velocity in the free-flow domain is required. Therefore, we follow the same lines as Beavers and Joseph (1967). They state that the slip velocity along the interface is proportional to the shear stress at the interface. With the simplification of Saffman (1971), i.e. neglecting the small tangential velocity in the porous medium at the interface, the Beavers-Joseph-Saffman condition can be written as, (Layton et al., 2002),

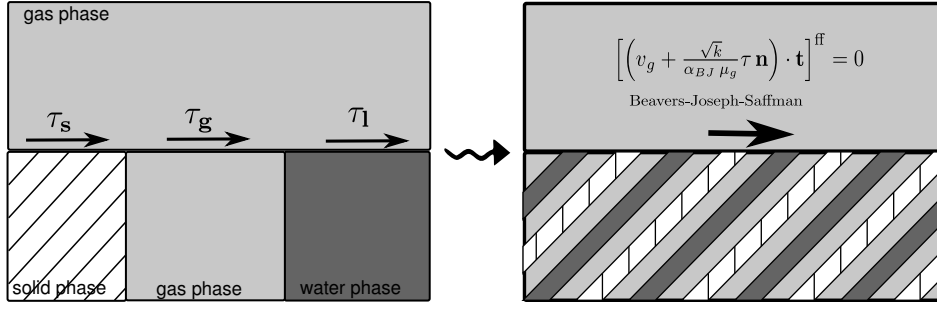


**Figure 3.6:** Mechanical equilibrium at the pore-scale and at the REV-scale (tangential component). The coupling conditions on the REV-scale have to account for the traction between the gas phase in the free-flow region and the gas, solid and water phase in the porous medium (reproduced from Mosthaf et al., 2011).

$$\left[ \left( \mathbf{v}_g + \frac{\sqrt{K_i}}{\alpha_{BJ} \mu_g} \boldsymbol{\tau} \mathbf{n} \right) \cdot \mathbf{t}_i \right]^{\text{ff}} = 0, \quad i \in \{1, \dots, \text{dim}-1\} \quad (3.12)$$

where  $\mathbf{t}_i$ ,  $i \in \{1, \dots, \text{dim}-1\}$ , denotes a basis of the tangent plane of the interface  $\Gamma$ . The parameter  $K_i$  is the corresponding component of the porous-medium permeability and equals  $K_i = (\mathbf{K} \mathbf{t}_i) \cdot \mathbf{t}_i$ .

The Beavers-Joseph coefficient  $\alpha_{BJ}$  has to be determined numerically or experimentally and has to be valid for a two-phase system. Figure 3.6 illustrates that the Beavers-Joseph coefficient should account for the traction between the gas phase in the free-flow region and the gas, solid and water phases in the porous medium. With a difference in viscosity between gas and water of three orders of magnitude, the no-slip condition is assumed to be valid not only for the solid phase but also for the liquid-phase surface. Thus, the Beavers-Joseph coefficient is also a function of the water saturation  $S_l$ .

The determination of the Beavers-Joseph coefficient for two-phase systems will be a demanding task. However, it remains to be seen whether the tangential velocity at the free-flow side of the interface has a significant influence on the evaporation process. If numerical experiments will show a significant impact of this condition, equation (3.12) might be replaced by a more sophisticated condition, e.g. derived from volume-averaging theory, in order to account more precisely for the influence of the multi-phase behaviour, the surface roughness, the boundary layer and the shear stresses at the interface.

Additional to the mechanical equilibrium, the continuity of fluxes across the interface has to be guaranteed. The mass-balance requires the sum of the fluxes at the interface

to be equal to zero. In the free-flow region, one phase is present, whereas in the porous medium we have to take both fluid phases into account. Direct evaporation of the normal water flux is assumed. Hence, the gas phase in the free-flow region takes up both the gas and liquid mass flux and the continuity equation for the normal phase fluxes reads:

$$[\varrho_g \mathbf{v}_g \cdot \mathbf{n}]^{\text{ff}} = - [(\varrho_g \mathbf{v}_g + \varrho_l \mathbf{v}_l) \cdot \mathbf{n}]^{\text{pm}}. \quad (3.13)$$

### 3.4.2 Thermal equilibrium

The assumption of local thermal equilibrium at the interface provides two continuity conditions for the primary variable  $T$  and for the associated heat flux,

$$[T]^{\text{ff}} = [T]^{\text{pm}}, \quad (3.14)$$

and

$$[(\varrho_g h_g \mathbf{v}_g - \lambda_g \nabla T) \cdot \mathbf{n}]^{\text{ff}} = - [(\varrho_g h_g \mathbf{v}_g + \varrho_l h_l \mathbf{v}_l - \lambda_{\text{pm}} \nabla T) \cdot \mathbf{n}]^{\text{pm}}. \quad (3.15)$$

As we assume that the normal water flux from the porous medium evaporates totally and immediately at the interface (see equation (3.13)) the enthalpy of vaporization  $\Delta h_{\text{vap}}$  is included in the formulation of enthalpy to account for the phase change. For alternatives to this equilibrium condition, we refer to Alazmi and Vafai (2001).

### 3.4.3 Chemical equilibrium

The chemical equilibrium at the interface can be considered as an equilibrium between three compartments and two phases (see figure 3.7). On the micro scale, the equilibrium of the chemical potentials of the component water  $\psi_\alpha^w$ ,  $\alpha \in \{l, g\}$  can be stated from pair-wise considerations corresponding to figure 3.7, under the assumption that the gas phase is separated by the interface,

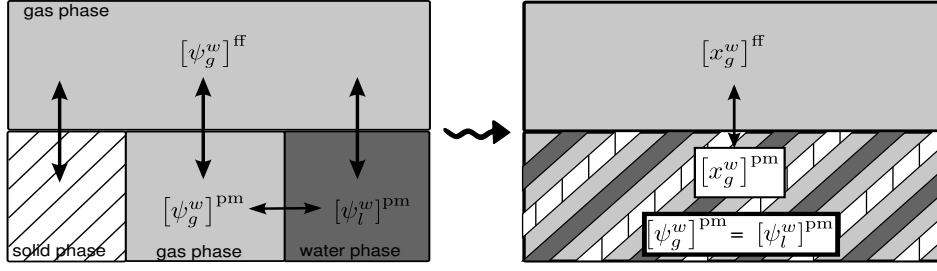


**Figure 3.7:** Chemical equilibrium at the pore-scale and at the REV-scale. On the micro-scale, equilibrium conditions between the gas phase in the free-flow region and the two phases in the porous medium have to be formulated, consisting of continuity of chemical potential. On the REV-scale, continuity of chemical potential between the phases inside the porous medium is assumed and continuity of mole fractions is applied as coupling condition between the gas phase in the free flow and porous medium (reproduced from Mosthaf et al., 2011).

$$[\psi_g^w]^{\text{ff}} = [\psi_l^w]^{\text{pm}}, \quad (3.16a)$$

$$[\psi_g^w]^{\text{ff}} = [\psi_g^w]^{\text{pm}}. \quad (3.16b)$$

In the subdomain model, the equilibrium between the gas and the liquid phase within the porous medium,  $[\psi_l^w]^{\text{pm}} = [\psi_g^w]^{\text{pm}}$ , is already satisfied (see section 3.2). As a consequence, only (3.16b) has to be imposed at the interface. On the REV-scale, continuity of the chemical potential cannot be postulated since the continuity of the normal forces (3.11c) leads to a jump in the gas-phase pressure. As stated before, this pressure difference is due to differences in the model concepts applied in the subdomains. More precisely, it is due to the application of the potential theory in the porous-medium region where shear stresses are not explicitly resolved. These small differences in pressure cause discontinuities in the chemical potentials and/or mole fractions. Assuming all components to be ideal, the difference in the chemical potential can be written as (Atkins and de Paula, 2006):

$$\psi^{\text{ff}}(p_g^{\text{ff}}) - \psi^{\text{pm}}(p_g^{\text{pm}}) = \left[ \mathfrak{R}T \ln \left( x_g^w \frac{p_g}{p_0} \right) \right]^{\text{ff}} - \left[ \mathfrak{R}T \ln \left( x_g^w \frac{p_g}{p_0} \right) \right]^{\text{pm}} = \ln \left( \frac{[x_g^w p_g]^{\text{ff}}}{[x_g^w p_g]^{\text{pm}}} \right)^{\mathfrak{R}T}, \quad (3.17)$$

where  $p_0$  is the reference pressure and  $\mathfrak{R}$  is the universal gas constant. However, the

magnitude of the difference in chemical potential is not known and a condition for the mole fractions cannot be deduced. Therefore, we assume the continuity of the mole fractions as a coupling condition:

$$[x_g^\kappa]^{\text{ff}} = [x_g^\kappa]^{\text{pm}}, \quad \kappa \in \{a, w\}. \quad (3.18)$$

Naturally, the continuity of the component fluxes across the interface is required for  $\kappa \in \{w, a\}$ :

$$\begin{aligned} & \left[ \left( \varrho_g \mathbf{v}_g x_g^\kappa - D_g^\kappa \varrho_g \nabla x_g^\kappa \right) \cdot \mathbf{n} \right]^{\text{ff}} = \\ & - \left[ \left( \varrho_g \mathbf{v}_g x_g^\kappa - D_g^{\kappa, \text{pm}} \varrho_g \nabla x_g^\kappa + \varrho_l \mathbf{v}_l x_l^\kappa - D_l^{\kappa, \text{pm}} \varrho_l \nabla x_l^\kappa \right) \cdot \mathbf{n} \right]^{\text{pm}}. \end{aligned} \quad (3.19)$$

Based on the same reasoning as for the total mass fluxes, the component fluxes of both fluid phases of the porous medium that flow across the interface are added and balanced with the component fluxes in the gas phase of the free flow. Summing up equations (3.19) for  $\kappa \in \{w, a\}$  results in the continuity of total mass flux (3.13). Two of the three conditions (3.13) and (3.19) can be chosen equivalently, according to the set of balance equations that is used in the submodels.

Note that the diffusion coefficients in both domains differ from each other. For the free-flow domain, the binary diffusion coefficient  $D_g^\kappa$  (dependent on temperature and pressure) is used, whereas for the porous medium, the diffusion coefficients  $D_\alpha^{\kappa, \text{pm}}$  are functions of the properties of the solid porous medium and the fluids.

Furthermore, if the liquid phase at the porous-medium side of the interface disappears, the previously mentioned primary-variable switch is triggered in the porous medium and the mole fraction  $x_g^w$  is used as a primary variable instead of the saturation. The coupling simplifies to a single-phase two-component system. Water can be transferred only by vapour diffusion and by advective transport in the gas phase over the porous-medium–free-flow interface.

The applicability of the presented coupling concept is shown in Mosthaf et al. (2011) for evaporation from a partially saturated porous medium influenced by an ambient

air flow. The influence of temperature, Beavers-Joseph coefficient and permeability is investigated in Baber et al. (2012). The Beavers-Joseph coefficient was found to have a negligible influence on the evaporation rate. Mosthaf et al. (2014) assesses the influence of porosity, permeability, heat conductivity, radiation and  $p_c$ - $S_l$  relation. They find, that the evaporation rate is influenced by pore-scale-induced non-linearities, which have to be included in the REV-scale model. Especially the surface-water content was found to be important.

The presented simple interface concept allows the coupling of one-phase Stokes and two-phase Darcy flow. It can describe mass, component, momentum and energy transport inside the subdomains and across the interface. Hence, evaporation and condensation at the interface as well as the mutual influence of the subdomain conditions can be simulated. In the next chapter, a first step towards the consideration of pore-scale interface effects is shown and the coupling concept is extended to account for drop dynamics at the interface.

## 4 Conceptual and mathematical model: Coupling concepts for a complex interface

The concept of a simple interface was explained in detail in the last section (3.4) (Mosthaf et al., 2011, Baber et al., 2012). However, the formation of drops or films on the porous surface have a significant influence but have not been considered in the REV-scale coupling approaches until now.

In case of an interface layer between free and porous-medium flow, a region much thinner than the surrounding domains strongly influences the behaviour of the whole system. Hence, an adequate description for these possibly complex, heterogeneous, thin structures has to be found. One possibility is to use a micro- or pore-network model to resolve the interface region (transition zone or interface layer). In section 4.1, a first step towards a coupled micro-macro model is shown. The interface layer is described by a bundle-of-tubes concept and integrated monolithically into the coupled system. The coupling concept is explained theoretically, but has never been implemented and tested. A concept including drop dynamics is the ultimate goal of this work and an intensive analysis showed that a full tube model is not required to describe drop formation.

The coupling concept of the simple interface is extended further to account for drop dynamics on the free-flow side of the interface (see section 4.2). The drops are not resolved but integrated into the REV-scale coupling concept which accounts for the physics of drop formation, growth and detachment (Baber et al., 2014). The resulting complex interface includes the mass and energy of drops that form on the interface.

In both the bundle-of-tubes and the drop coupling concept the definition of the pressure condition is challenging due to the scale-dependent definition of pressure. The issue

of the definition and combination of pore- and REV-scale pressure and the resulting conditions for mechanical equilibrium are summarised and discussed in section 4.3.

All balance equations and coupling conditions are developed for non-isothermal two-phase two-component flow in a hydrophobic porous medium in contact with a non-isothermal one-phase two-component free flow. All assumptions from the previous section hold: local thermodynamic equilibrium is attempted, a rigid solid phase with no slip on the solid surface is assumed and direct evaporation of water at the interface is enforced.

## 4.1 Complex interface: Bundle-of-tubes model

As mentioned before, the interaction of free-flow and porous-medium systems (see sections 3.2 and 3.3) can be determined by an interface layer. Possibly, its complex structure cannot be described by a simple interface. In the case of transvascular flow (see section 6), for example, the micro-vascular wall is a thin heterogeneous structure determining the exchange between vascular and tissue compartment. In diapers, layers of different thickness ensure the absorption and retention of fluids. Such thin, heterogeneous structures can be described as 2D-continua (see section 2.2) or resolved by pore-network models. In both cases, the coupling to surrounding full-dimensional macro-models is necessary. To include a pore-scale interface model, coupling conditions from the free-flow to the pore-scale model and from the pore-scale to the porous-medium model have to be defined. As a first step, the pore-scale model will be substituted with a **bundle-of-tubes concept** of thickness  $\delta$  with a known analytic solution (see figure 4.1). This description is based on the pore-size distribution which is sorted into classes of tubes with mean radius  $\bar{r}_{\text{pore}}$  with  $f_{\bar{r}_{\text{pore}}}$  percent of pores and  $n_{\bar{r}_{\text{pore}}} = \frac{\Phi_{\text{A}\Gamma} f_{\bar{r}_{\text{pore}}}}{\Lambda_{\text{pore}}}$  pores per class (see figure 4.2 and Gurau et al. (2008)). The pores are assumed to be straight and circular so that corner flow does not occur. Furthermore, gravity is neglected. Incompressible Poiseuille flow occurs inside the tubes perpendicular to the interface (Benziger et al., 2005):

$$v_{\text{pore}} = -\frac{(\bar{r}_{\text{pore}})^2}{8\mu_g} \frac{\Delta p_g}{\delta}. \quad (4.1)$$

The coupling concept for free and porous-medium flow across a bundle-of-tubes model is first described for one phase and one pore (see figure 4.3). Then, it is shown for several

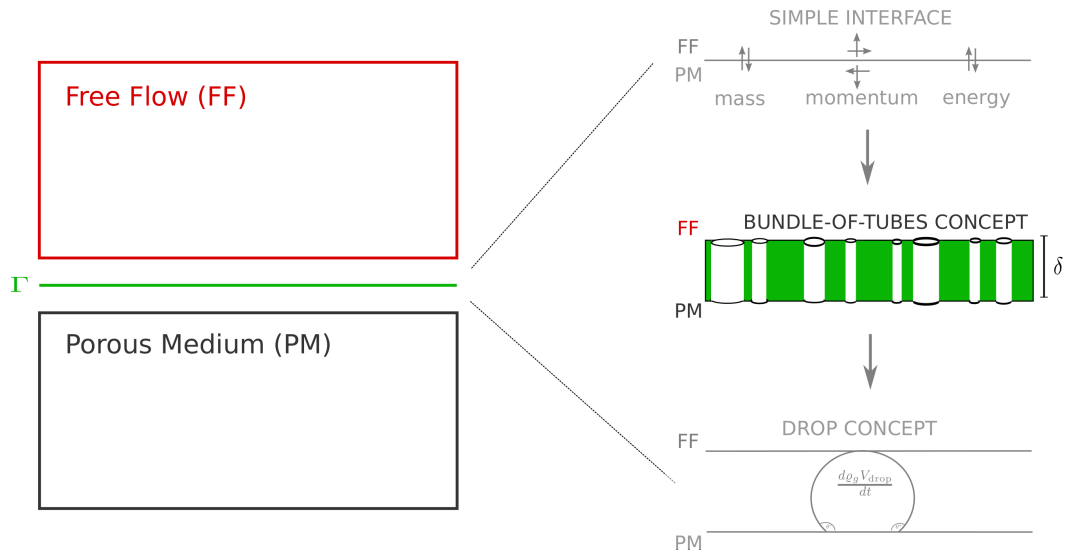


**Figure 4.1:** A pore-scale bundle-of-tubes approach couples free-flow and porous-medium region.

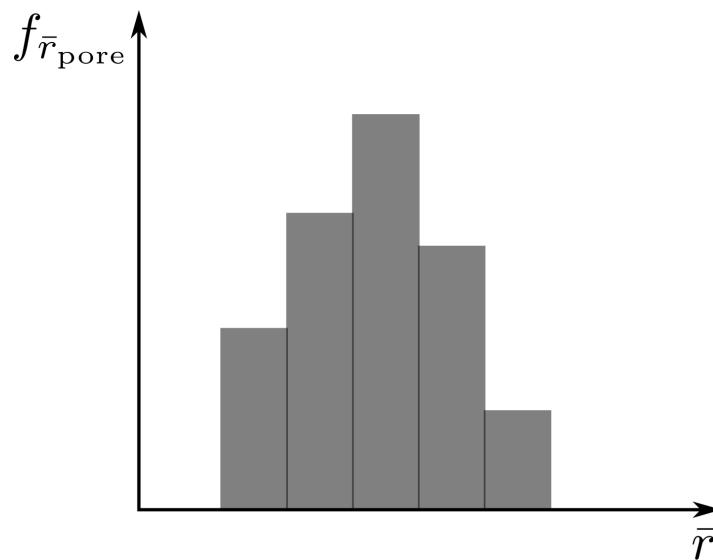


**Figure 4.2:** Pore-size distribution at the interface which is sorted into classes of tubes with mean radius  $\bar{r}_{pore}$  with  $f_{\bar{r}_{pore}}$  percent of pores and  $n_{\bar{r}_{pore}}$  pores per class.

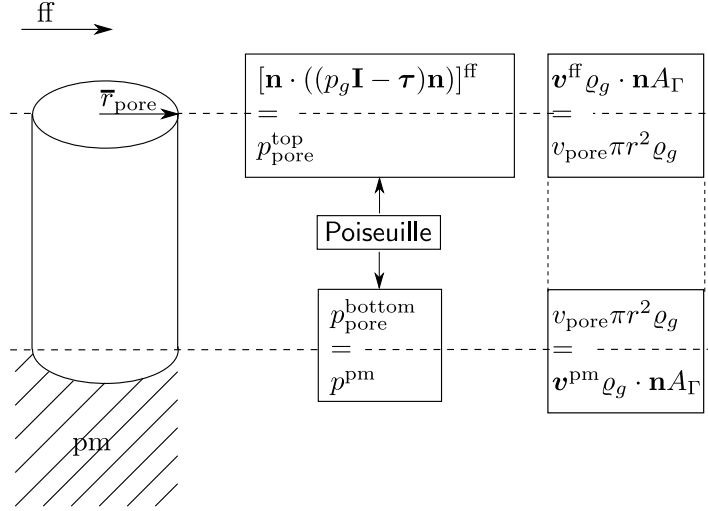


**Figure 4.3:** Force and flux balance for one pore.

tubes. Finally, it is expanded to couple a one-phase free-flow to a two-phase porous-medium system. The free-flow system is simplified to the Stokes equation neglecting inertial forces.

Figure 4.3 shows that the flux from the porous medium across the interface  $\mathbf{f}^{\text{pm}} \cdot \mathbf{n} = \mathbf{v}_g^{\text{pm}} \rho_g \cdot \mathbf{n} A_\Gamma$  has to be equal to the flux in the pore  $f_{\text{pore}} = v_{\text{pore}} \rho_g \pi (\bar{r}_{\text{pore}})^2$ , which in turn has to equal the free-flow flux  $\mathbf{f}^{\text{ff}} \cdot \mathbf{n} = \mathbf{v}_g^{\text{ff}} \rho_g \cdot \mathbf{n} A_\Gamma$ . Equation (4.2) is sufficient as coupling condition for the conservation of mass:

$$[\rho_g \mathbf{v}_g \cdot \mathbf{n}]^{\text{pm}} = [\rho_g \mathbf{v}_g \cdot \mathbf{n}]^{\text{ff}}. \quad (4.2)$$

To define mechanical equilibrium, pore- and macro-scale pressure have to be combined. As mentioned in section 3.1, Hassanizadeh and Gray (1993) and Nordbotten et al. (2008), the transition from pore- to REV-scale pressure is challenging. The REV-scale models (see sections 3.2 and 3.3) only provide averaged quantities. Here, the micro-scale pore pressure  $p_{\text{pore}}$  is assumed to be equal to the macro-scale porous-medium pressure  $p^{\text{pm}}$  at the bottom of the tubes. This assumption is discussed in detail in section 4.3. In the free-flow region, the normal shear stress has to be considered  $p_{\text{pore}} = [\mathbf{n} \cdot ((p_g \mathbf{I} - \boldsymbol{\tau}) \mathbf{n})]^{\text{ff}}$  due to the different model concepts employed in the free-flow and tube model. Consequently,

the following equilibrium conditions can be defined (see also figure 4.3):

$$[\mathbf{n} \cdot ((p_g \mathbf{I} - \mu_g \nabla \mathbf{v}_g) \mathbf{n})]^{ff} = p_{\text{pore}}^{\text{top}}, \quad (4.3)$$

$$p_{\text{pore}}^{\text{top}} = v_{\text{pore}} \frac{8\mu_g}{(\bar{r}_{\text{pore}})^2} \delta + p_{\text{pore}}^{\text{bottom}}, \quad (4.4)$$

$$p_{\text{pore}}^{\text{bottom}} = p_g^{\text{pm}}. \quad (4.5)$$

In Equation (4.4), the pressure at the bottom (see equation (4.5)) and the pressure at the top of the pore (see equation (4.3)) are related by a one-dimensional (1D) pipe flow described by the Hagen-Poiseuille equation (4.1). These conditions can be combined to the definition of mechanical equilibrium:

$$[\mathbf{n} \cdot ((p_g \mathbf{I} - \boldsymbol{\tau}) \mathbf{n})]^{ff} = \underbrace{v_{\text{pore}} \frac{8\mu_g \delta}{(\bar{r}_{\text{pore}})^2}}_{\Delta p} + p_g^{\text{pm}} \quad \text{with} \quad v_{\text{pore}} = \frac{[\mathbf{v}_g \cdot \mathbf{n}]^{\text{pm}} A_\Gamma}{\pi (\bar{r}_{\text{pore}})^2}. \quad (4.6)$$

The pore velocity  $v_{\text{pore}}$  results from the continuity of fluxes.

For a bundle of tubes, the continuity condition (4.2) and the mechanical equilibrium (4.6) remain valid. To obtain the pore velocity, the flux  $\mathbf{f}^{ff}$  coming from the free-flow or  $\mathbf{f}^{\text{pm}}$  coming from the porous-medium region has to be divided up into the fluxes through parallel pores. According to Helmig and Class (2004), the energy loss in all tubes of a parallel tube system has to be equal. Assuming Poiseuille flow and a constant velocity across the tube height  $\delta$ , and neglecting gravity yields the same pressure difference in all pores but different velocities and fluxes. Thus, it is not necessary to find an appropriate averaging procedure for the pore pressure. The pore pressure is used directly in the definition of mechanical equilibrium.

Flux continuity yields:

$$[\varrho_g \mathbf{v}_g \cdot \mathbf{n}]^{\text{pm}} A_\Gamma = [\varrho_g \mathbf{v}_g \cdot \mathbf{n}]^{ff} A_\Gamma = \Phi \sum_{\bar{r}_{\text{pore}}} -\frac{(\bar{r}_{\text{pore}})^2}{8\mu_g} \varrho_g \frac{\Delta p_g}{\delta} \pi (\bar{r}_{\text{pore}})^2 n_{\bar{r}_{\text{pore}}}. \quad (4.7)$$

Here, all fluxes through the pores are summed up (Balhoff et al., 2008) and are set equal to the fluxes of the REV-scale models to obtain a mass-conservative flow field. Note, that the pore velocity has to be multiplied by the porosity  $\Phi$  to bridge the gap between pore- and REV-scale. Consequently, the pressure difference  $\Delta p$  needed for equation (4.6)

can be expressed as:

$$\Delta p = \frac{[\varrho_g \mathbf{v}_g \cdot \mathbf{n}]^{\text{pm}} A_\Gamma \delta}{\Phi \sum_{\bar{r}_{\text{pore}}} -\frac{(\bar{r}_{\text{pore}})^2}{8\mu_g} \varrho_g \pi (\bar{r}_{\text{pore}})^2 n_{\bar{r}_{\text{pore}}}}. \quad (4.8)$$

The reasoning from above can also be applied to a two-phase porous-medium system in contact with gaseous free flow. In this case, the ratio of water-filled pores to the total number of pores has to be known. Water has to overcome the entry pressure to enter a pore. The entry pressure is given by the Young-Laplace equation:

$$p_c = \frac{2\gamma_{lg} \cos \theta}{\bar{r}_{\text{pore}}}, \quad (4.9)$$

where  $\gamma_{lg}$  is the surface tension and  $\theta$  is the contact angle between wetting phase and solid material. Pores are invaded by water once the porous-medium water pressure  $p_l^{\text{pm}}$  is larger than the sum of free-flow gas pressure and capillary pressure of the curved interface:

$$p_g^{\text{ff}} + \frac{2\gamma_{lg} \cos \theta}{\bar{r}_{\text{pore}}} \leq p_l^{\text{pm}}. \quad (4.10)$$

The applicability of this microscopic pressure equilibrium to the macro-scale is discussed in section 4.3.2. With equation (4.10), the pores which fill with water can be identified. In a hydrophobic medium, like fuel-cell diffusion media, the largest pores are filled first. Tubes are assumed to fill instantaneously with water once the entry pressure is overcome. Thus, the tubes are either fully saturated with water or fully saturated with gas. Knowing the respective cross-section of water- and gas-filled pores,  $A_{\Gamma l}$  and  $A_{\Gamma g}$ , the flux continuity and mechanical equilibrium can be defined. The fluxes from the porous-medium split up into the water- and gas-filled pores. Following the same reasoning as in section 3.4.1, all water coming from the porous medium or from the water-filled pores has to end up in the free-flow region causing complete evaporation at the interface. Consequently, the flux-continuity condition looks similar to equation (3.13):

$$\begin{aligned} & [(\varrho_g \mathbf{v}_g + \varrho_l \mathbf{v}_l) \cdot \mathbf{n}]^{\text{pm}} A_\Gamma \\ &= \Phi \sum_{\bar{r}_{\text{pore}} \in g} v_{\text{pore}}(\bar{r}_{\text{pore}}) \varrho_g A_{g,\text{pore}} n_{\bar{r}_{\text{pore}}} + \Phi \sum_{\bar{r}_{\text{pore}} \in l} v_{\text{pore}}(\bar{r}_{\text{pore}}) \varrho_l A_{l,\text{pore}} n_{\bar{r}_{\text{pore}}} \\ &= [\varrho_g \mathbf{v}_g \cdot \mathbf{n}]^{\text{ff}} A_\Gamma. \end{aligned} \quad (4.11)$$

Here, the first term behind the first equals sign sums up all fluxes through gas-filled pores ( $\bar{r}_{\text{pore}} \in g$ ), the second term sums up all fluxes through water-filled pores ( $\bar{r}_{\text{pore}} \in l$ ).

Furthermore, the gas and water fluxes from the porous medium equal the gas and water fluxes in the pore-scale model respectively:

$$[\varrho_l \mathbf{v}_l \cdot \mathbf{n}]^{\text{pm}} A_{\Gamma l} = \Phi \sum_{\bar{r}_{\text{pore}} \in l} v_{\text{pore}}(\bar{r}_{\text{pore}}) \varrho_l A_{l,\text{pore}} n_{\bar{r}_{\text{pore}}}, \quad (4.12)$$

$$[\varrho_g \mathbf{v}_g \cdot \mathbf{n}]^{\text{pm}} A_{\Gamma g} = \Phi \sum_{\bar{r}_{\text{pore}} \in g} v_{\text{pore}}(\bar{r}_{\text{pore}}) \varrho_g A_{g,\text{pore}} n_{\bar{r}_{\text{pore}}}, \quad (4.13)$$

where  $A_{\Gamma l} = \sum_{\bar{r}_{\text{pore}} \in l} A_{l,\text{pore}} = \sum_{\bar{r}_{\text{pore}} \in l} \pi(\bar{r}_{\text{pore}})^2$  is the area of the interface available for water flow and  $A_{\Gamma g} = \sum_{\bar{r}_{\text{pore}} \in g} A_{g,\text{pore}} = \sum_{\bar{r}_{\text{pore}} \in g} \pi(\bar{r}_{\text{pore}})^2$  is the area of the interface available for gas flow.

The pressure condition for the gas phase is the same as condition (4.6). Pore and porous-medium water pressure at the bottom of water-filled pores are assumed to be equal. At the top of the pore, meaning at the interface to the free flow, the capillary pressure has to be considered. Here, the pore-scale capillary pressure (4.9) converts the pore water pressure into the pore gas-phase pressure. Employing an area-weighted average, the definition of mechanical equilibrium is given by:

$$[\mathbf{n} \cdot ((p_g \mathbf{I} - \boldsymbol{\tau}) \mathbf{n})]^{\text{ff}} A_{\Gamma} = p_g^{\text{top}} A_{\Gamma g} + (p_l^{\text{top}} - p_c) A_{\Gamma l}, \quad (4.14)$$

where the pressure at the top of the pore-model  $p_{\alpha}^{\text{top}}$  is defined as:

$$p_{\alpha}^{\text{top}} = p_{\alpha}^{\text{pm}} + \frac{[\varrho_{\alpha} \mathbf{v}_{\alpha} \cdot \mathbf{n}]^{\text{pm}} A_{\Gamma \alpha} \delta}{\Phi \sum_{\bar{r}_{\text{pore}} \in \alpha} \frac{-(\bar{r}_{\text{pore}})^2}{8\mu_g} \varrho_g \pi(\bar{r}_{\text{pore}})^2 n_{\bar{r}_{\text{pore}}}}. \quad (4.15)$$

The conditions (4.11) and (4.15) include the flow resistance of the interface defined by a bundle-of-tubes model. As in section 3.4, the Beavers-Joseph-Saffman condition (3.12) defines the tangential slip velocity at the interface. The Beavers-Joseph coefficient  $\alpha_{\text{BJ}}$  has to be determined dependent on the ratio of water- and gas-filled pores. The coupling concept needs to be extended to component and energy transport.

The general concept can be transferred to couple a pore-network model to the free and porous-medium REV-scale models. Balhoff et al. (2008) showed the coupling of

pore-network and REV-scale porous-medium models using mortar elements. One of the main advantages of the mortar method is that the pressure is mapped from the mortar space onto the subdomains so that flux continuity is given (Arbogast and Brunson, 2007). The understanding gained by coupling pore- and REV-scale models might help to develop appropriate 2D-continuum descriptions for a complex interface layer. Moreover, a pore-scale model provides information about the location of water-filled pores so that the effects of the variation of the surface water content discussed in Mosthaf et al. (2014) can be captured.

## 4.2 Complex interface: Drop concept<sup>16</sup>

In the previous section, the interface was resolved and the pores approximated by a bundle-of-tubes concept. Now, the description is modified, giving the interface REV-character. In contrast to the simple interface concept explained in section 3.4, the interface can now store mass and energy. Hence, the REV-scale coupling conditions from section 3.4 are extended to a complex interface which accounts for drop dynamics (see figure 4.4). Note, that this section is an extension of section 3.4. All assumptions and explanations noted therein will not be mentioned explicitly again.

When a two-phase porous medium is in contact with free gas flow, it may happen that water flowing towards the free-flow region does not fully evaporate at the interface. Driven by capillary forces, the water emerges from the pores as liquid phase and forms drops or puddles on the porous-medium surface. These drops will grow and merge until they detach eventually due to the drag force exerted by the gas flow. Decreasing the cross-section available for the free gas flow, the drops have a significant influence on the flow conditions within the free-flow region. The emergence and growth of drops and their influence and interaction with the free gas flow is a complex interplay of different processes and forces. Sinha and Wang (2008) point out that the interface wettability and the corresponding water behaviour influence the saturation within the porous medium. Water removal from the surface by gas drag is significantly influenced by the wettability

---

<sup>16</sup>Parts of this section are published in Baber, K., Flemisch, B., and Helmig, R. (2014). Modelling drop dynamics at the interface between free and porous-medium flow using the mortar method. submitted to International Journal of Heat and Mass Transfer.

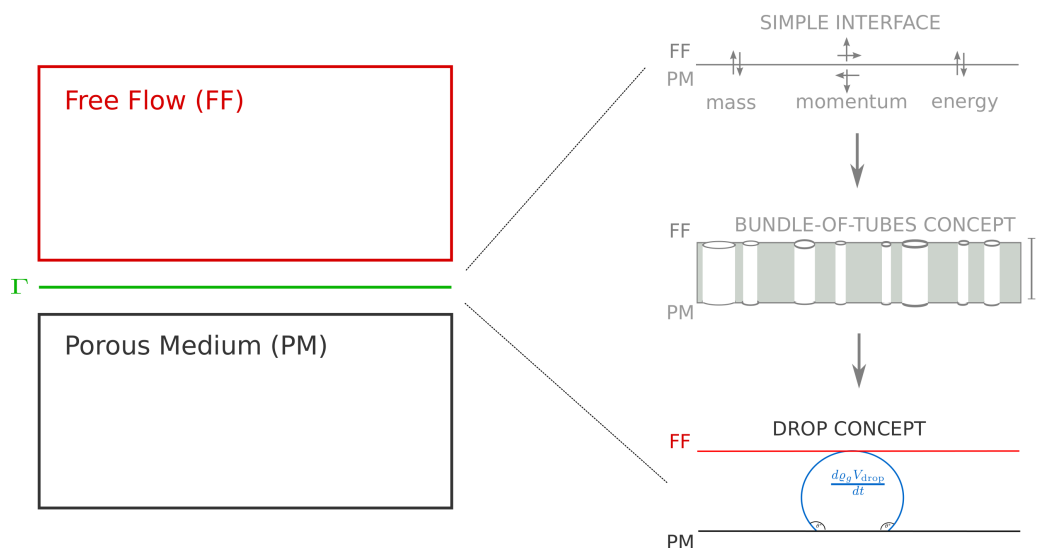


**Figure 4.4:** The interface concept accounts for drop formation, growth and detachment. The coupling conditions account for the mass and energy of the drop.

(see section 2.4). In the following, a hydrophobic medium is considered motivated by the hydrophobic gas-diffusion layer of PEM fuel cells.

The model describes drop formation, growth and detachment. Merging or coalescence of drops cannot be resolved by the model since the drop surfaces and distances are not tracked by the averaged continuum approach. The model neither describes the fate of the drops after they are detached. A detached drop can either slide on the porous-medium surface, lift and float or wick into the film flow in the corners of the gas channel. Such processes are not yet resolved by the current model since the focus is on the interface description and drop formation. Thus, the influence of the hydrophilic gas-channel walls cannot be assessed by the developed model.

Direct simulations have been employed to describe the formation of drops from partially saturated porous media and their fate (Theodorakakos et al., 2006, Qin et al., 2012d, Cho et al., 2012b). The motivation of this work, however, is to integrate the occurrence of droplets into the REV-scale interface concept. The formation, growth and detachment as well as the influence on the free gas flow is described in an averaged manner without resolving the drops. The coupling conditions for free flow and porous-medium flow (see section 3.4) will be extended based on phenomenological descriptions of the pore-scale processes.

To account for the drops as part of the coupling conditions, assumptions have to be

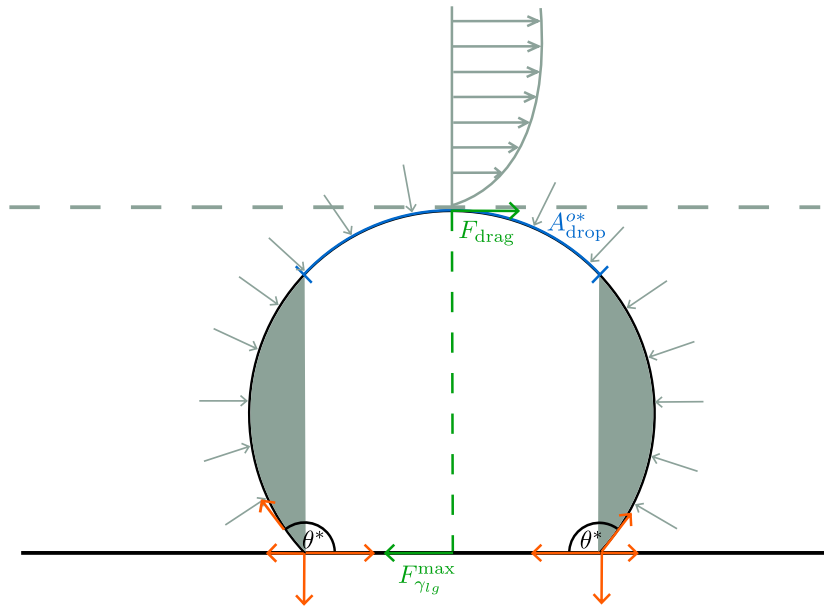


**Figure 4.5:** Simplified spherical drop.

made (see figure 4.5):

- static, equilibrium conditions and applicability of Young's equation,
- symmetrical, non-deformed drop, except for calculating the retention force  $F_{\gamma_{lg}}^{\max}$ ,
- constant pressure around drop,
- constant curvature of the drop surface,
- rapid mixing: constant temperature, mole fractions and pressure inside the drop,
- neglect gravity (see section 2.4),
- slow free flow: the applicability of expressions for evaporative fluxes derived for drops in still air and constant-contact-angle evaporation mode is assumed (Picknett and Bexon, 1977, Erbil et al., 2002, Song et al., 2011)(see section 2.4),
- to calculate the retention force:
  - The maximally sustained contact-angle hysteresis is taken as a material parameter (see section 2.4). According to Quéré et al. (1998) and Extrand and Gent (1990), it is characteristic for a combination of liquid and solid and not dependent on the drop volume.

- A circular contact line is assumed, neglecting elongation of the contact area (Chen et al., 2005, Kumbur et al., 2006).

It was said in section 2.4, that Young’s equation (2.5) is only valid under equilibrium and if drops do not touch the channel walls (Kandlikar et al., 2014). A drop emerging from a porous medium grows due to the water flux from the porous medium and partly evaporates. Sinha and Wang (2008) describe the drop-growth process on a mixed wet surface. In reality, the contact angle varies while the drop is growing until a threshold value is reached. Theodorakakos et al. (2006) claim that the drop shape does not change during the growth process as long as the drop is not subjected to an external flow field. In that case, the drag force of the GC-flow field leads to deformation and the dynamic change in contact angle determines the drop shape. Due to these processes, the drops are not in equilibrium and contact-angle hysteresis occurs. Kandlikar et al. (2014) state that measurements of the dynamically varying contact angle are required to understand the droplet behaviour and interaction with the gas-channel walls. Nevertheless, equilibrium and static conditions are assumed here. The static contact angle  $\theta^*$  being a material parameter is used to calculate the radius of curvature and all other geometric information (see equations (2.1)-(2.4)). These assumptions are generally made in the literature (Chen et al., 2005, Kumbur et al., 2006).

### 4.2.1 REV drop concept

To realise the REV interface concept indicated above, an area of influence for one drop (a drop-REV)  $\Omega_{\text{drop}}$  is chosen, where the total interface area  $A_{\Gamma}$  is an integral multiple of  $|\Omega_{\text{drop}}|$ :  $A_{\Gamma} = n \cdot |\Omega_{\text{drop}}|$   $n \in \mathbb{N}$  (see figure 4.6). All water-filled pores within one  $\Omega_{\text{drop}}$  feed one single drop. Thus, there is only one drop per drop-REV. The choice of  $\Omega_{\text{drop}}$  determines the possible number of drops. The numerical realisation and the resulting limitations and numerical results are discussed in chapter 5 and 7.3.3.

Figure 4.6 illustrates the conceptual idea. On the left-hand side, free flow and porous medium are coupled across the interface  $\Gamma$ . The interface conditions have to account for the pore-scale processes depicted on the right-hand side in an averaged continuum manner. The drop can be imagined as part of the interface sitting between bottom free-flow and top porous-medium boundary. Free flow and porous medium interact directly across  $A_{\text{free}}$  and through the drop across the contact area  $A_{\text{drop}}^{\text{CA}}$ . To fulfil the

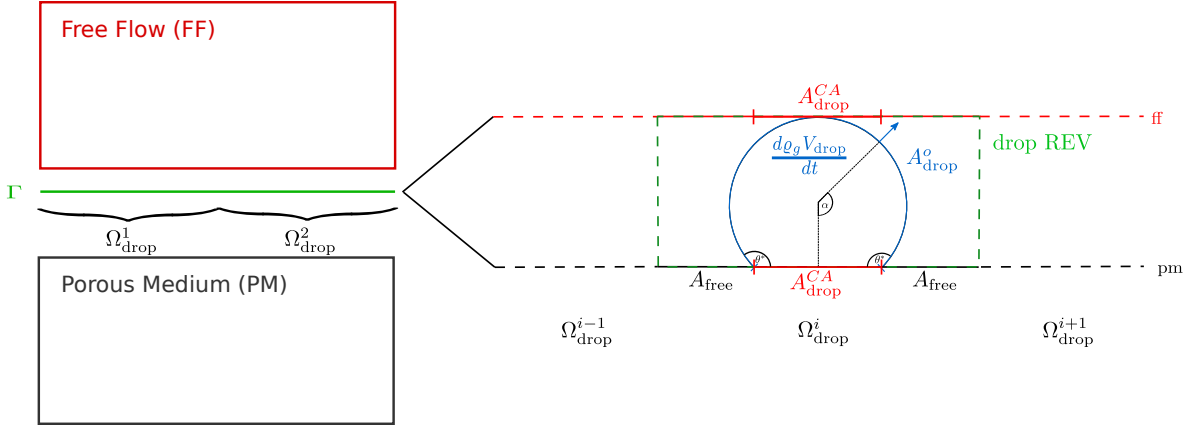


**Figure 4.6:** Conceptual model: The interface  $\Gamma$  between free flow and porous medium is divided into an integral number of areas of influence  $\Omega_{\text{drop}}$ . There is one drop per area of influence. The area of influence is partly covered by the drop  $\Omega_{\text{drop}} = A_{\text{free}} + A_{\text{drop}}^{\text{CA}}$ .

conservation laws, mass that enters the drop across  $A_{\text{drop}}^{\text{CA}}$  from the porous medium can either be stored within the drop or enter the free-flow region across an area equivalent to  $A_{\text{drop}}^{\text{CA}}$ . Following the REV approach further, the exact location of drop-free and drop-covered interface is not needed. Only the area fractions of each interface status are required:  $a_{\text{drop}} = \frac{A_{\text{drop}}^{\text{CA}}}{|\Omega_{\text{drop}}|}$  and  $a_g = \frac{A_{\text{free}}}{|\Omega_{\text{drop}}|}$ . Equivalently,  $a_{\text{drop}}^o = \frac{A_{\text{drop}}^o}{|\Omega_{\text{drop}}|}$  describes the relation of the drop-surface area  $A_{\text{drop}}^o$  and the area of influence  $\Omega_{\text{drop}}$ .

The decision for a continuum description entails that the local phenomena of drop formation and resulting local pressure loss or resulting local changes in the water content cannot be described. It is inherent of a continuum description that local distributions cannot be resolved but average quantities like saturation or an average drop volume are defined. The averaged quantity of interest here is the fraction of the interface which is covered by drops  $a_{\text{drop}}$ . This area fraction is used to form an area-weighted average of the coupling conditions with and without drop. The interplay of flow field and deformed drop is complicated and cannot be fully reproduced by the envisaged continuum description.

## 4.2.2 Drop formation

To describe the drop formation, the top layer of the porous medium is considered to be a bundle of tubes (see figure 4.7 and section 4.1). The bundle-of-tubes approximation describes the top layer of thickness  $\delta$  where the pores of the porous medium do not intersect any more and enter the free-flow region. This description is based on the

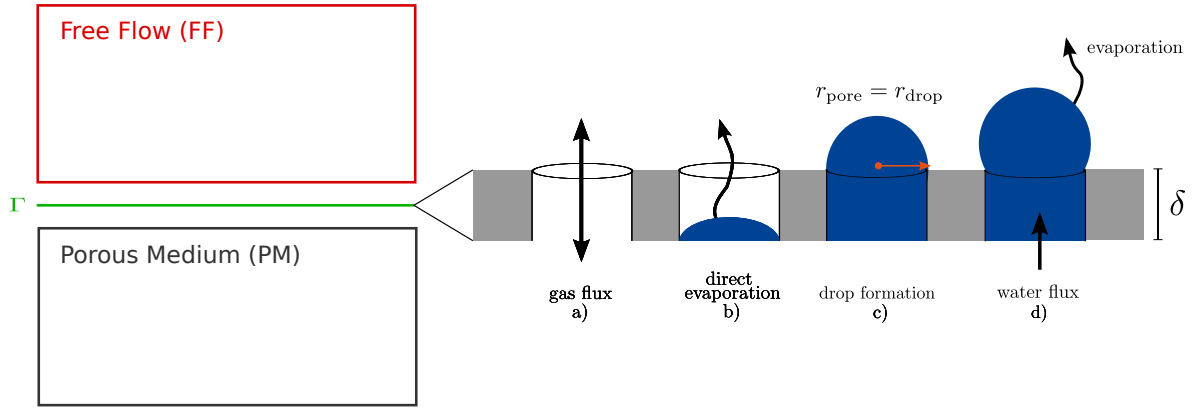


**Figure 4.7:** A bundle-of-tubes model describes the interface region between porous medium and free flow representing pores ending in the free-flow region. Possible pore constitutions are: a) gas flux through pore, b) water meniscus in pores with direct evaporation, c) spherical caps with a diameter equal to the pore diameter, d) a drop fed by the porous medium, evaporating into the free-flow region.

assumption that the pore space of the fibrous gas-diffusion layer is made of capillary tubes. The bundle-of-tubes model at the interface is based on the pore-size distribution at the interface which is sorted into classes of tubes with mean radius  $\bar{r}_{\text{pore}}$  with  $f_{\bar{r}_{\text{pore}}}$  percent of pores and  $n_{\bar{r}_{\text{pore}}} = \frac{\Phi A_{\Gamma} f_{\bar{r}_{\text{pore}}}}{A_{\text{pore}}}$  pores per class (Gurau et al., 2008). We assume that the porosity at the interface and inside the porous medium are the same (Gurau and Mann, 2010). Note that this pore-scale model is not explicitly included as a pore-network model and coupled to the surrounding macro models. Only its concept and physics are used to derive the conditions for drop formation.

Assuming circular pores that do not have corner flow, three conditions are possible for pores at the interface (see figure 4.7). Pores can allow gas flow (see figure 4.7 a.)). Other pores can have a water meniscus at the bottom where direct evaporation happens (see figure 4.7 b.)). Equation (3.13) already accounts for the case of direct evaporation (see section 3.4). Hence, it covers cases a) and b) of the possible pore conditions. Finally, pores can be covered by drops (see figure 4.7 d)). In the following, the smallest entity that is considered a drop is a spherical cap with the diameter of a pore (see figure 4.7 c)).

The static pore model (bundle of tubes) is employed to determine which classes of tubes will be invaded by water based on the conditions in the porous-medium and the free-flow region. The change of the pore constitution from gas to water saturated is considered to be instantaneous. The opposite process, gas imbibing pores and displacing water

menisci, is not of interest for the averaged model description in the porous medium. The challenge is now to use the macroscopic information provided by the REV-scale models in combination with the pore-model concept.

The two-phase porous-medium model does not resolve the water distribution locally, but only provides averaged quantities. As in the previous section, we assume that the pore-scale water pressure is equal to the macro-scale water pressure  $p_l^{\text{pm}}$  in the porous medium. For the vertical movement of the meniscus inside the pores, the influence of shear stress of the surrounding phases is negligible (Hassanizadeh and Gray, 1993). Hence, the gas pressure in the free-flow region  $p_g^{\text{ff}}$  is employed directly. Please be referred to section 4.3 for a detailed discussion of these assumptions.

Water accumulates in the GDL until a threshold pressure is reached. Caps form on water-filled pores. Once the cap radius equals the pore radius, it is considered a drop (see figure 4.7 c.)). This is the limit case where the drop has the minimum radius  $r_{\text{drop}} = \bar{r}_{\text{pore}}$ , meaning that the pressure which has to be overcome by the pressure of the water phase in the porous medium to let the drop grow is at a maximum (Gurau and Mann, 2009, 2010). Hence, drops form on all pores where the porous-medium water pressure  $p_l^{\text{pm}}$  is larger than the sum of the free-flow forces and the capillary pressure of the curved drop surface:

$$p_g^{\text{ff}} + \frac{2\gamma_{lg}}{\bar{r}_{\text{pore}}} \leq p_l^{\text{pm}}. \quad (4.16)$$

Knowing the pore-size distribution, it is now possible to derive the area of the interface made up by water-filled pores. We assume that spherical caps with  $r = \bar{r}_{\text{pore}}$  form on all pore classes for which condition (4.16) is fulfilled. Adding up all cap volumes  $V_{\text{cap}} = \frac{2}{3}\pi(\bar{r}_{\text{pore}})^3$  within an area of influence  $\Omega_{\text{drop}}$ , the total drop volume is estimated:

$$V_{\text{drop}} = \sum_{\bar{r}_{\text{pore}} \in \Omega_{\text{drop}}} V_{\text{cap}}(\bar{r}_{\text{pore}}) \cdot n_{\bar{r}_{\text{pore}}}. \quad (4.17)$$

After checking whether the porous-medium flow conditions can provide the estimated water volume, the drop radius  $r_{\text{drop}}$  can be calculated assuming the drop to have the form of a spherical cap (see equation (2.1)):

$$r_{\text{drop}} = \sqrt[3]{\frac{\frac{3}{\pi} V_{\text{drop}}}{(1 - \cos \theta^*)^2 (2 - \cos \theta^*)}}. \quad (4.18)$$

With the drop radius, the drop surface  $A_{\text{drop}}^{\circ}$  and drop contact area  $A_{\text{drop}}^{\text{CA}}$  can be calculated (see figure 4.6 and equations (2.2) and (2.3)). The area fractions of drop-covered  $a_{\text{drop}} = \frac{A_{\text{drop}}^{\text{CA}}}{|\Omega_{\text{drop}}|}$  and drop-free  $a_g = \frac{A_{\text{free}}}{|\Omega_{\text{drop}}|}$  interface are calculated and used to obtain the complete coupling conditions for the interface (see section 4.2.4). The conditions without drops are given in (3.11c) to (3.19). In the following section, the coupling conditions for the drop-covered interface are derived.

### 4.2.3 Coupling conditions for the drop-covered interface

Based on the previously mentioned assumptions, it is now possible to derive the coupling conditions on the drop. Since the drops are not resolved, all conditions have to be valid at the interface, meaning at the drop contact area  $A_{\text{drop}}^{\text{CA}}$  to fit into the interface coupling concept.

#### Flux balance

Balancing the total mass fluxes across the interface yields:

$$\underbrace{\frac{\partial}{\partial t} \int_{V_{\text{drop}}} \varrho_{l,\text{drop}} dV}_{\frac{d(\varrho_{l,\text{drop}} V_{\text{drop}})}{dt}} + \int_{A_{\text{drop}}^{\text{CA}}} [\varrho_l \mathbf{v}_l \cdot \mathbf{n}]^{\text{pm}} dx = \int_{A_{\text{drop}}^{\text{CA}}} -[\varrho_g \mathbf{v}_g \cdot \mathbf{n}]^{\text{ff}} dx \quad (4.19)$$

Where the interface is covered by drops, the gas phase cannot flow from the porous medium into the free-flow region and all water leaving the porous-medium increases the drop volume  $V_{\text{drop}}$  (see first term in equation (4.19)). To estimate the mass of water stored inside the drop volume  $V_{\text{drop}}$ , the density of water inside the drop is assumed to be equal to the water density in the porous medium.

The balance of the component and energy fluxes is given accordingly for  $\kappa \in \{w, a\}$ :

$$\begin{aligned} \underbrace{\frac{\partial}{\partial t} \int_{V_{\text{drop}}} \varrho_{l,\text{drop}} x_{l,\text{drop}}^{\kappa} dV}_{\lambda_{V_{\text{drop}}}} + \int_{A_{\text{drop}}^{\text{CA}}} [(\varrho_l \mathbf{v}_l x_l^{\kappa} - \varrho_l D_l^{\kappa, \text{pm}} \nabla x_l^{\kappa}) \cdot \mathbf{n}]^{\text{pm}} dx \\ = - \int_{A_{\text{drop}}^{\text{CA}}} [(\varrho_g \mathbf{v}_g x_g^{\kappa} - \varrho_g D_g^{\kappa} \nabla x_g^{\kappa}) \cdot \mathbf{n}]^{\text{ff}} dx = - \int_{A_{\text{drop}}^{\circ}} f_{\text{evap}}^{\kappa}(r_{\text{drop}}) dx, \quad (4.20) \end{aligned}$$

$$\begin{aligned} \frac{\partial}{\partial t} \int_{V_{\text{drop}}} \varrho_{l,\text{drop}} u_{l,\text{drop}} dV + \int_{A_{\text{drop}}^{\text{CA}}} [(\varrho_l \mathbf{v}_l h_l - \lambda_{\text{pm}} \nabla T) \cdot \mathbf{n}]^{\text{pm}} dx \\ = - \int_{A_{\text{drop}}^{\text{CA}}} [(\varrho_g \mathbf{v}_g h_g - \lambda_g \nabla T) \cdot \mathbf{n}]^{\text{ff}} dx. \end{aligned} \quad (4.21)$$

In equation (4.20),  $\lambda_{V_{\text{drop}}}$  is a Lagrange multiplier introduced as new unknown on the interface, which will be explained in more detail in section 5. The evaporation from the droplet surface  $f_{\text{evap}}^\kappa$  has to be equal to the flux into the free-flow region (see equation (4.20)). Figure 4.6 illustrates that the conceptual drop model sees the drop as part of the interface. The drop is situated between porous medium and free flow. Hence, everything that evaporates across the drop surface has to enter the free-flow region across an area equivalent to  $A_{\text{drop}}^{\text{CA}}$ . According to Erbil et al. (2002) and Song et al. (2011) the evaporative flux can be estimated depending on the drop radius  $r_{\text{drop}}$  and the static contact angle  $\theta^*$ :

$$\int_{A_{\text{drop}}^{\text{CA}}} f_{\text{evap}}^\kappa dx = 4\pi r_{\text{drop}} D_g^w \varrho_l (x_{g,\text{drop}}^w - x_{g,\infty}^w) f(\theta^*). \quad (4.22)$$

Possible expressions for the geometric factor  $f(\theta^*)$  are given in section 2.4.

The major difference compared to the flux-continuity conditions on a drop-free interface is that mass and heat can be stored inside the drops. Hence, the interface can now store mass and energy and is not a simple interface devoid of thermodynamic properties any more.

### Mechanical equilibrium

The equilibrium of normal forces is known at the drop surface  $A_{\text{drop}}^{\text{o}}$ . The inside pressure has to balance the outside pressure and the capillary pressure caused by the curvature (see figure 4.8):

$$\int_{A_{\text{drop}}^{\text{o}}} [\mathbf{n} \cdot ((\varrho_g^m \mathbf{v}_g \otimes \mathbf{v}_g + p_g \mathbf{I} - \boldsymbol{\tau}) \mathbf{n})]^{\text{ff}} + \frac{2\gamma_l g}{r_{\text{drop}}} dx = \int_{A_{\text{drop}}^{\text{o}}} p_{\text{drop}} dx. \quad (4.23)$$

With increasing drop size ( $r_{\text{drop}} \uparrow$ ), the pressure within the drop decreases, encouraging more water to feed the drop. This condition physically acts on the drop surface  $A_{\text{drop}}^{\text{o}}$  and not on the contact area of the drop  $A_{\text{drop}}^{\text{CA}}$ . Since the drops are not resolved, equation

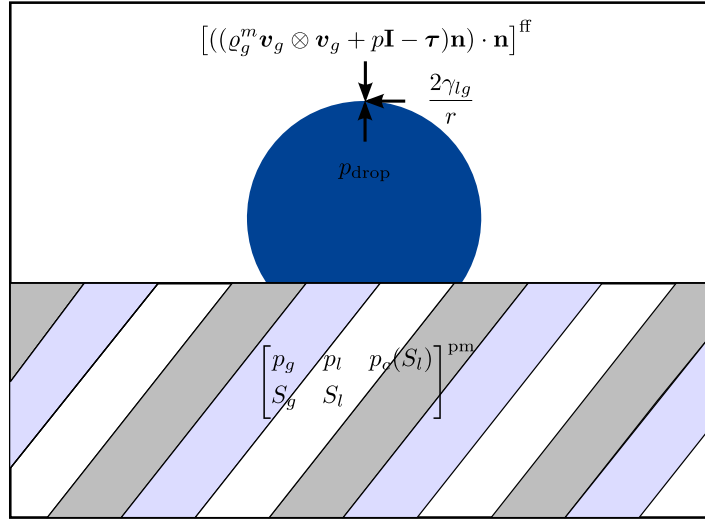


**Figure 4.8:** Force balance with drop: internal and external pressure forces related through capillary pressure.

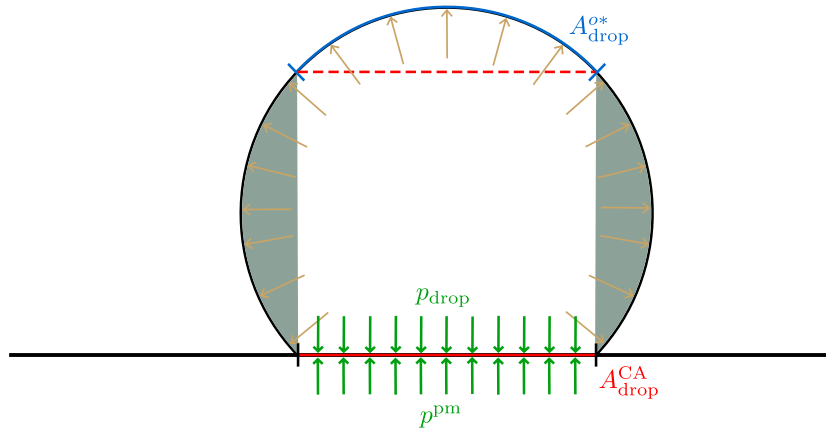


**Figure 4.9:** Internal force balance on a drop.

(4.23) has to be transformed into a condition at the interface, thus at the drop contact area  $A_{\text{drop}}^{\text{CA}}$ .

Figure 4.9 illustrates the internal pressure acting normal to the drop surface. Only the forces on the drop's cap  $A_{\text{drop}}^{o*}$  have to be considered since forces acting on the grey shaded areas cancel out. Considering normal forces, the projected surface is relevant for the calculation of the pressure force. The projected surface of the drop's cap  $A_{\text{drop}}^{o*}$  is equal to the contact area  $A_{\text{drop}}^{\text{CA}}$ . Hence, the integral of the inside pressure  $p_{\text{drop}}$  over the drop surface  $A_{\text{drop}}^o$  is equal to the integral over the contact area  $A_{\text{drop}}^{\text{CA}}$ :

$$\int_{A_{\text{drop}}^o} p_{\text{drop}} dx = \int_{A_{\text{drop}}^{\text{CA}}} p_{\text{drop}} dx = \int_{A_{\text{drop}}^{\text{CA}}} p_l^{\text{pm}} dx. \quad (4.24)$$

At the contact area, the internal drop pressure has to be equal to the porous-medium pressure of the liquid phase  $p_l^{\text{pm}}$  since a continuous fluid phase exists and the microscopic pressure is assumed to be equal to the REV-scale pressure (Gurau et al., 2008, Gurau and Mann, 2009).

The same reasoning is applied to the outside pressure but cannot be applied to the capillary pressure which is still integrated over the drop surface, yielding:

$$\int_{A_{\text{drop}}^{\text{CA}}} [\mathbf{n} \cdot ((\rho_g^m \mathbf{v}_g \otimes \mathbf{v}_g + p_g \mathbf{I} - \boldsymbol{\tau}) \mathbf{n})]^{\text{ff}} dx + \int_{A_{\text{drop}}^o} \frac{2\gamma_{lg}}{r_{\text{drop}}} dx = \int_{A_{\text{drop}}^{\text{CA}}} p_l^{\text{pm}} dx, \quad (4.25)$$

as definition of mechanical equilibrium. It is an assumption, that the integral of the normal forces  $[\mathbf{n} \cdot ((\rho_g^m \mathbf{v}_g \otimes \mathbf{v}_g + p_g \mathbf{I} - \boldsymbol{\tau}) \mathbf{n})]^{\text{ff}}$  over the drop surface and the drop contact area are equal. Even if the pressure is constant around the drop, the contribution of the normal shear stresses and normal inertial forces might be different. However, we assume a fully developed flow field on top of the drop and slow changes due to slowly growing drops. Furthermore, the normal shear forces on the side of the drop are neglected.

### Chemical equilibrium

The water-saturated gas directly above the drop in the free-flow region is in chemical equilibrium with the water phase of the drop:

$$[x_g^w]^{\text{ff}} = \frac{p_{\text{sat,Kelvin}}^w}{p_g^{\text{ff}}} [x_l^w]^{\text{pm}}. \quad (4.26)$$

The saturated vapour pressure is calculated using the Kelvin equation (Galvin, 2005, Butt et al., 2007), since the curvature of the drop leads to higher evaporation rates (see section 2.4). The mole fraction of water in the liquid phase in the drop corresponds to the respective mole fraction in the porous medium.

### Thermal equilibrium

Assuming local thermal equilibrium, the temperature  $T^{\text{pm}}$  of the porous medium at the drop contact area is equal to the temperature  $T_{\text{drop}}$  inside the drop. Assuming a constant drop temperature and again local thermal equilibrium, drop and free-flow gas temperature  $T_g^{\text{ff}}$  have to be equal, too:

$$T^{\text{pm}} = T_{\text{drop}} = T_g^{\text{ff}}. \quad (4.27)$$

#### 4.2.4 Combined coupling conditions for the drop-covered and drop-free interface

The division of the interface in drop-covered  $A_{\text{drop}}^{\text{CA}}$  and drop-free  $A_{\text{free}}$  area is an idealisation and only area fractions  $a_{\text{drop}}$  and  $a_g$  are known being an outcome of the continuum description (see section 4.2.1). The integrals given in the previous section are valid for every arbitrary control-volume size. Without a fixed and defined control volume (or control area), the integral formulation of equations (4.19)-(4.25) can be transformed directly to a differential formulation. The set of differential coupling conditions for drop-covered surfaces is combined with those given in section 3.4 to obtain the total coupling framework. The area weighted average of the coupling conditions with and without drop yields the complete set of coupling conditions for the whole interface area  $A_{\Gamma}$ .

### Flux balance

Combining conditions (3.13) and (4.19) yields the overall condition for the total mass flux:

$$\begin{aligned}
& \underbrace{\frac{\partial (\varrho_{l,\text{drop}} V_{\text{drop}})}{\partial t}}_{\frac{\partial \lambda_{V_{\text{drop}}/x_l^w}}{\partial t}} + [\varrho_g \mathbf{v}_g \cdot \mathbf{n} + \varrho_l \mathbf{v}_l \cdot \mathbf{n}]^{\text{pm}} a_g \Omega_{\text{drop}} + [\varrho_l \mathbf{v}_l \cdot \mathbf{n}]^{\text{pm}} a_{\text{drop}} \Omega_{\text{drop}} \\
& = [\varrho_g \mathbf{v}_g \cdot \mathbf{n}]^{\text{ff}} \underbrace{(a_{\text{drop}} + a_g)}_{=1} \Omega_{\text{drop}}. \quad (4.28)
\end{aligned}$$

The total component balance across the interface is obtained averaging (3.19) and (4.20):

$$\begin{aligned}
& \underbrace{\frac{\partial (\varrho_{l,\text{drop}} x_{l,\text{drop}}^\kappa V_{\text{drop}})}{\partial t}}_{\frac{\partial \lambda_{V_{\text{drop}}}}{\partial t}} \\
& + \sum_{\alpha \in \{l,g\}} [(\varrho_\alpha \mathbf{v}_\alpha x_\alpha^\kappa - D_\alpha^{\kappa,\text{pm}} \varrho_\alpha \nabla x_\alpha^\kappa) \cdot \mathbf{n}]^{\text{pm}} a_g \Omega_{\text{drop}} + [(\varrho_l \mathbf{v}_l x_l^\kappa - D_l^{\kappa,\text{pm}} \varrho_l \nabla x_l^\kappa) \cdot \mathbf{n}]^{\text{pm}} a_{\text{drop}} \Omega_{\text{drop}} \\
& = -[(\varrho_g \mathbf{v}_g x_g^\kappa - D_g^\kappa \varrho_g \nabla x_g^\kappa) \cdot \mathbf{n}]^{\text{ff}} \underbrace{(a_{\text{drop}} + a_g)}_{=1} \Omega_{\text{drop}}. \quad (4.29)
\end{aligned}$$

The total energy balance results from (3.15) and (4.21):

$$\begin{aligned}
& \frac{\partial (\varrho_{l,\text{drop}} u_{l,\text{drop}} V_{\text{drop}})}{\partial t} \\
& + [(\varrho_g h_g \mathbf{v}_g + \varrho_l h_l \mathbf{v}_l - \lambda_{\text{pm}} \nabla T) \cdot \mathbf{n}]^{\text{pm}} a_g \Omega_{\text{drop}} + [(\varrho_l h_l \mathbf{v}_l - \lambda_{\text{pm}} \nabla T) \cdot \mathbf{n}]^{\text{pm}} a_{\text{drop}} \Omega_{\text{drop}} \\
& = -[(\varrho_g h_g \mathbf{v}_g - \lambda_g \nabla T) \cdot \mathbf{n}]^{\text{ff}} \underbrace{(a_{\text{drop}} + a_g)}_{=1} \Omega_{\text{drop}}. \quad (4.30)
\end{aligned}$$

### Mechanical equilibrium

The continuity of normal forces across drop-free and drop-covered interface is given combining (3.11c) and (4.25):

$$[\mathbf{n} \cdot ((\rho_g^m \mathbf{v}_g \otimes \mathbf{v}_g + p_g \mathbf{I} - \boldsymbol{\tau}) \mathbf{n})]^{ff} \underbrace{(a_{\text{drop}} + a_g)}_{=1} = p_g^{\text{pm}} a_g + \left( p_l^{\text{pm}} - \frac{2\gamma_{lg} a_{\text{drop}}^o}{r_{\text{drop}} a_{\text{drop}}} \right) a_{\text{drop}}. \quad (4.31)$$

An area-weighted average is questionable in case of the mechanical equilibrium. A combination of equation (3.11c) and (4.25) means averaging pore and REV-scale pressure definitions. The water and gas pressure inside the porous medium are connected by the macroscopic capillary pressure which is of different order than the capillary pressure exerted by the curved drop surface. Consequently, a combined condition leads to a non-physical jump in the gas pressure across the interface (see section 7.3.2). A critical discussion of this condition and its consequences is given in section 4.3.1. As in the previous sections, the Beavers-Joseph-Saffman condition (3.12) can be employed as condition for the tangential free-flow velocity at the interface. The Beavers-Joseph coefficient  $\alpha_{\text{BJ}}$  needs to be determined as function of the fraction of the interface covered by drops  $a_{\text{drop}}$ , the drop height and diameter, and the saturation at the interface. This is beyond the scope of this work.

### Chemical equilibrium

By averaging (3.18) and (4.26), the definition of the total local chemical equilibrium boils down to:

$$[x_g^w]^{ff} = [x_g^w]^{\text{pm}} a_g + \frac{p_{\text{sat,Kelvin}}^w}{p_g^{ff}} [x_l^w]^{\text{pm}} a_{\text{drop}} \quad (4.32)$$

### Thermal equilibrium

Local thermal equilibrium is still given by the continuity of temperature (see equations (3.14) and (4.27)).

The drop volume  $V_{\text{drop}}$  is an outcome of the model. From the drop volume, the drop radius, which is needed for the force balance (4.31), can be calculated (see equation (4.18)). Furthermore, a new partition of the interface in drop-covered and drop-free area is calculated yielding the area fractions  $a_g$  and  $a_{\text{drop}}$  for the next Newton step. The

formulation of the drop volume is based on the assumption of a constant contact angle  $\theta^*$ , with the drop height being  $h = r_{\text{drop}}(1 - \cos \theta^*)$ .

### 4.2.5 Pore-velocity approach

In equations (4.19) and (4.20), the REV-scale water flux from the porous medium feeds the drop. An alternative way of determining the flux feeding the drop is based on an analytical solution on the pore-scale. As in section 4.1 and in the condition for drop formation (see section 4.2.2), the very top of the porous medium is described by a bundle-of-tubes concept of thickness  $\delta$ . Similar to Berning et al. (2009), the water flux from the porous medium can be estimated using the Hagen-Poiseuille equation:

$$\mathbf{f}^{\text{pm}} \cdot \mathbf{n} = \Phi f_{\text{pore}} = \Phi \sum_{\bar{r}_{\text{pore}} \in l} -\varrho_l \frac{(\bar{r}_{\text{pore}})^2}{8\mu_l} \frac{\lambda_{p_{\text{drop}}} - p_l^{\text{pm}}}{\delta} \pi (\bar{r}_{\text{pore}})^2 n_{\bar{r}_{\text{pore}}}, \quad (4.33)$$

where  $\bar{r}_{\text{pore}}$  is the average pore diameter,  $p_l^{\text{pm}}$  is the REV-scale porous-medium pressure,  $\delta$  is the thickness of the imagined bundle-of-tubes model and  $\lambda_{p_{\text{drop}}}$  is a Lagrange multiplier standing for the internal drop pressure. As in section 4.1, a constant pressure gradient for all pores within a grid cell is assumed. The pore velocity is multiplied by the porosity  $\Phi$  to get from the pore velocity to the Darcy velocity. If the drop pressure and the porous-medium pressure are not assumed to be equal, equation (4.33) provides the flux through water-filled pores. Berning et al. (2009) use a similar approach justified by the fact that drops form on characteristic sites often predefined during the manufacturing process.

The pore-velocity approach requires that both the mechanical equilibrium next to the drop (3.11c) and the mechanical equilibrium at the drop (4.25) must be satisfied individually. An area-weighted average as in equation (4.31) is not done. Equation (3.11c) is employed as coupling condition between the free-flow and porous-medium gas-phase pressures.  $\lambda_{p_{\text{drop}}}$  is introduced in equation (4.33) as a Lagrange multiplier standing for the water pressure inside the drop which is defined by the Young-Laplace equation (see equation (4.25)):

$$\left( [\mathbf{n} \cdot ((\varrho_g^m \mathbf{v}_g \otimes \mathbf{v}_g + p_g \mathbf{I} - \boldsymbol{\tau}) \mathbf{n})]_{\text{ff}} + \frac{2\gamma_{lg}}{r_{\text{drop}}} \frac{a_{\text{drop}}^o}{a_{\text{drop}}} \right) a_{\text{drop}} = \lambda_{p_{\text{drop}}} a_{\text{drop}}. \quad (4.34)$$

The implementation of this condition is explained in chapter 5.

The mole fraction within the drop also depends on the flux through the pores. The diffusive flux in the short pores is neglected and an upwinding to the mole fraction in the advective part is applied. This is based on the assumption, that water always flows from the porous-medium into the drop. The component flux feeding the drop can be expressed as:

$$\mathbf{f}^{\text{pm}} \cdot \mathbf{n} = \Phi f_{\text{pore}} = \Phi \sum_{\bar{\Gamma}_{\text{pore}} \in l} -\varrho_l x_l^{w,\text{pm}} \frac{(\bar{\Gamma}_{\text{pore}})^2}{8\mu_l} \frac{\lambda_{p_{\text{drop}}} - p_l^{\text{pm}}}{\delta} \pi \bar{\Gamma}_{\text{pore}}^2 n_{\bar{\Gamma}_{\text{pore}}}. \quad (4.35)$$

The applicability of the pore-velocity approach briefly explained here is assessed in section 7.3.5. It avoids the area-weighted average of the pressure conditions (3.11c) and (4.25). However, equation (4.35) is still based on a mixture of scales. The flux determined with the Hagen-Poiseuille equation depends on the difference between the microscopic internal drop pressure and the macroscopic porous-medium water pressure. This issue is discussed in section 4.3.1.

## 4.2.6 Drop detachment

The drops deform due to the drag force exerted by the gas flow, leading to contact-angle hysteresis and elongation of the contact area (see figure 2.8 and section 2.4). Eventually, if the drops reach a critical size, the forces exerted by the flow field lead to detachment of the drops. A drop gets detached, if the drag force exerted by the gas flow is bigger than the retention force due to surface effects:

$$F_{\text{drag}}(\mathbf{V}_{\text{drop}}) > F_{\gamma_{lg}}^{\text{max}}(\mathbf{V}_{\text{drop}}).$$

Detachment can be due to sliding, rolling or lifting of the drop. Note, that sliding and rolling still leads to coverage of the porous medium. However, we do not distinguish between these detachment mechanisms and assume that the drop leaves the porous-medium surface once  $F_{\text{drag}}(\mathbf{V}_{\text{drop}}) > F_{\gamma_{lg}}^{\text{max}}(\mathbf{V}_{\text{drop}})$  and is then transported by the flow field. These transport processes are not described in the scope of this work. In the future, the exact behaviour of the drops (sliding, rolling, lifting) and film flow have to be included in the free-flow model.

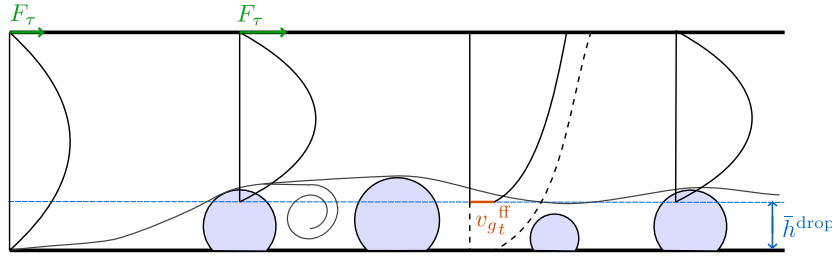


**Figure 4.10:** Free flow influenced by drops.

The calculation of drag and retention force is discussed in section 2.4. Both contact-angle hysteresis and deformation of the contact area yield a retention force (Extrand and Gent, 1990). The maximal retention force  $F_{\gamma_{lg}}^{\max}(V_{\text{drop}})$  can be calculated depending on the contact area of the drop, the surface tension  $\gamma_{lg}$ , the static contact angle  $\theta^*$  and maximally sustained contact-angle hysteresis  $\Delta\theta^{\max}$ . Theodorakakos et al. (2006) stress that the detachment process can only be captured properly if the de-wetting processes of a sliding drop and the dynamic change in contact angle is considered. We neglect the deformation of the contact line and the influence of the drops on each other, and assume a circular contact area. Additionally, we regard the maximally sustained contact angle hysteresis as crucial parameter for detachment and neglect the dynamic deformation process. Kumbur et al. (2006) provide an expression for the surface-tension force assuming a linear variation of the contact angle along the circular contact surface:

$$F_{\gamma_{lg}}^{\max} = \gamma_{lg} r_{\text{drop}}^{\text{CA}} \pi \left[ \frac{\sin(\Delta\theta^{\max} - \theta^*) - \sin\theta^*}{\Delta\theta^{\max} - \pi} + \frac{\sin(\Delta\theta^{\max} - \theta^*) - \sin\theta^*}{\Delta\theta^{\max} + \pi} \right].$$

The drag force can be estimated from a force balance of the flow field surrounding the drop or from expressions which depend on the drag coefficient. These expressions and alternatives for the calculation of the retention force can be found in section 2.4. The different ways for the calculation of the drag force are compared in section 7.3.4 based on numerical simulations.

#### 4.2.7 Influence of drops on the free gas flow

Drops influence the free-flow conditions, if their height is significant in comparison to the height of the free-flow region. This is the case in the gas channel of a PEM fuel cell. Drops reduce the cross-section available for the gas flow and cause a significant

pressure drop (see figure 4.10). Qin et al. (2012b) find that the pressure loss inside the gas channel is three times as large if drops are present compared to a situation without drops.

Using the Navier-Stokes equations, the diameter of the channel cannot be adjusted during the calculation, since the drop geometry is not resolved by the REV interface approach. Alternatively, the decrease in cross-section can be included in an averaged way. The flow across the original channel can be restricted in every discretisation cell by multiplication with a restriction coefficient based on geometric considerations. In fuel cells, laminar flow conditions prevail and flow velocities range from 1-15 m/s (Kandlikar et al., 2014). Hence, flow separation occurs on the drop surface (see figure 4.10). The average drop height  $\bar{h}_{\text{drop}}$  (see blue line in figure 4.10) is used to determine the ratio of new reduced cross-section and the originally available cross-section:  $\frac{A(d_{GC} - \bar{h}_{\text{drop}})}{A_{GC}(d_{GC})}$ . By implementing such a restriction coefficient, a more realistic flow velocity and an increased pressure drop can be obtained. Consequently, the contributing forces for the drag force can be determined directly from the velocity profile and the pressure distribution (see section 4.2.6).

Moreover, the boundary condition for the free-flow region at the interface has to be adjusted. So far, the Beavers-Joseph condition (3.12) is proposed which accounts for the effect of the porous surface on the tangential free-flow velocity. The influence of the drops would have to be included in the determination of the Beavers-Joseph coefficient  $\alpha_{\text{BJ}}$ .

Unfortunately, the implementation of a restriction coefficient causes spurious oscillations caused by the box discretisation of the free-flow domain (see chapter 5). It can be tested once the improved discretisation based on a staggered-grid is implemented.

### 4.3 Discussion of the pressure condition

In sections 3.4, 4.1 and 4.2 coupling concepts are presented in which continuum models of different scales are involved. The coupling of different concepts causes inconsistencies at the interface for which solutions have to be found. The free-flow model based on the Navier-Stokes equations (see section 3.3) is the same on the pore-scale and on the REV-scale. In the porous-medium region, an averaged REV-scale model based on Darcy's

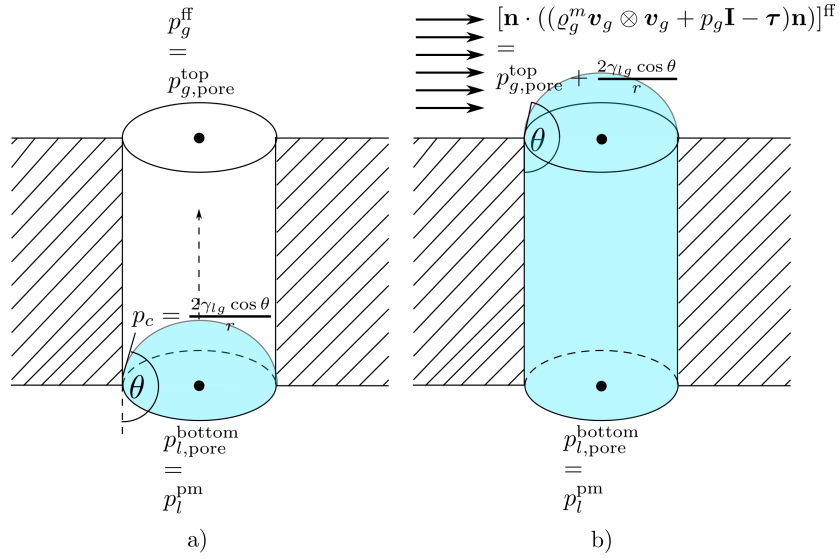


**Figure 4.11:** a) pressure equilibrium determining whether a meniscus will move inside a pore, b) mechanical equilibrium on top of a water-filled pore.

law is employed (see section 3.2). The tube model from section 4.1 and the droplets from section 4.2 are micro- or pore-scale features at the interface. It was mentioned in section 3.1 that the definition of phase and capillary pressures on different scales and the transition from one scale to the other is a current research challenge. During the last sections it became clear that this complicates the definition of mechanical equilibrium at the interface and at the water meniscus inside a pore.

As shown in figure 4.11, two settings must be distinguished: figure 4.11, a) shows the pressure equilibrium determining whether water will invade the pore (discussed in section 4.3.2), figure 4.11, b) depicts the mechanical equilibrium on top of a water-filled pore (discussed in section 4.3.1).

In the following, the pressure condition which is based on the mechanical equilibrium of forces is discussed for the three cases described in the last sections:

- direct coupling of two REV-scale models (section 3.4),
- inclusion of a pore-scale bundle-of-tubes approach at the interface between the two REV-scale models (section 4.1),
- and the drop concept which is based on a pore-scale consideration of the droplets which is transferred into REV-scale coupling conditions.

Then, the condition used to decide which pores are filled with water and on which pores drops form is discussed. It is based on the Young-Laplace equation and is needed for the tube- and drop-interface concept (see sections 4.1 and 4.2.1).

The discussion is based on three main assumptions which are discussed in more detail in the following section:

- the pore-scale and the porous-medium averaged pressure are equal,
- for the vertical movement of the water meniscus inside a pore, viscous forces can be neglected (see figure 4.11, a) and Hassanizadeh and Gray (1993)),
- in the formulation of the mechanical equilibrium at the interface between free flow and the adjacent model, viscous and inertial forces have to be considered (see figure 4.11, b)).

### 4.3.1 Discussion of the mechanical-equilibrium condition

The correct scale and pressure in the definition of mechanical equilibrium has to be chosen and justified for each of the coupling concepts. The **direct coupling** of free and porous-medium systems is done consistently on the REV-scale: the Navier-Stokes model is still valid and the capillary pressure employed in the derivation of the mechanical equilibrium (see equation (4.36b)) is based on the macroscopic capillary-pressure–saturation relation. A difference in the gas-pressure across the interface results due to the different treatment of the shear stresses and inertial forces in the submodels (see also equation (3.11c) in section 3.4):

$$\left[ A_g \mathbf{n} \cdot \left( (\varrho_g^m \mathbf{v}_g \otimes \mathbf{v}_g + p_g \mathbf{I} - \boldsymbol{\tau}) \mathbf{n} \right) \right]^{\text{ff}} = [p_g A_g]^{\text{pm}} \quad (4.36a)$$

$$\left[ A_l \mathbf{n} \cdot \left( (\varrho_g^m \mathbf{v}_g \otimes \mathbf{v}_g + p_g \mathbf{I} - \boldsymbol{\tau}) \mathbf{n} \right) \right]^{\text{ff}} = \underbrace{[(p_l - p_c(S_l)) A_l]^{\text{pm}}}_{p_g} \quad (4.36b)$$

---


$$(4.36a) + (4.36b) \quad \left[ \mathbf{n} \cdot \left( (\varrho_g^m \mathbf{v}_g \otimes \mathbf{v}_g + p_g \mathbf{I} - \boldsymbol{\tau}) \mathbf{n} \right) \right]^{\text{ff}} = [p_g]^{\text{pm}}. \quad (4.36c)$$

Introducing a **bundle-of-tubes model** at the interface necessitates the transition from the REV-scale to the pore-scale and vice versa. Naturally, a microscopic pressure distribution cannot be inferred from a macroscopic pressure field, since all fluctuations

below the size of the REV have been averaged out. The transition from micro- to macro-scale by volume-averaging has a long tradition (Bear, 1972). However, the correct averaging operator for the phase pressures in multi-phase systems is still debated (Nordbotten et al., 2008, Korteland et al., 2010), as is the meaning of the averaged phase pressure itself with respect to the micro-scale pressure. The meaning and definition of the macroscopic capillary pressure is discussed as well. As mentioned in section 3.1, the microscopic definition must not be applied directly on the REV-scale. The main and most crucial assumption of the coupling concept involving a bundle of tubes is that pore-pressure and average porous-medium pressure are equal (see figure 4.11):

$$p_{\alpha,\text{pore}} = p_{\alpha}^{\text{micro}} = p_{\alpha}^{\text{pm}}. \quad (4.37)$$

Condition (4.37) is based on the assumption that the microscopic pressure does not fluctuate significantly within an REV or a grid cell. Moreover, the concept of parallel tubes with the same energy loss in all tubes (Helmig and Class, 2004) leads to the same pressure gradient inside the tubes within an REV, suggesting a constant pore-pressure at the interface between porous medium and tube model. As explained in section 4.1, the Hagen-Poiseuille equation (4.1) is used to describe the flow inside the pores. For the definition of mechanical equilibrium between the top of the pores and the free-flow region (see figure 4.11, b)), shear stresses have to be considered. The Poiseuille equation does not account for viscous forces explicitly, causing the same jump in the gas pressure as for the simple interface (see equation (4.36c)). If the Navier-Stokes equations were used in the pores, the gas-phase pressure would be continuous but no analytical solution would be at hand. Following the same reasoning as in equation (4.36b), the following condition results on top of the drops (see also equation (4.14) in section 4.1):

$$[\mathbf{n} \cdot ((p_g \mathbf{I} - \boldsymbol{\tau}) \mathbf{n})]^{\text{ff}} = p_{g,\text{pore}}^{\text{top}} A_{\Gamma g} + (p_{l,\text{pore}}^{\text{top}} - p_c) A_{\Gamma l}. \quad (4.38)$$

Here,  $p_c = \frac{2\gamma_{lg} \cos \theta}{\bar{r}_{\text{pore}}}$  is the microscopic capillary pressure relating the pore water pressure to the pore gas pressure, which is then coupled to the normal force of the free-flow system. Since the Navier-Stokes equations are valid on the pore- and REV-scale, this condition is consistent. The pore pressure at the top of the pores is related to the pressure at the bottom by the Hagen-Poiseuille equation. Employing again assumption (4.37) and postulating the continuity of fluxes, we define the top pore pressure of phase

$\alpha$  as (see also equation (4.15) in section 4.1):

$$p_\alpha^{\text{top}} = p_\alpha^{\text{bottom}} + \frac{[\varrho_\alpha \mathbf{v}_\alpha \cdot \mathbf{n}]^{\text{pm}} A_{\Gamma\alpha} \delta}{\Phi \sum_{\bar{\Gamma}_{\text{pore}}} -\frac{(\bar{\Gamma}_{\text{pore}})^2}{8\mu_g} \varrho_g \pi (\bar{\Gamma}_{\text{pore}})^2 n_{\bar{\Gamma}_{\text{pore}}}} = p_\alpha^{\text{pm}} + \frac{[\varrho_\alpha \mathbf{v}_\alpha \cdot \mathbf{n}]^{\text{pm}} A_{\Gamma\alpha} \delta}{\Phi \sum_{\bar{\Gamma}_{\text{pore}}} -\frac{(\bar{\Gamma}_{\text{pore}})^2}{8\mu_g} \varrho_g \pi (\bar{\Gamma}_{\text{pore}})^2 n_{\bar{\Gamma}_{\text{pore}}}} \quad (4.39)$$

The **drop concept** poses similar challenges as the tube-interface model since the droplets are micro-scale features which are integrated into the REV-scale coupling concept. On the micro-scale, the definition of the mechanical equilibrium on the drop surface is given as (see also equation (4.23) and figure 4.8 in section 4.3.1):

$$\int_{A_{\text{drop}}^o} [\mathbf{n} \cdot ((\varrho_g^m \mathbf{v}_g \otimes \mathbf{v}_g + p_g \mathbf{I} - \boldsymbol{\tau}) \mathbf{n})]^\text{ff} + \frac{2\gamma l_g}{\Gamma_{\text{drop}}} dx = \int_{A_{\text{drop}}^o} p_{\text{drop}} dx. \quad (4.40)$$

The normal forces of the free-flow region include the viscous and inertial forces, since the mechanical equilibrium on top of the drop has to be treated analogously to the mechanical equilibrium on the interface between pores and free-flow region (see figure 4.11 b)). Assuming a constant pressure within the drop and pressure continuity at the contact line, the integral of the drop pressure over the drop surface is transformed into the integral of the averaged porous-medium water pressure over the drop contact area (see also equation (4.24) in section 4.1 for a more detailed explanation):

$$\int_{A_{\text{drop}}^o} p_{\text{drop}} dx = \int_{A_{\text{drop}}^{\text{CA}}} p_{\text{drop}} dx = \int_{A_{\text{drop}}^{\text{CA}}} p_i^{\text{pm}} dx. \quad (4.41)$$

Again, microscopic pressure  $p_{\text{drop}}$  and macroscopic pressure  $p_i^{\text{pm}}$  are assumed to be equal.

Since the drops are integrated into the interface coupling concept, their size, shape and position is not resolved. Hence, the exact distribution of pressure and viscous forces around the drop is not available. Direct simulations using the VOF-method could provide the exact flow and pressure field (Cho et al., 2012a,b), but are beyond the scope of this work. Therefore, we assume that the changes in the pressure, inertial and viscous force field are small and that the integral over the drop surface can be transformed into the integral over the drop contact area:

$$\int_{A_{\text{drop}}^o} [\mathbf{n} \cdot ((\varrho_g^m \mathbf{v}_g \otimes \mathbf{v}_g + p_g \mathbf{I} - \boldsymbol{\tau}) \mathbf{n})]^\text{ff} = \int_{A_{\text{drop}}^{\text{CA}}} [\mathbf{n} \cdot ((\varrho_g^m \mathbf{v}_g \otimes \mathbf{v}_g + p_g \mathbf{I} - \boldsymbol{\tau}) \mathbf{n})]^\text{ff}. \quad (4.42)$$

The integral of the capillary pressure cannot be transformed into an expression valid on

the drop contact area. The surface tension  $\gamma_{lg}$  acts along the curved drop surface and cannot be projected onto a flat interface. Consequently, the mechanical equilibrium for the drop can be formulated in a differential form as (see also equation (4.25) in section 4.2.3):

$$[\mathbf{n} \cdot ((\varrho_g^m \mathbf{v}_g \otimes \mathbf{v}_g + p_g \mathbf{I} - \boldsymbol{\tau}) \mathbf{n})]^{ff} a_{\text{drop}} + \frac{2\gamma_{lg}}{r_{\text{drop}}} a_{\text{drop}}^o = p_l^{\text{pm}} a_{\text{drop}}. \quad (4.43)$$

The microscopic capillary pressure is combined with the macroscopic porous-medium pressure as a direct consequence of assumption (4.37). An alternative would be to find a macroscopic correlation for capillary pressure as a function of the drop radius  $r_{\text{drop}}$ , the contact angle  $\theta^*$ , contact angle hysteresis  $\Delta\theta^{\text{max}}$ , free-flow velocity and pressure. Such a correlation does not yet exist to the author's knowledge.

As explained in section 4.2.4, the coupling conditions on the drop are combined with those valid for a drop-free interface by an area-weighted average. The definition of the mechanical equilibrium results as (see also equation (4.31) in section 4.2.4):

$$[\mathbf{n} \cdot ((\varrho_g^m \mathbf{v}_g \otimes \mathbf{v}_g + p_g \mathbf{I} - \boldsymbol{\tau}) \mathbf{n})]^{ff} a_{\text{drop}} = p_l^{\text{pm}} a_{\text{drop}} - \frac{2\gamma_{lg}}{r_{\text{drop}}} a_{\text{drop}}^o \quad (4.44a)$$

$$[\mathbf{n} \cdot ((\varrho_g^m \mathbf{v}_g \otimes \mathbf{v}_g + p_g \mathbf{I} - \boldsymbol{\tau}) \mathbf{n})]^{ff} a_g = p_g^{\text{pm}} a_g \quad (4.44b)$$

$$\frac{[\mathbf{n} \cdot ((\varrho_g^m \mathbf{v}_g \otimes \mathbf{v}_g + p_g \mathbf{I} - \boldsymbol{\tau}) \mathbf{n})]^{ff}}{[\mathbf{n} \cdot ((\varrho_g^m \mathbf{v}_g \otimes \mathbf{v}_g + p_g \mathbf{I} - \boldsymbol{\tau}) \mathbf{n})]^{ff}} = p_g^{\text{pm}} a_g + \underbrace{\left( p_l^{\text{pm}} \right)}_{(p_g^{\text{pm}} + p_c(S_l))} a_{\text{drop}} - \frac{2\gamma_{lg}}{r_{\text{drop}}} a_{\text{drop}}^o. \quad (4.44c)$$

Equation (4.44c) clearly shows a conflict between microscopic and macroscopic pressure. The condition relates the water pressure in the porous medium with the gas pressure in the free-flow region via the microscopic capillary pressure of the drop. At the same time, the water pressure is related to the porous-medium gas pressure through the macroscopic capillary-pressure-saturation relation (see figure 4.12). As the magnitude of the microscopic and macroscopic capillary pressure may differ by orders of magnitude, a significant but non-physical jump in the gas-phase pressures at the interface can occur. This is shown in chapter 7 and can be mitigated by choosing an appropriate  $p_c$ - $S_l$ -curve.

The same problem arises in the alternative pore-velocity approach presented in section 4.2.5. The pressure conditions (4.44a) and (4.44b) are not combined. Equation (4.40) defines the internal drop pressure. The internal drop pressure is used to estimate the water flux feeding the drop using the Hagen-Poiseuille equation (4.33). The pressure gradient

$$\begin{array}{ccc}
 [\mathbf{n} \cdot ((\varrho_g^m \mathbf{v}_g \otimes \mathbf{v}_g + p_g \mathbf{I} - \boldsymbol{\tau}) \mathbf{n})]^{ff} = p_g^{pm} & & \\
 \downarrow p_c = \frac{2\gamma_{lg}}{r_{drop}} a_{drop}^o & & \downarrow p_c(S_l) \\
 \lambda_{p_{drop}} & \xleftrightarrow{\text{Hagen-Poiseuille}} & p_l^{pm}
 \end{array}$$

**Figure 4.12:** The free-flow normal force, the porous-medium phase pressures  $p_g^{pm}$  and  $p_l^{pm}$  and the internal drop pressure  $\lambda_{p_{drop}}$  are related by microscopic and macroscopic capillary-pressure formulations.

driving the flux corresponds to the gradient between drop pressure and porous-medium water pressure. Figure 4.12 illustrates the conflict: the normal forces in the free-flow region are set equal to the porous-medium gas pressure (see equation (4.44b)). The internal drop pressure  $\lambda_{p_{drop}}$  is estimated using a microscopic capillary-pressure expression. The porous-medium water pressure is calculated using a macroscopic expression. Hence, the difference in microscopic and macroscopic capillary pressure determines the magnitude of the pressure gradient used in the Poiseuille equation.

### 4.3.2 Discussion of the Young-Laplace condition

The choice of the correct scale and pressure is also important when determining whether pores are filled with gas or water (see equation (4.10)) and whether drops form (see equation (4.16)). To decide whether tubes are water-filled, a force-balance at the meniscus between water and gas phase inside a pore with radius  $\bar{r}_{pore}$  is drawn up. Here, the vertical movement of the meniscus is important (see figure 4.11, a)), but will not be resolved by the model. On the pore-scale, the condition for water invading the pore is given by:

$$p_g^{micro} + \frac{2\gamma_{lg} \cos \theta}{\bar{r}_{pore}} \leq p_l^{micro}.$$

Once the water pressure  $p_l^{micro}$  exceeds gas and capillary pressure the tube will be filled with water instantaneously. Hassanizadeh and Gray (1993) state that the viscous effects of the phases interacting with the water meniscus inside the pore can be neglected. Hence, the microscopic gas pressure can be substituted with the gas pressure in the free-flow region on top of the pore (see figure 4.11, a)). With assumption (4.37), condition (4.10)

results:

$$p_g^{\text{ff}} + \frac{2\gamma_{lg} \cos \theta}{\bar{r}_{\text{pore}}} \leq p_l^{\text{pm}}.$$

As water forming a cap of radius  $\bar{r}_{\text{pore}}$  is considered a drop, the condition for drop formation is similar to the condition determining whether tubes get filled by water (see section 4.2.2). Again, a bundle-of-tubes concept is used and the water-phase pressure inside the porous-medium is assumed to be equal to the pore pressure (see assumption (4.37)). Drops form, if the porous-medium water pressure is larger than the sum of free-flow gas pressure and capillary pressure of the drop surface (see equation (4.16)):

$$p_g^{\text{ff}} + \frac{2\gamma_{lg}}{\bar{r}_{\text{pore}}} \leq p_l^{\text{pm}}.$$

Here, the microscopic capillary pressure is at a maximum with a contact angle of  $\theta = 90^\circ$ . This corresponds to a water cap (see figure 4.7). Microscopic and macroscopic pressure definitions are mixed, resulting from assumption (4.37).

The discussion above has shown that the choice and combination of scales has a significant impact on the model. Due to combinations of microscopic and macroscopic pressure formulations, the interface might dominate the system, causing pressure jumps at the interface and non-physical pressure gradients. The problems can be solved by a sound correlation between pore and average phase pressure and, more important, by a definition of a macroscopic capillary pressure at the interface, which should depend on the drop deformation, drop size and interface material properties. The capabilities of the different model concepts are evaluated in chapters 6 and 7.

## 5 Numerical model<sup>17</sup>

The implementation of the presented model is based on the modelling toolbox DuMu<sup>x</sup>. "DuMu<sup>x</sup> is a free and open-source simulator for flow and transport processes in porous media, which is based on the Distributed and Unified Numerics Environment (DUNE) (Bastian et al., 2008). Its main intention is to provide a sustainable and consistent framework for the implementation and application of model concepts, constitutive relations, discretisations and solvers" (Flemisch et al., 2011). The spatial discretisation of the geometric domain and the designation of subdomains are based on the software package DUNE-Multidomaingrid (Müthing and Bastian, 2010), which allows to represent arbitrarily complex subdomain shapes with conforming interfaces. For the management of the different subdomains and their associated function spaces, we employ PDELab (Bastian et al., 2010) and its extension DUNE-Multidomain. DUNE-Multidomain allows a transparent definition of local operators and variables on the individual subdomains and supports the assembly of a global system matrix. The global matrix contains the submatrices for the two subdomains and the coupling matrices. The ability to assemble a global matrix enables us to solve the strongly coupled non-linear system in a fully implicit fashion without any subdomain-iteration scheme.

The mortar method, a numerical domain-decomposition technique (Ewing et al., 2000, Wohlmuth, 2000, Arbogast and Brunson, 2007, Helmig et al., 2009), is employed for the implementation of the coupled system of equations (tables 3.1, 3.3, equations (4.28) to (4.32)). Mostly, this technique is used in case of non-conforming meshes. Here, its use is motivated by the fact that additional degrees of freedom are specified on the

---

<sup>17</sup>Most parts of this chapter are published in Baber, K., Mosthaf, K., Flemisch, B., Helmig, R., Müthing, S., and Wohlmuth, B. (2012). Numerical scheme for coupling two-phase compositional porous-media flow and one-phase compositional free flow. *IMA Journal of Applied Mathematics*, 77(6):887–909. first published online July 26, 2012 and Baber, K., Flemisch, B., and Helmig, R. (2014). Modelling drop dynamics at the interface between free and porous-medium flow using the mortar method. submitted to International Journal of Heat and Mass Transfer.

interface. The storage of water within the drop  $\lambda_{V_{\text{drop}}} = \varrho_l x_l^w V_{\text{drop}}$  (see equation (4.29)) is introduced as unknown so that the drop volume is an inherent result of the model. As mentioned in section 4.2.5, the internal drop pressure  $\lambda_{p_{\text{drop}}}$  is another Lagrange multiplier, if the water flux feeding the drop is estimated based on the pore-scale velocity.

In this chapter, the mortar method and its application to the coupling concept with drops (see section 4.2) is explained in section 5.2. Details of the implementation that go beyond the mortar method are summarised in section 5.3. Note that the bundle-of-tubes model from section 4.1 has never been implemented. The mortar method allowing for an interpolation of variables between fine and coarse grids would, however, be the method of choice for a future implementation. It has proved its worth in Balhoff et al. (2008) for the coupling of pore-scale and REV-scale models.

An implementation without the mortar method based on a simple-interface description is explained in Baber et al. (2012). It is used for the numerical experiments of transvascular exchange (see chapter 6).

General information about the spatial and temporal discretisation common to all models is given in the next section. In the following, the notation for super- and subscripts is the following:  $n$  stands for the time step,  $m$  stands for the Newton iteration,  $i$  is the node in box  $B_i$  or the subdomain,  $j$  is the adjacent node or the adjacent subdomain, and  $k$  is the node in element  $E$ . Note that the mathematical models presented in chapters 3 and 4 are formulated in moles. The implementation in DuMu<sup>x</sup> allows for mole or mass fractions so that the user has to be careful to use the correct quantities and formulations.

## 5.1 Discretisation

For the discretisation of the coupled model, the implicit Euler time integration and a vertex-centred control-volume finite-element method (also called box method, Huber and Helmig (2000)) in space is used. The method is locally mass conservative. We are aware of the fact that more advanced discretisation methods are available. For our purposes, however, a relatively simple scheme is sufficient, since the intention of this work is to investigate extensions of the coupling concept towards complex processes at the interface.

The computational domain is covered by a structured FE grid (primal mesh). The values of all primary variables are computed at the vertices which are the corners of the elements. The dual mesh which describes the finite volumes is obtained by connecting the centres of gravity of each element with the associated edge midpoints. Thus, each Finite Volume (FV) is associated with a vertex (see box  $B_i$  in figure 5.1a). The FE mesh divides the boxes  $B_i$  into sub-control volumes  $v_i^k$  (see figure 5.1b).

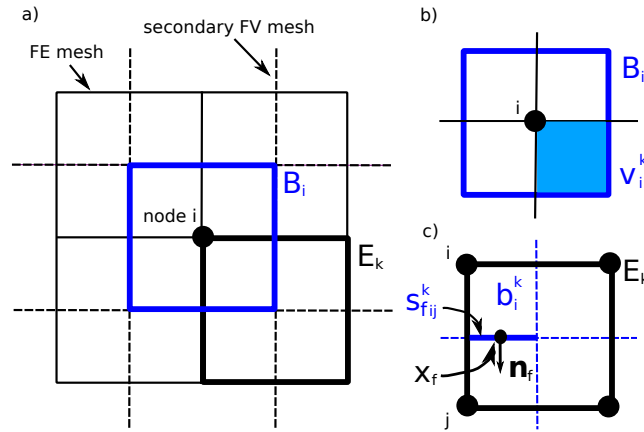


**Figure 5.1:** Schematic description of the spatial discretisation (box scheme).

We consider a quadrilateral grid and approximate all primary variables using piecewise bilinear functions (equal-order method), which are mapped from the standard-reference-element basis functions. The balance equations are integrated over the control volumes and the divergence theorem is applied. The method of weighted residuals with piecewise constant weighting functions characteristic for box  $B_i$  leads to the general discretised form for one box  $B_i$ :

$$|B_i| \frac{\hat{u}_i^{n+1} - \hat{u}_i^n}{\Delta t} + \sum_{s_f(i)} \mathbf{f}(\tilde{u}^{n+1}(x_f)) \cdot \mathbf{n}_f - |B_i| q_i^{n+1} = 0, \quad (5.1)$$

where  $|B_i|$  is the volume of box  $B_i$ ,  $\hat{u}_i^{n+1}$  is the solution at node  $i$  with  $u$  standing for one of the primary variables listed in tables 3.1 and 3.3,  $s_f(i)$  are all sub-control-volume faces of the box  $B_i$  and  $\mathbf{n}_f$  is the outward normal of the respective sub-control-volume face, its norm corresponds to the size of the sub-control-volume face  $|s_f|$ . Equation 5.1 consists of storage, flux and source/sink  $q_i^{n+1}$  terms. The fluxes  $\mathbf{f}$  may be composed of an advective and a diffusive part and are computed on the control-volume boundaries  $s_f$  at the integration points  $x_f$  (see figure 5.1c). A finite-element approximation for

each primary variable is done,  $\tilde{\mathbf{u}}^{n+1}(\mathbf{x}_f) = \sum_{k \in E} N_k(\mathbf{x}_f) \hat{\mathbf{u}}_k^{n+1}$ , where  $k$  are the nodes of the element  $E$ . Furthermore, a fully-upwind scheme is applied to the advective part. Following the general procedure employed for finite-element methods, local operators are assembled for each element and then merged for the whole domain. This means, that the discretised equations are evaluated element-wise, looping over the sub-control volumes inside an element  $E$  (see figure 5.1c). Baber et al. (2012) provide a detailed explanation of the discretised system of equations.

In the free-flow domain, a stabilisation technique similar to Franca et al. (1993) is generalised and implemented for the Navier-Stokes equations. However, instabilities and oscillations might still occur, especially at the interface corners. A staggered-grid approach is currently implemented at the institute. It will improve the stability of the system, but has not yet been employed for this work.

The arising non-linear system is solved fully implicitly applying a standard Newton solver

$$\underbrace{\left( \frac{\partial \mathbf{R}}{\partial \mathbf{u}} \right)_{n+1,m}}_{\mathbf{J}(\mathbf{u}^{n+1,m})} \underbrace{(\mathbf{u}^{n+1,m} - \mathbf{u}^{n+1,m-1})}_{\Delta \mathbf{u}} = -\mathbf{R}(\mathbf{u}^{n+1,m}). \quad (5.2)$$

Here,  $\mathbf{J}(\mathbf{u}^{n+1,m})$  is the Jacobi matrix calculated by numerical differentiation,  $\Delta \mathbf{u}$  is the correction to the primary-variable vector  $\mathbf{u}$  and  $\mathbf{R}(\mathbf{u}^{n+1,m})$  is the residuum at time-level  $n+1$  and iteration  $m$ . The linear problem at each Newton iteration step is solved using the direct linear solver *SuperLU* (Demmel et al., 1999). In the time integration, we use a heuristic time-step control based on the convergence rate of the Newton solver. A target number  $n_{\text{target}}$  of Newton iterations is defined. Depending on the actual number of iterations  $n_{\text{it}}$ , the new time-step size is chosen:

$$\Delta t^{n+1} = \begin{cases} \Delta t^n \left( \frac{1}{1 + \frac{n_{\text{it}} - n_{\text{target}}}{n_{\text{target}}}} \right) & n_{\text{max}} > n_{\text{it}} > n_{\text{target}}, \\ \Delta t^n \left( 1 + \frac{n_{\text{target}} - n_{\text{it}}}{1.2 n_{\text{target}}} \right) & n_{\text{it}} \leq n_{\text{target}}, \end{cases} \quad (5.3)$$

where  $\Delta t^n$  is the time-step size of time step  $n$ . The time-step size is halved if  $n_{\text{it}}$  exceeds the maximum number of iterations  $n_{\text{max}}$ .

## 5.2 The mortar method

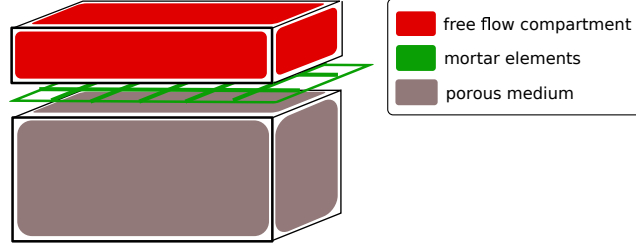


**Figure 5.2:** Mortar elements between free-flow and porous-medium compartment: Introducing Lagrange multipliers as new unknowns at the interface.

As mentioned in section 2.1, the domain  $\Omega$  is divided into two non-overlapping subdomains  $\Omega^{\text{ff}}$  and  $\Omega^{\text{pm}}$  (see figure 2.2b) with the common interface  $\Gamma = \partial\Omega^{\text{ff}} \cap \partial\Omega^{\text{pm}}$ . Mortar elements are introduced between free-flow and porous-medium compartment (see figure 5.2). The mortar method is explained on the basis of the general form of the balance equation:

$$\frac{\partial M(\mathbf{u})}{\partial t} + \nabla \cdot (\mathbf{f}(\mathbf{u})) - q = 0 \quad (5.4)$$

where  $\mathbf{u} \in \mathbf{u}(\mathbf{v}_g^{\text{ff}}, p_g^{\text{ff}}, x_g^{w,\text{ff}}, T^{\text{ff}}, S_l^{\text{pm}} \text{ or } x_g^{w,\text{pm}}, T^{\text{pm}})$  is an entry of the solution vector of the primary variables of the subdomains,  $M(\mathbf{u})$  is the storage,  $\mathbf{f}(\mathbf{u})$  the flux and  $q$  the source/sink term. Equation (5.4) is integrated over the domain  $\Omega^i$  and multiplied by a test function  $\omega$ :

$$\int_{\Omega^i} \frac{\partial M(\mathbf{u})}{\partial t} \omega \, d\Omega^i + \int_{\Omega^i} \nabla \cdot (\mathbf{f}(\mathbf{u})) \omega \, d\Omega^i - \int_{\Omega^i} q \omega \, d\Omega^i = 0. \quad (5.5)$$

Integration by parts yields:

$$\int_{\Omega^i} \frac{\partial M(\mathbf{u})}{\partial t} \omega \, d\Omega^i + \int_{\Omega^i} \nabla \mathbf{f}(\mathbf{u}) \cdot \nabla \omega \, d\Omega^i - \int_{\partial\Omega^i \setminus \Gamma} \mathbf{f}(\mathbf{u}) \cdot \mathbf{n} \omega \, d\Omega^i - \int_{\Gamma} \underbrace{\mathbf{f}(\mathbf{u}) \cdot \mathbf{n}}_{\lambda} \omega \, d\Gamma - \int_{\Omega^i} q \omega \, d\Omega^i = 0, \quad (5.6)$$

where  $\Gamma$  is the interface between domain  $i$  and  $j$ .

On the outer boundaries  $\partial\Omega^i \setminus \Gamma$  either Dirichlet or Neumann conditions are imposed:

$$\begin{aligned} p_g &= p_D \quad \text{on } \partial\Omega_D^{\text{pm}}, & \mathbf{f}_m \cdot \mathbf{n} &= \sum_{\kappa} \mathbf{f}_N^{\kappa}, \quad \text{on } \partial\Omega_N^{\text{pm}}, \\ S_l &= S_D \quad \text{on } \partial\Omega_D^{\text{pm}}, & \mathbf{f}^{\kappa} \cdot \mathbf{n} &= \mathbf{f}_N^{\kappa}, \quad \text{on } \partial\Omega_N^{\text{pm}}, \\ T &= T_D \quad \text{on } \partial\Omega_D^{\text{pm}}, & \mathbf{f}_T \cdot \mathbf{n} &= \mathbf{f}_{T,N} \quad \text{on } \partial\Omega_N^{\text{pm}}, \end{aligned}$$

where  $\partial\Omega^{\text{pm}} = \partial\Omega_D^{\text{pm}} \cup \partial\Omega_N^{\text{pm}} \cup \Gamma$ ,  $\partial\Omega_D^{\text{pm}} \cap \partial\Omega_N^{\text{pm}} = \emptyset$ , in the porous-medium region, and

$$\begin{aligned} \mathbf{v}_g &= \mathbf{v}_{g,D} \quad \text{on } \partial\Omega_D^{\text{ff}}, & \mathbf{f}_v \cdot \mathbf{n} &= \mathbf{f}_{v,N} \quad \text{on } \partial\Omega_N^{\text{ff}}, \\ p_g &= p_{g,D} \quad \text{on } \partial\Omega_D^{\text{ff}}, & \mathbf{f}_m \cdot \mathbf{n} &= \sum_{\kappa} \mathbf{f}_N^{\kappa} \quad \text{on } \partial\Omega_N^{\text{ff}}, \\ x_g^w &= x_{g,D}^w \quad \text{on } \partial\Omega_D^{\text{ff}}, & \mathbf{f}^{\kappa} \cdot \mathbf{n} &= \mathbf{f}_N^{\kappa} \quad \text{on } \partial\Omega_N^{\text{ff}}, \\ T &= T_D \quad \text{on } \partial\Omega_D^{\text{ff}}, & \mathbf{f}_T \cdot \mathbf{n} &= \mathbf{f}_{T,N} \quad \text{on } \partial\Omega_N^{\text{ff}}, \end{aligned} \tag{5.7}$$

where  $\partial\Omega^{\text{ff}} = \partial\Omega_D^{\text{ff}} \cup \partial\Omega_N^{\text{ff}} \cup \Gamma$ ,  $\partial\Omega_D^{\text{ff}} \cap \partial\Omega_N^{\text{ff}} = \emptyset$ , in the free-flow domain.

The normal flux across the interface  $\Gamma$  is represented by the Lagrange multiplier  $\lambda$  (see equation (5.6)). It ensures flux continuity across the interface. Additionally, the continuity condition at the interface is enforced in a weak sense as

$$\int_{\Gamma} (\mathbf{u}^i - \mathbf{u}^j) \cdot \boldsymbol{\xi} \, dx = 0, \tag{5.8}$$

where  $\boldsymbol{\xi}$  is a Lagrange-multiplier test function and  $i$  and  $j$  are neighbouring subdomains.

The application of the mortar method to the coupling of the component and energy balance equations (see tables 3.2 and 3.3) is straight forward. The Lagrange multipliers are defined as

$$\lambda_x := \mathbf{f}^\kappa \cdot \mathbf{n} = \left( \varrho_g \mathbf{v}_g x_g^\kappa - D_g^\kappa \varrho_g \nabla x_g^\kappa \right)^{\text{ff}} \cdot \mathbf{n}^{\text{ff}} = - \sum_{\alpha \in \{l, g\}} \left( \varrho_\alpha \mathbf{v}_\alpha x_\alpha^\kappa - D_\alpha^{\kappa, \text{pm}} \varrho_\alpha \nabla x_\alpha^\kappa \right)^{\text{pm}} \cdot \mathbf{n}^{\text{pm}}, \quad (5.9)$$

$$\lambda_T := \mathbf{f}_T \cdot \mathbf{n} = \left( \varrho_g h_g \mathbf{v}_g - \lambda_g \nabla T \right)^{\text{ff}} \cdot \mathbf{n}^{\text{ff}} = - \left( \varrho_g h_g \mathbf{v}_g + \varrho_l h_l \mathbf{v}_l - \lambda_{\text{pm}} \nabla T \right)^{\text{pm}} \cdot \mathbf{n}^{\text{pm}}. \quad (5.10)$$

The corresponding continuity conditions are:

$$\int_{\Gamma} \left( [x_g^w]^{\text{ff}} - [x_g^w]^{\text{pm}} a_g - \frac{p_{\text{sat, Kelvin}}^w}{p_g^{\text{ff}}} [x_l^w]^{\text{pm}} a_{\text{drop}} \right) \xi \, d\mathbf{x} = 0, \quad (5.11)$$

$$\int_{\Gamma} (T^{\text{ff}} - T^{\text{pm}}) \xi \, d\mathbf{x} = 0. \quad (5.12)$$

For the momentum transfer, the mortar method has to be applied in a different way. This is due to the fact that in the porous medium, the pressure is a primal variable and the mass flux a dual variable, while the opposite holds in the free-flow domain. It would be straight forward if pressure and velocity were both primary variables (if a mixed formulation was used) (Layton et al., 2002). Not using a mixed formulation, we choose the Lagrange multipliers and continuity conditions as:

$$\lambda_p := (\mathbf{f}_v \mathbf{n}) \cdot \mathbf{n} = [(\varrho_g^m \mathbf{v}_g \otimes \mathbf{v}_g + p_g \mathbf{I} - \boldsymbol{\tau}) \mathbf{n}]^{\text{ff}}, \quad (5.13)$$

$$\lambda_{v_x} := [\mathbf{v}_g \cdot \mathbf{t}]^{\text{ff}}, \quad (5.14)$$

$$\lambda_{v_y} := \mathbf{f}_m \cdot \mathbf{n} = [(\varrho_g \mathbf{v}_g + \varrho_l \mathbf{v}_l) \cdot \mathbf{n}]^{\text{pm}}, \quad (5.15)$$

$$\int_{\Gamma} \left( \left[ p_g^{\text{pm}} a_g + \left( p_l^{\text{pm}} - \frac{2\gamma l_g a_{\text{drop}}^o}{r_{\text{drop}} a_{\text{drop}}} \right) a_{\text{drop}} \right] - \lambda_p \right) \xi \, dx = 0, \quad (5.16)$$

$$\int_{\Gamma} \left( \left[ \left( \frac{\sqrt{K_i}}{\alpha_{\text{BJ}} \mu_g} \boldsymbol{\tau} \mathbf{n} \right) \cdot \mathbf{t} \right] - \lambda_{v_x} \right) \xi \, dx = 0, \quad (5.17)$$

$$\int_{\Gamma} \left( \left[ \mathbf{v}_g^{\text{ff}} \cdot \mathbf{n} \right] - \lambda_{v_y} \right) \xi \, dx = 0. \quad (5.18)$$

The duality of flux and continuity conditions characteristic for the mortar method is given by the coupling conditions since fluxes are substituted by primary variables. These Lagrange multipliers are not imperative, but a direct coupling as shown in Baber et al. (2012) would be sufficient. In the future, a combination of direct coupling (see Baber et al. (2012)) and mortar coupling is envisaged introducing Lagrange multipliers only where appropriate and necessary.

Additionally, the Lagrange multiplier for the storage term within the drop needs to be defined. The presented coupling concept provides three conditions for the component flux: the component flux across the drop-free interface (3.19), the component flux feeding the drop (4.20) and the combined condition for the whole interface (4.29). Equation (4.29) is used as coupling condition for the free-flow and porous-medium component-balance equations implemented via Lagrange multipliers (see equation (5.9)). The evaporative flux from the drop surface is assumed to be equal to the normal flux into the free-flow region. The component balance for the drop (4.20)

$$\frac{d\lambda_{V_{\text{drop}}}}{dt} + [\varrho_l \mathbf{v}_l x_l^\kappa - D_l^{\kappa, \text{pm}} \varrho_l \nabla x_l^\kappa]^{\text{pm}} \cdot \mathbf{n} a_{\text{drop}} \Omega_{\text{drop}} = -f_{\text{evap}}^\kappa(r_{\text{drop}}) \Omega_{\text{drop}}, \quad (5.19)$$

defines the Lagrange multiplier  $\lambda_{V_{\text{drop}}}$  which is used henceforth in equations (4.28) to (4.30). Here, the evaporative flux is calculated directly depending on the drop size (see equation (2.19)).

Below, the implementation is visualised providing a schematic of the global system matrix (inside the braces). It contains the submatrices for the two subdomains (top left, red and middle, grey), the coupling matrices between free flow and interface (top right, red) and porous medium and interface (middle right, grey), as well as the definitions of the Lagrange multipliers and continuity conditions in the bottom row (green). The first

column in front of the brace references the employed coupling conditions. Furthermore, the variables relevant in the respective conditions are indicated.

Eq. (3.12), (5.14):	Equation (3.8)		$\lambda_{v_x}$
Eq. (4.31), (5.13):	Equation (3.8)		$\lambda_p$
	Equation (3.7)		
Eq. (4.29), (5.9):	Equation (3.6)		$\lambda_x$
Eq. (4.30), (5.10):	Equation (3.9)		$\lambda_T$
Eq. (4.28), (5.15):		Equation (3.4)	$\lambda_{v_y} + \frac{\Delta\lambda_{V_{\text{drop}} \frac{1}{x_l^w}}}{\Delta t}$
Eq. (4.29), (5.9):		Equation (3.3)	$\lambda_x + \frac{\Delta\lambda_{V_{\text{drop}}}}{\Delta t}$
Eq. (4.30), (5.10):		Equation (3.5)	$\lambda_T + \frac{\Delta\lambda_{V_{\text{drop}} \frac{u_l}{x_l^w}}}{\Delta t}$
Equation (5.17):	$\boldsymbol{\tau}^{\text{ff}}, \alpha_{\text{BJ}}$		$\lambda_{v_x}$
Equation (5.18):	$\mathbf{v}_g^{\text{ff}} \cdot \mathbf{n}$		$\lambda_{v_y}$
Equation (5.16):		$p_g^{\text{pm}}, p_l^{\text{pm}}, \Gamma_{\text{drop}}$	$\lambda_p$
Equation (5.11):	$x_g^{w\text{ff}}$	$x_g^{w\text{pm}}, x_l^{w\text{pm}}$	
Equation (5.12):	$T_g^{\text{ff}}$	$T^{\text{pm}}$	
Equations (5.19):	$-\Gamma_{\text{evap}}^\kappa(\Gamma_{\text{drop}})$	$x_l^{w\text{pm}}, \mathbf{v}_l^{\text{pm}}$	$\frac{\Delta\lambda_{V_{\text{drop}}}}{\Delta t}$

If the pore-velocity approach from section 4.2.5 is used to estimate the flux feeding the drop (see second term in equation (5.19)), equation (4.25) defines the internal drop pressure which is an additional unknown on the interface. A new Lagrange multiplier,  $\lambda_{p_{\text{drop}}}$ , is introduced:

$$\left( [\mathbf{n} \cdot ((\varrho_g^m \mathbf{v}_g \otimes \mathbf{v}_g + p_g \mathbf{I} - \boldsymbol{\tau}) \mathbf{n})]^{\text{ff}} + \frac{2\gamma l g}{r_{\text{drop}}} \frac{a_{\text{drop}}^o}{a_{\text{drop}}} \right) a_{\text{drop}} = \lambda_{p_{\text{drop}}} a_{\text{drop}}, \quad (5.20)$$

which is used in equation (4.33). Due to the introduction of another unknown, the system matrix is changed to:

Eq. (3.12), (5.14):	Equation (3.8)		$\lambda_{v_x}$
Eq. (4.31), (5.13):	Equation (3.8)		$\lambda_p$
	Equation (3.7)		
Eq. (4.29), (5.9):	Equation (3.6)		$\lambda_x$
Eq. (4.30), (5.10):	Equation (3.9)		$\lambda_T$
Eq. (4.28), (5.15):		Equation (3.4)	$\lambda_{v_y} + \frac{\Delta\lambda_{V_{\text{drop}}}}{\Delta t} \frac{x_l^w}{x_l^g}$
Eq. (4.29), (5.9):		Equation (3.3)	$\lambda_x + \frac{\Delta\lambda_{V_{\text{drop}}}}{\Delta t}$
Eq. (4.30), (5.10):		Equation (3.5)	$\lambda_T + \frac{\Delta\lambda_{V_{\text{drop}}}}{\Delta t} \frac{u_l}{x_l^w}$
Equation (5.17):	$\boldsymbol{\tau}^{\text{ff}}, \alpha_{\text{BJ}}$		$\lambda_{v_x}$
Equation (5.18):	$\boldsymbol{v}_g^{\text{ff}} \cdot \mathbf{n}$		$\lambda_{v_y}$
Equation (3.11c):		$p_g^{\text{pm}}$	$\lambda_p$
Equation (5.11):	$x_g^{\text{wff}}$	$x_g^{\text{wpm}}, x_l^{\text{wpm}}$	
Equation (5.12):	$T_g^{\text{ff}}$	$T^{\text{pm}}$	
Equations (4.35):	$-\mathbf{f}_{\text{evap}}^\kappa(\Gamma_{\text{drop}})$	$x_l^{\text{wpm}}, p_l^{\text{pm}}, \lambda_{p_{\text{drop}}}$	$\frac{\Delta\lambda_{V_{\text{drop}}}}{\Delta t}$
Equations (5.20):	$p_g^{\text{ff}}, \Gamma_{\text{drop}}$		$\lambda_{p_{\text{drop}}}$

The main difference between the two system matrices is the implementation of the pressure condition and the flux feeding the drop. In the first matrix, the free-flow normal stresses are coupled by the Lagrange multiplier  $\lambda_p$  to the weighted sum of the porous-medium gas and water pressures. The flux feeding the drop is given by the macro-scale water flux coming from the porous medium. In the second implementation, the free-flow normal stresses are related to the gas-phase porous-medium pressure only. The internal drop pressure is introduced as new unknown  $\lambda_{p_{\text{drop}}}$ . It depends on the free-flow gas pressure and the capillary pressure at the drop surface which is a function of the drop radius. The water flux feeding the drop is estimated on the pore-scale and is proportional to the difference between porous-medium water pressure  $p_l^{\text{pm}}$  and internal drop pressure  $\lambda_{p_{\text{drop}}}$ . The second approach avoids forming the weighted sum of the

porous-medium phase pressures and is motivated by the work of Berning et al. (2009). Both systems are implemented in DuMu<sup>x</sup> and compared in chapter 7.

### 5.2.1 Model assumptions required for the implementation

In the previous section, it was shown that the discretised general balance equation (5.6) includes the normal fluxes across the interface  $\Gamma$ . According to the choice of the Lagrange multipliers, these fluxes are substituted by the normal fluxes specified in the according coupling condition. Comparing (5.9) and (5.10) with the flux coupling conditions (4.29) and (4.30) reveals that they differ in the gas flux across the drop contact area. The model assumption for the implementation is that the mass, component and energy fluxes from the porous medium across the interface fulfil:

$$\mathbf{f}_m \cdot \mathbf{n} = \sum_{\alpha \in \{l, g\}} [\varrho_\alpha \mathbf{v}_\alpha]^{\text{pm}} \cdot \mathbf{n} a_g + [\varrho_l \mathbf{v}_l]^{\text{pm}} \cdot \mathbf{n} a_{\text{drop}} = \sum_{\alpha \in \{l, g\}} [\varrho_\alpha \mathbf{v}_\alpha]^{\text{pm}} \cdot \mathbf{n} \quad (5.21)$$

$$\mathbf{f}^\kappa \cdot \mathbf{n} = \sum_{\alpha \in \{l, g\}} [\varrho_\alpha \mathbf{v}_\alpha x_\alpha^\kappa - D_\alpha^{\kappa, \text{pm}} \varrho_\alpha \nabla x_\alpha^\kappa]^{\text{pm}} \cdot \mathbf{n} a_g + [\varrho_l \mathbf{v}_l x_l^\kappa - D_l^{\kappa, \text{pm}} \varrho_l \nabla x_l^\kappa]^{\text{pm}} \cdot \mathbf{n} a_{\text{drop}} \quad (5.22)$$

$$\begin{aligned} &= \sum_{\alpha \in \{l, g\}} (\varrho_\alpha \mathbf{v}_\alpha x_\alpha^\kappa - D_\alpha^{\kappa, \text{pm}} \varrho_\alpha \nabla x_\alpha^\kappa) \cdot \mathbf{n}^{\text{pm}} \\ \mathbf{f}_T \cdot \mathbf{n} &= \sum_{\alpha \in \{l, g\}} [(\varrho_g h_g \mathbf{v}_g + \varrho_l h_l \mathbf{v}_l - \lambda_{\text{pm}} \nabla T) \cdot \mathbf{n}]^{\text{pm}} a_g + [(\varrho_l h_l \mathbf{v}_l - \lambda_{\text{pm}} \nabla T) \cdot \mathbf{n}]^{\text{pm}} a_{\text{drop}} \quad (5.23) \end{aligned}$$

$$= \sum_{\alpha \in \{l, g\}} (\varrho_\alpha h_\alpha \mathbf{v}_\alpha - \lambda_{\text{pm}} \nabla T)^{\text{pm}} \cdot \mathbf{n}^{\text{pm}}$$

These assumptions are realised as the porous-medium flux is forced to be equal to the according free-flow flux by the Lagrange multiplier.

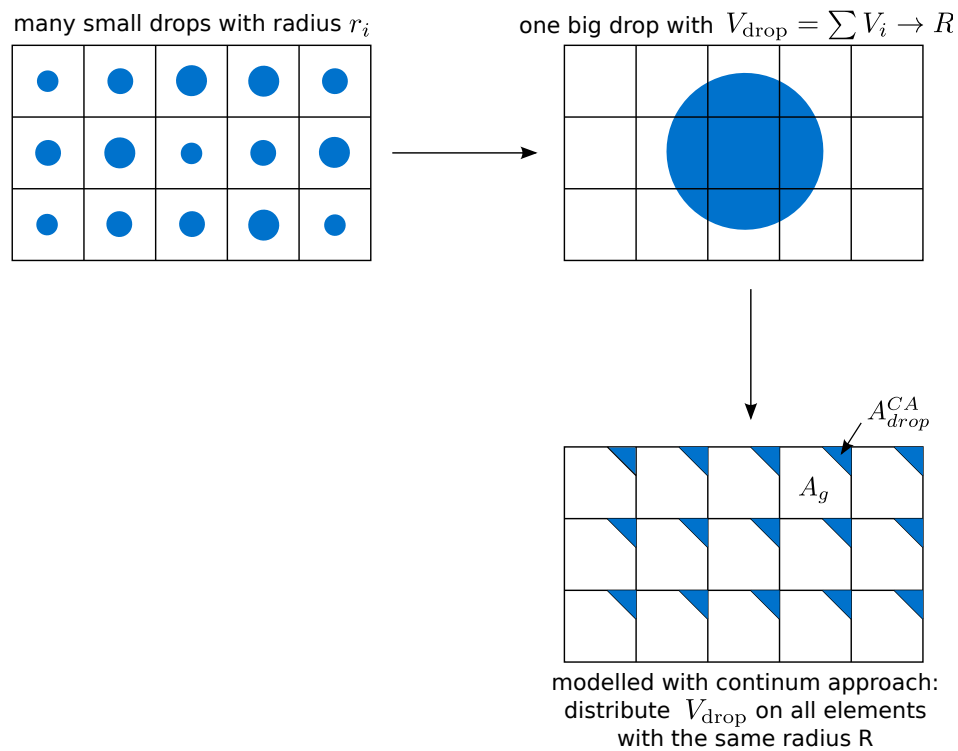


**Figure 5.3:** Visualisation of the REV drop concept: instead of one small drop per grid cell, the volumes are assembled to form one large drop per drop REV. Drop radius and the area weighting  $a_g$  and  $a_{\text{drop}}$  are calculated from the large drop and are valid for all contributing cells.

## 5.3 Droplet-specific implementation

In section 4.2.1, the REV drop concept was explained. Modelling one drop per grid cell would result in a non-physical number of very small drops. Instead, one big drop per grid-cell cluster  $\Omega_{\text{drop}}$  is assumed.

The model is solved for the Lagrange multiplier  $\lambda_{V_{\text{drop}}}$  which is essentially the volumetric contribution of each node to the whole drop. The water from all grid cells within one drop REV  $\Omega_{\text{drop}}$  is then aggregated to form one big physical drop (see figure 5.3):

$$V_{\text{drop}} = \sum_{i \in \Omega_{\text{drop}}} \frac{\lambda_{V_{\text{drop}}} x_{l,i}^w}{\rho_{l,i} x_{l,i}^w}.$$

The drop radius  $r_{\text{drop}}$  and the area distributions  $a_g$  and  $a_{\text{drop}}$  needed for the coupling conditions (equations (4.28) to (4.32)) are calculated from the total drop volume  $V_{\text{drop}}$  and are then valid for all contributing cells during the next Newton step (see figure 5.3).  $r_{\text{drop}}$ ,  $a_g$  and  $a_{\text{drop}}$  can hence be seen as effective quantities.

Alternatively, a coarse spatial discretisation of the mortar elements could be chosen such that the size of the mortar elements corresponds to the drop REV  $\Omega_{\text{drop}}$ . In that case, the total volume would be a primary variable of the model. The benefit of such an implementation is questionable, since the total volume would have to be redistributed to the contributing nodes to fulfil the mass-balance at the interface.

Until now, the area of influence  $\Omega_{\text{drop}}$  has to be chosen as input parameter. Consequently, the number and distribution of drops is given in advance (Berning et al., 2009) and has to be chosen wisely according to the physical problem. The influence of the choice of  $\Omega_{\text{drop}}$  is investigated in section 7.3.3.

The total work flow is illustrated in figure 5.4. The system starts fully gas-saturated. It switches to a two-phase system due to the water production by the electro-chemical reaction. As long as the pressure and flux of the water produced by the electro-chemical reaction is not sufficient to form a drop, a non-isothermal compositional two-phase system is solved. The porous medium is coupled to the free flow in the gas distributor using the simple-interface coupling conditions without drops (see equations (3.11c) - (3.19)). Between Newton steps the concept of the static pore model is used to determine

the state of the interface for the next Newton step (see figure 5.4 and section 4.2.2). When the drop-formation condition is fulfilled, the initial drop properties are calculated and the drop-coupling conditions are used until the drop detaches. The drop detachment condition (section 4.2.6) is evaluated after each time step. If the drop is close to detaching or detached the time-step is reduced to capture the actual detachment point.

All balance equations and geometrical relations are given in 3D. As a first step, the models presented in chapters 3 and 4 are implemented in 2D. Naturally, 2D models are a poor representation of reality and cannot account for realistic flow patterns. However, they are sufficient to prove the functionality and applicability of the developed model concepts and allow to draw first conclusions about the dominating physical processes and about the most crucial parameters. In a 2D concept, the drops become cylinders (Chen et al., 2005). This affects the geometrical relations like drop volume, drop contact area or drop surface as follows:

$$V_{\text{drop}} = \frac{(r_{\text{drop}})^2}{2} (2\theta^* - \sin \theta^*) b, \quad (5.24)$$

$$A_{\text{drop}}^o = 2\theta^* r_{\text{drop}} b, \quad (5.25)$$

$$A_{\text{drop}}^{\text{CA}} = 2r_{\text{drop}} \sin \theta^* b, \quad (5.26)$$

where  $b$  is the depth of the 2D system. The calculation of the retention force does not depend on the drop radius any more which is in agreement with the expression provided in Chen et al. (2005):

$$F_{\gamma_{lg}}^{\text{max}} = \pi (r_{\text{drop}} \sin \theta_a) \gamma_{lg} \cos(\pi - \theta_a) + \pi (r_{\text{drop}} \sin \theta_a) \gamma_{lg} \cos \theta_r. \quad (5.27)$$

The evaporative flux  $f_{\text{evap}}^{\kappa}$  for a two-dimensional setting considering advective transport is given in appendix A.2.

The numerical concept presented in this chapter is employed to simulate drop dynamics in a simplified setup motivated by the processes occurring at the cathode side of a PEM fuel cell in chapter 7.

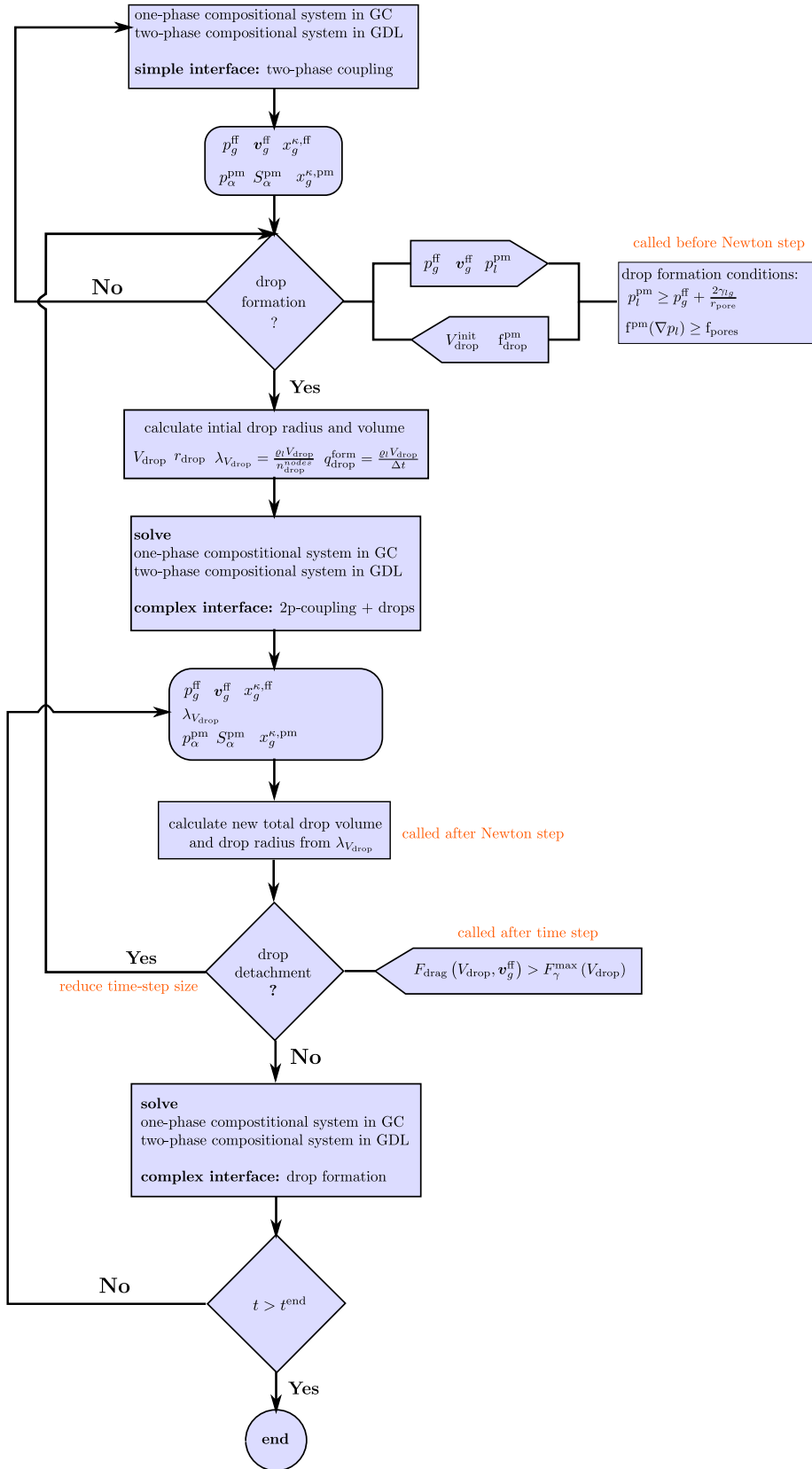


**Figure 5.4:** Visualisation of the implementation: Before each Newton step, the formation of new drops is checked and calculated. Then the drop grows and the new drop properties are calculated. At the end of a time step, the detachment condition is evaluated.



## 6 Application and results: Transvascular exchange

In the previous chapters, a toolbox has been presented containing coupling approaches and interface descriptions with different levels of complexity. In the following, the applicability of the simple interface concept to the physiological application of transvascular exchange is shown. In this application, the micro-vascular wall is an interface layer which separates the free blood flow and the porous tissue, regulating the flow and transport processes between these two domains.

The model contributes to the description of the distribution process of therapeutic agents to their target tumour cells. The distribution process of nutrients, metabolites and therapeutic agents involves different scales. The largest scale is the scale of the whole organism, followed by the organ and tumour level. At the organ level, macro- and micro-circulation, the surrounding tissue and the sub-scale of transvascular exchange, where the structure of the capillary wall is resolved, have to be taken into account. Finally, the smallest scale of interest is the cellular scale where the interaction of therapeutic agent and target cells occurs. Therapeutic agents distribute in the circulatory system and reach the surrounding tissue by crossing the micro-vascular wall of the smallest blood vessels. This wall has a complex structure and acts as the main regulator of substance exchange. Since substance exchange only occurs in the smallest vessels, the capillaries, the current project focuses on the description of the exchange and regulation processes between vascular and tissue space (transvascular exchange), trying to provide a better understanding of one of the limiting processes in the distribution of therapeutic agents. The cell-selective transmembrane protein TRAIL (tumour-necrosis factor related apoptosis inducing ligand), which induces apoptosis<sup>18</sup> of the target tumour cells, is considered as typical therapeutic agent.

---

<sup>18</sup>"Programmed cell death in a multi-cellular organism" (Erbertseder, 2012).

In the following, the theoretical background and the relevant processes are explained (see section 6.1). Based on the characteristics of the application, the appropriate model and interface concept is identified (see section 6.2). Finally, results for the prediction of transport of therapeutic agents from the vascular to the tissue space are shown in section 6.3. A critical discussion of the applicability of the chosen model concept is given in section 6.4.

## 6.1 Physiological background<sup>19</sup>

Transvascular exchange involves three compartments: flow and transport inside the capillary blood vessels, distribution in the surrounding tissue and flow and transport through the micro-vascular wall. First, the properties of fluids and solids are described. Then, transvascular exchange is explained. A detailed discussion of all involved materials and fluids, and of the occurring processes is given in Baber (2009).

**Blood** is a suspension of cells in blood plasma. It is a non-Newtonian fluid with pseudo-plastic behaviour which is strongly influenced by the concentration and state of the red blood cells (Junqueira et al., 2002). The viscosity of blood depends on the flow conditions, the vessel diameter, haematocrit<sup>20</sup> and fluid composition (Schmidt and Lang, 2007). In the smallest capillaries, the red blood cells deform and accumulate in the vessel center, forming a lubrication film of plasma near the vessel walls. As a consequence, the viscosity in the smallest blood vessels decreases significantly (Fåhræus-Lindquist-Effect). Red blood cells are not able to cross the capillary wall. Thus, only blood plasma and the transported substances therein are able to filtrate into the tissue space. The blood flow in the larger vessels is pulsating due to the influence of the heart beat. In the smaller vessels, the influence diminishes and can be neglected in the capillaries (Schmidt and Lang, 2007). Flow velocities are between 0.5 to 1 mm/s (Thews and Vaupel, 2007, Schmidt and Lang, 2007). Inside the blood vessels, degradation processes occur (Erbertseder et al., 2012).

---

<sup>19</sup>Parts of this section are taken from Baber, K. (2009). Modeling the transfer of therapeutic agents from the vascular space to the tissue compartment (A continuum approach). Master's thesis, Dep. of Hydromechanics and Modeling of Hydrosystems, IWS, University of Stuttgart.

<sup>20</sup>The volumetric fraction of red blood cells (Schmidt and Lang, 2007).

**Blood plasma** and **interstitial fluid** have the same material properties. The Newtonian fluids are composed of more than 90% water. The fractions of proteins, ions, organic compounds and hormones vary inside the blood vessels and in the tissue space.

**Blood vessels** are flexible tubes. Starting at the heart with the largest blood vessel, the aorta, the vessel system branches into arteries, arterioles and capillaries. The vessels are classified into macro- and micro-circulation depending on their radius. The macro-circulation is a system of mere blood channels with relatively thick vessels walls. Substance exchange with the surrounding tissue only occurs in the smallest blood vessels, the capillaries (Junqueira et al., 2002). Capillaries have a diameter of 5 to 15  $\mu\text{m}$  and are about 0.25 to 1 mm long. The capillary network and the surrounding tissue is called *capillary bed* with an inter-capillary distance of about 100  $\mu\text{m}$  (Netti et al., 1997).

**Tissue** is the building material of the body (Schiebler, 2005). It is a dynamic aggregation of cells which have the same morphological and functional properties. Tissue is an elastic medium composed of fixed and mobile cells, fibres, amorphous ground substance and interstitial fluid. The flow velocity of interstitial fluid is in the  $\text{mm}/\text{s}$ -range (Fu et al., 2005).

There are four basic types of tissue in the human body (Schiebler, 2005):

- **connective tissue** - structure and support of the human body,
- **epithelial tissue** - lining of internal and external surfaces, fulfils functions like separation, protection and transport of substances,
- **muscle tissue** - generation of force and motion,
- **nervous tissue** - communication between and control of body parts.

In the tissue space, a vivid interaction between cells and surrounding substances occurs. The therapeutic agent binds to the target tumour cells (termed *adsorption* in the following) and degradation processes happen.

The vascular and tissue spaces are separated by the **capillary** or **micro-vascular wall**. It is a thin (thickness  $\approx 2 \mu\text{m}$ ), complex and heterogeneous structure that regulates transvascular exchange. It consists of one layer of endothelial cells which are fixed to a basal membrane which is the border to the surrounding tissue (see figure 6.1). On the luminal side, the capillary wall is covered by a negatively charged layer of proteins called

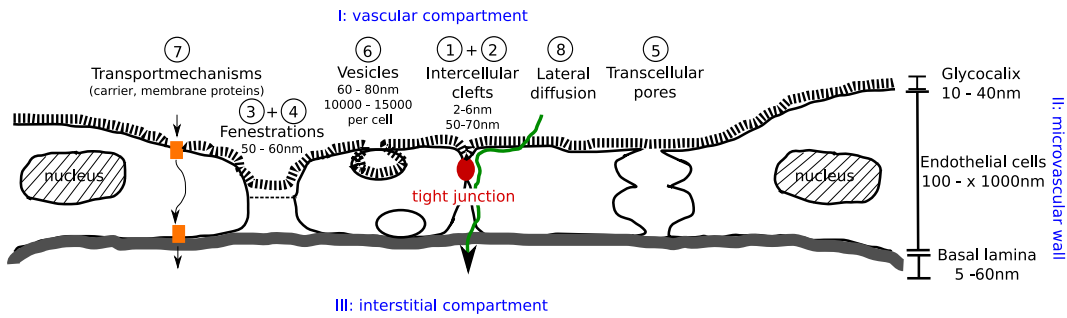
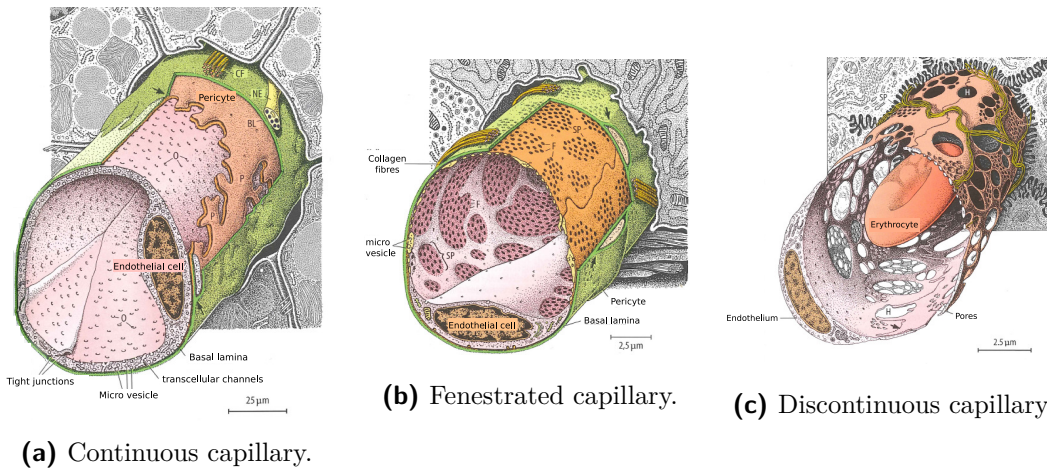


**Figure 6.1:** Structure of the capillary wall showing a variety of para- and transcellular pathways. 1+2) Intercellular clefts of different diameter, 3+4) open and closed fenestrations, 5) pores of fused vesicles, 6) vesicles, 7+8) transcellular transport mechanisms. The exact structure is strongly dependent on anatomic location and physiological/pathological conditions (Baber, 2009).



(a) Continuous capillary.

(b) Fenestrated capillary.

(c) Discontinuous capillary.

**Figure 6.2:** Capillary types (R. Krstic (1991) Human Microscopic Anatomy, in Junqueira et al. (2002), with kind permission of Springer, Heidelberg).

glycocalyx (Sugihara-Seki and Fu, 2005, Hughes, 2000, Stace and Damiano, 2001). The endothelial cells are the rate limiting barrier to extravasation of plasma components of all sizes from electrolytes to proteins (Junqueira et al., 2002, Schmidt and Lang, 2007). The endothelium is impermeable for the red blood cells. Moreover, the basal lamina acts as a permeability barrier and the glycocalyx serves as an additional molecular filter, maintaining a low permeability to macro-molecules (Sugihara-Seki and Fu, 2005, Michel and Curry, 1999). The electro-chemical processes induced by the negatively charged glycocalyx influence transvascular exchange of charged macro-molecules significantly and are explained in detail in Stace and Damiano (2001).

The exact structure, and thus the permeability of the capillary wall, is strongly dependent

---

on the anatomic location and physiological and pathological conditions (Junqueira et al., 2002). Continuous capillaries (see figure 6.2a) have almost impermeable walls and are found e.g. in the skin, the lung and especially in the brain. Fenestrated capillaries (see figure 6.2b) exhibit intracellular pores and clefts ranging from 50 nm to 100 nm in diameter (Petrak and Goddard, 1989, Junqueira et al., 2002, Schmidt and Lang, 2007). They can be found in tissue where a high mass-transfer rate between blood vessels and tissue occurs, e.g. the pancreas. Discontinuous capillaries (see figure 6.2c) can be found in the bone marrow, liver and spleen. Their walls are highly permeable.

In order to allow substance exchange, a variety of different para- and transcellular pathways are embedded in the micro-vascular wall. Baber (2009) identify eight principle pathways (see figure 6.1). Paracellular pathways are pores and clefts between and within endothelial cells. They are permeable to hydrophilic and polar substances and macro-molecules. Pores through the tight junctions that connect endothelial cells with each other are selective due to a network of protein strands and most likely impermeable for macro-molecules like proteins. The macro-molecules can pass through pores within cells, so-called fenestrations. It is assumed in the following, that these pathways are not interconnected and that flow occurs perpendicular to the flow in the blood vessels (Formaggia et al., 2009). Transcellular pathways go through endothelial cells and facilitate the passage of water, small hydrophilic and lipid-soluble substances, including the respiratory gases  $CO_2$  and  $O_2$  (Schmidt and Lang, 2007). The transcellular pathways are strongly selective and might involve substance-specific signalling processes. Depending on the wall structure and physiological and pathological conditions, the relevance of the respective pathways may vary. Renkin (1978) states that quantitative roles of one pathway with respect to another are not known. Petrak and Goddard (1989) suggest that only a very small volume of fluid is transported by vesicles, that water and solutes pass mainly through small pores and that macro-molecular transport is almost entirely convective. The number and configuration of the above mentioned pathways as well as the glycocalyx and the basal lamina determine the permeability of the vessel wall. Additionally, permeability depends on the size, charge and constitution of the respective substance (Chauhan et al., 2011). Not all pathways might be available for synthetic macro-molecules like therapeutics. The distribution of these substances cannot rely on receptor-mediated pathways, but it depends on convective and diffusive transport through paracellular pathways (Renkin, 1978).

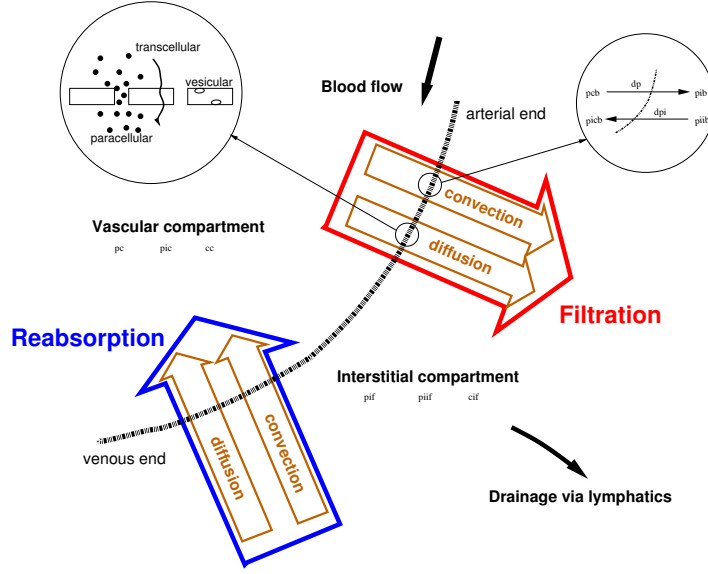


**Figure 6.3:** Pressure significantly decreases along the capillary. In combination with osmotic pressure, this leads to inward and outward flow.

Transvascular exchange through the paracellular pathways is driven by gradients in pressure, osmotic pressure and concentration. Solvent flow across the capillary wall is generally described by the Starling-law (Curry, 1984):

$$\mathbf{f}_m = K_{\text{wall}} \varrho_{\text{if}} [(p_{\text{cap}} - p_{\text{tiss}}) - \sigma_d (\pi_{\text{cap}} - \pi_{\text{tiss}})]. \quad (6.1)$$

The net convective flux is the difference between the flux induced by the pressure gradient and the osmotically induced flux. The proportionality constant that relates solvent flow to pressure gradient is called hydraulic conductivity  $K_{\text{wall}}$ . This constant describes the conductivity of the micro-vascular wall to water. The parameter  $\sigma_d$  describes the selectivity of the semi-permeable membrane, here the micro-vascular wall, to the solutes inducing osmotic pressure (Sugihara-Seki and Fu, 2005). It is called osmotic reflection coefficient and influences the effectiveness of the osmotic-pressure gradient (Kurbel et al., 2001). According to Jain (1987a), it is close to 1 for macro-molecules and close to 0 for micro-molecules. The effectiveness of the osmotic pressure depends on the structure and permeability of the micro-vascular wall and  $\sigma_d$  varies according to the anatomical location.

Solute transport is given by the Kedem-Katchalsky equation:

$$\mathbf{f}^\kappa = D_{\text{wall}}^\kappa \varrho_{\text{if}} (x_{\text{cap}}^\kappa - x_{\text{tiss}}^\kappa) + \mathbf{f}_m (1 - \sigma_f) x_{\text{cap}}^\kappa. \quad (6.2)$$

Equation 6.2 specifies solute flow due to convective and diffusive transport. Diffusion is proportional to the concentration gradient. The according proportionality constant is the vascular diffusive permeability  $D_{\text{wall}}^{\kappa}$  which depends on the transported substance. The filtration reflection coefficient  $\sigma_f$  stands for the retardation of solutes with respect to the solvent due to membrane obstructions (Sugihara-Seki and Fu, 2005).  $K_{\text{wall}}$ ,  $D_{\text{wall}}^{\kappa}$ ,  $\sigma_d$  and  $\sigma_f$  depend on the structure of the micro-vascular wall and on size, charge and configuration of the molecule. The properties change even along one vessel. The vessel wall tends to get more permeable towards the venous end of the capillaries and the post-capillary venules (Jain, 1987a).

The pressure inside the capillaries decreases significantly from the arterial to the venous end of the vessel while the interstitial pressure remains almost constant. In combination with the osmotic-pressure gradient induced by concentration differences across the micro-vascular wall, this induces outward flow at the arterial end and inward flow at the venous end of the vessel (see figure 6.3). The difference between phase and osmotic pressure is called *effective pressure*. According to Schmidt and Lang (2007), about 90% of the filtrate is reabsorbed. The amount varies depending on the physiological and pathological conditions. The net outward flow is taken up by the lymphatic system.

The **lymphatic system** is the body's drainage system. Parallel to the blood vessels, a network of lymphatic vessels absorbs the filtrate from the capillaries and transports it back to the blood stream. The uptake of interstitial fluid by the initial lymphatics is called *lymph drainage*. About 2l per day are drained from the tissue space (Schiebler, 2005). The lymphatic system regulates the interstitial pressure and is responsible for the immune defence, filtering the lymph flow in the lymph nodes. Please be referred to Ackermann (2013) for an overview of the lymphatic system.

Chauhan et al. (2011) find that the **tumour** properties and the tumour micro-environment impede all steps in the distribution process of therapeutic agents. The increased solid stress caused by uncontrolled cell proliferation compresses the blood vessels and reduces blood flow. The immature, abnormal and tortuous vascular network poses a geometric resistance to the blood flow, decreasing the flow velocity further. Highly permeable vessel walls yield an increased fluid leakage into the surrounding tissue. In combination with a missing lymph-drainage system, this increases the interstitial and osmotic pressure significantly, limiting transvascular exchange to diffusion. The dense interstitial matrix hinders the transport in the tissue space.

## 6.2 Coupled model for transvascular exchange: Assumptions

Focusing on the exchange processes, we consider one capillary blood vessel surrounded by tissue instead of the whole capillary bed. Interaction with surrounding vessels is not included. Flow and transport across the micro-vascular wall involve three compartments: the vascular and the interstitial compartment, and the micro-vascular wall. Each of these regions has a complex structure and is composed of numerous different components. Furthermore, different fluids, namely blood and interstitial fluid, and a variety of solutes, like red and white blood cells, proteins, molecular substances and therapeutics, are involved in the transport processes. Not all of the solutes are able to pass the micro-vascular wall and for the rest different transcellular pathways apply. This complex system is simplified in the following and a decision for the description of the interface is discussed. We assume isothermal conditions ( $T=310.15\text{ K}$ ) and fully dissolved substances, and neglect the influence of gravity due to the small system size.

The **vascular compartment** is described by the one-phase (blood) two-component (blood and therapeutic agent) free-flow model from section 3.3 based on the following assumptions:

- Blood can be described as incompressible, Newtonian fluid, because flow properties and velocities are constant inside one capillary.
- Pulsation from the heart beat can be neglected in the remote capillaries.
- The influence of the red blood cells is neglected and the therapeutic agent is the only transported substance.
- Blood flow is described with the Stokes equations justified by very low Reynolds numbers ( $Re = \frac{d_{\text{cap}} \varrho_{\text{blood}}^m v_{\text{cap}}}{\mu_{\text{blood}}} \approx 0.006$ ).
- The degradation of the therapeutic agent is described by a sink term for equation (3.6) (Erbertseder, 2012):

$$q_{\text{deg}}^{\kappa} = \varrho_{\text{blood}} k x_{\text{cap}}^{\kappa} \quad \text{with} \quad k = \frac{\ln 2}{t_{1/2}}. \quad (6.3)$$

For the flow processes in the **tissue compartment**, the model from section 3.2 is simplified to a one-phase (interstitial fluid) two-component (interstitial fluid and therapeutic agent) model. The following assumptions are made:

- Uniting all “solid” components (fibres, cells, amorphous ground substance) into one solid phase and neglecting elasticity and plasticity, tissue is described as a homogeneous, isotropic, rigid porous medium.
- All cellular components are assumed to be immobile. The exchange and interaction between cells and interstitial fluid is neglected.
- Darcy’s law is applied, justified by low Reynolds numbers.
- The interstitial fluid is incompressible and has Newtonian properties.
- Lymph drainage and the interaction of the therapeutic agent with the target cells is described by sink terms entering equations (3.3) and (3.4) (Erbertseder, 2012, Ackermann, 2013).

$$q_{\text{lymph}}^{\kappa} = K_{\text{lymph}} \frac{A_{\text{lymph}}}{V_{\text{tiss}}} (p_{\text{tiss}} - p_{\text{lymph}}) \varrho_{\text{if}} x_{\text{tiss}}^{\kappa}, \quad (6.4)$$

$$q_{\text{lymph}} = K_{\text{lymph}} \frac{A_{\text{lymph}}}{V_{\text{tiss}}} (p_{\text{tiss}} - p_{\text{lymph}}) \varrho_{\text{if}}. \quad (6.5)$$

The interstitial pressure  $p_{\text{tiss}}$  is a primary variable of the porous-medium model, the pressure inside the lymph vessel is set to a constant literature value. The hydraulic conductivity of the lymph vessel  $K_{\text{lymph}}$  describes the uptake of interstitial fluid through the lymphatic valves.

Adsorption of the therapeutic agent depends on the receptor-ligand concentration in the tissue  $R_0$  and on the binding and detachment rates  $k_{\text{on}}$  and  $k_{\text{off}}$ :

$$q_{\text{ads}}^{\kappa} = (k_{\text{on}} x_{\text{tiss}}^{\kappa} \varrho_{\text{if}} - k_{\text{off}}) R_0. \quad (6.6)$$

The best representation of the thin and complex structure of the **capillary wall** would be a pore-scale description as shown in section 4.1. The paracellular pathways could be represented by non-intersecting, circular pores yielding a bundle-of-tubes description. To obtain a realistic representation, different properties could be assigned to the pores by varying e.g. diameter and permeability. Tight-junction strands and diaphragms

obstructing some of the pathways could be included as additional resistance. The tube model could be extended to account for the fibre matrix of the glycocalyx and its electro-chemical properties by combining a fibre-matrix model (Sugihara-Seki and Fu, 2005, Fu et al., 2005) with macro-molecular transport influenced by an electric field (Stace and Damiano, 2001). However, knowledge about the exact properties and about the relevance of the different pathways for the respective synthetic therapeutic agent is scarce. Even after intense discussions with physiologists, the relevant pathways and justified simplifications could not be identified. That is why, as a first step, the capillary wall is described on the REV-scale as a thin porous-medium layer that differs from the porous-medium describing the tissue space (Formaggia et al., 2009). Since the micro-vascular wall is only one layer of cells which is only  $1\ \mu\text{m}$  to  $2\ \mu\text{m}$  thick, it is highly questionable if a volume-averaging process can be justified. Due to heterogeneities and the high aspect ratio the choice of an REV is a demanding task. A 2D-continuum description would be more appropriate (see section 2.2), but is postponed to further research.

In summary, the following simplifications are applied to obtain a description of the capillary wall:

- It is represented by a thin, rigid, homogeneous, anisotropic (lower lateral permeability) porous layer.
- Individual pathways and components are not resolved. Permeability and diffusivity values are assigned to the whole region in accordance with the Starling and Kedem-Katchalsky equations (see equations (6.1) and (6.2)) allowing bi-directional flow. From the units of these parameters it can be deduced that the parameters describing the micro-vascular wall,  $K_{\text{wall}}$  and  $D_{\text{wall}}^{\kappa}$ , are interface parameters. The physiological parameters are integrated into the porous-medium approach by multiplication with the thickness of the capillary wall (Baber, 2009).
- The electro-chemical influence of the glycocalyx, the selectivity of pathways and binding or reactions are neglected.
- The osmotic-pressure gradient across the wall is assumed to be constant. Osmotic pressure is not modelled depending on changes in the concentration of proteins and other solutes. Consequently, the effective pressure  $p^{\text{eff}} = p - \pi$  is the primary variable in the subdomains.

- In the porous-medium representing the capillary wall, the transport equation (3.3) includes the reflection coefficient  $\sigma_f$  to account for the retardation of the transported substance with respect to fluid flow. Please be referred to Ischinger (2013) for a more detailed explanation.

Essentially, the model consists of one free-flow and two porous-medium regions. The upper boundary of the capillary wall is the interface between free-flow and porous-medium model. The domains are coupled using the simple interface approach described in section 3.4.

## 6.3 Results<sup>21</sup>

The results shown in this section were obtained in the scope of two independent studies. In Ischinger (2013), the general model concept is analysed under healthy conditions and a parameter study and sensitivity analysis based on an intensive literature review is carried out. Ackermann (2013) investigates the influence of degradation, lymph drainage and adsorption in healthy and tumour tissue. Both studies assume radial symmetry yielding the 2D setup depicted in figure 6.4. It includes the vascular compartment (white), the wall (light grey) and the tissue compartment (dark grey). The green line indicates the coupling interface. Please note that figure 6.4 is only a schematic and does not represent the actual geometry. Figure 6.4 also illustrates the boundary conditions. The therapeutic agent enters from the left capillary boundary specified by a time-dependent Dirichlet condition obtained from Erbertseder (2012). At the right free-flow and at the porous-medium boundaries outflow conditions are set allowing mass and momentum to leave the domain freely. The initial concentration of therapeutic agent in the tissue is zero. The pressure values are determined by the effective pressure and given in table 6.1.

### 6.3.1 The reference case

Ischinger (2013) selects parameters for a reference case which are also used by Ackermann (2013). The parameters are shown in table 6.1. Adsorption, degradation and lymph

---

<sup>21</sup>The results were obtained in the scope of the independent studies of Felix Ischinger (Ischinger, 2013) and Sina Ackermann (Ackermann, 2013).

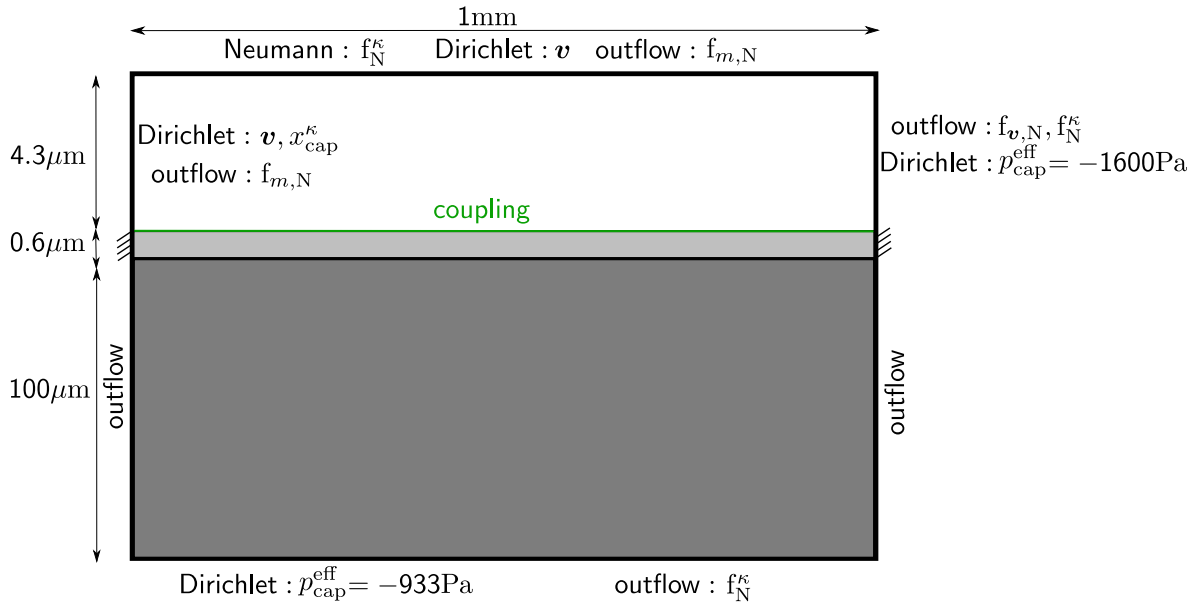


**Figure 6.4:** Numerical setup of the model for transvascular exchange: the top region corresponds to half of the capillary blood vessel, symmetry conditions are assumed on the top boundary, blood and therapeutic agent enter from the left. The bottom region corresponds to the tissue space, the interstitial pressure is fixed at the bottom boundary, all other boundaries are outflow conditions. The two regions are separated by the thin porous medium representing the capillary wall.

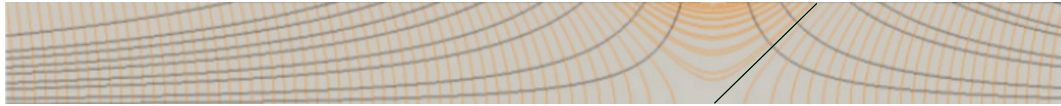


**Figure 6.5:** Isobars (grey) and stream lines (orange) in the tissue compartment. The grey line depicts the border stream line: left of the black line fluid is reabsorbed coming from the bottom of the tissue. Therapeutic agent reaches the right part only by diffusion. (with kind permission of Ischinger (2013))

flow were neglected in the reference case. Figure 6.5 shows the streamlines in the tissue compartment (dark grey area in figure 6.4). In the first two-thirds of the domain, the effective pressure is larger in the capillary than in the tissue. Filtration from the capillary into the tissue occurs. The blood pressure in the capillary decreases significantly towards the venous end, so that the gradient in the effective pressure is reversed (see figure 6.6). In the right part of the domain, fluid flows from the bottom of the tissue space into the capillary. In between, the streamlines form an arch where the filtrate is directly reabsorbed by the capillary. Both flow directions are influenced by the reflection coefficient  $\sigma_f$ . Figure 6.7 illustrates the resulting mass-fraction distribution of the therapeutic agent. First, the therapeutic agent spreads in the vascular compartment.

**Table 6.1:** Parameter values for simulations with healthy tissue. The symbols listed under “Sink terms” are explained in section 6.2.

Symbol	Meaning	Value	Unit
<b>Capillary</b>			
$\rho_{\text{blood}}^m$	mass density of blood	1045	kg/m <sup>3</sup>
$\mu_{\text{blood}}$	dynamic viscosity of blood	2.8	mPa s
$p_{\text{cap}}$	pressure	4 000	Pa
$\nabla p_{\text{cap}}$	pressure gradient	-2 000 000	Pa/m
$\pi_{\text{cap}}$	osmotic pressure	3 600	Pa
$T$	temperature	37	°C
$D_{\text{cap}}^\kappa$	diffusion coefficient	$2.19 \cdot 10^{-11}$	m <sup>2</sup> /s
<b>Micro-vascular wall</b>			
$\rho_{\text{if}}^m$	mass density of interstitial fluid	1025	kg/m <sup>3</sup>
$\mu_{\text{if}}$	dynamic viscosity of interstitial fluid	1.3	mPa s
$T$	temperature	37	°C
$D_{\text{wall}}^\kappa \cdot h_{\text{wall}}$	diffusion coefficient	$4.8 \cdot 10^{-16}$	m <sup>2</sup> /s
$K_{\text{wall}} \cdot h_{\text{wall}}$	horizontal permeability	$1.0 \cdot 10^{-24}$	m <sup>2</sup>
$K_{\text{wall}} \cdot h_{\text{wall}}$	vertical permeability	$2.34 \cdot 10^{-20}$	m <sup>2</sup>
$\Phi_{\text{wall}}$	porosity	0.03	-
$\tau$	tortuosity	$3.38 \cdot 10^{-4}$	-
$\sigma_{\text{f}}$	solvent-drag reflection coefficient	0.83	-
<b>Tissue</b>			
$p_{\text{tiss}}$	pressure	0	Pa
$\pi_{\text{tiss}}$	osmotic Pressure	933	Pa
$T$	temperature	37	°C
$D_{\text{tiss}}^\kappa$	diffusion coefficient	$1.3 \cdot 10^{-12}$	m <sup>2</sup> /s
$\mathbf{K}$	isotropic permeability	$6.5 \cdot 10^{-18}$	m <sup>2</sup>
$\Phi$	porosity	0.22	-
$\tau$	tortuosity	0.124928	-
<b>Sink terms</b>			
$K_{\text{lymph}}$	permeability of the lymph-vessel wall	$1.9 \cdot 10^{-12}$	m/Pa s
$p_{\text{lymph}}$	lymphatic pressure	-1 200	Pa
$\frac{A_{\text{lymph}}}{V_{\text{tiss}}}$	ratio of surface area and volume	3.0	1/m
$t_{1/2}$	half-life of the therapeutic agent	21 600	s

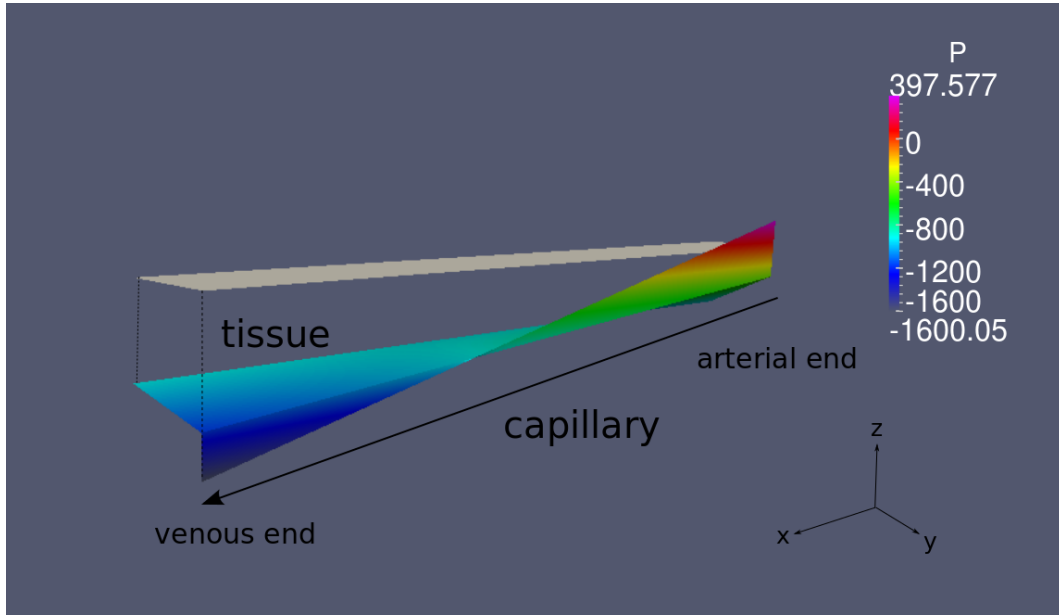


**Figure 6.6:** Interstitial pressure: the grey plane represents the size of the tissue compartment, above is the capillary wall. There is a strong pressure gradient across the capillary wall. Pressure significantly decreases from the arterial to the venous end. (with kind permission of Ackermann (2013))

Due to the high flow velocities, the mass fraction in the capillary reaches its maximum value quickly. Then, the therapeutic agent enters the tissue space crossing the capillary wall. In the left part, the therapeutic agent comes from the capillary and leaves the domain through the outflow boundary at the bottom of the domain. The mass fraction reaches a value determined by the mass fraction in the capillary and the reflection coefficient  $X_{\text{tiss}}^{\kappa} = (1 - \sigma_f)X_{\text{cap}}^{\kappa} = (1 - 0.83) 2.989 \cdot 10^{-7} \text{ kg/kg} = 5.08 \cdot 10^{-8} \text{ kg/kg}$  (see figure 6.8). In the middle part, where the streamlines form an arch, the mass fraction reaches the value in the capillary eventually, forming a local maximum (see bump in figure 6.8). As long as the mass fractions are not equal in the vascular and interstitial compartment, the transport from the capillary is larger than the uptake into the capillary due to the upwinding of the mass fraction in the advective transport. The therapeutic agent enters the tissue and pools up below the capillary wall being held back by the reflection coefficient. The local maximum is mitigated by higher diffusion and reflection coefficients (see figure 6.9). In the right part of the domain, the mass fraction of therapeutic agent is small since fluid flows from the bottom of the tissue towards the capillary. This part can only be supplied with therapeutic agent by diffusion.

**Figure 6.7:** Distribution of therapeutic agent (red) within the two-dimensional model domain in healthy tissue. (with kind permission of Ackermann (2013))



**(a)** Initial conditions of the simulation. A very small amount of therapeutic agent (red) can be seen at the top left corner.



**(b)** The therapeutic agent is carried through the capillary by the blood flow (red area at the top).



**(c)** It reaches the venous end of the capillary before entering the tissue.



**(d)** Slowly, the therapeutic agents crosses the micro-vascular wall and is transported into the tissue.



**(e)** It spreads from the top left corner towards the bottom right corner of the model domain.



**(f)** After a simulation time of 30 000s, the whole model domain has been reached by the therapeutic molecules.

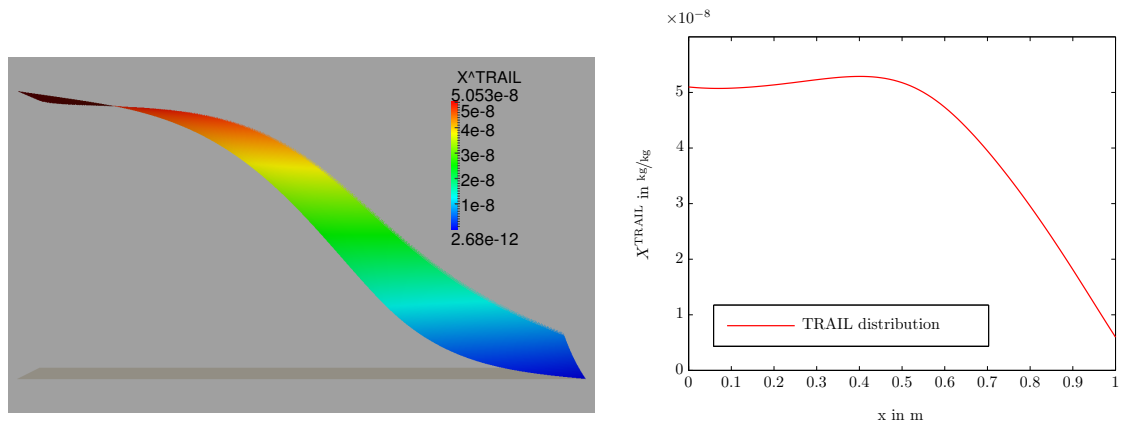


**Figure 6.8:** Surface plot of the mass fraction of therapeutic agent in the tissue compartment. The line plot of the mass fraction just below the capillary wall has a local maximum due to the reflection coefficient. (with kind permission of Ischinger (2013))

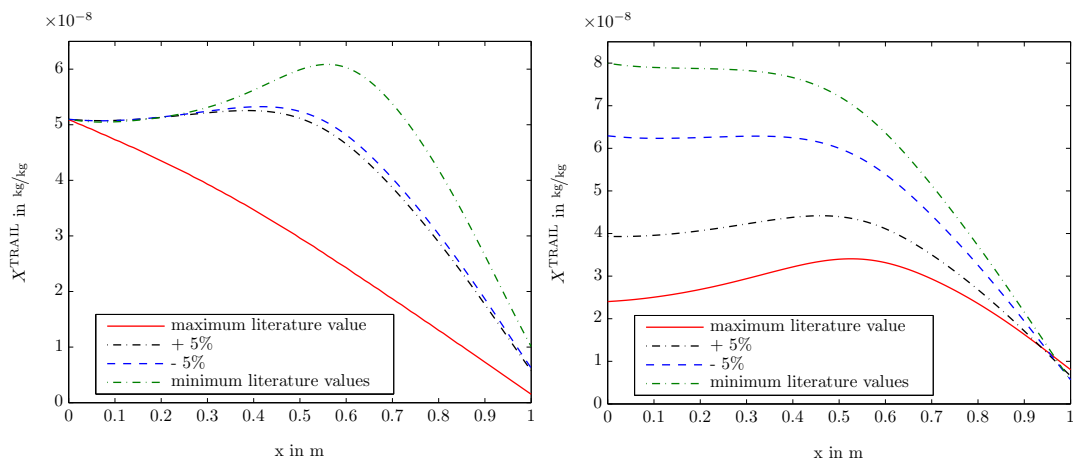


**Figure 6.9:** Line plots of mass fraction in the tissue parallel to the capillary wall for different diffusion coefficients (left) and reflection coefficients (right). The values are taken from the literature review and the variation of  $\pm 5\%$  refers to the reference value given in table 6.1. Higher diffusion and reflection coefficients cause a more even distribution of the therapeutic agent. (with kind permission of Ischinger (2013))

### 6.3.2 Parameter study and sensitivity analysis

Ischinger (2013) performs a sensitivity analysis to identify the parameters most crucial for transvascular exchange. He carries out four simulations for each parameter, using the smallest and largest literature value and varying each parameter by  $\pm 5\%$  with respect to the reference value given in table 6.1. Saltelli et al. (2000) state that a variation of 5% is the theoretical limit for a local parameter-sensitivity analysis in non-linear models. The results are compared based on the normalised integral mass fraction of the therapeutic agent:

$$\varepsilon = \frac{\chi_{\text{tiss}}^{\kappa}(t, \mathbf{p}_{i \neq j}, p_j + \Delta p_j)}{\Delta p_j} \frac{p_j}{\chi_{\text{tiss}}^{\kappa}(t, \mathbf{p}_i)}, \quad (6.7)$$

where  $\chi_{\text{tiss}}^{\kappa}$  is the mass fraction of therapeutic agent integrated over the tissue compartment as a function of all parameters,  $\mathbf{p}$  are the parameters of interest,  $\Delta p_j$  is the variation of the parameter  $j$  and  $\varepsilon$  is the normalised sensitivity coefficient. A positive value of  $\varepsilon$  means that a positive variation of a parameter entails an increase in the integral mass fraction. A negative values indicates a decrease in mass fraction. Figure 6.10 shows the results of the sensitivity analysis. In the **capillary compartment**, the diffusion coefficient  $D_{\text{cap}}^{\kappa}$ , the viscosity  $\mu_{\text{blood}}$  and the density  $\varrho_{\text{blood}}$  are varied. These parameters do not influence the system significantly due to the advectively dominated fast flow regime. The fluid properties of the interstitial fluid have no significant influence either.

The variation of the diffusion coefficient of the **capillary wall**  $D_{\text{wall}}^{\kappa}$ , of the porosity  $\Phi_{\text{wall}}$  and of the height of the capillary wall  $h_{\text{wall}}$  have the expected effect: an increase in diffusion coefficient or porosity increases the permeability of the wall and leads to higher mass fractions in the tissue compartment. An increase in the wall thickness has the opposite effect. Figure 6.10 shows negative values of  $\varepsilon$  for a variation of the wall permeability  $K_{\text{wall}}$  meaning that an increase in permeability leads to lower concentrations in the tissue. This unexpected result can be explained based on the flow field described in the previous section. A high permeability yields high concentrations in the left part where filtration occurs, but also a higher uptake in the right part of the domain. These two competing effects can yield on overall reduction of the concentration. The reflection coefficient  $\sigma_f$  has the highest impact on the distribution of therapeutic agent (see figure 6.10). This is not surprising as it scales the advective flow across the capillary wall.

The consequences of the variation of **tissue** parameters like diffusion coefficient  $D_{\text{tiss}}^{\kappa}$ ,

	$+var$	$+5\%$	$-5\%$	$-var$
$D_{cap}^{\kappa}$	-0,0021989	-0,0028154	-0,0030540	-0,0007600
$\mu_{blood}$	4,7719e-5	4,7719e-5	9,5438e-5	9,5438e-5
$Q_{blood}$	-0,0029920	-0,0028631	-0,0031494	-0,0029920
$h_{wall}$	-0,2386417	-0,5030993	-0,1012116	-0,3695440
$\mu_{if}$	0,0238678	0,0210440	0,0173696	0,0121122
$Q_{if}$	0,0029347	0,0030063	0,0030540	0,0034238
$D_{wall}^{\kappa}$	0,2901433	0,2762441	0,2720926	0,209705
$D_{tiss}^{\kappa}$	-0,0475614	-0,1933089	-0,2040456	-0,0289408
$K_{wall,yy}$	0,0020205	-0,0109276	-0,0135521	-0,0650221
$K_{tiss}$	-0,0033161	-0,0066329	-0,0078259	-0,0261356
$\Phi_{wall}$	0,2878410	0,2746217	0,2705179	0,2208689
$\Phi_{tiss}$	-0,205087	-0,2431750	-0,2580156	-0,3453712
$\sigma_f$	-3,0567983	-3,2450217	-3,4240150	-3,5089077

**Figure 6.10:** Results of the sensitivity analysis: the normalized sensitivity coefficient  $\varepsilon$  is shown for each varied parameter. Red illustrates a high influence ( $\varepsilon \geq 0.5$ ), yellow illustrates medium influence ( $\varepsilon = 0.25$ ), green means no influence ( $\varepsilon = 0.0$ ). In between the color scale is linear. (with kind permission of Ischinger (2013))

permeability or porosity are all unexpected: an increase of these parameters always leads to a lower concentration of therapeutic agent (see negative  $\varepsilon$  in figure 6.10). Again, this is due to the fact that higher diffusivity and permeability not only increase the filtration into the tissue, but also the uptake into the capillary and the transport across the domain boundaries. The porosity is part of the definition of the effective diffusion coefficient in porous media (see table 3.2). Hence, an increase in porosity increases the effective diffusion coefficients and entails the respective consequences.

Naturally, the flow field has a strong influence on the distribution of the therapeutic agent. Most effects of the parameter variation can only be explained because both filtration and reabsorption take place. A change in the effective pressures which causes outward flow along the whole capillary changes the characteristics of the whole system (Ischinger, 2013).

### 6.3.3 Influence of lymph drainage, degradation and adsorption

Ackermann (2013) extends the model to account for degradation, lymph drainage and adsorption. In the circulatory system, the concentration of therapeutic molecules can be reduced by metabolic transformation, for example. In healthy tissue, excess interstitial fluid is drained by the lymphatic system carrying therapeutic molecules away from the target cells. Tumour tissue differs considerably from healthy tissue. The blood vessels are more tortuous, elongated and possibly dilated. They have highly permeable walls with a low reflection coefficient. Tumour tissue has higher porosities and permeabilities (see table 6.2) and does not have a functioning lymphatic system. The therapeutic agent interacts with the target tumour cells, reducing its amount in the tissue. Furthermore, a higher interstitial pressure is generally observed (Jain, 1987b). A summary of the most important tumour properties can be found in Erbertseder (2012). The employed parameters are listed in table 6.2.

Ackermann (2013) analyses the influence of degradation and lymph drainage in healthy tissue adding the sink terms (6.3), (6.5) and (6.4) to the reference case shown in the previous section. The sink terms are set in all nodes of the respective domain. She finds that degradation reduces the integral amount of therapeutic agent in the tissue space  $\chi_{\text{tiss}}^{\kappa}$  by only  $1.34 \cdot 10^{-3} \%$ . The lymph-drainage term caused a non-physiological increase

**Table 6.2:** Parameter values for simulations with tumour tissue differing from the healthy case shown in table 6.1. The symbols listed under “Sink terms” are explained in section 6.2.

Symbol	Meaning	Value	Unit
<b>Capillary</b>			
$p_{\text{cap}}$	pressure	767	Pa
$\nabla p_{\text{cap}}$	pressure gradient	-490 000	Pa/m
$\pi_{\text{cap}}$	osmotic pressure	2660	Pa
<b>Micro-vascular wall</b>			
$K_{\text{wall}} \cdot h_{\text{wall}}$	horizontal permeability	$5.064 \cdot 10^{-24}$	$\text{m}^2$
$K_{\text{wall}} \cdot h_{\text{wall}}$	vertical permeability	$5.064 \cdot 10^{-20}$	$\text{m}^2$
$\Phi_{\text{wall}}$	porosity	0.04	-
$\tau$	tortuosity	$16.9 \cdot 10^{-4}$	-
$\sigma_{\text{f}}$	solvent-drag reflection coefficient	0.75	-
<b>Tissue</b>			
$p_{\text{tiss}}$	pressure	133	Pa
$\pi_{\text{tiss}}$	osmotic Pressure	1995	Pa
$\mathbf{K}$	isotropic permeability	$2.14 \cdot 10^{-17}$	$\text{m}^2$
$\Phi$	porosity	0.27	-
$\tau$	tortuosity	0.71	-
<b>Sink terms</b>			
$k_{\text{on}}$	kinetic constant (forward reaction)	100	$\text{m}^3/\text{mol s}$
$k_{\text{off}}$	kinetic constant (backward reaction)	0	$1/\text{s}$
$R_0$	receptor concentration	$1.7 \cdot 10^{-5}$	$\text{mol}/\text{m}^3$
$t_{1/2}$	half-life of the therapeutic agent	21 600	s

in therapeutic agent of about  $10^{-5}$  %. Possibly, local minima in the effective interstitial pressure cause non-physiological filtration from the lymph vessels into the tissue.

In tumour tissue, the influence of degradation and of adsorption of therapeutic agents to target tumour cells is accounted for by the sink terms (6.3) and (6.6). In expression (6.6), the release of therapeutic molecules from the tumour cells back to the tissue is independent of the amount of bound substances. With a given value for the backward reaction rate  $k_{\text{off}} = 10^{-3}$ , the adsorption term becomes a source for the therapeutic agent. However, no literature values for  $k_{\text{off}}$  could be found which relate the backward-reaction rate to the amount of bound substance. As a first solution,  $k_{\text{off}}$  was set to zero so that no TRAIL molecule that is already bound to a tumour cell is released again. This overestimates the amount of therapeutic agent affected by adsorption yielding a reduction of 0.44 %. Degradation caused a negligible reduction of  $1.47 \cdot 10^{-7}$  %.

In conclusion, the effect of degradation can be neglected in both healthy and tumour tissue, if only one capillary is considered. It might become more important if the network of supplying blood vessels is included in the model. No conclusions can be drawn about the influence of lymph drainage due to the incorrect results. Since tumours do not have a functioning lymphatic system, the effect of lymph drainage is of little importance for the prediction of the percentage of tumour cells which react to the administered therapeutic agent. The latter can only be predicted correctly by a cell model which resolves the binding of therapeutic agent to the target tumour cells as well as the reaction of the cells to the bound substances. Such a model is developed by Hasenauer et al. (2010a) and combined with a model for the distribution of therapeutic agent from the circulatory systems to the target tumour cells by Erbertseder (2012). The estimated reduction of therapeutic agent due to the reaction with tumour cells based on reaction constants already showed the expected considerable influence (Ackermann, 2013).

## 6.4 Discussion

The presented model reproduces the basic processes of transvascular exchange. It simulates filtration and reabsorption of fluid and reveals the influence of wall and tissue parameters on the final distribution of therapeutic agents. Nevertheless, it is only a first step towards modelling transvascular exchange across the micro-vascular wall since the

employed concepts are of limited applicability and information about the physiological processes and parameters is scarce.

The main limitation of the model with respect to the physiological reality is that all structural properties like glycocalyx, basal membrane and the variety of pathways are lumped into the effective properties permeability  $K_{\text{wall}}$ , diffusivity  $D_{\text{wall}}^{\kappa}$  and porosity. The electro-chemical properties are neglected and smooth, rigid structures are assumed. A three-dimensional pore-scale model of the capillary wall would yield new insights in the relevance of the respective structures and pathways, but requires well-founded assumptions about the physiological properties. Additionally, the distribution of therapeutic agents is significantly influenced by the neighbouring capillaries. Modelling the whole capillary bed or at least several capillary blood vessels would increase the reliability of the predicted concentrations. Eventually, a detailed model for transvascular exchange could be coupled to the model developed in Erbertseder (2012). The distribution process in the circulatory system is modelled with a vascular-graph model (Reichold, 2011). The capillary bed is described with a double-continuum approach (Erbertseder et al., 2012) where the description of the exchange between vascular and tissue compartment could be improved. Finally, the distribution of therapeutic agents is used as input for a cell-population model to predict the number of tumour cells which undergo apoptosis (Hasenauer et al., 2010b).

Besides the physiological limitations, conceptual limitations need to be addressed. The capillary wall, which is an interface layer, is described as an independent domain. The coupling between vascular free-flow and porous wall compartment which is based on the simple interface concept is motivated mathematically. Alternatively, the capillary wall could be described either as a pore-scale tube model (see section 4.1) or as a 2D-continuum (see section 2.2). Furthermore, the application of REV-scale approaches to the thin porous structures needs to be revised.

Concluding, the results of this section prove the applicability of the simple interface concept and motivate a more complex interface description.

# 7 Application and results: Water management in PEM fuel cells

In the previous chapters, a toolbox has been presented containing coupling approaches and interface descriptions with different levels of complexity. In the following, the applicability of the drop concept is shown on the basis of an application from the technical field.

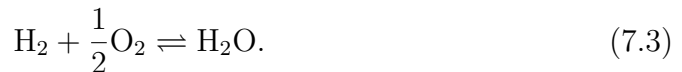
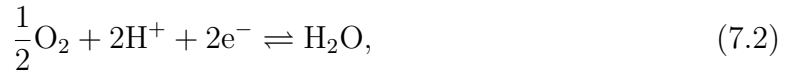
The increased energy consumption of society and industry and the related increase in emissions lead to a gradual change of course in the environmental and energy policy. To fulfil the political guidelines and to realise a sustainable and environmentally friendly energy supply, the energy demand must be reduced by increasing efficiency and uncovering energy-saving potentials. Additionally, the use of renewable energy sources like solar, wind or water power needs to be increased. A technology like PEM fuel cells fits in this economical and political framework in many ways. The production of hydrogen can buffer unneeded energy peaks caused by the temporal variation of natural energy sources. Hydrogen production is one answer to the demand for energy-storage capacities. The development of fuel-cell vehicles can satisfy the increasing social demand for mobility efficiently and with low emissions. To reach market maturity, the production costs of PEM fuel cells need to be significantly reduced and durability needs to be increased. Apart from an alternative to the high platinum demand, the water management "remains one of the outstanding areas for research" (Kandlikar et al., 2014). The optimisation of the water management in PEM fuel cells is based on a good understanding of the occurring multi-phase transport processes, which is obtained through experimental and numerical investigations (Wang et al., 2011, Rosén et al., 2012, Roth et al., 2013, Wang et al., 2011). As in-situ experiments are very demanding, numerical simulations are "an essential tool for the investigation of multi-phase transport and spatio-temporal behaviour of water" (Gurau and Mann, 2009).

Water management in PEM fuel cells involves two-phase flow as well as component and energy transport in the porous diffusion layer which is in direct contact with the gas channel. The interfacial phenomena significantly influence the water management (Gurau and Mann, 2009). The focus of this work is on the transfer mechanisms at the interface between GC and GDL, hence, at the interface between porous fibre structure and free gas flow. The goal is to describe drop dynamics at the gas-channel gas-diffusion layer interface using the REV-scale coupled model from sections 4.2 and 5.

In the following, the theoretical background and the relevant processes of the application are explained (see section 7.1). Based on the characteristics of the application, the most appropriate model and interface concept is identified (see section 7.2). Finally, results showing the influence of different parameters on the drop dynamics at the cathode side of PEM fuel cells are presented in section 7.3. A critical discussion of the applicability of the chosen concept is given in section 7.4.

## 7.1 Technical background

<sup>22</sup>PEM fuel cells convert the chemical energy of the hydrogen-oxygen oxidation-reduction reaction into electricity:



The reactants oxygen and hydrogen are supplied through the gas channels and diffuse through the gas-diffusion layers to the Catalyst Layer (CL) (see figure 7.1). The two half-reactions (7.1) and (7.2) occur in the CL and are spatially separated by an electrolyte membrane (see figure 7.1). Reaction (7.1) occurs at the anode side, producing electrons. Reaction (7.2) occurs at the cathode, consuming electrons. The electrolyte membrane allows the flow of protons from anode to cathode side but forbids the transport of electrons, so that the electrons are forced through an external circuit, creating an

---

<sup>22</sup>This paragraph is partly published in Baber, K., Flemisch, B., and Helmig, R. (2014). Modelling drop dynamics at the interface between free and porous-medium flow using the mortar method. submitted to International Journal of Heat and Mass Transfer.

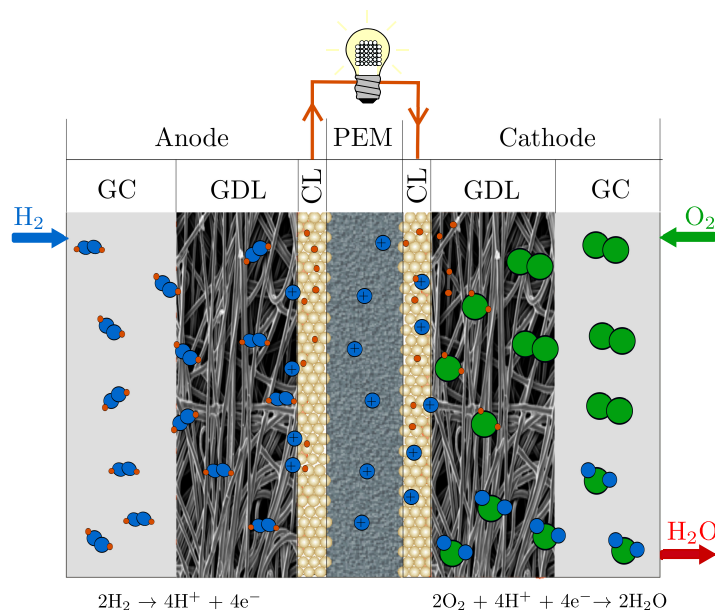


**Figure 7.1:** Schematic of a fuel cell. Oxygen and hydrogen are supplied through the gas channels (GC), diffuse through the gas-diffusion layers (GDL) and react in the catalyst layer (CL). Water is produced. Anode and cathode are separated by a proton-conducting membrane (PEM).

electrical current. The hydrogen protons produced at the anode side and transported through the membrane react with oxygen and electrons at the cathode, forming water (see figure 7.1). Additionally, water is transferred through the membrane by electro-osmotic drag, diffusion and advection (O’Hayre et al., 2006). The produced water humidifies the membrane keeping up proton conductivity. Excess water needs to be removed via the gas-diffusion layer and the gas channel to keep the reaction sites free and to prevent mass-transport losses. The situation where water prevents the reacting gases from reaching the reaction sites is referred to as *flooding* (Carton et al., 2012). Flooding typically causes the limiting current of PEM fuel cells (Gurau and Mann, 2009). Hence, a good water management is crucial to ensure performance and durability and thus commercial and technical attractiveness (Wu et al., 2009). The water distribution is significantly influenced by drops forming at the hydrophobic GDL/GC-surface (Gurau and Mann, 2009, Cho et al., 2012a). In the next sections, the components of a PEM fuel-cell are explained.

### 7.1.1 Gas channel

Instead of one big gas chamber on top of the porous electrodes, a system of small flow channels guarantees a constant flow of reactants and a homogeneous reactant concentration due to convective mixing. The flow structures are edged into a material which has to fulfil several requirements. It should have a high thermal and electrical conductivity, since the bipolar plates harvest the electrical current and conduct excess heat. It should be resistive against corrosion, gas tight and cost effective, and it should have a high mechanical strength. The most frequently used materials are graphite or stainless steel (O'Hayre et al., 2006). The channel walls are generally hydrophilic while the GDL surface is hydrophobic.

Water flowing towards the GC through the GDL forms drops and slugs on the bottom of the gas channel disturbing the gas-flow field and causing a significant pressure loss. The hydrophilicity of the GC walls supports film-flow formation as drops wick into the gas-channel corners. According to Kandlikar et al. (2014), hydrophilic walls yield a more even water distribution and lower pressure losses. Qin et al. (2012b) find that a compromise for the GC-wall contact angle has to be found to ensure drop removal from the GDL surface (hydrophilic side walls) and high water-removal rates due to film flow (hydrophobic side walls). To increase the water-removal capability, the flow pattern is optimised (O'Hayre et al., 2006). Parallel channels have the advantage of low pressure losses, but water build-up can cause high mass-transfer losses. A serpentine flow field has a higher water removal capability but also a higher pressure drop. The interdigitated flow field yields the largest pressure drop. However, due to the forced convection of reactant gas through the diffusion layer, mass transport and water management are improved. In general, a compromise between a large pressure drop at high gas velocities and efficient water removal, and low pressure drop at low velocities and poor water removal has to be found.

According to O'Hayre et al. (2006) and Kandlikar et al. (2014) gas flow in fuel-cell flow channels is laminar ( $Re^{\max} = \frac{2.4 \text{ kg/m}^3 \cdot 1 \cdot 10^{-3} \text{ m} \cdot 16 \text{ m/s}}{1.9 \cdot 10^{-5} \text{ Pas}} \approx 2021$ ). Kandlikar et al. (2014) analyse air flow velocities between 1.59 m/s and 15.89 m/s and observe a pressure loss of 1.5-11 kPa. Gopalan and Kandlikar (2014) assume velocities between 0.48 m/s and 7.23 m/s and investigate the influence of the channel geometry on the drop transport

characteristics. They obtain a correlation between the pressure drop and drop detachment for a trapezoidal cross-section and velocities below 4 m/s.

Flow in fuel-cell gas channels can be modelled using the Navier-Stokes equations. However, capturing the two-phase flow conditions of reactant gas and water drops, slugs and films is challenging. Berning et al. (2009, 2010) use the 3D Navier-Stokes equation, neglecting the interaction between gas and water phase and assuming the phase pressures to be equal. Gurau et al. (2008), Gurau and Mann (2010) and He et al. (2007) include two-phase drag by source and sink terms which depend on the velocity difference, the Reynolds number, the water saturation and the drop diameter. See and Kandlikar (2012) present a 1D gas-channel model estimating the two-phase pressure drop based on empirical relations considering local water saturation, phase exchange and mass fluxes. Qin et al. (2012b) propose a 1D model based on the Hagen-Poiseuille equation. The hydraulic conductivity depends on the hydraulic diameter, which in turn depends on the size of the drops and the thickness of the water film.

### 7.1.2 Gas-diffusion layer

The gas-diffusion layer is positioned between gas channel and catalyst layer. It is a transition zone from the channel-land architecture of the gas channel to the reaction site, providing a homogeneous fuel supply to the catalyst layer. It also ensures water and heat transport from the reaction site to the gas channel and current conductivity from the bipolar plates to the catalyst layer (Mathias et al., 2003, Gurau and Mann, 2009, Chan et al., 2012). Furthermore, the GDL provides mechanical protection for the catalyst layer.

In PEM fuel cells, the GDL is made of roughly 200-400  $\mu\text{m}$  thick carbon-fibre paper (see figure 7.1). Many different varieties exist ranging from coated or filled carbon cloths to carbon-filled non-woven webs. Mathias et al. (2003) give an overview of existing patents, materials and manufacturing processes. The GDL has a high porosity of about 70-80 %. According to Mathias et al. (2003), who measure the pore-size distribution using mercury porosimetry, about 90 % of the pores have a diameter of 10  $\mu\text{m}$  or higher. The average pore diameter is around 20-40  $\mu\text{m}$ , and the maximal pore size is around 250  $\mu\text{m}$  (Benziger et al., 2005).

Often a Polytetrafluoroethylene (PTFE) (“Teflon”) coating is applied to increase hydrophobicity of the GDL, yielding better water removal but lower diffusion coefficients for the gas phase (Mathias et al., 2003, Chan et al., 2012). Sinha and Wang (2008) analyse the influence of wettability using pore-network models. They find an optimal fraction of hydrophobic and hydrophilic pores reducing mass-transport losses to a minimum. Hydrophobic media cause fingering yielding high local but low overall saturations (Shahraeeni and Hoorfar, 2013). Benziger et al. (2005) stress the advantages of a bimodal pore-size distribution with mixed wettability, because such a combination ensures both gas supply and water removal. As explained in sections 2.4 and 4.2, the wetting properties and the contact angle are crucial for water transport and drop formation. Mathias et al. (2003) measure advancing  $\theta_a = 170^\circ$ , receding  $\theta_r = 134^\circ$  and static  $\theta^* = 140\text{-}150^\circ$  contact angles at the surface of a PTFE-treated carbon-fibre paper.

The properties determining liquid transport are gas- and liquid permeability and diffusivity. Intrinsic permeability determines the advective flow properties. According to Mathias et al. (2003), in-plane permeability and through-plane permeability are around  $5 \cdot 10^{-12} - 10 \cdot 10^{-12} \text{ m}^2$ . Note that in-plane permeabilities are much more important for fuel cell performance especially in case of interdigitated flow fields, since through-plane gas transport is dominated by diffusion. Water flow is predominantly driven by capillary forces, while advection is important under the bipolar plates (Benziger et al., 2005).

Parameter estimation and the derivation of expressions for effective parameters like the effective diffusion coefficient, capillary pressure or effective heat conductivity are a research field of its own. Since the GDL is a porous medium, the effective diffusion coefficient includes the influence of porosity and tortuosity. Different expressions for the effective diffusion coefficient in a fibrous, hydrophobic porous medium are obtained in Nam and Kaviany (2003), Acosta et al. (2006), Berning et al. (2009), Das et al. (2010) and Rosén et al. (2012):

$$D_g^{\kappa,\text{pm}} = D_g^\kappa \Phi \left( \frac{\Phi - 0.11}{1 - 0.11} \right)^k (1 - S_l)^l, \quad \text{or} \quad (7.4)$$

$$D_g^{\kappa,\text{pm}} = D_g^\kappa \Phi \tau (S_g)^m. \quad (7.5)$$

The exponents  $k$ ,  $l$  and  $m$  are determined experimentally and clearly show the anisotropy of the gas-diffusion medium. Some values are given in table 7.1.

**Table 7.1:** Exponents for the empirical definitions of the diffusion coefficient (see equations (7.4) and (7.5)).

Symbol	Value	Reference
$k$	0.521 in plane	Nam and Kaviany (2003)
	0.785 through plane	Nam and Kaviany (2003)
	0.91 in plane	Rosén et al. (2012)
	2.2 through plane	Rosén et al. (2012)
$l$	2	Nam and Kaviany (2003)
	2.1 in plane	Rosén et al. (2012)
	3 through plane	Rosén et al. (2012)
$m$	1.5	Das et al. (2010)
	1	Acosta et al. (2006)
	2 in plane	Rosén et al. (2012)
	3.5 through plane	Rosén et al. (2012)

Gostick et al. (2006) stress that many GDL materials have a bimodal pore-size distribution due to the employed carbon powder. Mixed-wettability and the bimodal pore-size distributions complicate the determination of the appropriate capillary-pressure–saturation and relative-permeability–saturation relationship. Gostick et al. (2006) claim that the Van-Genuchten model fits better to the experimental data than the Brooks-Corey model as it captures the slow rise of the  $p_c$ - $S$  curve at high wetting-phase saturations. Dwenger et al. (2012) measure  $p_c$ - $S$  relations of mixed-wet gas-diffusion media under compression. The results show a strongly hysteretic behaviour for low compression levels, which disappears completely under realistic pressure loads. The influence of the capillary-pressure–saturation relationship on the drop dynamics at the interface is analysed in section 7.3.4.

Another effective parameter, that needs to be determined carefully, is the effective heat conductivity of anisotropic diffusion media. Transient conditions and cold-start scenarios with a steep temperature evolution are most interesting for fuel-cells research. Acosta et al. (2006) use a constant heat conductivity independent of other material properties or the water saturation. Using the high value of the heat conductivity of the solid material, they overestimated the heat conduction and observed only minor temperature gradients. Das et al. (2010) and Pharoah et al. (2006) propose the following expression:

$$\lambda_{\text{pm}} = \Phi\lambda_{\text{void}} + (1 - \Phi)\lambda_s. \quad (7.6)$$

The effective thermal conductivity is strongly dependent on the wetting properties, the pore size and pore distribution of the system. The invasion and distribution pattern of the water phase significantly influences the thermal conductivity and causes a non-linear behaviour which is not captured by this approach.

The introduction of an additional Micro-Porous Layer (MPL) between GDL and CL increases the cell performance reducing ohmic losses and improving water removal and mechanical stability (Chan et al., 2012). The MPL, however, limits the advective transport due to low porosities and permeabilities ( $\mathbf{K} = 1.3 \cdot 10^{-13} \text{ m}^2$  (Pant et al., 2012)) and reduces the diffusive gas transport significantly (Kandlikar et al., 2014). The MPL is between 38-112  $\mu\text{m}$  thick with pore sizes between 7-133 nm (Chan et al., 2012). The MPL is generally purely hydrophobic. Since the mean free-path length of the gas molecules is larger than the small pore size, Knudsen diffusion or Knudsen flow occurs (Helmig, 1997). In that case, the molecules collide more often with the system borders than with each other, causing a slip velocity on the walls and increasing flow (Bear, 1972). Eventually, continuum fluid mechanics cannot be applied any more and statistical mechanics must be used. The movement of the single molecules can be described as a diffusive process using Fick's law of diffusion with a diffusion coefficient which depends on the pore diameter, temperature and the molecular mass of the gas (Chan et al., 2012). In a transition region between continuum flow and molecular dynamics, both molecular and Knudsen diffusion are important. Both Fickian and Knudsen diffusion occur in the MPL and the Knudsen diffusion coefficient accounts for 80 % of the effective diffusion of the MPL-GDL assembly (Chan et al., 2012). According to Mathias et al. (2003) and Pant et al. (2012), it is not necessary to consider Knudsen diffusion within the gas-diffusion layer, because the mean pore diameter of several 10s of microns is larger than the mean free path length of the gas.

Modelling flow and transport processes in gas-diffusion media is done either on the pore-scale, using pore-network models, or on the REV scale, assuming that an REV can be defined. The latter assumption is questionable because of the thin heterogeneous structure of the GDL and the high aspect ratio (Qin and Hassanizadeh, 2014). This assumption and an alternative description based on 2D continua are discussed in section 2.2. Flow processes in the GDL are slow at most operating conditions so that Darcy's law can be used on the REV-scale and an extension to the Forchheimer equation is not necessary (Pant et al., 2012).

### 7.1.3 Catalyst layer and membrane<sup>23</sup>

The membrane is approximately 50  $\mu\text{m}$  thick. It is composed of a polymer electrolyte which conducts protons and water but not electrons. The reaction or catalyst layer consists of a carbon-supported catalyst (mostly platinum) and an ionomer<sup>24</sup>. The CL is 10  $\mu\text{m}$  thick and has a bimodal pore-size distribution of 20-40 nm within the agglomerates and 40-400 nm between the agglomerates. The cathodic electro-chemical reaction (see equation (7.2)) occurs at the boundary of catalyst, ionomer and pore space. The ionomer supplies the hydrogen protons, while the pore-space supplies oxygen and removes product water. Water is produced as liquid in the pore-space or in the ionomer. From the ionomer water enters the pore-space by electro-osmotic discharge. It is also transported through the membrane by electro-osmotic drag. The boundary of pore space, ionomer and catalyst is mostly described as a 1D straight line, but can also be resolved in detail assuming thermodynamic equilibrium between ionomer and pore space.

### 7.1.4 Electro-chemistry

The information about the electro-chemistry in fuel cells presented in this section is summarised from O'Hayre et al. (2006). We explained above that the reaction (7.3) is split into two half reactions separated by a semi-permeable membrane and that the transferred electrons produce a current. Ideally, high current densities  $i$  and high voltages  $E$  are desired to obtain an optimal fuel-cell performance. Theoretically, the maximum voltage of a PEM fuel cell can be calculated based on the reaction kinetics. The difference in Gibbs free energy of the oxygen-hydrogen red-ox reaction of  $\Delta g = 237 \text{ kJ/mol}$  yields a reversible voltage of:

$$E_0 = \frac{-\Delta g}{n_e \cdot F} = \frac{237 \text{ kJ/mol}}{2 \cdot 96485.3364 \text{ C/mol}} = 1.228 \text{ V}, \quad (7.7)$$

where  $n_e$  is the number of transferred electrons and  $F$  is the Faraday constant. The Faraday constant converts the number of electrons into a quantity of charge. Equation

<sup>23</sup>The information in this section is taken from Gurau and Mann (2009).

<sup>24</sup>A polymer with a significant proportion of constitutional units which have ionisable or ionic groups, or both (Jenkins et al., 1996).

(7.7) predicts an ideal reversible electro-chemical cell voltage  $E_0 = 1.228$  V assuming constant pressure and temperature during the reaction. The dependence of the reversible cell voltage  $E_0$  on temperature and pressure can be estimated using equations (7.8) and (7.9):

$$\left(\frac{dE_0}{dT}\right)_p = \frac{\Delta s}{n_e \cdot F}, \quad (7.8)$$

$$\left(\frac{dE_0}{dp}\right)_T = \frac{\Delta V^n}{n_e \cdot F}, \quad (7.9)$$

According to O'Hayre et al. (2006), both pressure and temperature turn out to have a minimal effect on the reversible voltage. The dependence on composition is given by the Nernst equation:

$$E = E_0 - \frac{\mathfrak{R}T}{n_e \cdot F} \ln \frac{\prod a_{products}^{m_i}}{\prod a_{reactants}^{m_i}}, \quad (7.10)$$

where  $a^{m_i}$  is the activity of each component raised to the power of its stoichiometric coefficient  $m_i$ .

Ideally, the cell voltage stays constant with increasing current density, leading to a steadily increasing power density. However, losses occur, leading to a decrease in cell voltage  $E$  with increasing current (see figure 7.2). At low current, activation losses dominate. With increasing current, ohmic losses become more and more important. Additionally, mass transport limitations in the catalyst layer lead to a reduction in cell voltage (Gurau et al., 2008). At high current, mass-transport limitations in the GDL lead to a limit voltage. The three main losses, activation, ohmic and mass-transport losses, are described in the following.

Under equilibrium, forward and reverse reaction occur at the same rate. A so-called exchange current density  $i_0$  is produced:

$$i_0 = i_{\text{forward}} = i_{\text{reverse}}. \quad (7.11)$$

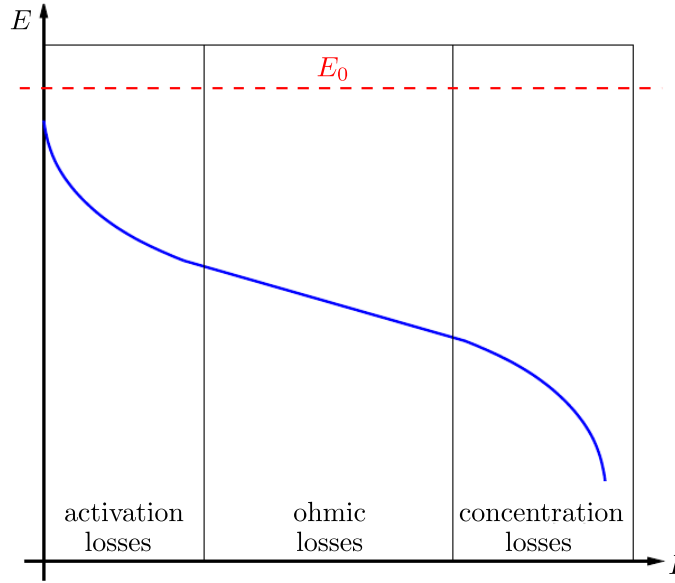


**Figure 7.2:** Schematic of voltage-current diagram for a PEM fuel cell under current load (after Ochs, 2008).

To obtain a net current density, the reaction is shifted from equilibrium to the forward reaction, meaning to the reaction of hydrogen and oxygen to water. Therefore, the cathode activation energy is reduced by introducing a catalyst and by decreasing the electrode potential by  $\eta_{\text{act}}$ . Here,  $\eta_{\text{act}}$  is called activation loss, because it corresponds to the fraction of the reversible voltage  $E_0$  sacrificed to change the activation energy. The activation losses are responsible for the initial decrease in the cell voltage shown in figure 7.2. The current gained by a reduction of  $\eta_{\text{act}}$  can be estimated by the Butler-Volmer equation:

$$i = i_0 \left( \frac{c^{O_2}}{c_0^{O_2}} \exp \left( \frac{\alpha n_e - F \eta_{\text{act}}}{\mathfrak{R}T} \right) - \frac{c^{H_2O}}{c_0^{H_2O}} \exp \left( \frac{-(1 - \alpha) n_e - F \eta_{\text{act}}}{\mathfrak{R}T} \right) \right), \quad (7.12)$$

where  $c^\kappa$  and  $c_0^\kappa$  are the concentrations of the rate-limiting species  $\kappa$  at the catalyst layer and at reference conditions, and  $\alpha$  is the charge-transfer coefficient.

Electrons and ions have to be transported from one electrode to the other. The resistance to charge transport results in a voltage loss obeying Ohm's law:

$$\eta_{\text{ohmic}} = i R_{\text{ohm}}.$$

The specific ohmic resistance  $R_{\text{ohm}}$  depends on the electronic and ionic resistance. The latter is directly dependent on the water content of the membrane. Figure 7.2 illustrates that the ohmic voltage loss causes a linear decrease in fuel-cell voltage at medium current densities. Ohmic losses can be minimized by making the electrolyte as thin as possible and by using high-conductivity materials.

The losses due to insufficient mass transport are called concentration losses. A lower reactant and a higher product concentration affects the thermodynamic reversible fuel-cell voltage  $E_0$  and shifts the reaction equilibrium towards the reverse reaction. To keep the current density stable, the activation losses increase. The negative influence of low reactant concentration on the reversible fuel cell-voltage can be estimated with the Nernst equation (7.10). The increase in the activation losses is defined by the Butler-Volmer equation (7.12). Combining the two effects, the concentration losses are given by:

$$\eta_{\text{conc}} = \frac{\mathfrak{R}T}{2n_e\text{-F}} \ln \frac{c^{\text{O}_2}}{c_0^{\text{O}_2}} + \frac{\mathfrak{R}T}{\alpha n_e\text{-F}} \ln \frac{c^{\text{O}_2}}{c_0^{\text{O}_2}}. \quad (7.13)$$

The consideration of all three losses leads to the actual cell voltage under load:

$$E(i) = E_0 - \eta_{\text{act}}(i) - \eta_{\text{ohmic}}(i) - \eta_{\text{conc}}(i). \quad (7.14)$$

Equation (7.14) in combination with the definition of the individual losses yields an expression for the local current density as a function of reversible cell voltage  $E_0$ , actual cell voltage  $E$ , ohmic resistance and reactant concentration:

$$i = \frac{1 - S_l}{R_{\text{ohm}}} \left[ E_0 - E - \frac{\mathfrak{R}T}{\alpha n_e\text{-F}} \left( \ln \frac{|i|}{|i_0|} - \ln \frac{p_g^{\text{O}_2}}{p_g^{\text{O}_2,\text{ref}}} - \left( \frac{\alpha}{2} + 1 \right) \ln \frac{p_g^{\text{O}_2}}{p_g^{\text{O}_2,\text{in}}} \right) \right], \quad (7.15)$$

where  $p_g^{\text{O}_2}$ ,  $p_g^{\text{O}_2,\text{ref}}$  and  $p_g^{\text{O}_2,\text{in}}$  is the partial pressure of oxygen at the catalyst layer, at reference conditions and at the inlet.

According to Gurau et al. (2008), the water saturation in the catalyst-layer pores as well as the water content in the ionomer significantly influence fuel-cell performance.

Hence, equation (7.15) includes the water saturation at the GDL-CL interface (Acosta et al., 2006, Ochs, 2008, Walter, 2008).

Dependent on the current density, source and sink terms for oxygen, water and energy are calculated:

- oxygen consumption:

$$q^{O_2} = \frac{i}{4F}, \quad (7.16)$$

- water production and water transport through the membrane:

$$q^{H_2O} = \frac{i}{2F} + n_{H_2O} \frac{i}{F}. \quad (7.17)$$

We assume that all water is produced in the CL pores and neglect the transfer between ionomer and pores. The water transport number  $n_{H_2O}$  includes the processes of electro-osmotic drag, convection and back-diffusion in the membrane (Wang et al., 2001). For a discussion of more elaborate membrane models be referred to Wu et al. (2009).

- heat production:

$$q_T = (E_0 - E)i. \quad (7.18)$$

Equation (7.15) and the resulting source and sink terms form the employed electro-chemistry model accounting for the effects of the hydrogen-oxygen oxidation-reduction reaction in the catalyst layer at the cathode side.

## 7.2 Coupled model for water management in fuel cells: Assumptions<sup>25</sup>

Focusing on the water management and on the interface processes between GDL and GC, the model is restricted to the cathode side of a PEM fuel cell. The developed 2D

<sup>25</sup>This section is partly published in Baber, K., Flemisch, B., and Helmig, R. (2014). Modelling drop dynamics at the interface between free and porous-medium flow using the mortar method. submitted to International Journal of Heat and Mass Transfer.

model includes a simple description of the catalyst layer (see section 7.1.4), a fully hydrophobic gas-diffusion layer and the gas channel. It does not include a micro-porous layer or the membrane. Wang et al. (2001) and Gurau and Mann (2009) state that gravitational forces are small compared to the capillary forces. Hence, the influence of gravity is neglected in the following.

In the **gas channel**, the laminar, fully developed gas flow is described by the non-isothermal multi-component model presented in section 3.3. As calculations accounting for the inertial term lead to oscillations (see section 7.3.1) and as the focus clearly is on the interface treatment, inertial forces are neglected until a more suitable spatial discretisation is available. The two-phase characteristics of the GC flow (see section 7.1.1) are not resolved in the scope of this work. Drop formation, growth and detachment are part of the interface description, but the influence of the drops on the flow field are not included. Film flow in the gas-channel corners is not considered either. Hence, the parasitic pressure loss cannot be predicted correctly.

The **gas-diffusion layer** is considered as a fully hydrophobic, rigid porous medium. The effect of compression is not considered. The flow and transport processes in the GDL are described by the non-isothermal two-phase multi-component model given in section 3.2, assuming that an REV-scale approach is applicable (Gurau and Mann, 2009). Since the MPL is not part of the model, Knudsen diffusion is not considered.

Apart from the optimization and description of the bulk properties, the interface properties, meaning the properties determining the transition between different layers, are crucial (Mathias et al., 2003). Two coupled models are developed to analyse these interface processes.

The first focuses on the influence of the electro-chemical reaction (see section 7.3.1). It considers the three components oxygen, nitrogen and water in both phases and includes the electro-chemistry model presented in section 7.1.4. The gas channel and the porous gas-diffusion layer are coupled by the simple interface concept (see section 3.4) so that drop dynamics are not included.

Gurau and Mann (2009) stress that "the local saturation inside the diffusion media changes in time, depending strongly on the location and stage of formation of the pendant and sessile droplets, which form, grow, and detach at the cathode GDL-channel

interface.” That is why the second model shows the applicability of the interface drop-concept presented in section 4.2. This two-component (water and air) model, focuses on the drop dynamics at the interface and does not include an electro-chemistry model. The results are shown in sections 7.3.2 to 7.3.5.

## 7.3 Results

In this section, the results of the simulations inspired by water-management in fuel cells are presented. All results are produced with the mathematical and numerical models presented in chapters 3 to 5 and in Baber et al. (2012). The models are adapted to the setting of PEM fuel cells based on the assumptions stated in the previous section. First, simulations neglecting the drop dynamics illustrate the effect of the electro-chemistry on the coupled system (see section 7.3.1). Then, the main simulations focus on the drop formation, growth and detachment at the GDL-GC interface including the influence of electro-chemistry only by constant source and sink terms (see sections 7.3.2 to 7.3.4). The influence of the contact angle, contact-angle hysteresis, capillary pressure, free-flow velocity and the detachment mechanism is tested with a simplified model in section 7.3.4. The applicability of the pore-velocity approach suggested in section 4.2.5 is tested in section 7.3.5.

The approaches are based on a common set of parameters listed in table 7.2. The porous gas-diffusion layer has isotropic material properties, except for the anisotropic permeability field. The effective porous-diffusion coefficient is calculated based on the heuristic approach used by Acosta et al. (2006) (see equation (7.5)). The effective thermal conductivity of the multi-phase system is determined by equation (7.6). Table 3.2 summarises further constitutive relations and fluid properties. The influence of a temperature-dependent surface tension  $\gamma_{lg}$  proved to be negligible. Hence,  $\gamma_{lg}$  is kept constant. The capillary-pressure and relative-permeability–saturation relations were measured by Acosta et al. (2006) and are shown in figures 7.3a and 7.3b. The negative sign of capillary pressure is due to the numerical implementation. As mentioned before, the GDL is assumed to be fully hydrophobic and hysteresis is neglected. Furthermore, the residual saturation is assumed to be zero improving the stability of the program. He et al. (2007) provide a formula for estimating the maximally sustained contact-angle hysteresis in dependence of the static contact angle:  $\Delta\theta^{\max} = \frac{0.2\theta^*}{1.1} \approx 25^\circ$ . We choose a

**Table 7.2:** Parameter values used in the fuel-cell simulations.

Symbol	Meaning	Value	Unit	Source
<b>Gas-diffusion layer</b>				
$\Phi$	porosity	0.8	-	Gurau, Mann (2010)
$\mathbf{K}$	intrinsic permeability			
	$K_{xx}$	$7.5 \cdot 10^{-12}$	$\text{m}^2$	Gurau, Mann (2010)
	$K_{yy}$	$3.9 \cdot 10^{-11}$	$\text{m}^2$	Gurau, Mann (2010)
$S_g^R$	residual saturation	0.0	-	
$S_l^R$	residual saturation	0.0	-	
$\theta^*$	contact angle	130	$^\circ$	Theodorakakos (2006)
$\Delta\theta^{\max}$	contact-angle hysteresis	20	$^\circ$	Cho et al. (2012a,b)
$\lambda_s$	fibre-matrix heat conductivity	15.6	W/K m	Acosta et al. (2006)
$c_s$	fibre-matrix heat capacity	710	W/kg K	Acosta et al. (2006)
$\rho_s$	density of the fibre matrix	140	$\text{kg}/\text{m}^3$	Acosta et al. (2006)
<b>Fluid properties</b>				
$\gamma_{lg}$	surface tension	0.0625	N/m	Acosta et al. (2006)
<b>Catalyst layer</b>				
$\Phi$	porosity	0.07	-	Acosta et al. (2006)

value of  $20^\circ$  to be conservative. Since the temperature dependence of the surface tension is neglected, contact-angle hysteresis is not dependent on temperature either.

Table 7.3 summarises the boundary and initial conditions. The gas-flow velocity in the gas channel lies in the middle of the range given by Theodorakakos et al. (2006) and Kandlikar et al. (2014). The humidity of the inflow gas and the initial water saturation in the porous-medium varies depending on the setup. All simulations are run on a  $15 \times 51$  grid for the  $1.5 \text{ mm} \times 5.1 \text{ mm}$  domain.

### 7.3.1 Simple interface model with electro-chemistry

Figure 7.4 illustrates the 2D setup and boundary conditions: the top region corresponds to the gas channel where a parabolic velocity profile is specified with no slip on the top and bottom boundary. A non-isothermal one-phase three-component model is used. The gas-phase consisting of oxygen, nitrogen and water vapour flows from left to right. The bottom regions correspond to the gas-diffusion layer and catalyst layer. Here, a non-isothermal two-phase three-component model is used. Neumann no-flow conditions are specified at the bottom, left and right boundaries. At the bottom, source and sink

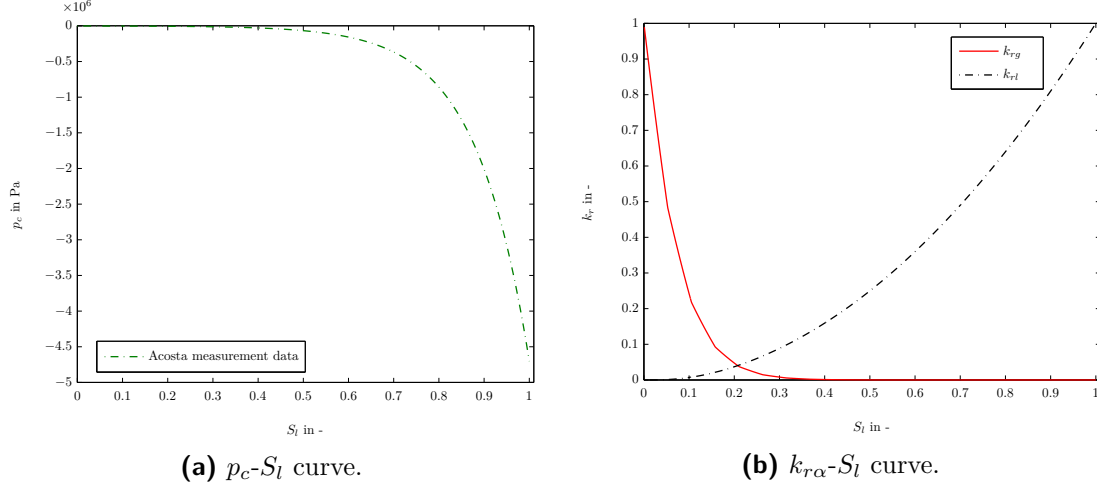


**Figure 7.3:** The capillary-pressure–saturation and the relative-permeability–saturation curve measured by Acosta et al. (2006).

**Table 7.3:** Initial and boundary conditions.

Symbol	Value	Unit
<b>Gas channel</b>		
$\mathbf{v}_g^{\text{ff}}$	$(6, 0)^T$	m/s
$p_g^{\text{ff}}$	$2.5 \cdot 10^5$	Pa
$x_g^{\text{O}_2}$	0.21	-
$X_g^w, x_g^{\text{H}_2\text{O}}$	0.075, 0.02	-
$T^{\text{ff}}$	343.15	K
<b>Gas-diffusion layer</b>		
$p_g^{\text{pm}}$	$2.5 \cdot 10^5$	Pa
$T^{\text{pm}}$	343.15	K
$S_l$	0.1-0.45	-
$x_g^{\text{O}_2}$	0.21	-

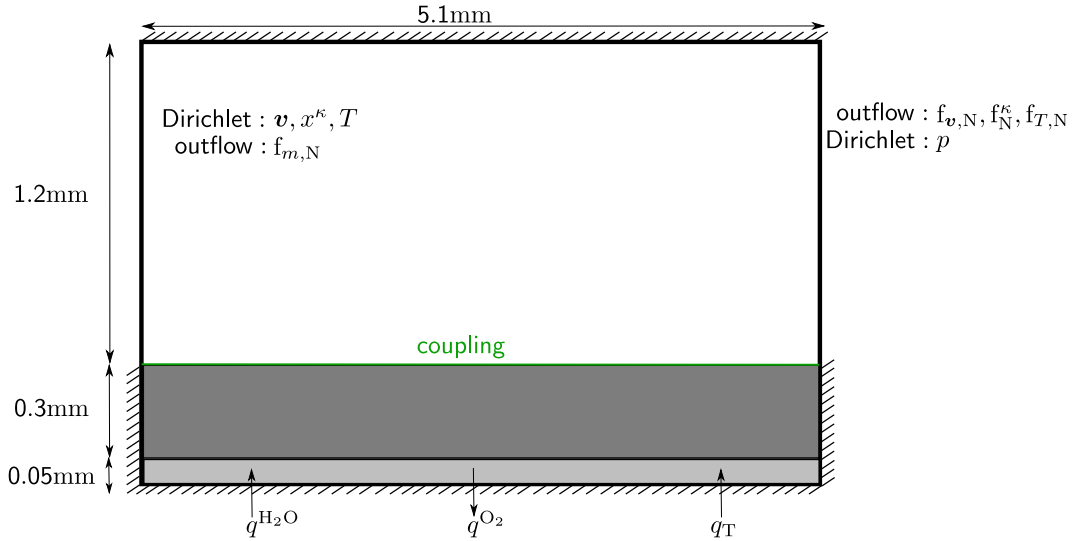


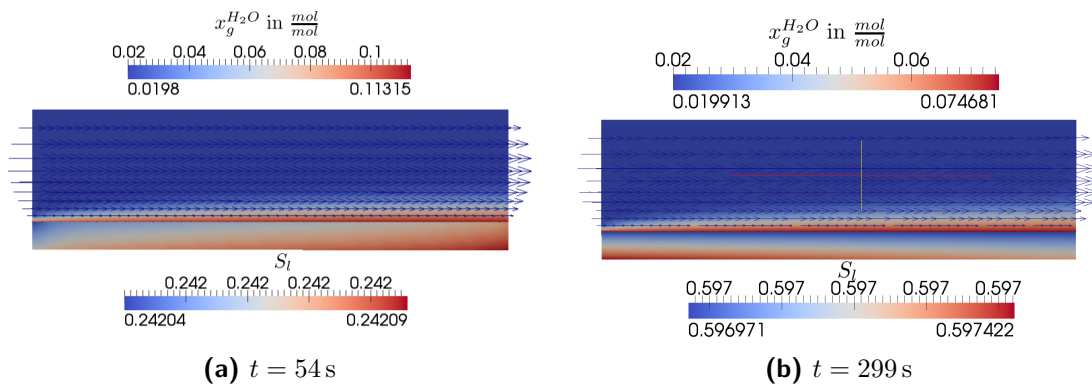
**Figure 7.4:** Numerical setup of the fuel-cell model: the top region corresponds to the gas channel where a parabolic velocity profile is specified with no slip on the top boundary. The gas phase flows from left to right. At the inlet, the mole fraction of water is set to  $0.02 \text{ mol/mol}$ . The bottom regions correspond to the gas-diffusion layer and catalyst layer. Neumann no-flow conditions are specified at all porous-medium boundaries. The water saturation is set to 0.1 initially. At the bottom, source and sink terms for water, oxygen and energy represent the catalyst layer and the current density is calculated.

terms for water, oxygen and energy represent the catalyst layer. Outflow conditions are set for the mass balance in the free-flow region and for free-flow momentum and component flux at the right boundary allowing the boundary flux to establish freely. Table 7.4 lists the parameters for the electro-chemistry model made up of equations (7.15) to (7.18). GC and GDL are coupled based on the simple interface concept from section 3.4.

Figures 7.5 to 7.8 show the distribution of water, oxygen, gas-phase pressure and temperature. Water is produced in the catalyst layer at the bottom of the domain and flows towards the interface due to capillary forces driven by a gradient of  $\nabla p_c = 1.68 \cdot 10^6 \text{ Pa/m}$ . The water pressure in the gas-diffusion layer is constant. The water evaporates at the interface increasing the mole fraction of water in the gas channel. As the production rate is larger than the evaporation rate, the water saturation in the GDL increases from initially  $S_l = 0.1$  to  $S_l = 0.6$ . Oxygen is consumed by the chemical reaction, leading to a significant decrease in the catalyst layer. In figure 7.7a, the small pressure fluctuations cannot be captured by the DuMu<sup>x</sup> output of the absolute pressure values. The pressure drop in the gas-channel is only 3 Pa. The oxygen consumption

**Table 7.4:** Parameter values of the electro-chemistry model based on Acosta et al. (2006).

Symbol	Meaning	Value	Unit
$E$	cell voltage	0.5	V
$E_0$	reversible cell voltage	1.191	V
$E_{th}$	thermo-neutral cell voltage	1.4836	V
$\Delta g_0$	free activation enthalpy	$73 \cdot 10^3$	J/mol
$i_0$	exchange current density	$1.87 \cdot 10^{-8}$	A/cm <sup>2</sup>
$T_{ref}$	reference temperature	353.15	K
$p_g^{O_2,ref}$	partial pressure of oxygen at reference conditions	$5 \cdot 10^5$	Pa
$v$	load transfer number	0.5	-
$a_{fc}$	surface increasing factor	60	-
$n_{H_2O}$	water transport number	0.2327	-
$R_{ohm}$	ohmic specific resistance	0.25	$\Omega/cm^2$
$\delta_{mem}$	thickness of the membrane	$87.5 \cdot 10^{-6}$	m
$\lambda_{mem}$	heat conductivity of the membrane	0.43	W/m K
$\delta_{shoulder}$	thickness of the shoulder	$3 \cdot 10^{-6}$	m
$\lambda_{shoulder}$	heat conductivity of the shoulder	14.7	W/m K
$n_{e-}$	number of transferred electrons	2	-

**Figure 7.5:** Distribution of the mole fraction of water in the gas phase  $x_g^{H_2O}$  in the free-flow region and of the water saturation  $S_l$  in the porous medium. The arrows indicate the free-flow velocity.

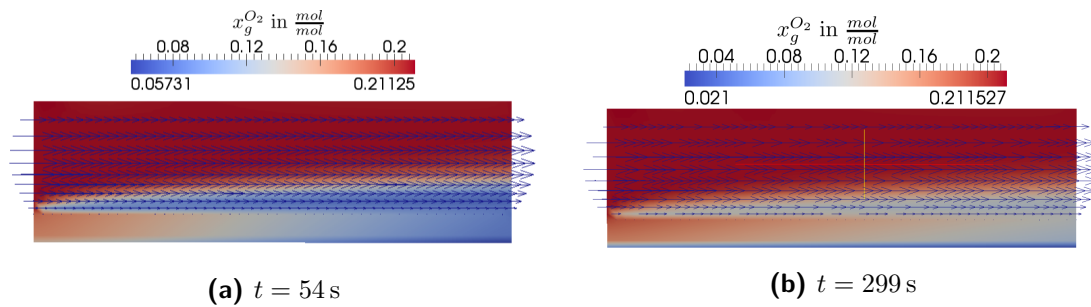


**Figure 7.6:** Distribution of the mole fraction of oxygen in the gas phase  $x_g^{O_2}$  in the free-flow region and the porous medium. The arrows indicate the free-flow velocity.

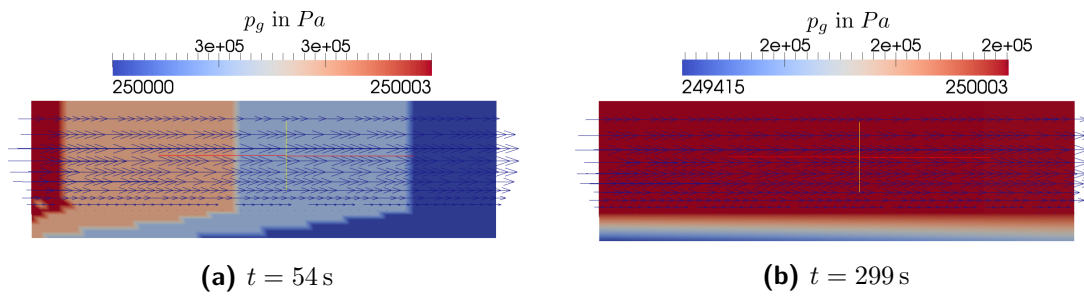


**Figure 7.7:** Distribution of the gas-phase pressure  $p_g$  in the free-flow region and the porous medium. The arrows indicate the free-flow velocity.

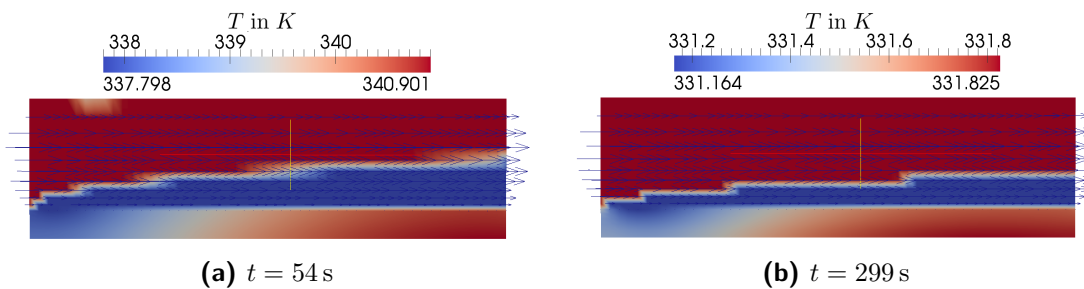


**Figure 7.8:** Distribution of the temperature  $T$  in the gas-phase in the free-flow region and the porous medium scaled to the porous medium. The arrows indicate the free-flow velocity.

causes a vertical gradient in the gas-phase pressure across the GDL at a later point in time, inducing advective flow towards the CL (see figure 7.7b and Gurau and Mann (2009)). The evaporative cooling at the interface and the heat generated by the reaction cause a horizontal temperature gradient in the GDL (see figure 7.8). The temperature drops by 12 K directly above the interface.

The simple interface concept from section 3.4 yields continuous gas-phase pressure, mole fraction and temperature as well as continuous fluxes across the interface.

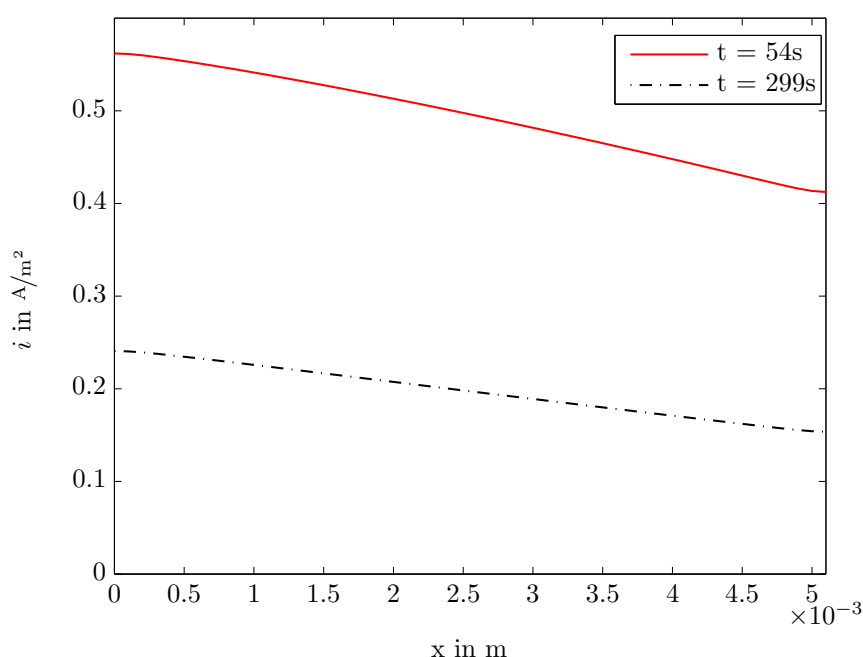


**Figure 7.9:** Current density  $i$  in the catalyst layer at the bottom of the domain.

Figure 7.9 illustrates the outcome of the electro-chemistry model. The current density decreases from left to right and over time as oxygen is consumed and water produced. The source and sink terms behave accordingly as suggested by the linear dependence on  $i$  (see equations (7.16) to (7.18)).

The Reynolds number characterising the gas-channel flow ( $Re = \frac{2.4 \text{ kg/m}^3 \cdot 1.2 \cdot 10^{-3} \text{ m} \cdot 6 \text{ m/s}}{1.9 \cdot 10^{-5} \text{ Pas}} \approx 909$ ) suggests laminar non-creeping conditions. Hence, inertial forces should be considered. Calculations with a gas-velocity of 2 m/s show spurious oscillations in the GC pressure field, which disturb the flow field significantly (see figure 7.10a). The oscillations increase with increasing velocity so that calculations with a gas velocity of 6 m/s did not converge.

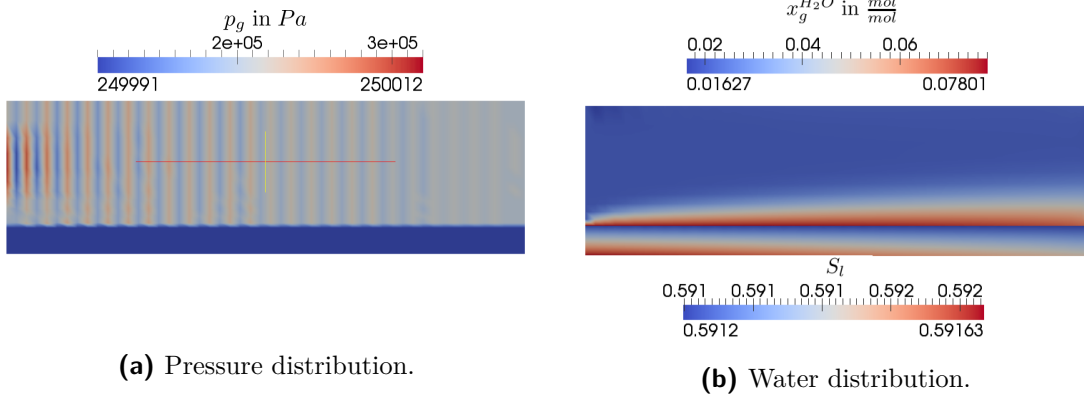


**Figure 7.10:** Pressure field and water distribution after 305 s: The inertial term in the Navier-Stokes equations causes oscillations in the pressure field in the free-flow region, which extend into the porous medium. The water distribution is not affected.

A comparison of the results with and without inertial term showed a minor influence on the conditions in the porous medium. Figure 7.10b depicts the water distribution which is very similar to the distribution shown in figure 7.5b. Based on these findings, the inertial term is neglected in the following and the Stokes equations are employed to describe the flow conditions in the gas channel.

### 7.3.2 Coupled model with drop formation: The reference case<sup>26</sup>

Figure 7.11 illustrates the setup for the drop model. It is similar to the previous setup but here a non-isothermal two-component model with the components water and air is employed. The Neumann-flux conditions at the bottom of the domain are based on the electro-chemical source and sink terms of the previous case ( $f_N^{H2O} = -7.2 \cdot 10^{-4} \text{ kg/m}^2\text{s}$ ,  $\sum_{\kappa} f_N^{\kappa} = -2.8 \cdot 10^{-3} \text{ kg/m}^2\text{s}$ ). The Neumann conditions are constant over time and an electro-chemistry model is not included. The temperature at the bottom is specified by a constant Dirichlet condition. The water saturation is set to an initial value of  $S_l = 0.45$ . The inlet mass fraction of water in the free-flow region is  $X_g^w = 0.075 \text{ kg/kg}$ .

Figures 7.12a and 7.12b show the water and temperature distribution when the drop formation is suppressed. Differences leap out when comparing these results with the previous section where an actual electro-chemistry model was used. The water saturation

<sup>26</sup>This section is partly published in Baber, K., Flemisch, B., and Helmig, R. (2014). Modelling drop dynamics at the interface between free and porous-medium flow using the mortar method. submitted to International Journal of Heat and Mass Transfer.

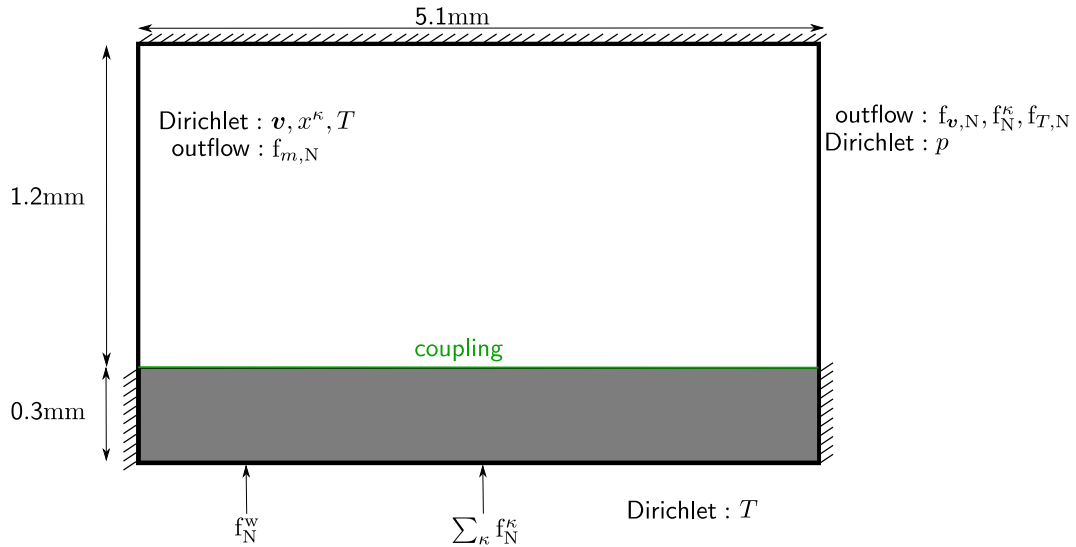


**Figure 7.11:** Numerical setup of the fuel-cell model: the top region corresponds to the gas channel where a parabolic velocity profile is specified with a no-slip condition on the top and bottom boundary. The gas phase flows from left to right. The bottom region corresponds to the gas-diffusion layer. Neumann no-flow conditions are specified at the left and right boundaries. At the bottom, Neumann fluxes for water and air represent the catalyst layer.

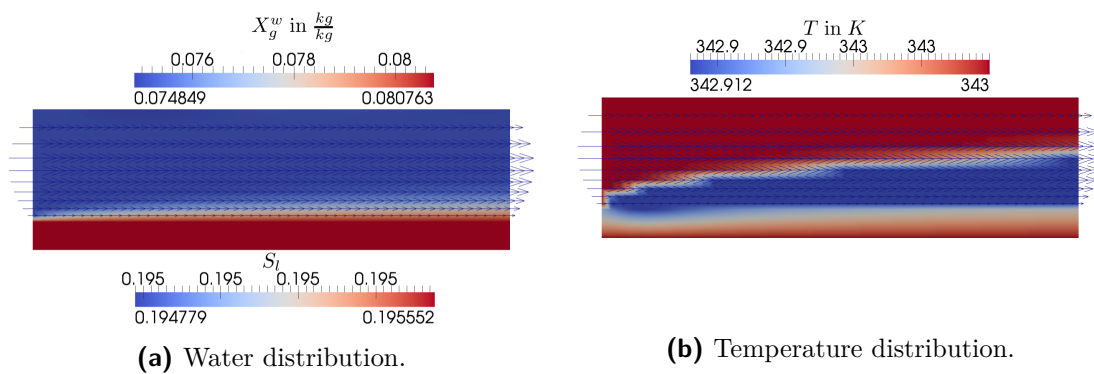


**Figure 7.12:** Water distribution and temperature field after 293s without drops. The arrows indicate the free-flow velocity.

**Table 7.5:** Pore distribution of the gas-diffusion layer after Acosta et al. (2006).

Class	Mean pore radius	Percentage
0-100 nm	$5 \cdot 10^{-8}$ m	15 %
100 nm - 1 $\mu$ m	$5 \cdot 10^{-7}$ m	30 %
1 $\mu$ m - 10 $\mu$ m	$5 \cdot 10^{-6}$ m	30 %
10 $\mu$ m - 100 $\mu$ m	$5 \cdot 10^{-5}$ m	25 %

in the GDL decreases suggesting that the evaporation rate at the interface is higher than the water supply by the Neumann condition at the bottom of the domain (compare figures 7.5b and 7.12a). Additionally, the cooling at the interface is smaller suggesting a lower evaporation rate (compare figures 7.8b and 7.12b). Probably, this is due to a lower water production rate at the bottom and a higher humidity in the inlet gas stream. As in the previous section, the interface quantities and fluxes are continuous.

Now, the influence of the drop dynamics at the interface is investigated. As a starting point, we consider the formation of one drop inside the domain choosing the area of influence equal to the area of the interface:  $\Omega_{\text{drop}} = A_{\Gamma}$ . For the drop-formation condition (see section 4.2.2), the pore-size distribution of the GDL at the interface needs to be known. Table 7.5 provides a pore-size distribution taken from Acosta et al. (2006).

Figure 7.13 (black dashed-dotted line) shows the volume of the drop over time obtained with the complete coupled model from section 4.2. A stagnation of the drop growth can be observed causing a slight increase of the water saturation compared to calculations without drops (compare figures 7.12a and 7.14a). Eventually, the full drop model causes oscillations at the interface (see figure 7.14b). The stagnation is due to the fact that the drop grows slowly losing some of its mass by evaporation. This affects the contact-area of the drop and reduces the fraction of the interface  $a_{\text{drop}}$  that allows water to flow into the drop. A steady state is reached when the water flux feeding the drop balances the evaporation from the drop surface.

Neglecting the evaporation from the drop surface by setting  $f_{\text{evap}}^{\kappa} = 0$  in equations (4.20), (4.28) and (4.29), cyclic drop formation, growth and detachment can be observed (see figure 7.13, red solid line, the simulation was stopped after 300s). The duration of one cycle is roughly 2 min. This behaviour is in good, qualitative agreement with the results of Berning et al. (2010). Theodorakakos et al. (2006) show relations between

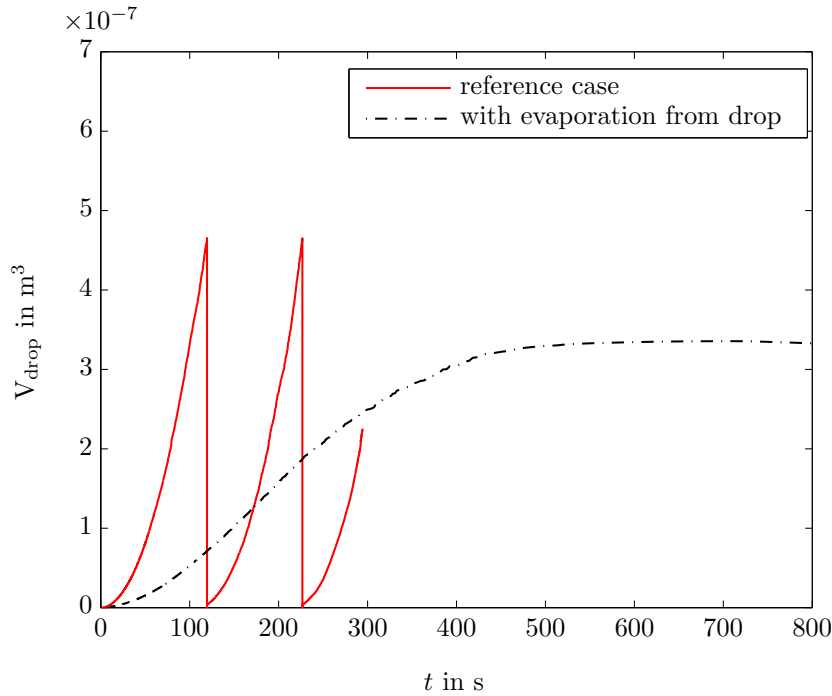


**Figure 7.13:** Drop volume  $V_{\text{drop}}$  over time showing cyclical drop formation and detachment and the influence of evaporation from the drop surface. The corresponding maximal drop height is approximately 0.7 mm.

drop diameter and gas velocities obtaining diameters of 1.25 - 1.6 mm dependent on the GDL material. The maximum diameter of the drop shown in figure 7.13 is roughly 1 mm. The depicted drop volume corresponds to a maximum interface-coverage ratio of  $a_{\text{drop}} = 0.18$ , meaning that 18 % of the interface are covered by water.

The water saturation in the GDL is smaller than without drops (compare figures 7.12a and 7.15b). The drops improve the water removal from the gas-diffusion layer. The pressure field is still similar to the results from section 7.3.1, causing gas flow from the gas-channel into the gas-diffusion layer (see figure 7.16a) and a water flux towards the interface (see figure 7.16b). As the influence of the drops on the gas-flow and pressure field in the gas channel is not part of the model, the parasitic pressure drop in the gas channel is underestimated being only 3 Pa compared to values of 1.5-11 kPa observed by Kandlikar et al. (2014).

The drop model causes discontinuities at the interface. The course of gas pressure and mass fraction are parallel but show a jump directly related to the coupling conditions (4.31) and (4.32). Figure 7.17 shows that the free-flow gas pressure lies between porous-

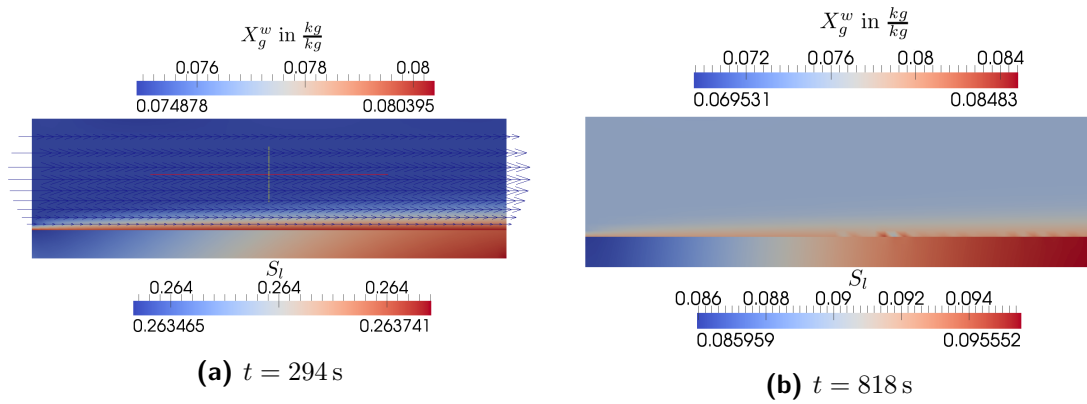


**Figure 7.14:** Distribution of the mass fraction of water in the gas phase  $X_g^w$  in the free-flow region and of the water saturation  $S_l$  in the porous medium with drop evaporation. At a later point in time, oscillations occur at the interface.

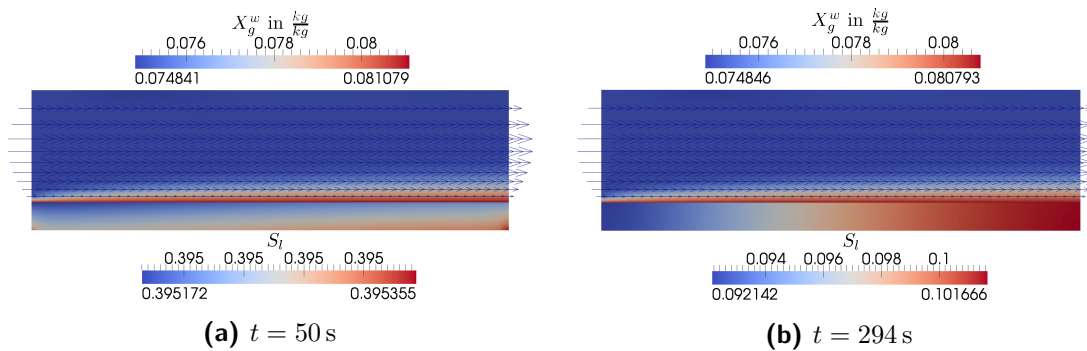


**Figure 7.15:** Distribution of the mass fraction of water in the gas phase  $X_g^w$  in the free-flow region and of the water saturation  $S_l$  in the porous medium without drop evaporation. The arrows indicate the free-flow velocity.

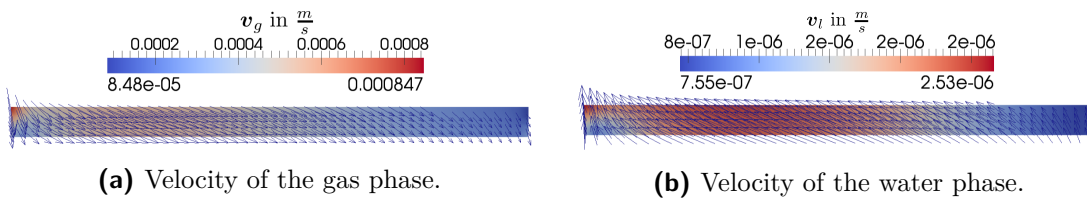


**Figure 7.16:** Velocity field of water and gas phase in the porous medium at  $t = 294$  s

medium water and gas pressure. The pressure jump at the interface is an outcome of the pressure condition discussed in section 4.3. It can be much larger dependent on the magnitude of the water saturation and the capillary pressure in the porous medium. As defined by condition (4.27), the temperature is still continuous across the interface. The discontinuity in total mass fluxes across the interface shown in figure 7.18 corresponds to the storage inside the drop and reflects its cyclic variation. The total mass fluxes are continuous when the drop is detached. Even though the evaporative flux from the drop surface into the free-flow region is zero, the flux entering the free-flow region  $\mathbf{f}_m^{\text{ff}}$  is not zero in figure 7.18. The mass flux  $\mathbf{f}_m^{\text{ff}}$  corresponds to the direct evaporation and the gas flux next to the drop across the drop-free fraction of the interface.

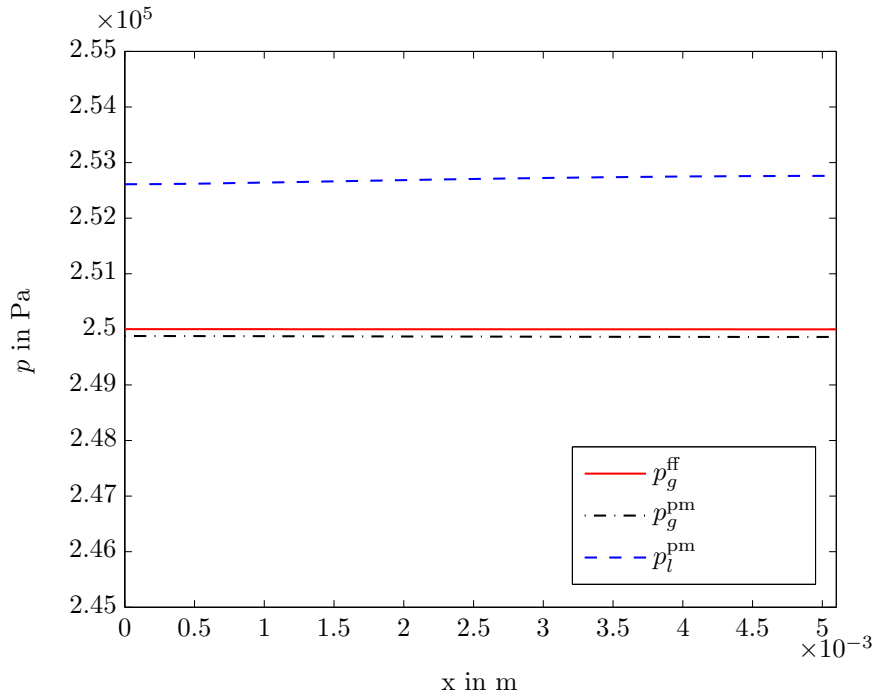


**Figure 7.17:** Pressure  $p$  at the interface at  $t = 294$  s.

### 7.3.3 Influence of the choice of $\Omega_{\text{drop}}$

As stressed in section 4.2.1 and 5.3, the area of influence for one drop  $\Omega_{\text{drop}}$  has to be chosen in advance. It determines the number of drops that form on the interface a priori and has to be chosen carefully dependent on the material properties and in accordance

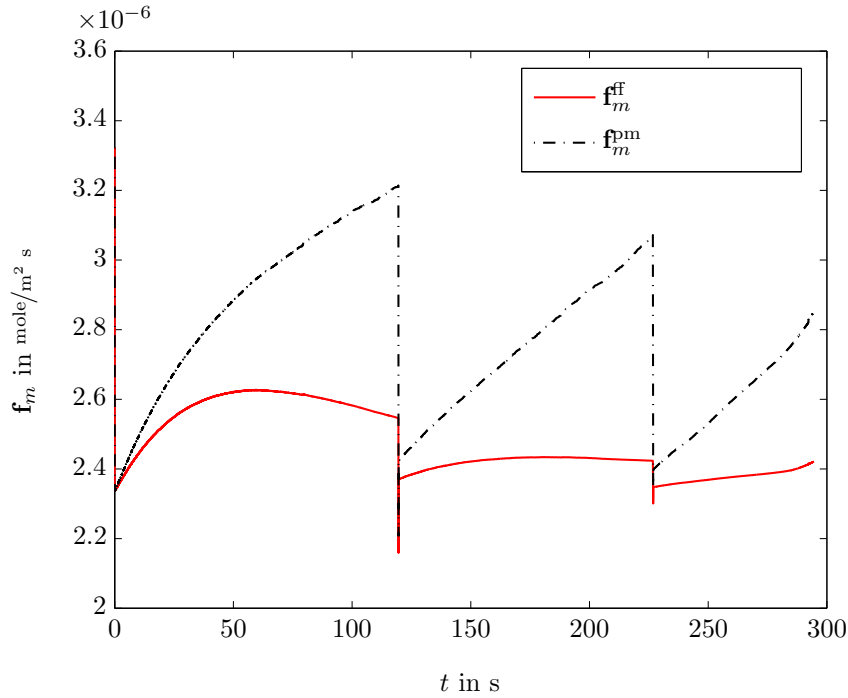


**Figure 7.18:** Total mass fluxes  $\mathbf{f}_m$  across the interface plotted over time. The fluxes from the free-flow  $\mathbf{f}_m^{\text{ff}}$  and the porous-medium  $\mathbf{f}_m^{\text{pm}}$  region are discontinuous due to the storage in the drop.

with experimental observations. Having shown results for one drop on the 5.1 mm-long interface, we show now results for two drops (see figure 7.19) and four drops (see figure 7.20).

Several drops with different growth behaviour yield different capillary pressures influencing the pressure condition (4.31). To avoid oscillations in the free-flow region which cannot deal with locally varying pressure-boundary conditions, the pressure condition (4.31) is simplified so that only the gas-phase pressures are coupled (see equation (3.11c)). The resulting drop volumes and the growth behaviour is different for each of the drops. The drops near the inlet grow faster than the drops further down stream. This is in accordance with the water-phase flow field shown in figure 7.16b, where the water flux towards the interface is much larger in the left than in the right part of the GDL domain. The growth behaviour does not appear to change significantly for more than one drop (compare figures 7.13, 7.19 and 7.20). The growth rate seems not only to be determined by the water flux in the porous medium but to be dominated by the interface conditions.

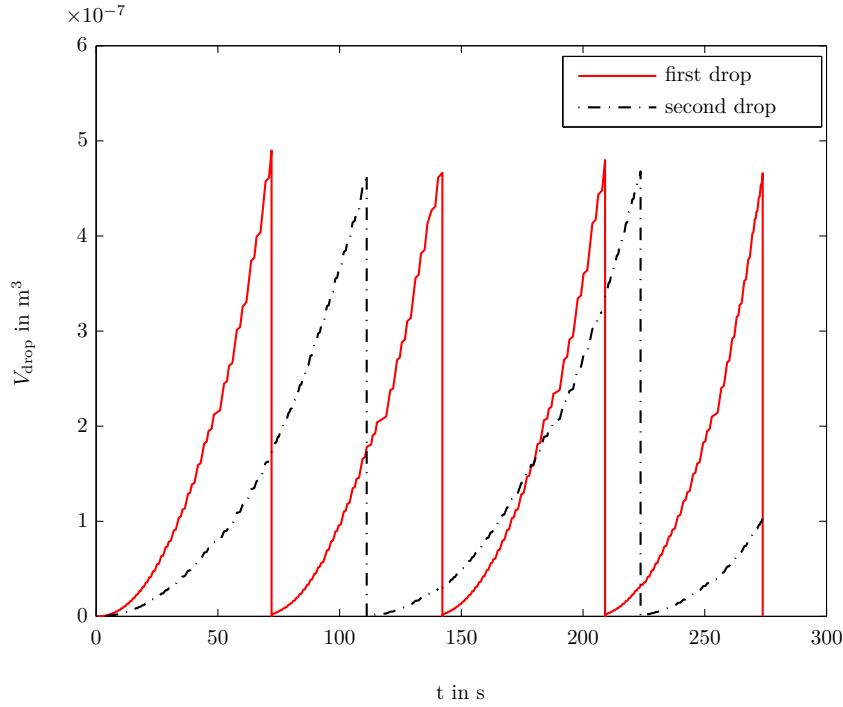


**Figure 7.19:** Drop volume  $V_{\text{drop}}$  over time showing the first and second drop for a simulation with two drops forming at the interface ( $\Omega_{\text{drop}} = 0.5A_{\Gamma}$ ).

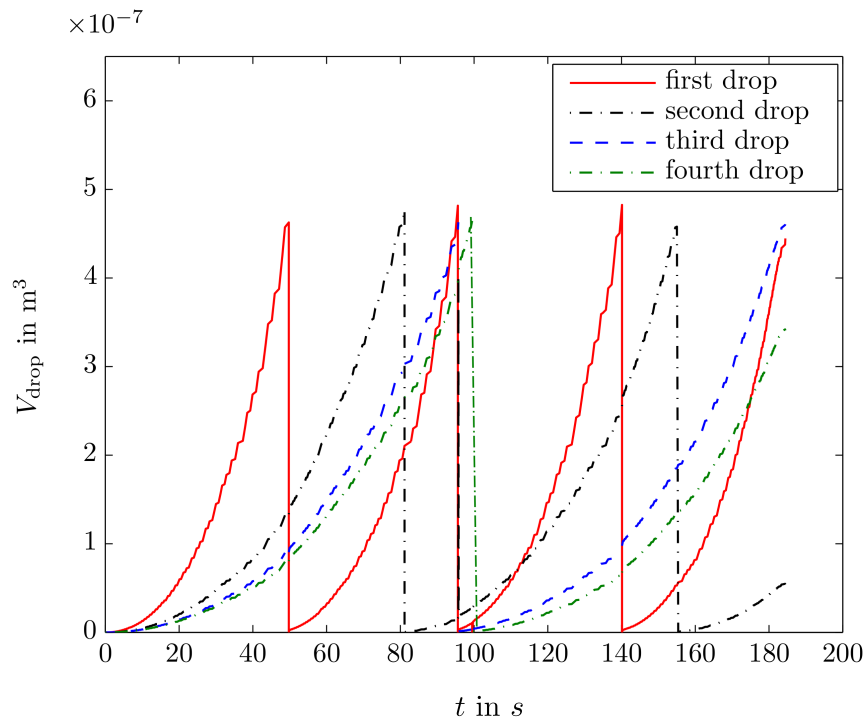
**Table 7.6:** Interface coverage ratio  $a_{\text{drop}}$ .

	one drop	two drops	four drops	Hussaini and Wang (2009)
$a_{\text{drop}}$ in %	18	32	57	20-60

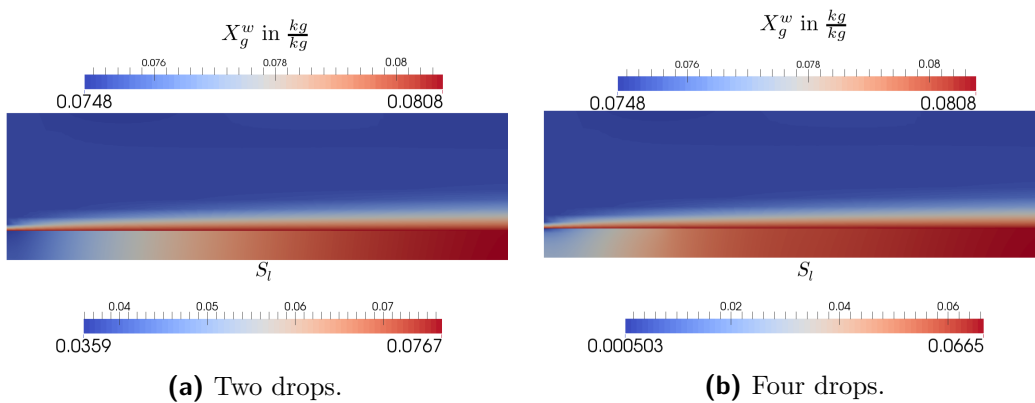
The water distribution in the GDL decreases faster and further with an increasing number of drops (see figures 7.21a and 7.21b).

Figure 7.22 shows the total mass fluxes across the interface from porous-medium (black dashed-dotted line) to the free-flow region (solid red line). As the drops do not detach at the same time and at least one drop is present at the interface at any time, the normal fluxes at the interface differ by the mass stored inside the drops. The flux across the drop-free part of the interface corresponds to  $\mathbf{f}_m^{\text{ff}}$  and is constant over time.

Kandlikar et al. (2014) stress the importance of the visualisation and quantification of the interface coverage by water. The data found in the literature varies strongly. Sergi and Kandlikar (2011) determine the area-coverage ratio experimentally and find



**Figure 7.20:** Drop volume  $V_{\text{drop}}$  over time showing for a simulation with four drops forming at the interface ( $\Omega_{\text{drop}} = 0.25A_{\Gamma}$ ).



**Figure 7.21:** Distribution of the mass fraction of water in the gas-phase  $X_g^w$  in the free-flow region and of the water saturation  $S_l$  in the porous medium for a different number of drops.

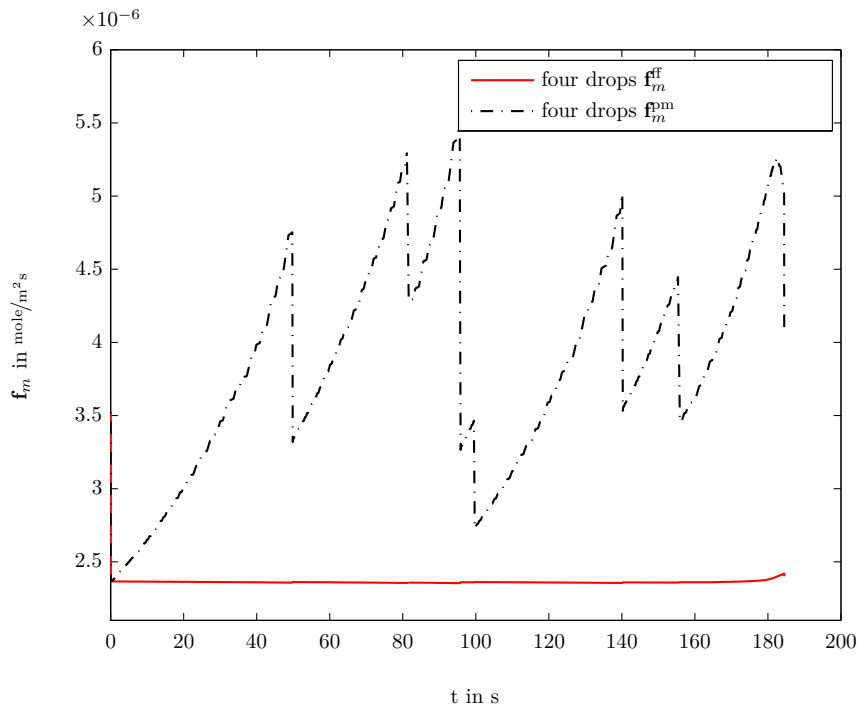


**Figure 7.22:** Total mass fluxes  $\mathbf{f}_m$  across the interface plotted over time. The fluxes from the free-flow into the porous-medium region are discontinuous due to the storage in the drop.

a low value of 4% at low stoichiometric ratios and a current density of  $i = 0.2 \text{ A/cm}^2$  at the cathode. Hussaini and Wang (2009) determine wetted-area ratios of 20-60% for current densities of  $i = 0.2 \text{ A/cm}^2$  experimentally. They observe that the wetted-area ratio depends on the stoichiometric ratio and the relative humidity of the inflow gas stream. Table 7.6 lists the values obtained with the interface-drop approach presented in this work for one, two and four drops. Naturally, the fraction of the interface covered by water increases with the number of drops. The values are in agreement with the range provided by Hussaini and Wang (2009).

### 7.3.4 Parameter study with a simplified model

To analyse the influence of the GDL and GC properties and of the detachment condition, an isothermal model with constant fluid properties is employed. Again, only one drop is considered. Figure 7.23 shows that the drops grow faster with the simplified model and that the consideration of the evaporative flux from the drop surface still leads to

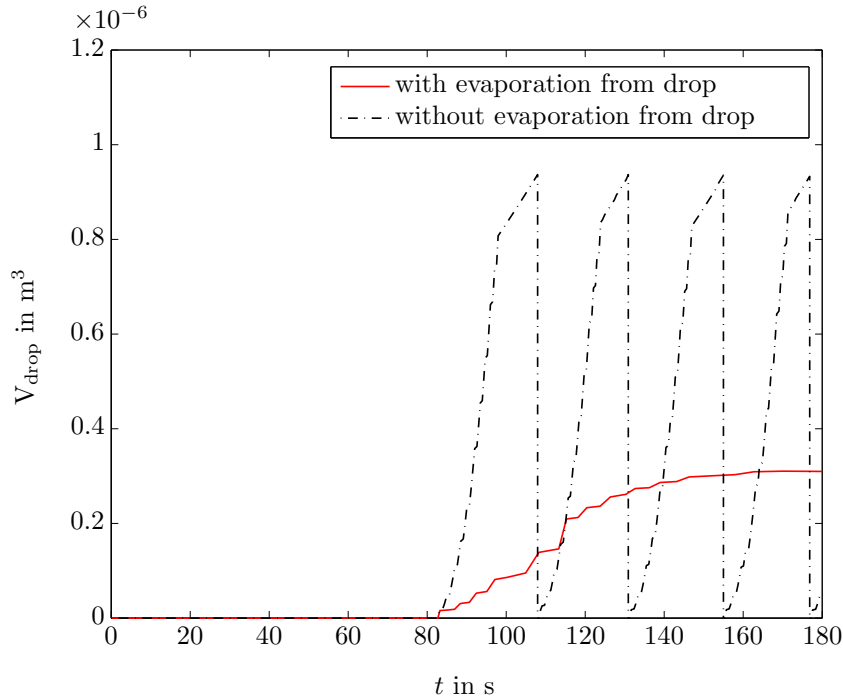


**Figure 7.23:** Drop volume  $V_{\text{drop}}$  over time showing that drops do not form until the drop-formation condition is fulfilled. Evaporation still shows a stagnation of the growth process. The corresponding maximal drop height is approximately 0.95 mm.

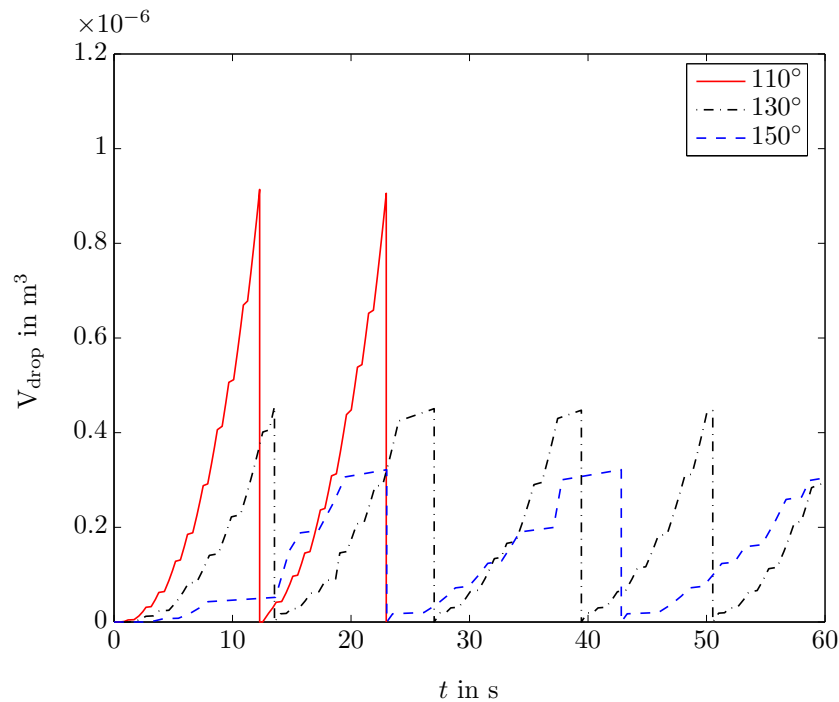
a stagnation of the growth process. The significant difference to the full drop model used in the previous section is not fully understood. The good convergence rate and the qualitatively correct results, however, qualify the model to be used for the parameter study.

Figure 7.23 also proves the applicability of the drop-formation condition. The calculations are started with a low initial water saturation of  $S_l = 0.1$  causing relatively low water pressures. As long as the drop-formation condition (4.16) is not fulfilled, the drop volume is zero and the saturation in the porous-medium increases. Once a critical saturation level of  $S_l = 0.42$  is reached, drops form, grow and detach (black dashed-dotted line in figure 7.23).

### Influence of GDL properties

In general, the variation of the GDL properties like hydrophobicity or  $p_c$ - $S_l$  relation yields the expected results.

Increasing the contact angle means increasing the hydrophobicity of the GDL. Figure 7.24 shows that drops detach at smaller volumes for larger contact angles. A large contact angle means a smaller contact area for a given volume. This yields a smaller retention force. At the same time, the drop growth is slowed down significantly due to the decreased area available for the water flux feeding the drop.



**Figure 7.24:** Drop volume  $V_{\text{drop}}$  over time showing the influence of a variation in contact angle.

A higher maximal value for the contact-angle hysteresis means that the drop can deform further. Naturally, this means a later detachment point (see figure 7.25). Extrand and Gent (1990) analyse the retention of drops on solid surfaces and conclude that drops are better retained the larger the supported contact-angle hysteresis.

Different capillary-pressure–saturation relations can be found in the literature. Figure 7.26 shows the Van-Genuchten parametrisation with parameters given by Gostick et al. (2006). Moreover, the relation measured by Acosta et al. (2006) (see figure 7.3a) and linear relations are tested. The effects of a variation of the  $p_c$ - $S_l$  curve turn out to be negligible as can be seen in figure 7.27. This supports the conclusion drawn above, that the drop dynamics are mainly governed by the interface conditions.

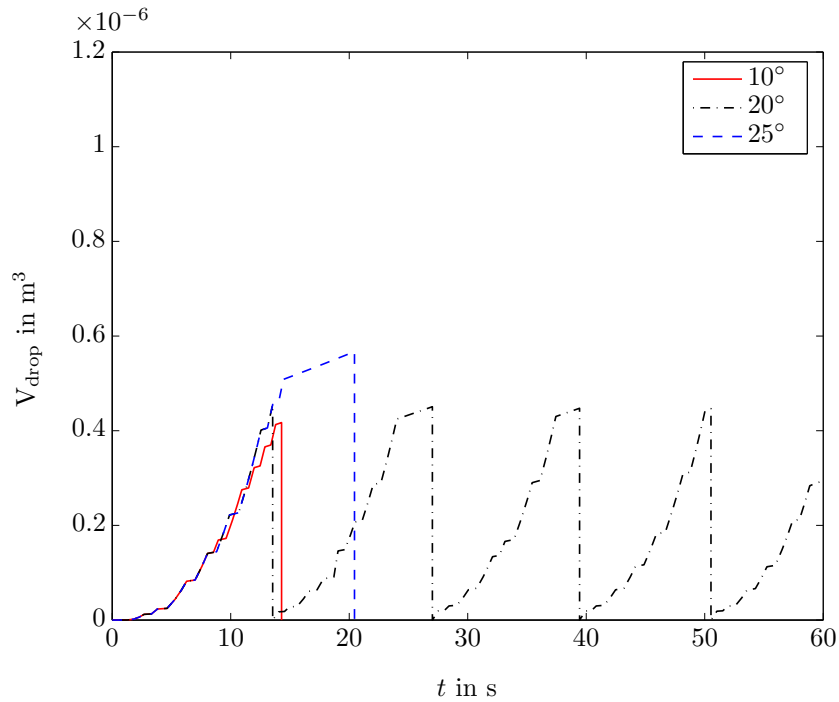


**Figure 7.25:** Drop volume  $V_{\text{drop}}$  over time showing the influence of the maximally sustained contact-angle hysteresis.

### Influence of GC conditions

As expected, higher gas velocities in the gas channel cause faster detachment (see figure 7.28).

Since the gas velocity influences the pressure condition and the condition for the normal fluxes, it also affects the growth rate slightly. Large velocities yield a faster growth.

### Analysis of drop detachment

As explained in sections 2.4 and 4.2.6, the drag force exerted by the GC flow field can be calculated in different ways. Figure 7.29 compares the calculation of a force balance considering shear and pressure forces (Chen et al., 2005) with two expressions for the drag coefficient:  $c_w = \frac{30}{\sqrt{Re}}$  and equation (2.10). The complex empirical expression for the drag coefficient given by Cho et al. (2012b) (equation (2.10)) and the force-balance approach predict the same drop volume when detachment happens. The slowed growth

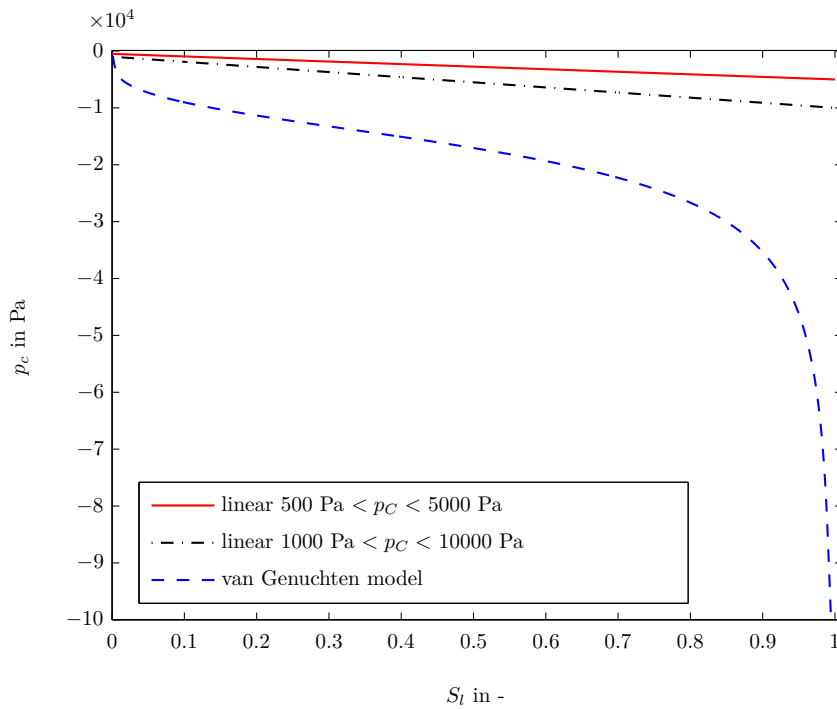


**Figure 7.26:** The different capillary-pressure-saturation curves.

of the red line in figure 7.29 at larger volumes just before the detachment point cannot be explained.

The retention force is estimated based on equation (5.27) in all three cases. As the 2D retention force does not depend on the drop size or the drop-wall interactions, it overestimates the possible drop volume.

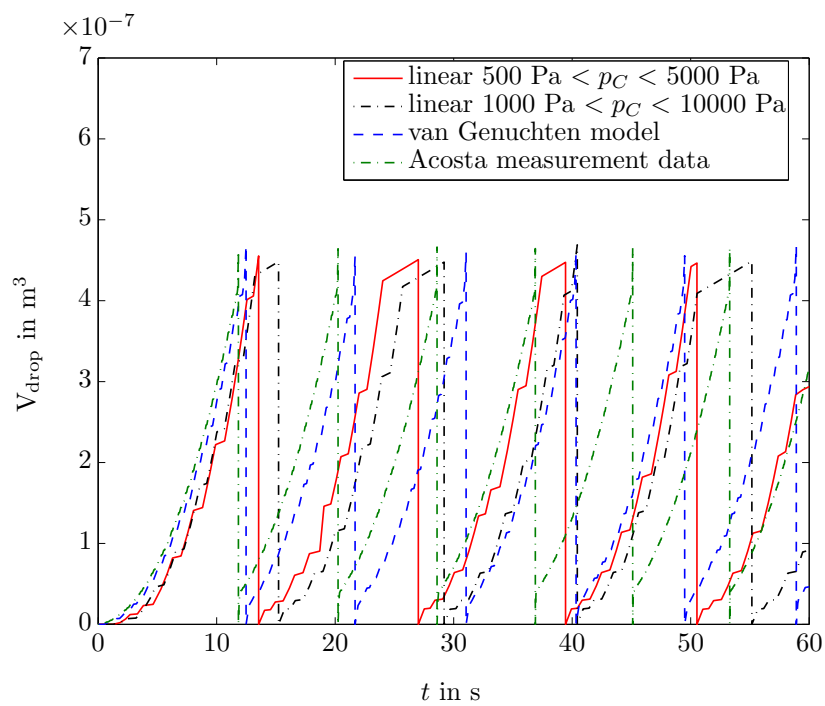


**Figure 7.27:** Drop volume  $V_{\text{drop}}$  over time showing the influence of the variation of the capillary-pressure-saturation curve.

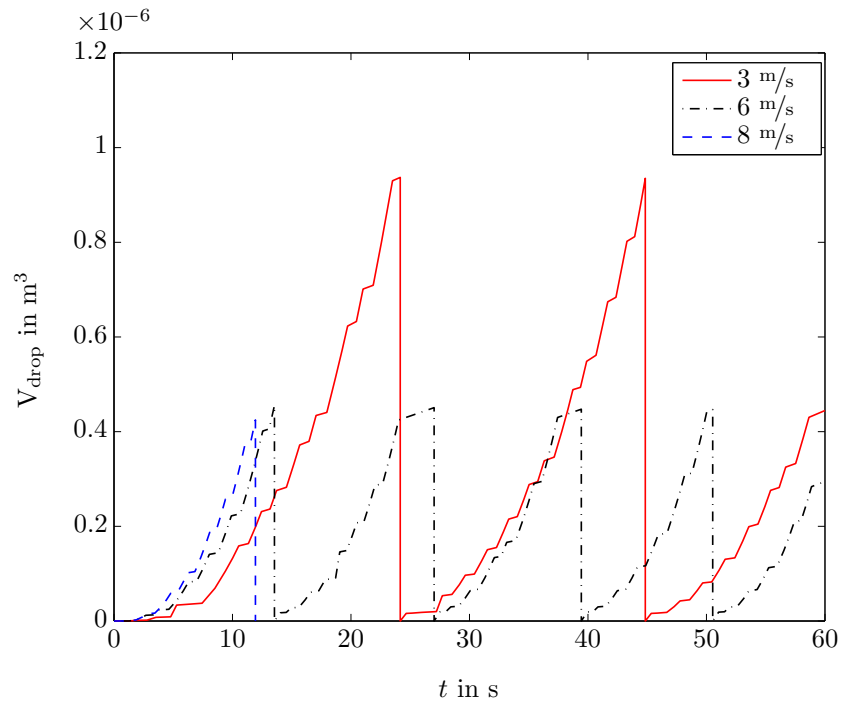


**Figure 7.28:** Drop volume  $V_{\text{drop}}$  over time showing the influence of the variation of the maximal free-flow velocity.

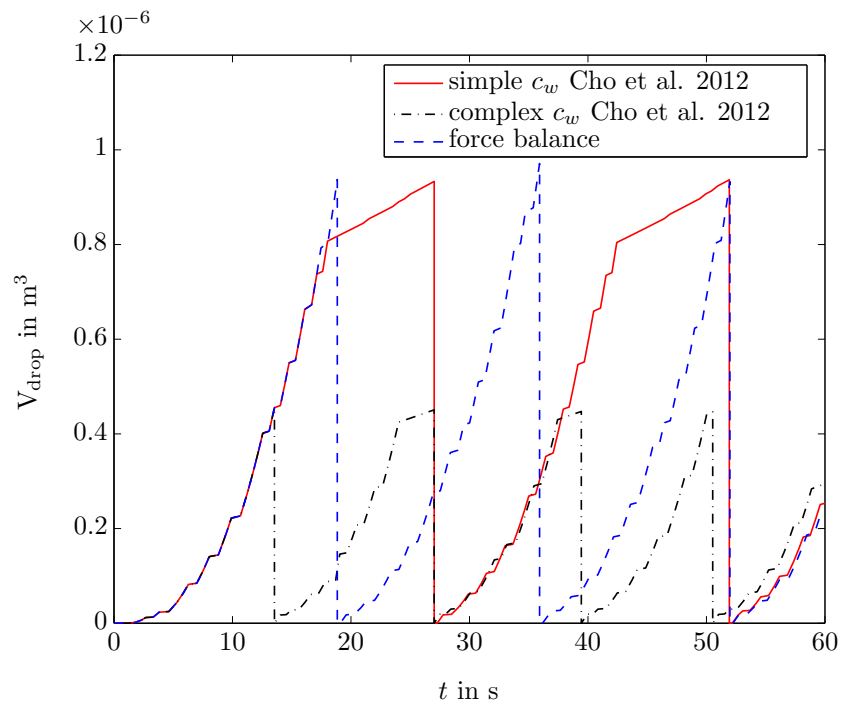


**Figure 7.29:** Drop volume  $V_{\text{drop}}$  over time showing the influence of the drag-force calculation.

### 7.3.5 Pore-velocity approach

An alternative approach for the calculation of the flux feeding the drop was presented in section 4.2.5. It is based on a pore-scale calculation of the velocity at the interface which depends on the pressure in the porous-medium and inside the drop (see section 4.3 for a detailed explanation). Its implementation was laid out in chapter 5.

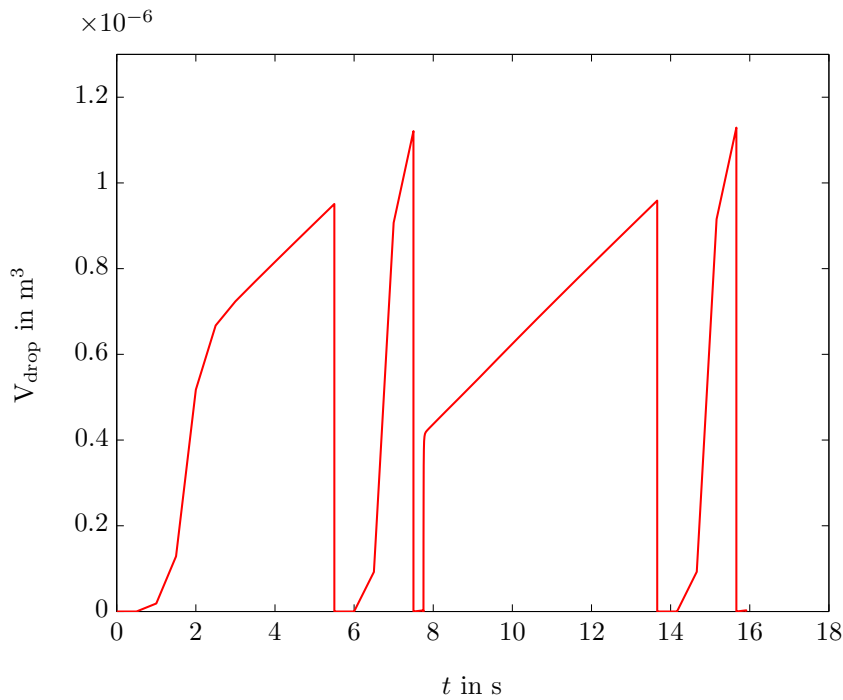


**Figure 7.30:** Drop volume  $V_{\text{drop}}$  over time calculated with the pore-velocity approach.

As presumed in section 4.3, it is hard to find a stable setup since microscopic and macroscopic capillary pressure are of different order of magnitude, causing enormous pore velocities. The phase pressure, the capillary pressure and the saturation determine the flux feeding the drop. The example shown in figure 7.30 is based on a linear capillary-pressure–saturation relation with a maximal value of  $p_c = 10000$  Pa. It shows a growth rate which is about ten times as large as in the previous sections. Eventually, the model breaks because the interface fluxes become too large.

In conclusion, the pore-velocity yields a continuous gas pressure at the interface. However, the combination of microscopic and macroscopic pressure causes high fluxes, making this approach infeasible up to now.

## 7.4 Discussion<sup>27</sup>

The results presented in the previous sections prove the applicability of the interface drop model. They show that it is possible to include drop dynamics in the REV-scale coupling conditions between free and porous-medium flow. Drop formation, growth and detachment are represented correctly, if the evaporation from the drop surface is neglected. Once the drop model is coupled to the electro-chemistry model shown in section 7.3.1, it will be able to predict the mutual dependence of the drop dynamics, the conditions in the GDL and the electro-chemical reaction. The simulations for a higher number of drops suggest that the interface conditions dominate the system. The parameter study with a simplified setup showed that the model behaves according to our expectations. Unfortunately, the promising approach based on the pore-scale velocity is not stable and overestimates the drop-growth rate.

Despite the promising results, the model is not predictive and cannot produce quantitative results which could be used to improve real fuel cells. According to Theodorakakos et al. (2006) and Kandlikar et al. (2014) two main effects limit the exchange processes at the interface between gas channel and gas-diffusion layer:

1. coverage of the interface by drops, slugs and films,
2. blockage of the gas channel and disruption of the fully developed flow field affecting heat and mass transfer.

The presented model captures the first point, but not the second. The free-flow model must be improved such that the influence of the drops on the flow conditions, the fate of the detached drops and film flow in the hydrophilic channel corners are included. Pressure loss is of practical interest and should be an outcome of the model. A first step in this direction is the improvement of the discretisation scheme to obtain a stable implementation of the laminar Navier-Stokes equation. Furthermore, an extension to 3D is required to represent the flow field in the GC, the water distribution in the GDL and the retention force correctly. The description of the GDL would become more realistic if mixed wettability was taken into account.

---

<sup>27</sup>This section is partly published in Baber, K., Flemisch, B., and Helmig, R. (2014). Modelling drop dynamics at the interface between free and porous-medium flow using the mortar method. submitted to International Journal of Heat and Mass Transfer

Possibly, the simple drop condition used by Qin et al. (2012b) could be substituted by the drop distribution predicted in this work to describe the water transport and pressure loss in the GC more accurately. Furthermore, the porous components of the fuel cell, the catalyst, micro-porous and gas-diffusion layers, could be described by the 2D-continuum approach presented by Qin and Hassanizadeh (2014). The coupling to the free-flow region would have to be derived based on the assumptions and concepts presented in this work.

Concluding, this chapter demonstrates the applicability of the new interface concept which accounts for drop dynamics at the interface and highlights the required aspects of future research.

# 8 Final remarks

## 8.1 Summary and conclusions

The objective of this work is the development of model concepts and methods for the coupling of free flow and flow in porous media. Coupling concepts of varying complexity ranging from a simple to a pore-scale to a complex interface approach are derived and presented in chapters 3 and 4 (left column in figure 8.1). The main focus is on the development and testing of a coupling concept that accounts for drop dynamics at the interface. The developed concepts are based on the assumption of thermodynamic equilibrium and on flux balances. Processes like turbulent free flow, boundary layer effects, radiation and pore-scale features, like the pore water content at the interface, are not considered in the scope of this work (see Mosthaf et al. (2014)). The applicability and the limitations of these concepts are assessed on the basis of two applications: transvascular exchange and drop dynamics in Polymer-Electrolyte Membrane (PEM) fuel cells (center column in figure 8.1). The model is implemented in the C++ simulator DuMu<sup>x</sup> (Flemisch et al., 2011), using the mortar method.

**The simple interface concept** In Mosthaf et al. (2011) and Baber et al. (2012), we develop a concept for coupling non-isothermal compositional two-phase flow in the porous-medium with a non-isothermal compositional single-phase system in the free-flow region. The concept is based on the two-domain approach with a simple interface devoid of thermodynamic properties. This is explained in section 3.4.

In this work, the simple interface concept is applied to model transvascular exchange (see chapter 6). Therapeutic agents distribute in the circulatory system of the body and are delivered to the organ level. In the smallest blood vessels, the therapeutic substances cross the blood-vessel walls and enter the surrounding interstitial space. The current

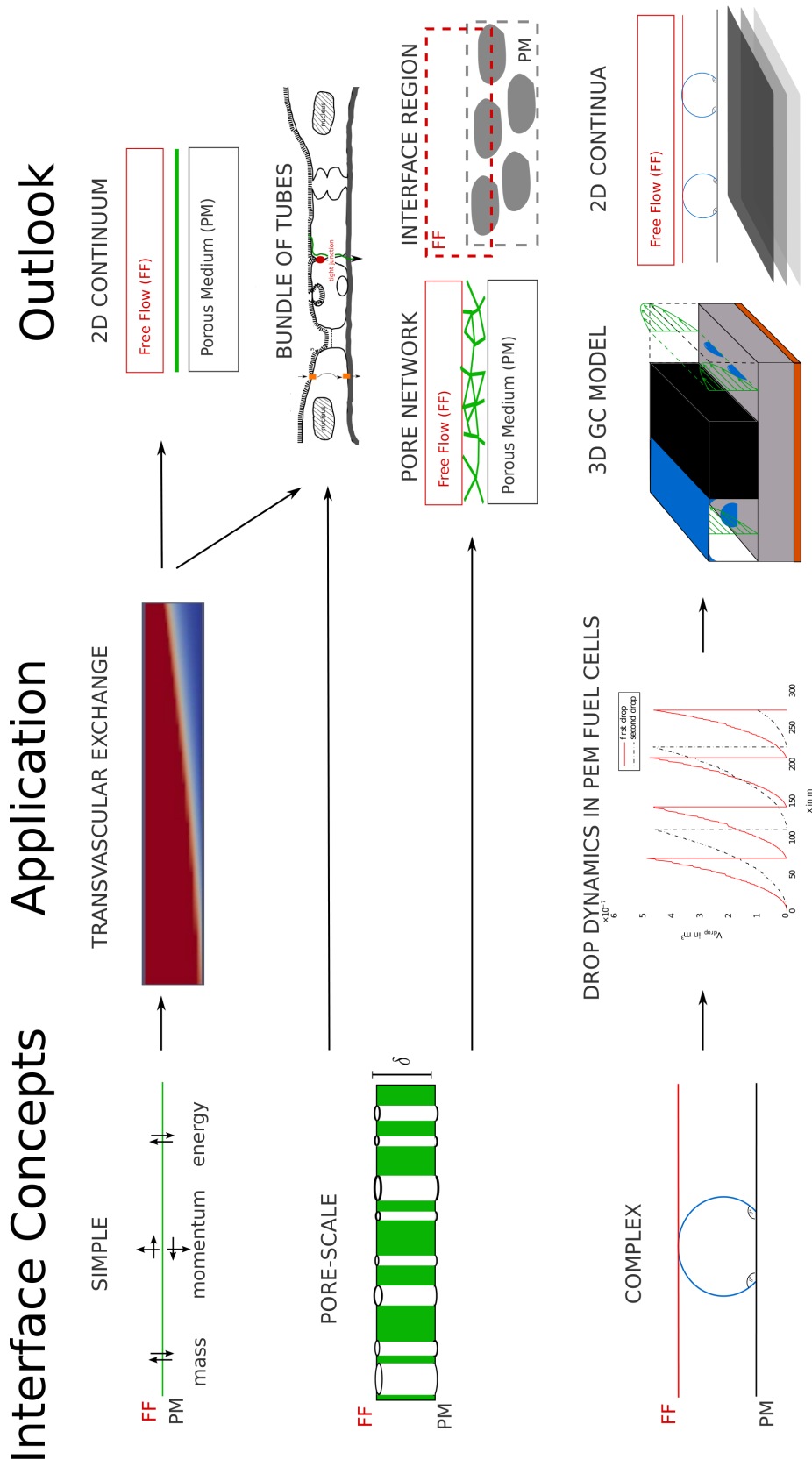


**Figure 8.1:** Graphical abstract: the left column illustrates the coupling concepts developed in this work, the centre column shows the example applications and the right column illustrates possibilities for further research.

---

project focuses on the description of the exchange and regulation processes between vascular and tissue space, trying to provide a better understanding of one of the limiting processes in the distribution of therapeutic agents. As a first step, the micro-vascular wall is described as a thin porous layer with effective properties, using a continuum approach. The simple interface coupling concept is used to couple the free flow in the blood vessels to the porous vessel wall and the surrounding tissue.

The presented model reproduces the basic processes of transvascular exchange. It simulates filtration and reabsorption and reveals the influence of wall and tissue parameters on the final distribution of therapeutic agents. Nevertheless, it is only a first step towards modelling transvascular exchange across the micro-vascular wall. The employed concepts are of limited applicability since information about the physiological processes and parameters is scarce.

The limitations of the model are caused by the description of the micro-vascular wall. Its complex structure and the influence of the different pathways cannot be resolved by the presented approach. Moreover, the applicability of a continuum approach is questionable in case of the thin micro-vascular wall. Alternatively, the vessel wall could be described by two opposing approaches: either as a pore-scale tube model (see section 4.1 and figure 8.1) or as an averaged two-dimensional (2D)-continuum (see section 2.2 and figure 8.1).

**The bundle-of-tubes concept** In some applications, the complex structure of the interface and the processes happening therein cannot be described by a simple interface devoid of thermodynamic properties. Complex interface layers might separate the free-flow and porous-medium region and dominate the exchange processes. In the case of transvascular flow (section 6), for example, the micro-vascular wall is a thin heterogeneous structure determining the exchange between vascular and tissue compartment. In other examples, the processes in the interface region, which are influenced by both the free-flow and the porous-medium domain (right column in figure 8.1), cannot be resolved by the Representative-Elementary Volume (REV)-scale approaches. Salt deposition, for example, occurs only in a very thin layer directly at the interface between the soil and the ambient air.

In such cases, it might be beneficial to resolve the interface layer or interface region on the pore-scale. A first step towards a resulting coupled pore-/REV-scale model is

presented in section 4.1. The interface is described by a bundle-of-tubes approach. The coupling concept between the one-phase free-flow, the pore-scale and the two-phase porous-medium model is based on flux continuity and the assumption that pore- and REV-scale pressure are equal.

**The complex interface concept**<sup>28</sup> We develop an interface concept at the REV-scale which describes drop formation, growth and detachment on a hydrophobic interface between free and porous-medium flow (see section 4.2). The interface stores the mass and energy of the drops without resolving them. The direct exchange between free-flow and porous-medium region next to the drop is also part of the coupling concept since it preserves the exchange processes described by the simple interface concept. The fraction of the interface which is covered by drops is used to obtain an area-weighted average of the coupling conditions with and without drop so that coupling conditions for the whole interface are obtained.

The temporal evolution of the drop volume is an outcome of the model. The number of drops that can form on the interface is defined a priori by choosing the size of the drop REV. This should be done in accordance with experimental observations.

The complex interface concept captures drop formation, growth and detachment. These processes are influenced by the conditions of both the free-flow and porous-medium region. Neither the influence of the drops on the free-flow conditions nor film flow or merging of drops is included. A detached drop can either slide on the porous-medium surface, lift and float, or wick into the film flow in the corners of the free-flow channel. Such processes are crucial for the prediction of flooding but are not yet resolved by the current model since the focus is on the interface description.

The model is applied to simulate drop formation in the cathode of PEM fuel cells (see chapter 7). In fuel cells, water is generated by the electro-chemical reaction in the catalyst layer and flows through the hydrophobic porous fibre structure of the Gas-Diffusion Layer (GDL). Reaching the Gas Channel (GC), water forms drops on the hydrophobic interface between GC and GDL. The drops significantly influence the

---

<sup>28</sup>Parts of this paragraph are published in Baber, K., Flemisch, B., and Helmig, R. (2014). Modelling drop dynamics at the interface between free and porous-medium flow using the mortar method. submitted to International Journal of Heat and Mass Transfer

---

water management in fuel cells which must be optimised to achieve good performance and durability.

The results show that it is possible to include drop dynamics in the REV-scale coupling conditions between free and porous-medium flow. Drop formation, growth and detachment are represented correctly, if the evaporation from the drop surface is neglected. The interface-coverage ratio, which is an indicator for the quality of the water management, can be predicted. The simulations for a higher number of drops suggest that the interface conditions dominate the system. A parameter study shows that interface wettability and free-flow velocity have a significant influence on the drop growth and detachment.

The formulation of mechanical equilibrium in the pore-scale and complex interface concept is challenging due to the scale-dependent definition of pressure (see section 4.3). Since microscopic and macroscopic pressure formulations are combined, the interface might dominate the system, causing pressure jumps at the interface and non-physical pressure gradients. This can be deduced from the numerical results which show a jump in the gas-phase pressure across the interface. This can cause significant pressure gradients in the porous medium in dependence on the chosen boundary conditions.

The pore-velocity approach, which is presented as an alternative for the estimation of the water flux feeding the drop (see section 4.2.5), avoids the area-weighted average of the pressure condition and yields a continuous gas pressure at the interface. However, the combination of microscopic and macroscopic pressure yields high fluxes, causing instabilities and making this approach infeasible up to now.

These problems could be solved by a sound correlation between pore and average phase pressure or by a definition of a macroscopic capillary pressure at the interface which should depend on the drop size, drop number, saturation and interface material properties like the contact angle. The correct definition of average pressure is still a research challenge and is beyond the scope of this work.

In summary, this work reveals the potential of the developed coupling concepts to deal with realistic problems and exposes the need for further improvement and development.

## 8.2 Outlook

The two applications considered in this work motivate further research and an extension of the coupling concepts. Some ideas for future work are illustrated in the right column of figure 8.1.

**Transvascular exchange** It was mentioned above that the description of the microvascular wall should be improved. In a pore-scale interface model, the paracellular pathways could be represented by non-intersecting, circular pores yielding a bundle-of-tubes description (see figure 8.1). To obtain a realistic representation, different properties could be assigned to the pores by varying e.g. diameter and permeability. Tight-junction strands and diaphragms obstructing some of the pathways could be included as additional resistance. The tube model could be extended to account for the fibre matrix of the glycocalyx and its electro-chemical properties by combining a fibre-matrix model (Sugihara-Seki and Fu, 2005, Fu et al., 2005) with macro-molecular transport influenced by an electric field (Stace and Damiano, 2001).

Alternatively, a description of the capillary wall as 2D continuum should be envisaged. The challenge is the formulation of the exchange terms and coupling conditions between 2D continuum and free flow. Qin and Hassanizadeh (2014) presented only a coupling of 2D continua representing porous media. As the interfaces still match, and as the 2D continuum provides normal fluxes and the distribution of the primary variables in the lateral extent of the interface, the coupling should be possible.

Besides, modelling the whole capillary bed or at least several capillary blood vessels would increase the reliability of the predicted concentrations.

**Pore-scale interface description** The presented concept covers one- and two-phase flow but needs to be extended to component and energy transport. As mentioned above, the properties of the bundle-of-tubes model can be extended to mimic the paracellular pathways of the capillary wall. Possibly, a 2D-continuum description can then be derived by homogenisation.

The general concept can be transferred to couple a full pore-network model to the free and porous-medium REV-scale models (right column in figure 8.1).

Concluding, a pore-scale interface description is well suited for interface layers and can enhance the understanding of the occurring processes. However, the efficiency of the coupled model can be limited by the high computational costs of the pore-scale interface model. An intelligent numerical implementation, including e.g. a multi-time-step technique, needs to be found.

A pore-scale description of the interface region which is influenced by both the free and the porous-medium domain (right column in figure 8.1) requires more sophisticated pore-scale models. It is likely that a model just of the interface region would be sufficient to deepen the understanding of the exchange processes and a coupling to the surrounding REV-scale models is not required.

**Drop dynamics in fuel cells<sup>29</sup>** The presented model captures the coverage of the interface by drops which limit the exchange processes at the interface between gas channel and gas-diffusion layer, but it cannot predict the blockage of the gas channel and disruption of the flow field.

The free-flow model must be improved such that the influence of the drops on the flow conditions, the fate of the detached drops and film flow in the hydrophilic channel corners are included. Pressure loss is of practical interest and should be an outcome of the model. A first step in this direction is the improvement of the discretisation scheme to obtain a stable implementation of the laminar Navier-Stokes equation. Furthermore, an extension to three dimensions (3D) is required to represent the flow field in the GC, the water distribution in the GDL and the retention force correctly.

To describe the pressure loss in the GC more accurately, the obtained drop distribution could be fed to the one-dimensional phenomenological model for liquid water flooding in the cathode GC presented by Qin et al. (2012b). A direct coupling with this lower-dimensional model would require a completely different coupling concept.

The thin porous GDL is described as a fully hydrophobic porous-medium assuming that an REV can be found. The description of the GDL would become more realistic, if mixed wettability was taken into account. Moreover, the porous layers of the fuel cell could be described by a stack of 2D continua as suggested by Qin and Hassanizadeh (2014) (see

---

<sup>29</sup>Parts of this paragraph are published in Baber, K., Flemisch, B., and Helmig, R. (2014). Modelling drop dynamics at the interface between free and porous-medium flow using the mortar method. submitted to International Journal of Heat and Mass Transfer

right column in figure 8.1). Whether the complex interface concept can be transferred to couple 2D continua to the free-flow gas channel requires further investigation.

In the short term, the drop model should be coupled to the electro-chemistry model to assess the mutual dependence of the chemical reaction and the water distribution in the cell. Furthermore, evaporation from the drop surface has to be reconsidered.

# Bibliography

- Ackermann, S. (2013). Modeling transvascular flow - Analysing the influence of adsorption, degradation and lymph flow. Master's thesis, Dep. of Hydromechanics and Modeling of Hydrosystems, IWS, University of Stuttgart.
- Acosta, M., Merten, C., Eigenberger, G., Class, H., Helmig, R., Thoben, B., and Müller-Steinhagen, H. (2006). Modeling non-isothermal two-phase multicomponent flow in the cathode of PEM fuel cells. Journal of Power Sources, 159:1123–1141.
- Alazmi, B. and Vafai, K. (2001). Analysis of fluid flow and heat transfer interfacial conditions between a porous medium and a fluid layer. International Journal of Heat and Mass Transfer, 44:1735–1749.
- Arbogast, T. and Brunson, D. S. (2007). A computational method for approximating a Darcy-Stokes system governing a vuggy porous medium. Computational Geosciences, 11:207–218.
- Atkins, P. and de Paula, J. (2006). Physical Chemistry. W.H. Freeman and Company, New York.
- Baber, K. (2009). Modeling the transfer of therapeutic agents from the vascular space to the tissue compartment (A continuum approach). Master's thesis, Dep. of Hydromechanics and Modeling of Hydrosystems, IWS, University of Stuttgart.
- Baber, K., Flemisch, B., and Helmig, R. (2014). Modelling drop dynamics at the interface between free and porous-medium flow using the mortar method. submitted to International Journal of Heat and Mass Transfer.

- Baber, K., Mosthaf, K., Flemisch, B., Helmig, R., Müthing, S., and Wohlmuth, B. (2012). Numerical scheme for coupling two-phase compositional porous-media flow and one-phase compositional free flow. IMA Journal of Applied Mathematics, 77(6):887–909. first published online July 26, 2012.
- Balhoff, M. T., Thomas, S. G., and Wheeler, M. F. (2008). Mortar coupling and upscaling of pore-scale models. Computational Geosciences, 12:15–17.
- Bastian, P., Blatt, M., Dedner, A., Engwer, C., Klöforn, R., Kornhuber, R., Ohlberger, M., and Sander, O. (2008). A generic grid interface for parallel and adaptive scientific computing. Part II: Implementation and tests in DUNE. Computing, 82:121–138.
- Bastian, P., Heimann, D., and Marnach, S. (2010). Generic implementation of Finite Element methods in the Distributed and Unified Numerics Environment (DUNE). Kybernetika, 46:294–315.
- Basu, S., Nandakumar, K., and Masliyah, J. H. (1997). A model for detachment of a partially wetting drop from a solid surface by shear flow. Journal of Colloid and Interface Science, 190:253–257.
- Bear, J. (1972). Dynamics of Fluids in Porous Media. Courier Dover Publications, New York.
- Beavers, G. and Joseph, D. (1967). Boundary conditions at a naturally permeable wall. Journal of Fluid Mechanics, 30:197–207.
- Benziger, J., Nehlsen, J., Blackwell, D., Brennan, T., and Itescu, J. (2005). Water flow in the gas diffusion layer of PEM fuel cells. Journal of Membrane Science, 261:98–106.
- Berning, T. and Djilali, N. (2003). A 3D, multiphase, multicomponent model of the cathode and anode of a PEM fuel cell. Journal of The Electrochemical Society, 150:A1589–A1598.
- Berning, T., Odgaard, M., and Kær, S. K. (2009). A computational analysis of multiphase flow through PEMFC cathode porous media using the multifluid approach. Journal of The Electrochemical Society, 156(11):B1301–B1311.

- 
- Berning, T., Odgaard, M., and Kær, S. K. (2010). A study of multi-phase flow through the cathode side of an interdigitated flow field using a multi-fluid model. Journal of Power Sources, 195:4842–4852.
- Berning, T., Odgaard, M., and Kær, S. K. (2011). Water balance simulations of a polymer-electrolyte membrane fuel cell using a two-fluid model. Journal of Power Sources, 196:6305–6317.
- Blunt, M. (2000). An empirical model for three-phase relative permeability. SPE Journal, 5(4):435–445.
- Blunt, M., Jackson, M., Piri, M., and Valvatne, P. (2002). Detailed physics, predictive capabilities and macroscopic consequences for pore-network models of multiphase flow. Advances in Water Resources, 25:1069–1089.
- Bourges-Monnier, C. and Shanahan, M. E. R. (1995). Influence of evaporation on contact angle. Langmuir, 11:2820–2829.
- Brenner, K., Masson, R., Trenty, L., and Zhang, Y. (2014). Coupling of a two phase gas liquid compositional 3D Darcy flow with a 1D compositional free gas flow. unpublished.
- Brinkman, H. (1947). A calculation of the viscous force exerted by a flowing fluid on a dense swarm of particles. Applied Sciences Research, A1:27–34.
- Brooks, R. and Corey, A. (1964). Hydraulic properties of porous media. Hydrology Paper, (No. 3).
- Butt, H.-J., Golovko, D. S., and Bonaccorso, E. (2007). On the derivation of Young’s equation for sessile drops: Nonequilibrium effects due to evaporation. Journal of Physical Chemistry, 111:5277–5283.
- Butt, H.-J., Graf, K., and Kappl, M. (2003). Physics and Chemistry of Interfaces. Wiley-VCH Verlag & Co. KGaA, Weinheim.
- Cao, Y., Gunzburger, M., Hu, X., Hua, F., Wang, X., and Zhao, W. (2010). Finite element approximations for Stokes-Darcy flow with Beavers-Joseph interface conditions. SIAM Journal on Numerical Analysis, 47:4239–4256.

- Carton, J. G., Lawlor, V., Olabi, A. G., Hochenauer, C., and Zauner, G. (2012). Water droplet accumulation and motion in PEM (Proton Exchange Membrane) fuel cell mini-channels. Energy, 39:63–73.
- Chan, C., Zamel, N., Li, X., and Shen, J. (2012). Experimental measurements of effective diffusion coefficient of gas diffusion layer/microporous layer in PEM fuel cells. Electrochimica Acta, 65:13–21.
- Chandesris, M. and Jamet, D. (2006). Boundary condition at a planar fluid-porous interface for a Poiseuille flow. International Journal of Heat and Mass Transfer, 49:2137–2150.
- Chandesris, M. and Jamet, D. (2007). Boundary conditions at a fluid-porous interface: An a priori estimation of stress jump coefficients. International Journal of Heat and Mass Transfer, 50:3422–3436.
- Chandesris, M. and Jamet, D. (2009). Jump conditions and surface-excess quantities at a fluid/porous interface: A multi-scale approach. Transport in Porous Media, 78:419–438.
- Chauhan, V. P., Stylianopoulos, T., Boucher, Y., and Jain, R. K. (2011). Delivery of molecular and nanoscale medicine to tumors: Transport barriers and strategies. Annual Review of Chemical and Biomolecular Engineering, 2:281–298.
- Chen, J., Sun, S., and Wang, X.-P. (2014). A numerical method for a model of two-phase flow in a coupled free flow and porous media system. Journal of Computational Physics, 268(0):1–16.
- Chen, K. S., Hickner, M. A., and Noble, D. R. (2005). Simplified models for predicting the onset of liquid water droplet instability at the gas diffusion layer/ gas flow channel interface. International Journal of Energy Research, 29:1113–1132.
- Chen, Z., Huan, G., and Ma, Y. (2006). Computational Methods for Multiphase Flows in Porous Media. Society for Industrial and Applied Mathematics, Dallas.
- Chidyagwai, P. and Rivière, B. (2010). Numerical modelling of coupled surface and subsurface flow systems. Advances in Water Resources, 33:92–105.

- 
- Cho, S. C., Wang, Y., and Chen, K. S. (2012a). Droplet dynamics in a polymer electrolyte fuel cell gas flow channel: Forces, deformation, and detachment. I: Theoretical and numerical analyses. Journal of Power Sources, 206:119–128.
- Cho, S. C., Wang, Y., and Chen, K. S. (2012b). Droplet dynamics in a polymer electrolyte fuel cell gas flow channel: Forces, deformation, and detachment. II: Comparisons of analytical solution with numerical and experimental results. Journal of Power Sources, 210:191–197.
- Class, H. (2001). Theorie und numerische Modellierung nichtisothermer Mehrphasenprozesse in NAPL-kontaminierten porösen Medien. PhD thesis, Institut für Wasserbau, Universität Stuttgart.
- Class, H., Helmig, R., and Bastian, P. (2002). Numerical simulation on non-isothermal multiphase multicomponent processes in porous media. 1. An efficient solution technique. Advances in Water Resources, 25:533–550.
- Curry, F.-R. E. (1984). Mechanics and thermodynamics of transcapillary exchange. In Renkin, E. M., Michel, C., and Geiger, S., editors, Handbook of Physiology: The cardiovascular system. Microcirculation., volume IV, pages 309–374. American Physiological Society, Bethesda, MD.
- Das, P. K., Li, X., and Liu, Z.-S. (2010). Effective transport coefficients in PEM fuel cell catalyst and gas diffusion layers: Beyond Bruggeman approximation. Applied Energy, 87:2785–2796.
- Demmel, J., Eisenstat, S., Gilbert, J., Li, X., and Liu, J. (1999). A supernodal approach to sparse partial pivoting. SIAM Journal on Matrix Analysis and Applications, 20(3):720–755.
- Discacciati, M., Miglio, E., and Quarteroni, A. (2002). Mathematical and numerical models for coupling surface and groundwater flows. Applied Numerical Mathematics, 43:57–74.
- Discacciati, M. and Quarteroni, A. (2004). Convergence analysis of a subdomain iterative method for the finite element approximation of the coupling of Stokes and Darcy equations. Computing Visualization in Science, 6:93–103.

- Discacciati, M., Quarteroni, A., and Valli, A. (2007). Robin-Robin domain decomposition methods for the Stokes-Darcy coupling. SIAM Journal on Numerical Analysis, 45:1246–1268.
- Dwenger, S., Eigenberger, G., and Nicken, U. (2012). Measurement of capillary pressure-saturation relationships under defined compression levels for gas diffusion media of PEM fuel cells. Transport in Porous Media, 91:281–294.
- Eller, J., Rosén, T., Marone, F., Stampanoni, M., Wokaun, A., and Büchi, F. N. (2011). Progress in in situ x-ray tomographic microscopy of liquid water in gas diffusion layers of PEFC. Journal of The Electrochemical Society, 158(8):B963–B970.
- Erbertseder, K. (2012). A multi-scale model for describing cancer-therapeutic transport in the human lung. PhD thesis, Institut für Wasser- und Umweltsystemmodellierung, University of Stuttgart.
- Erbertseder, K., Reichold, J., Flemisch, B., Jenny, P., and Helmig, R. (2012). A coupled discrete / continuum model for describing cancer-therapeutic transport in the lung. PLoS ONE, 7(3):e31966.
- Erbil, H. Y., McHale, G., and Newton, M. I. (2002). Drop evaporation on solid surfaces: Constant contact angle mode. Langmuir, 18:2636–2641.
- Ewing, R., Lazarov, R., Lin, T., and Lin, Y. (2000). Mortar finite volume element approximations of second order elliptic problems. In East-West Journal of Numerical Mathematics. Citeseer.
- Extrand, C. W. and Gent, A. N. (1990). Retention of liquid drops by solid surfaces. Journal of Colloid and Interface Science, 138:431–442.
- Fetzer, T. (2012). Numerical analysis of the influence of turbulence on exchange processes between porous medium and free flow. Master’s thesis, Dep. of Hydromechanics and Modeling of Hydrosystems, IWS, University of Stuttgart, Stuttgart, Germany.
- Flemisch, B., Darcis, M., Erbertseder, K., Faigle, B., Lauser, A., Mosthaf, K., Müthing, S., Nuske, P., Tatomir, A., Wolff, M., and Helmig, R. (2011). Dumux: Dune for multi-(phase, component, scale, physics, ...) flow and transport in porous media. Advances in Water Resources, 34:1102–1112.

- 
- Formaggia, L., Quarteroni, A., and Veneziani, A. (2009). Cardiovascular Mathematics - Modelling and simulation of the circulatory system. Springer-Verlag, Milan.
- Franca, L., Hughes, T., and Stenberg, R. (1993). Incompressible Computational Fluid Dynamics. Chapter 4: Stabilized finite element methods for the Stokes problem. Cambridge University Press.
- Free Software Foundation (1991). GNU general public license, version 2. <http://www.gnu.org/licenses/old-licenses/gpl-2.0.html>.
- Fu, N., Adamson, R., and Curry, F.-R. E. (2005). Determination of microvessel permeability and tissue diffusion coefficient of solutes by laser scanning confocal microscopy. Journal of Biomechanical Engineering, 127:270–278.
- Galvin, K. (2005). A conceptually simple derivation of the Kelvin equation. Chemical Engineering Science, 60:4659–4660.
- Girault, V. and Rivière, B. (2009). DG approximation of coupled Navier-Stokes and Darcy equations by Beaver-Joseph-Saffman interface condition. SIAM Journal on Numerical Analysis, 47:2052–2089.
- Gopalan, P. and Kandlikar, S. G. (2014). Effect of channel materials and trapezoidal corner angles on emerging droplet behavior in proton exchange membrane fuel cell gas channels. Journal of Power Sources, 248:230–238.
- Gostick, J. T. (2013). Random pore network modeling of fibrous PEMFC gas diffusion media using Voronoi and Delaunay tessellations. Journal of the Electrochemical Society, 160(8):F731–F743.
- Gostick, J. T., Fowler, M. W., Ioannidis, M. A., Pritzker, M. D., Volkovich, Y. M., and Sakars, A. (2006). Capillary pressure and hydrophilic porosity in gas diffusion layers for polymer electrolyte fuel cells. Journal of Power Sources, 156:375–387.
- Goyeau, B., Lhuillier, D., Gobin, D., and Velarde, M. (2003). Momentum transport at a fluid-porous interface. International Journal of Heat and Mass Transfer, 46:4071–4081.
- Gray, W., Leijnse, A., Randall, L., and Blain, C. (1993). Mathematical tools for changing spatial scales in the analysis of physical systems. CRC Press, Boca Raton.

- Gurau, V. and Mann, J. A. (2009). A critical overview of computational fluid dynamics multiphase models for proton exchange membrane fuel cells. SIAM Journal on Applied Mathematics, 70(2):410–454.
- Gurau, V. and Mann, J. A. (2010). Effect of interfacial phenomena at the gas diffusion layer - channel interface on the water evolution in a PEMFC. Journal of The Electrochemical Society, 157(4):B512–B521.
- Gurau, V., Zawodzinski, T. A., and Mann, J. A. (2008). Two-phase transport in PEM fuel cell cathodes. Journal of Fuel Cell Science and Technology, 5:021009–1 – 021009–12.
- Haghighi, E., Shahraeeni, E., Lehmann, P., and Or, D. (2013). Evaporation rates across a convective air boundary layer are dominated by diffusion. Water Resources Research, 49:1602–1610.
- Hasenauer, J., Waldherr, S., Doszczak, M., Scheurich, P., and Allgöwer, F. (2010a). Density-based modeling and identification of biochemical networks in cell populations. In Proc. of 9th Int. Symp. on Dynamics and Control of Process Syst. (DYCOPS), pages 320–325.
- Hasenauer, J., Waldherr, S., Radde, N., Doszczak, M., Scheurich, P., and Allgöwer, F. (2010b). A maximum likelihood estimator for parameter distributions in heterogeneous cell populations. Procedia Computer Science, 1:1655–1663.
- Hassanizadeh, S. and Gray, W. (1989). Derivation of conditions describing transport across zones of reduced dynamics within multiphase systems. Water Resources Research, 25(3):529–539.
- Hassanizadeh, S. M. and Gray, W. G. (1993). Thermodynamic basis of capillary pressure in porous media. Water Resources Research, 29(10):3389–3405.
- He, G., Ming, P., Zhao, Z., Abudula, A., and Xia, Y. (2007). A two-fluid model for the two-phase flow in PEMFCs. Journal of Power Sources, 163:864–873.
- Helmig, R. (1997). Multiphase Flow and Transport Processes in the Subsurface - A Contribution to the Modeling of Hydrosystems. Springer-Verlag, Berlin.

- 
- Helmig, R. and Class, H. (2004). Hydromechanik. Lehrstuhl für Hydromechanik und Hydrosystemmodellierung, IWS, Universität Stuttgart, Stuttgart.
- Helmig, R., Weiss, A., and Wohlmuth, B. (2009). Variational inequalities for modeling flow in heterogeneous porous media with entry pressure. Computational Geosciences, 13:373–389.
- Herescu, A. and Allen, J. S. (2012). The influence of channel wettability and geometry on water plug formation and drop location in a proton exchange membrane fuel cell flow field. Journal of Power Sources, 216:337–344.
- Heywood, J., Rannacher, R., and Turek, S. (1996). Artificial boundaries and flux and pressure conditions for the incompressible Navier-Stokes equations. International Journal for Numerical Methods in Fluids, 22:325–352.
- Huber, R. and Helmig, R. (2000). Node-centered finite volume discretizations for the numerical simulation of multiphase flow in heterogeneous porous media. Computational Geosciences, 4:141–164.
- Hughes, D. (2000). Transvascular fluid dynamics. Veterinary Anaesthesia and Analgesia, 27:63–69.
- Hussaini, I. S. and Wang, C. Y. (2009). Visualization and quantification of cathode channel flooding in PEM fuel cells. Journal of Power Sources, 187:444–451.
- IAPWS (1994). IAPWS release on surface tension of ordinary water substance.
- IAPWS (2009). Revised release on the IAPWS formulation 1995 for the thermodynamic properties of ordinary water substance for general and scientific use.
- Ischinger, F. (2013). Modeling transvascular exchanges of therapeutic agents - Sensitivity analysis. Master's thesis, Dep. of Hydromechanics and Modeling of Hydrosystems, IWS, Univ. of Stuttgart.
- Jäger, W. and Mikelić, A. (2000). On the interface boundary condition of Beaver-Joseph-Saffman. Society of Industrial and Applied Mathematics, 60(4):1111–1127.
- Jäger, W. and Mikelić, A. (2009). Modeling effective interface laws for transport phenomena between an unconfined fluid and a porous medium using homogenization. Transport in Porous Media, 79:489–508.

- Jain, R. (1987a). Transport of molecules across tumor vasculature. Cancer and Metastasis Reviews, 6:559–593.
- Jain, R. (1987b). Transport of molecules in the tumor interstitium: A review. Cancer Research, 47:3039–3051.
- Jamet, D., Chandesris, M., and Goyeau, B. (2009). On the equivalence of the discontinuous one- and two-domain approaches for the modeling of transport phenomena at a fluid/porous interface. Transport in Porous Media, 78:403–418.
- Jenkins, A. D., Kratochvil, P., Stepto, R. F. T., and Suter, U. W. (1996). Glossary of basic terms in polymer science. International Union of Pure and Applied Chemistry, 68(12):2287–2311.
- Joekar-Niasar, V. (2010). The Immiscibles: Capillarity Effects in Porous Media - Pore-Network Modeling. PhD thesis, Utrecht University, Geoscience Faculty, Earth Sciences Department.
- Joekar-Niasar, V., Hassanizadeh, S. M., and Dahle, H. K. (2010). Non-equilibrium effects in capillarity and interfacial area in two-phase flow: Dynamic pore-network modelling. Journal of Fluid Mechanics, 655:38–71.
- Joekar-Niasar, V., Hassanizadeh, S. M., and Leijnse, A. (2008). Insights into the relationship among capillary pressure, saturation, interfacial area and relative permeability using pore-network modeling. Transport in Porous Media, 74:201–219.
- Junqueira, L., Carneiro, J., and Kelley, R. (2002). Histologie. Springer, Berlin, 5. edition.
- Kandlikar, S. G., See, E. J., Koz, M., Gopalan, P., and Banerjee, R. (2014). Two-phase flow in GDL and reactant channels of a proton exchange membrane fuel cell. International Journal of Hydrogen Energy, 39(0):6620–6636.
- Kays, W., Crawford, M., and Weigand, B. (2005). Convective Heat and Mass Transfer. McGraw-Hill, New York, 4th edition.
- Korteland, S., Bottero, S., Hassanizadeh, S. M., and Berentsen, C. W. J. (2010). What is the correct definition of average pressure? Transport in Porous Media, 84:153–175.
- Kumbur, E., Sharp, K., and Mench, M. (2006). Liquid droplet behavior and instability in a polymer electrolyte fuel cell flow channel. Journal of Power Sources, 161:333–345.

- 
- Kurbel, S., Kurbel, B., Belovari, T., Marić, S., Steiner, R., and Božić, D. (2001). Model of interstitial pressure as a result of cyclical changes in the capillary wall fluid transport. Medical Hypotheses, 57(2):161–166.
- Kuttanikkad, S. P., Prat, M., and Pauchet, J. (2011). Pore-network simulations of two-phase flow in a thin porous layer of mixed wettability: Application to water transport in gas diffusion layers of proton exchange membrane fuel cells. Journal of Power Sources, 196:1145–1155.
- Lauser, A., Hager, C., Helmig, R., and Wohlmuth, B. (2011). A new approach for phase transitions in miscible multi-phase flow in porous media. Advances in Water Resources, 34:957–966.
- Layton, J., Schieweck, F., and Yotov, I. (2002). Coupling fluid flow with porous media flow. SIAM Journal of Numerical Analysis, 40:2195–2218.
- Levy, T. and Sanchez-Palencia, E. (1975). On boundary conditions for fluid flow in porous media. International Journal of Engineering Science, 13:923–940.
- Luo, G., Ji, Y., Wang, C.-Y., and Sinha, P. K. (2010). Modeling liquid water transport in gas diffusion layers by a topologically equivalent pore network. Electrochimica Acta, 55:5332–5341.
- Magdoom, K. N., Pishko, G. L., Rice, L., Pampo, C., Siemann, D. W., and Sarntinoranont, M. (2014). MRI-based computational model of heterogeneous tracer transport following local infusion into a mouse hind limb tumor. PLoS ONE, 9(3):e89594.
- Mathias, M., Roth, J., Fleming, J., and Lehnert, W. (2003). Handbook of Fuel Cells - Fundamentals, Technology and Applications (Chapter 46: Diffusion media materials and characterisation), volume 3. John Wiley & Sons, New York.
- Michel, C. C. and Curry, F. E. (1999). Microvascular permeability. Physiological Reviews, 79:703–761.
- Millington, R. and Quirk, J. (1960). Permeability of porous solids. Transactions of the Faraday Society, 57:1200–1207.
- Mitropoulos, A. C. (2008). The Kelvin equation. Journal of Colloid and Interface Science, 317:643–648.

- Mosthaf, K., Baber, K., Flemisch, B., Helmig, R., Leijnse, A., Rybak, I., and Wohlmuth, B. (2011). A coupling concept for two-phase compositional porous media and single-phase compositional free flow. Water Resources Research, 47:W10522556.
- Mosthaf, K., Helmig, R., and Or, D. (2014). Modeling and analysis of evaporation processes from porous media on the REV scale. Water Resources Research, 50(2):1059–1079.
- Müthing, S. and Bastian, P. (2010). Dune-multidomaingrid: A metagrid approach to subdomain modelling. Proceedings of the DUNE User Meeting 2010, Stuttgart.
- Nam, J. H. and Kaviany, M. (2003). Effective diffusivity and water-saturation distribution in single- and two-layer PEMFC diffusion medium. International Journal of Heat and Mass Transfer, 46:4595–4611.
- Natarajan, D. and Nguyen, T. V. (2001). A two-dimensional, two-phase, multi-component, transient model for the cathode of a proton exchange membrane fuel cell using conventional gas distributors. Journal of The Electrochemical Society, 148:A1324–A1335.
- Netti, P., Baxter, L., Boucher, Y., Skalak, R., and Jain, R. (1997). Macro- and microscopic fluid transport in living tissues: Application to solid tumors. AIChE Journal, 43:818–831.
- Nordbotten, J. M., Celia, M. A., Dahle, H. K., and Hassanizadeh, S. M. (2008). On the definition of macroscale pressure for multiphase flow in porous media. Water Resources Research, 44:W06S02.
- Nuske, P., Joekar-Niasar, V., and Helmig, R. (2014). Non-equilibrium in multiphase multicomponent flow in porous media: An evaporation example. International Journal of Heat and Mass Transfer, 74:128–142.
- Ochoa-Tapia, J. A. and Whitaker, S. (1995). Momentum transfer at the boundary between a porous medium and a homogeneous fluid - I. Theoretical development. International Journal of Heat and Mass Transfer, 35:2635–2646.
- Ochs, S. (2008). Development of a multiphase multicomponent model of PEMFC. Technical report, IRTG NUPUS, Universität Stuttgart.

- 
- Oertel jr., H. (2012). Prandtl - Führer durch die Strömungslehre: Grundlagen und Phänomene. Springer Vieweg, Wiesbaden, 13. edition. überarb. Aufl. 2012.
- O'Hayre, R., Cha, S.-W., Colella, W., and Prinz, F. B. (2006). Fuel cell fundamentals. John Wiley & Sons, NewYork.
- Pant, L. M., Mitra, S. K., and Secanell, M. (2012). Absolute permeability and Knudsen diffusivity measurements in PEMFC gas diffusion layers and micro porous layers. Journal of Power Sources, 206:153–160.
- Petrak, K. and Goddard, P. (1989). Transport of macromolecules across the capillary walls. Advanced Drug Delivery Reviews, 3:191–214.
- Pharoah, J. G., Karan, K., and Sun, W. (2006). On effective transport coefficients in PEM fuel cell electrodes: Anisotropy of the porous transport layers. Journal of Power Sources, 161:214–224.
- Picknett, R. and Bexon, R. (1977). The evaporation of sessile or pendant drops in still air. Journal of Colloid and Interface Science, 61(2):336–350.
- Pishko, G. L., Astarý, G. W., Mareci, T. H., and Sarntinoranont, M. (2011). Sensitivity analysis of an image-based solid tumor computational model with heterogeneous vasculature and porosity. Annals of Biomedical Engineering, 39:2360–2373.
- Poling, B. E., Prausnitz, J. M., and O'Connell, J. P. (2001). The properties of gases and liquids. McGraw-Hill, Inc., New York, 5th edition.
- Prat, M. (1990). Modelling of heat transfer by conduction in a transition region between a porous medium and an external fluid. Transport in Porous Media, 5:71–95.
- Qin, C. (2012). Numerical Investigations on two-phase flow in polymer electrolyte fuel cells. PhD thesis, Utrecht University, Geosciences Faculty, Earth Sciences Department.
- Qin, C., Hassanizadeh, S. M., and Rensink, D. (2012a). Numerical study on liquid water flooding in gas channels used in polymer electrolyte fuel cell. Chemical Engineering Science, 82:223–231.

- Qin, C., Hassanizadeh, S. M., Rensink, D., and Fell, S. (2012b). One-dimensional phenomenological model for liquid water flooding in cathode gas channel of a polymer electrolyte fuel cell. Journal of the Electrochemical Society, 159(6):B737–B745.
- Qin, C., Rensink, D., Fell, S., and Hassanizadeh, S. M. (2012c). Two-phase flow modeling for the cathode side of a polymer electrolyte fuel cell. Journal of Power Sources, 197:136–144.
- Qin, C., Rensink, D., Hassanizadeh, S. M., and Fell, S. (2012d). Direct simulation of liquid water dynamics in the gas channel of a polymer electrolyte fuel cell. Journal of the Electrochemical Society, 159(4):B434–B443.
- Qin, C. Z. and Hassanizadeh, S. M. (2014). Multiphase flow through multilayers of thin porous media: General balance equations and constitutive relationships for a solid-gas-liquid three-phase system. International Journal of Heat and Mass Transfer, 70:693–708.
- Quéré, D., Azzopardi, M.-J., and Delattre, L. (1998). Drops at rest on a tilted plane. Langmuir, 14:2213–2216.
- Reichold, J. (2011). Cerebral Blood Flow Modeling. PhD thesis, ETH Zurich.
- Reid, R., Prausnitz, J., and Poling, B. (1987). The properties of gases & liquids. McGraw-Hill, Inc., New York.
- Renkin, E. (1978). Transport pathways through capillary endothelium pathways. Microvascular Research, 15:123–135.
- Rivière, B. (2005). Analysis of a discontinuous finite element method for the coupled Stokes and Darcy problems. Journal of Scientific Computing, 22(1):479–500.
- Rivière, B. and Kanschat, G. (2010). A strongly conservative finite element method for the coupling of Stokes and Darcy flow. Journal of Computational Physics, 229:5933–5943.
- Rivière, B. and Yotov, I. (2005). Locally conservative coupling of Stokes and Darcy flow. SIAM Journal of Numerical Analysis, 42:1959–1977.

- Rosén, T., Eller, J., Kang, J., Prasianakis, N. I., Mantzaras, J., and Büchi, F. N. (2012). Saturation dependent effective transport properties of PEFC gas diffusion layers. Journal of the Electrochemical Society, 159(9):F536–F544.
- Rosenzweig, R. and Shavit, U. (2007). The laminar flow field at the interface of a Sierpinski carpet configuration. Water Resources Research, 43:W10402.
- Roth, J., Eller, J., Marone, F., and Büchi, F. (2013). Investigation of the representative area of the water saturation in gas diffusion layers of polymer electrolyte fuel cells. The Journal of Physical Chemistry C, 117:25991–25999.
- Saffman, P. (1971). On the boundary condition at the surface of a porous medium. Studies in Applied Mathematics, 50(2):93–101.
- Saltelli, A., Chan, K., and Scott, E. (2000). Sensitivity analysis. Wiley, West Sussex.
- Schiebler, T. (2005). Anatomie - Histologie, Entwicklungsgeschichte, makroskopische und mikroskopische Anatomie, Topographie. Springer, Heidelberg, 9. edition.
- Schillberg, C. H. and Kandlikar, S. G. (2007). A review of models for water droplet detachment from the gas diffusion layer - gas flow channel interface in PEMFCs. In Proceedings of the Fifth International Conference on Nanochannels, Microchannels and Minichannels, ICNMM2007, Puebla, Mexico.
- Schlünder, E.-U. (1988). On the mechanism of the constant drying rate period and its relevance to diffusion controlled catalytic gas phase reactions. Chemical Engineering Science, 43 (10):2685–2688.
- Schmidt, R. and Lang, F. (2007). Physiologie des Menschen - mit Pathophysiologie. Springer, Heidelberg, 30. edition.
- See, E. J. and Kandlikar, S. G. (2012). A two-phase pressure drop model incorporating local water balance and reactant consumption in PEM fuel cell gas channels. ECS Transactions, 50:99–111.
- Sergi, J. M. and Kandlikar, S. G. (2011). Quantification and characterization of water coverage in PEMFC gas channels using simultaneous anode and cathode visualization and image processing. International Journal of Hydrogen Energy, 36:12381–12391.

- Shahraeeni, M. and Hoorfar, M. (2013). Experimental and numerical comparison of water transport in untreated and treated diffusion layers of proton exchange membrane (PEM) fuel cells. Journal of Power Sources, 238:29–47.
- Shavit, U. (2009). Special issue on "Transport phenomena at the interface between fluid and porous domains". Transport in Porous Media, 78:327–330.
- Sinha, P. K. and Wang, C.-Y. (2008). Liquid water transport in a mixed-wet gas diffusion layer of a polymer electrolyte fuel cell. Chemical Engineering Science, 63:1081–1091.
- Smith, J. and Humphrey, J. (2007). Interstitial transport and transvascular fluid exchange during infusion into brain and tumor tissue. Microvascular Research, 73:58–73.
- Song, H., Lee, Y., Jin, S., Kim, H.-Y., and Yoo, J. Y. (2011). Prediction of sessile drop evaporation considering surface wettability. Microelectronic Engineering, 88:3249–3255.
- Stace, T. and Damiano, E. R. (2001). An electrochemical model of the transport of charged molecules through the capillary glycocalyx. Biophysical Journal, 80(4):1670–1690.
- Sugihara-Seki, M. and Fu, B. (2005). Blood flow and permeability in microvessels. Fluid Dynamic Research, 37:82–132.
- Suresh, P. and Jayanti, S. (2010). Effect of air flow on liquid water transport through a hydrophobic gas diffusion layer of a polymer electrolyte membrane fuel cell. International Journal of Hydrogen Energy, 35:6872–6886.
- Theodorakakos, A., Ous, T., Gavaises, M., Nouri, J., Nikolopoulos, N., and Yanagihara, H. (2006). Dynamics of water droplets detached from porous surfaces of relevance to PEM fuel cells. Journal of Colloid and Interface Science, 300:673–687.
- Thews, G. and Vaupel, P. (2007). Vegetative Physiology. Springer Medizin Verlag Heidelberg.
- Valdes-Parada, F. J., Alvarez-Ramirez, J., Goyeau, B., and Ochoa-Tapia, J. A. (2009a). Computation of jump coefficients for momentum transfer between a porous medium

- and a fluid using a closed generalized transfer equation. Transport in Porous Media, 78:439–457.
- Valdes-Parada, F. J., Alvarez-Ramirez, J., Goyeau, B., and Ochoa-Tapia, J. A. (2009b). Jump condition for diffusive and convective mass transfer between a porous medium and a fluid involving adsorption and chemical reaction. Transport in Porous Media, 78:459–476.
- Valdes-Parada, F. J., Goyeau, B., and Ochoa-Tapia, J. A. (2006). Diffusive mass transfer between a microporous medium and an homogeneous fluid: Jump boundary condition. Chemical Engineering Science, 61:1692–1704.
- Valdes-Parada, F. J., Ochoa-Tapia, J. A., and Alvarez-Ramirez, J. (2007). Diffusive mass transport in the fluid-porous medium inter-region: Closure problem solution for the one-domain approach. Chemical Engineering Science, 62:6054–6068.
- van Genuchten, M. T. (1980). A closed-form equation for predicting the hydraulic conductivity of unsaturated soils. Soil Science Society Am. Journal, 44:892–898.
- Škvor, J. and Nezbeda, I. (2009). Percolation threshold parameters of fluids. Physical Review E, 79.
- Walter, L. (2008). Towards a model concept for coupling porous gas diffusion layer and gas distributor in PEM fuel cells. Master's thesis, Dep. of Hydromechanics and Modeling of Hydrosystems, IWS, University of Stuttgart.
- Wang, Y., Chen, K. S., Mishler, J., Cho, S. C., and Adroher, X. C. (2011). A review of polymer electrolyte membrane fuel cells: Technology, applications, and needs on fundamental research. Applied Energy, 88:981–1007.
- Wang, Z. H., Wang, C. Y., and Chen, K. S. (2001). Two-phase flow and transport in the air cathode of proton exchange membrane fuel cells. Journal of Power Sources, 94:40–50.
- Whitaker, S. (1999). The method of volume averaging. Kluwer Academic Publishers, Dordrecht.
- Wohlmuth, B. (2000). A mortar finite element method using dual space for the Lagrange multiplier. Society of Industrial and Applied Mathematics, 35:989–1012.

- Wu, H., Li, X., and Berg, P. (2009). On the modeling of water transport in polymer electrolyte membrane fuel cells. Electrochimica Acta, 54:6913–6927.
- Young, T. (1804). An essay on the cohesion of fluids. Philosophical Transactions of the Royal Society of London, 95:65–87.
- Zhang, F. Y., Yang, X. G., and Wang, C. Y. (2006). Liquid water removal from a polymer electrolyte fuel cell. Journal of The Electrochemical Society, 153(2):A225–A232.
- Zhao, G., Wu, J., Xu, S., Collins, M., Long, Q., König, C. S., Jiang, Y., Wang, J., and Padhani, A. (2007). Numerical simulation of blood flow and interstitial fluid pressure in solid tumor microcirculation based on tumor-induced angiogenesis. Acta Mechanica Sinica, 23:477–483.

# A Drop details

## A.1 Capillary pressure exerted by the curved drop surface

Work is exerted by the surface tension along the drop surface to give the drop its spheric shape. The surface tension has to balance the volume-changing work affecting the drop volume. With the surface of a sphere  $A = 4\pi r^2$  and its volume  $V = \frac{4}{3}\pi r^3$ , this leads to:

$$\gamma_{lg}dA = pdV, \quad (\text{A.1})$$

$$\gamma_{lg}8\pi r dr = p4\pi r^2 dr. \quad (\text{A.2})$$

This gives the pressure caused by the surface tension called capillary pressure:

$$p_c = \frac{2\gamma_{lg}}{r}. \quad (\text{A.3})$$

For spherical caps (volume given in equation (2.1)), the expression for the differential surface and contact area and for the differential volume element change to:

$$dA_{\text{drop}}^o = 4\pi r(1 - \cos \theta^*)dr \quad (\text{A.4})$$

$$dA_{\text{drop}}^{\text{CA}} = 2\pi r \sin \theta^{*2} dr \quad (\text{A.5})$$

$$dV_{\text{drop}} = \pi r^2(1 - \cos \theta^*)^2(2 + \cos \theta^*)dr. \quad (\text{A.6})$$

**Table A.1.1:** The magnitude of the geometric factor in the  $p_c$  calculation for a range of static contact angles relevant for PEM fuel cells.

	(A.10)	(A.11)
$\theta^* = 110^\circ$	0.899	0.798
$\theta^* = 120^\circ$	0.8	0.7
$\theta^* = 130^\circ$	0.897	0.794
$\theta^* = 140^\circ$	0.918	0.836
$\theta^* = 150^\circ$	0.945	0.89

With these definitions and Young's equation (2.5), the work for the change in drop surface, drop contact area and drop volume can be expressed as:

$$dW_{A_{\text{drop}}^o} = \gamma_{lg} 4\pi r (1 - \cos \theta^*) dr \quad (\text{A.7})$$

$$dW_{A_{\text{drop}}^{\text{CA}}} = (\gamma_{gs} - \gamma_{ls}) 2\pi r \sin \theta^{*2} dr = \gamma_{lg} \cos \theta^* 2\pi r \sin \theta^{*2} dr \quad (\text{A.8})$$

$$dW_{V_{\text{drop}}} = p\pi r^2 (1 - \cos \theta^*)^2 (2 + \cos \theta^*) dr \quad (\text{A.9})$$

Setting  $dW_{A_{\text{drop}}^o} = dW_{V_{\text{drop}}}$  and neglecting the work for changing the contact area yields:

$$p_c = \frac{2\gamma_{lg}}{r} \frac{2}{(1 - \cos \theta^*)(2 + \cos \theta^*)}. \quad (\text{A.10})$$

If the work for changing the contact area is considered, the capillary pressure of the drop curvature is defined as:

$$p_c = \frac{2\gamma_{lg}}{r} \frac{2(1 - \cos \theta^*) + \cos \theta^* \sin \theta^{*2}}{(1 - \cos \theta^*)(2 + \cos \theta^*)}. \quad (\text{A.11})$$

Equations (A.10) and (A.11) and the definition of capillary pressure of a spherical drop (A.3) differ only in a geometric factor. Table A.1.1 shows the magnitude of this factor for a range of static contact angles relevant for PEM fuel cells.

## A.2 Evaporation from drops

In the following, an estimate of the evaporative flux from a curved drop surface is given. It is based on the following expressions:

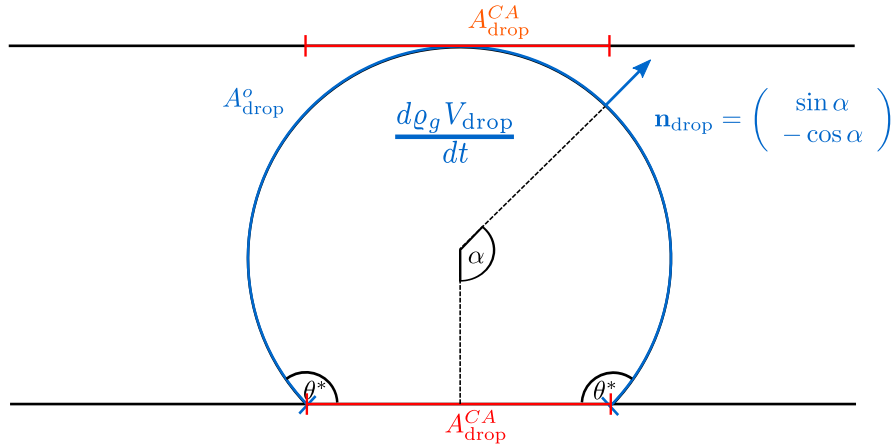


Figure A.2.1: Drop.

- saturated conditions prevail above the drop:

$$x_g^{w,\text{ff}} = x_{l,\text{drop}}^w \frac{p_{\text{sat,Kelvin}}^w}{p_g^{\text{ff}}}, \quad (\text{A.12})$$

where the Kelvin equation (2.17) is used to estimate the vapour pressure.

- the mass balance for the drop is expressed by the water flux feeding the drop, the mass that is stored inside the drop and the evaporative mass loss:

$$\int_{A_{\text{drop}}^{\text{CA}}} (\varrho_l \mathbf{v}_l x_l^{w,\text{pm}} - D_l^w \varrho_l \nabla x_l^{w,\text{pm}}) \cdot \mathbf{n} dx - \mathbf{f}_{\text{evap}}^\kappa - \frac{d}{dt} \int_{V_{\text{drop}}} \varrho_l x_{l,\text{drop}}^w dV = 0, \quad (\text{A.13})$$

with mass transport of saturated vapour:

$$\mathbf{f}_{\text{evap}}^\kappa = \int_{A_{\text{drop}}^{\text{o}}} (\varrho_g \mathbf{v}_g x_g^{w,\text{ff}} - D_g^w \varrho_l \nabla x_g^{w,\text{ff}}) \cdot \mathbf{n}_{\text{drop}} dx, \quad (\text{A.14})$$

- the energy balance of the drop, includes the enthalpy of vaporization:

$$\underbrace{\int_{A_{\text{drop}}^{\text{CA}}} (\varrho_l \mathbf{v}_l h_l - \lambda_{\text{pm}} \nabla T) \cdot \mathbf{n} dx - \int_{A_{\text{drop}}^{\text{o}}} (\varrho_g \mathbf{v}_g h_g - \lambda_g \nabla T) \cdot \mathbf{n}_{\text{drop}} dx}_{h_l - h_g = \Delta h_{\text{vap}}} - \frac{d}{dt} \int_{V_{\text{drop}}} \varrho_g u_g dV = 0 \quad (\text{A.15})$$

Mass and energy fluxes into the free-flow region occur in the direction normal to the drop across the drop surface  $A_{\text{drop}}^{\circ}$  (see figure A.2.1). Due to mass and energy conservation, the mass that evaporates and the energy flux have to end up in the free-flow region. Hence, the evaporative flux is equal to the normal free-flow flux:

$$\int_{A_{\text{drop}}^{\circ}} (\rho_g \mathbf{v}_g x_g^{w,\text{ff}} - D_g^w \rho_g \nabla x_g^{w,\text{ff}}) \cdot \mathbf{n}_{\text{drop}} dx = \int_{A_{\text{drop}}^{\text{CA}}} (\rho_g \mathbf{v}_g x_g^{w,\text{ff}} - D_g^w \rho_g \nabla x_g^{w,\text{ff}}) \cdot \mathbf{n}^{\text{ff}} dx. \quad (\text{A.16})$$

Song et al. (2011) and Erbil et al. (2002) provide expressions for  $f_{\text{evap}}^{\kappa}$  in three dimensions. For 2D simulations, an expression is derived in the following. One possibility is to follow the same reasoning as Song et al. (2011) and Erbil et al. (2002) where an expression for the area of evaporation in radial extension is given  $A(r) = 2\theta^*r$  and an integration from the drop surface ( $r = r_{\text{drop}}$ ) to infinity is performed.

We integrate from the drop surface to the channel top wall  $h_{GC}$ :

$$\begin{aligned} f_{\text{evap}}^{\kappa} &= -\rho_g D_g^w \frac{dx_g^{w,\text{ff}}}{dr} A(r) \\ -\rho_g D_g^w dx_g^{w,\text{ff}} &= \frac{f_{\text{evap}}^{\kappa}}{A(r)} dr \\ \int_{r_{\text{drop}}}^{h_{GC}} -\rho_g D_g^w dx_g^{w,\text{ff}} &= \int_{r_{\text{drop}}}^{h_{GC}} \frac{f_{\text{evap}}^{\kappa}}{2\theta^*r \frac{\pi}{180}} dr \\ -\rho_g D_g^w (x_g^{w,\text{ff}}|_{h_{GC}} - x_g^{w,\text{ff}}|_{r_{\text{drop}}}) &= \frac{\ln\left(\frac{h_{GC}}{r_{\text{drop}}}\right)}{2\theta^* \frac{\pi}{180}} f_{\text{evap}}^{\kappa} \end{aligned} \quad (\text{A.17})$$

This yields the following definition for the evaporative flux, considering only diffusive fluxes:

$$f_{\text{evap}}^{\kappa} = -2\theta^* \rho_g D_g^w \frac{180}{\pi} (x_g^{w,\text{ff}}|_{h_{GC}} - x_g^{w,\text{ff}}|_{r_{\text{drop}}}) \frac{1}{\ln\left(\frac{h_{GC}}{r_{\text{drop}}}\right)} \quad (\text{A.18})$$

Alternatively, an expression for the evaporative flux can be derived from (A.14). The surface integral in (A.14) is transformed to polar coordinates and then integrated with  $\mathbf{n}_{\text{drop}} = \begin{pmatrix} \sin \alpha \\ -\cos \alpha \end{pmatrix}$ . It is assumed that  $x_g^{w,\text{ff}} = x_{g,\text{sat}}^{w,\text{ff}}$  is constant around the drop at the drop surface.

$$\begin{aligned}
\mathbf{f}_{\text{evap}}^\kappa &= \int_{A_{\text{drop}}^\circ} (\rho_g \mathbf{v}_g x_g^{w,\text{ff}}) \cdot \mathbf{n}_{\text{drop}} d\mathbf{x} - \int_{A_{\text{drop}}^\circ} (D_g^w \rho_g \nabla x_g^{w,\text{ff}}) \cdot \mathbf{n}_{\text{drop}} d\mathbf{x} \\
&= 2r \rho_g x_g^{w,\text{ff}} \int_{\pi-\theta^*}^{\pi} (v_x \sin \alpha - v_y \cos \alpha) r d\alpha - 2r \rho_g D_g^w \int_{\pi-\theta^*}^{\pi} \left( \frac{\partial x_g^w}{\partial x} \sin \alpha - \frac{\partial x_g^w}{\partial y} \cos \alpha \right) r d\alpha \\
&= 2r \rho_g x_g^{w,\text{ff}} [v_x (-\cos(\pi) - (-\cos(\pi - \theta^*))) - v_y (\sin(\pi) - \sin(\pi - \theta^*))] \\
&\quad - 2r \rho_g D_g^w \left[ \frac{\partial x_g^w}{\partial x} (-\cos(\pi) - (-\cos(\pi - \theta^*))) - \frac{\partial x_g^w}{\partial y} (\sin(\pi) - \sin(\pi - \theta^*)) \right] \\
&= 2r \rho_g x_g^{w,\text{ff}} [v_x \underbrace{(1 + \cos(\pi - \theta^*))}_{-\cos(\theta^*)} - v_y \underbrace{(0 - \sin(\pi - \theta^*))}_{\sin \theta^*}] - 2r \rho_g D_g^w \left[ \frac{\partial x_g^w}{\partial x} (1 + \cos(\pi - \theta^*)) \right. \\
&\quad \left. - \frac{\partial x_g^w}{\partial y} (0 - \sin(\pi - \theta^*)) \right] \\
&= 2r \rho_g x_g^{w,\text{ff}} [v_x (1 - \cos(\theta^*)) + v_y (\sin(\theta^*))] - 2r \rho_g D_g^w \left[ \frac{\partial x_g^w}{\partial x} (1 - \cos(\theta^*)) + \frac{\partial x_g^w}{\partial y} (\sin(\theta^*)) \right]
\end{aligned} \tag{A.19}$$

Now, values for  $v_x, v_y, \frac{\partial x_g^w}{\partial x}, \frac{\partial x_g^w}{\partial y}$  have to be found. In reality these may vary around the drop and should have been integrated as well. Here, they are assumed to be constant, with  $\mathbf{v} = \mathbf{v}_\Gamma$  and  $\frac{\partial x_g^w}{\partial x_i} = \frac{x_{g,\text{GC}}^w - x_{g,\text{sat}}^w}{h_{\text{GC}} - h_{\text{drop}}}$ .



## B Software revisions

As mentioned in chapter 5, the coupled model is implemented in the free and open-source simulator DuMu<sup>x</sup> (Flemisch et al., 2011, Free Software Foundation, 1991). DuMu<sup>x</sup> is based on the Distributed and Unified Numerics Environment (DUNE) (Bastian et al. (2008), <http://www.dune-project.org>) inheriting functionality from the DUNE core modules and from the discretisation module dune-PDELab.

The spatial discretisation of the geometric domain and the designation of subdomains are based on the software package DUNE-Multidomaingrid (Müthing and Bastian (2010), <http://users.dune-project.org/projects/dune-multidomaingrid>) which allows to represent arbitrarily complex subdomain shapes with conforming interfaces. For the management of the different subdomains and their associated function spaces, we employ PDELab (Bastian et al., 2010) and its extension DUNE-Multidomain (<http://users.dune-project.org/projects/dune-multidomain>).

DuMu<sup>x</sup> can be obtained from the website <http://www.dumux.org/index.php> or via Subversion. The website offers an installation guide and a detailed handbook as well as a complete Doxygen class documentation. DuMu<sup>x</sup> can be downloaded as stable release tarball from the website. Besides, the version-control system Subversion allows an exact documentation of the whole development process.

Table B.0.1 lists the revision numbers of the modules used for the simulations of transvascular exchange (chapter 6, Ischinger (2013) and Ackermann (2013)) and drop dynamics in PEM fuel cells (chapter 7).

**Table B.0.1:** Software revisions used for the simulations of transvascular exchange (chapter 6, Ischinger (2013) and Ackermann (2013)) and drop dynamics in PEM fuel cells (chapter 7).

Module	Revision
<b>Transvascular exchange</b>	(Chapter 6)
dumux	9489
dumux-devel	9495
dune-common	7038
dune-geometry	333
dune-grid	8527
dune-istl	1726
dune-localfunctions	1117
dune-pdelab	2268
modified: dune/pdelab/backend/istlvectorbackend.hh	
dune-multidomain	03627ec55454ba7f32df71fb0dc67e5e21939419
modified: dune/pdelab/multidomain/couplinggridfunctionspace.hh	
dune-multidomaingrid	869e061bf66c16af8d8f8e2a3aa935631af36948
modified: dune/grid/multidomaingrid/indexsets.hh	
<b>Drop dynamics in PEM fuel cells</b>	(Chapter 7)
dumux-pub/Baber2014a	

## **Lebenslauf**

### **Persönliche Daten**

Name: Katherina Inés Baber  
Geburtsdatum: 17.11.1983  
Geburtsort: Neustadt am Rübenberge  
Staatsangehörigkeit: deutsch

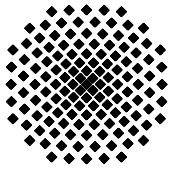
### **Ausbildung**

09/1996 - 06/2003 Ratsgymnasium Stadthagen  
09/2000 - 06/2001 Lycée Felix le Dantec, Lannion, France  
10/2003 - 05/2009 Studium der Umweltschutztechnik, Universität Stuttgart  
Diplomarbeit: "Modeling the transfer of therapeutic agents from the vascular space to the tissue compartment (a continuum approach)", NUPUS Stipendium  
09/2006 - 05/2007 Auslandsstudium, Department of Earth Sciences, University of Waterloo, Kanada, DAAD Stipendium  
seit 06/2009 Mitglied der Graduiertenschule Simulation Technology (GS SimTech)  
05/2012 - 07/2012 Forschungsaufenthalt, Department of Earth Sciences, Faculty of Geosciences, Utrecht University, Niederlande

### **Berufstätigkeit**

06/2009 - 05/2014 Wissenschaftliche Mitarbeiterin am Institut für Wasser- und Umweltsystemmodellierung der Universität Stuttgart, Lehrstuhl für Hydromechanik und Hydrosystemmodellierung  
seit 07/2014 Projektmanagerin, Technologieprojekt Wasserstoff Brennstoffzelle, BMW, München





## Institut für Wasser- und Umweltsystemmodellierung Universität Stuttgart

Pfaffenwaldring 61  
70569 Stuttgart (Vaihingen)  
Telefon (0711) 685 - 64717/64749/64752/64679  
Telefax (0711) 685 - 67020 o. 64746 o. 64681  
E-Mail: [iws@iws.uni-stuttgart.de](mailto:iws@iws.uni-stuttgart.de)  
<http://www.iws.uni-stuttgart.de>

### Direktoren

Prof. Dr. rer. nat. Dr.-Ing. András Bárdossy  
Prof. Dr.-Ing. Rainer Helmig  
Prof. Dr.-Ing. Silke Wieprecht

### Vorstand (Stand 19.08.2013)

Prof. Dr. rer. nat. Dr.-Ing. A. Bárdossy  
Prof. Dr.-Ing. R. Helmig  
Prof. Dr.-Ing. S. Wieprecht  
Prof. Dr. J.A. Sander Huisman  
Jürgen Braun, PhD  
apl. Prof. Dr.-Ing. H. Class  
Dr.-Ing. H.-P. Koschitzky  
Dr.-Ing. M. Noack  
Jun.-Prof. Dr.-Ing. W. Nowak, M.Sc.  
Dr. rer. nat. J. Seidel  
Dr.-Ing. K. Terheiden

### Emeriti

Prof. Dr.-Ing. habil. Dr.-Ing. E.h. Jürgen Giesecke  
Prof. Dr.h.c. Dr.-Ing. E.h. Helmut Kobus, PhD

### Lehrstuhl für Wasserbau und Wassermengenwirtschaft

Leiter: Prof. Dr.-Ing. Silke Wieprecht  
Stellv.: Dr.-Ing. Kristina Terheiden  
**Versuchsanstalt für Wasserbau**  
Leiter: Dr.-Ing. Markus Noack

### Lehrstuhl für Hydromechanik und Hydrosystemmodellierung

Leiter: Prof. Dr.-Ing. Rainer Helmig  
Stellv.: apl. Prof. Dr.-Ing. Holger Class  
**Jungwissenschaftlergruppe: Stochastische  
Modellierung von Hydrosystemen**  
Leiter: Jun.-Prof. Dr.-Ing. Wolfgang Nowak, M.Sc.

### Lehrstuhl für Hydrologie und Geohydrologie

Leiter: Prof. Dr. rer. nat. Dr.-Ing. András Bárdossy  
Stellv.: Dr. rer. nat. Jochen Seidel  
**Hydrogeophysik der Vadosen Zone**  
(mit Forschungszentrum Jülich)  
Leiter: Prof. Dr. J.A. Sander Huisman

### VEGAS, Versuchseinrichtung zur Grundwasser- und Altlastensanierung

Leitung: Jürgen Braun, PhD, AD  
Dr.-Ing. Hans-Peter Koschitzky, AD

## Verzeichnis der Mitteilungshefte

- 1 Röhnisch, Arthur: *Die Bemühungen um eine Wasserbauliche Versuchsanstalt an der Technischen Hochschule Stuttgart*, und Fattah Abouleid, Abdel: *Beitrag zur Berechnung einer in lockeren Sand gerammten, zweifach verankerten Spundwand*, 1963
- 2 Marotz, Günter: *Beitrag zur Frage der Standfestigkeit von dichten Asphaltbelägen im Großwasserbau*, 1964
- 3 Gurr, Siegfried: *Beitrag zur Berechnung zusammengesetzter ebener Flächen-tragwerke unter besonderer Berücksichtigung ebener Stauwände, mit Hilfe von Randwert- und Lastwertmatrizen*, 1965
- 4 Plica, Peter: *Ein Beitrag zur Anwendung von Schalenkonstruktionen im Stahlwasserbau*, und Petrikat, Kurt: *Möglichkeiten und Grenzen des wasserbaulichen Versuchswesens*, 1966

- 5 Plate, Erich: *Beitrag zur Bestimmung der Windgeschwindigkeitsverteilung in der durch eine Wand gestörten bodennahen Luftschicht, und*  
Röhnisch, Arthur; Marotz, Günter: *Neue Baustoffe und Bauausführungen für den Schutz der Böschungen und der Sohle von Kanälen, Flüssen und Häfen; Gesteigungskosten und jeweilige Vorteile, sowie Unny, T.E.: Schwingungsuntersuchungen am Kegelstrahlschieber, 1967*
- 6 Seiler, Erich: *Die Ermittlung des Anlagenwertes der bundeseigenen Binnenschiffahrtsstraßen und Talsperren und des Anteils der Binnenschiffahrt an diesem Wert, 1967*
- 7 *Sonderheft anlässlich des 65. Geburtstages von Prof. Arthur Röhnisch mit Beiträgen von* Benk, Dieter; Breitling, J.; Gurr, Siegfried; Haberhauer, Robert; Honekamp, Hermann; Kuz, Klaus Dieter; Marotz, Günter; Mayer-Vorfelder, Hans-Jörg; Miller, Rudolf; Plate, Erich J.; Radomski, Helge; Schwarz, Helmut; Vollmer, Ernst; Wildenhahn, Eberhard; 1967
- 8 Jumikis, Alfred: *Beitrag zur experimentellen Untersuchung des Wassernachschubs in einem gefrierenden Boden und die Beurteilung der Ergebnisse, 1968*
- 9 Marotz, Günter: *Technische Grundlagen einer Wasserspeicherung im natürlichen Untergrund, 1968*
- 10 Radomski, Helge: *Untersuchungen über den Einfluß der Querschnittsform wellenförmiger Spundwände auf die statischen und rammtechnischen Eigenschaften, 1968*
- 11 Schwarz, Helmut: *Die Grenztragfähigkeit des Baugrundes bei Einwirkung vertikal gezogener Ankerplatten als zweidimensionales Bruchproblem, 1969*
- 12 Erbel, Klaus: *Ein Beitrag zur Untersuchung der Metamorphose von Mittelgebirgsschneedecken unter besonderer Berücksichtigung eines Verfahrens zur Bestimmung der thermischen Schneequalität, 1969*
- 13 Westhaus, Karl-Heinz: *Der Strukturwandel in der Binnenschiffahrt und sein Einfluß auf den Ausbau der Binnenschiffskanäle, 1969*
- 14 Mayer-Vorfelder, Hans-Jörg: *Ein Beitrag zur Berechnung des Erdwiderstandes unter Ansatz der logarithmischen Spirale als Gleitflächenfunktion, 1970*
- 15 Schulz, Manfred: *Berechnung des räumlichen Erddruckes auf die Wandung kreiszylindrischer Körper, 1970*
- 16 Mobasseri, Manoutschehr: *Die Rippenstützmauer. Konstruktion und Grenzen ihrer Standsicherheit, 1970*
- 17 Benk, Dieter: *Ein Beitrag zum Betrieb und zur Bemessung von Hochwasserrückhaltebecken, 1970*

- 18 Gàl, Attila: *Bestimmung der mitschwingenden Wassermasse bei überströmten Fischbauchklappen mit kreiszylindrischem Staublech*, 1971, vergriffen
- 19 Kuz, Klaus Dieter: *Ein Beitrag zur Frage des Einsetzens von Kavitationserscheinungen in einer Düsenströmung bei Berücksichtigung der im Wasser gelösten Gase*, 1971, vergriffen
- 20 Schaak, Hartmut: *Verteilleitungen von Wasserkraftanlagen*, 1971
- 21 *Sonderheft zur Eröffnung der neuen Versuchsanstalt des Instituts für Wasserbau der Universität Stuttgart mit Beiträgen von* Brombach, Hansjörg; Dirksen, Wolfram; Gàl, Attila; Gerlach, Reinhard; Giesecke, Jürgen; Holthoff, Franz-Josef; Kuz, Klaus Dieter; Marotz, Günter; Minor, Hans-Erwin; Petrikat, Kurt; Röhnisch, Arthur; Rueff, Helge; Schwarz, Helmut; Vollmer, Ernst; Wildenhahn, Eberhard; 1972
- 22 Wang, Chung-su: *Ein Beitrag zur Berechnung der Schwingungen an Kegelstrahlschiebern*, 1972
- 23 Mayer-Vorfelder, Hans-Jörg: *Erdwiderstandsbeiwerte nach dem Ohde-Variationsverfahren*, 1972
- 24 Minor, Hans-Erwin: *Beitrag zur Bestimmung der Schwingungsanfachungsfunktionen überströmter Stauklappen*, 1972, vergriffen
- 25 Brombach, Hansjörg: *Untersuchung strömungsmechanischer Elemente (Fluidik) und die Möglichkeit der Anwendung von Wirbelkammerelementen im Wasserbau*, 1972, vergriffen
- 26 Wildenhahn, Eberhard: *Beitrag zur Berechnung von Horizontalfilterbrunnen*, 1972
- 27 Steinlein, Helmut: *Die Eliminierung der Schwebstoffe aus Flußwasser zum Zweck der unterirdischen Wasserspeicherung, gezeigt am Beispiel der Iller*, 1972
- 28 Holthoff, Franz Josef: *Die Überwindung großer Hubhöhen in der Binnenschifffahrt durch Schwimmerhebwerke*, 1973
- 29 Röder, Karl: *Einwirkungen aus Baugrundbewegungen auf trog- und kastenförmige Konstruktionen des Wasser- und Tunnelbaues*, 1973
- 30 Kretschmer, Heinz: *Die Bemessung von Bogenstaumauern in Abhängigkeit von der Talform*, 1973
- 31 Honekamp, Hermann: *Beitrag zur Berechnung der Montage von Unterwasserpipelines*, 1973
- 32 Giesecke, Jürgen: *Die Wirbelkammertriode als neuartiges Steuerorgan im Wasserbau*, und Brombach, Hansjörg: *Entwicklung, Bauformen, Wirkungsweise und Steuereigenschaften von Wirbelkammerverstärkern*, 1974

- 33 Rueff, Helge: *Untersuchung der schwingungserregenden Kräfte an zwei hintereinander angeordneten Tiefschützen unter besonderer Berücksichtigung von Kavitation*, 1974
- 34 Röhnisch, Arthur: *Einpreßversuche mit Zementmörtel für Spannbeton - Vergleich der Ergebnisse von Modellversuchen mit Ausführungen in Hüllwellrohren*, 1975
- 35 *Sonderheft anlässlich des 65. Geburtstages von Prof. Dr.-Ing. Kurt Petrikat mit Beiträgen von:* Brombach, Hansjörg; Erbel, Klaus; Flinspach, Dieter; Fischer jr., Richard; Gàl, Attila; Gerlach, Reinhard; Giesecke, Jürgen; Haberhauer, Robert; Hafner Edzard; Hausenblas, Bernhard; Horlacher, Hans-Burkhard; Hutarew, Andreas; Knoll, Manfred; Krummet, Ralph; Marotz, Günter; Merkle, Theodor; Miller, Christoph; Minor, Hans-Erwin; Neumayer, Hans; Rao, Syamala; Rath, Paul; Rueff, Helge; Ruppert, Jürgen; Schwarz, Wolfgang; Topal-Gökceli, Mehmet; Vollmer, Ernst; Wang, Chung-su; Weber, Hans-Georg; 1975
- 36 Berger, Jochum: *Beitrag zur Berechnung des Spannungszustandes in rotations-symmetrisch belasteten Kugelschalen veränderlicher Wandstärke unter Gas- und Flüssigkeitsdruck durch Integration schwach singulärer Differentialgleichungen*, 1975
- 37 Dirksen, Wolfram: *Berechnung instationärer Abflußvorgänge in gestauten Gerinnen mittels Differenzenverfahren und die Anwendung auf Hochwasserrückhaltebecken*, 1976
- 38 Horlacher, Hans-Burkhard: *Berechnung instationärer Temperatur- und Wärmespannungsfelder in langen mehrschichtigen Hohlzylindern*, 1976
- 39 Hafner, Edzard: *Untersuchung der hydrodynamischen Kräfte auf Baukörper im Tiefwasserbereich des Meeres*, 1977, ISBN 3-921694-39-6
- 40 Ruppert, Jürgen: *Über den Axialwirbelkammverstärker für den Einsatz im Wasserbau*, 1977, ISBN 3-921694-40-X
- 41 Hutarew, Andreas: *Beitrag zur Beeinflußbarkeit des Sauerstoffgehalts in Fließgewässern an Abstürzen und Wehren*, 1977, ISBN 3-921694-41-8, vergriffen
- 42 Miller, Christoph: *Ein Beitrag zur Bestimmung der schwingungserregenden Kräfte an unterströmten Wehren*, 1977, ISBN 3-921694-42-6
- 43 Schwarz, Wolfgang: *Druckstoßberechnung unter Berücksichtigung der Radial- und Längsverschiebungen der Rohrwandung*, 1978, ISBN 3-921694-43-4
- 44 Kinzelbach, Wolfgang: *Numerische Untersuchungen über den optimalen Einsatz variabler Kühlsysteme einer Kraftwerkskette am Beispiel Oberrhein*, 1978, ISBN 3-921694-44-2
- 45 Barczewski, Baldur: *Neue Meßmethoden für Wasser-Luftgemische und deren Anwendung auf zweiphasige Auftriebsstrahlen*, 1979, ISBN 3-921694-45-0

- 46 Neumayer, Hans: *Untersuchung der Strömungsvorgänge in radialen Wirbelkammerverstärkern*, 1979, ISBN 3-921694-46-9
- 47 Elalfy, Youssef-Elhassan: *Untersuchung der Strömungsvorgänge in Wirbelkammerdiolen und -drosseln*, 1979, ISBN 3-921694-47-7
- 48 Brombach, Hansjörg: *Automatisierung der Bewirtschaftung von Wasserspeichern*, 1981, ISBN 3-921694-48-5
- 49 Geldner, Peter: *Deterministische und stochastische Methoden zur Bestimmung der Selbstdichtung von Gewässern*, 1981, ISBN 3-921694-49-3, vergriffen
- 50 Mehlhorn, Hans: *Temperaturveränderungen im Grundwasser durch Brauchwasser-einleitungen*, 1982, ISBN 3-921694-50-7, vergriffen
- 51 Hafner, Edzard: *Rohrleitungen und Behälter im Meer*, 1983, ISBN 3-921694-51-5
- 52 Rinnert, Bernd: *Hydrodynamische Dispersion in porösen Medien: Einfluß von Dichteunterschieden auf die Vertikalvermischung in horizontaler Strömung*, 1983, ISBN 3-921694-52-3, vergriffen
- 53 Lindner, Wulf: *Steuerung von Grundwasserentnahmen unter Einhaltung ökologischer Kriterien*, 1983, ISBN 3-921694-53-1, vergriffen
- 54 Herr, Michael; Herzer, Jörg; Kinzelbach, Wolfgang; Kobus, Helmut; Rinnert, Bernd: *Methoden zur rechnerischen Erfassung und hydraulischen Sanierung von Grundwasserkontaminationen*, 1983, ISBN 3-921694-54-X
- 55 Schmitt, Paul: *Wege zur Automatisierung der Niederschlagsermittlung*, 1984, ISBN 3-921694-55-8, vergriffen
- 56 Müller, Peter: *Transport und selektive Sedimentation von Schwebstoffen bei gestautem Abfluß*, 1985, ISBN 3-921694-56-6
- 57 El-Qawasmeh, Fuad: *Möglichkeiten und Grenzen der Tropfbewässerung unter besonderer Berücksichtigung der Verstopfungsanfälligkeit der Tropfelemente*, 1985, ISBN 3-921694-57-4, vergriffen
- 58 Kirchenbaur, Klaus: *Mikroprozessorgesteuerte Erfassung instationärer Druckfelder am Beispiel seegangsbelasteter Baukörper*, 1985, ISBN 3-921694-58-2
- 59 Kobus, Helmut (Hrsg.): *Modellierung des großräumigen Wärme- und Schadstofftransports im Grundwasser*, Tätigkeitsbericht 1984/85 (DFG-Forschergruppe an den Universitäten Hohenheim, Karlsruhe und Stuttgart), 1985, ISBN 3-921694-59-0, vergriffen
- 60 Spitz, Karlheinz: *Dispersion in porösen Medien: Einfluß von Inhomogenitäten und Dichteunterschieden*, 1985, ISBN 3-921694-60-4, vergriffen
- 61 Kobus, Helmut: *An Introduction to Air-Water Flows in Hydraulics*, 1985, ISBN 3-921694-61-2

- 62 Kaleris, Vassilios: *Erfassung des Austausches von Oberflächen- und Grundwasser in horizontalebene Grundwassermodellen*, 1986, ISBN 3-921694-62-0
- 63 Herr, Michael: *Grundlagen der hydraulischen Sanierung verunreinigter Porengrundwasserleiter*, 1987, ISBN 3-921694-63-9
- 64 Marx, Walter: *Berechnung von Temperatur und Spannung in Massenbeton infolge Hydratation*, 1987, ISBN 3-921694-64-7
- 65 Koschitzky, Hans-Peter: *Dimensionierungskonzept für Sohlbelüfter in Schußrinnen zur Vermeidung von Kavitationsschäden*, 1987, ISBN 3-921694-65-5
- 66 Kobus, Helmut (Hrsg.): *Modellierung des großräumigen Wärme- und Schadstofftransports im Grundwasser*, Tätigkeitsbericht 1986/87 (DFG-Forschergruppe an den Universitäten Hohenheim, Karlsruhe und Stuttgart) 1987, ISBN 3-921694-66-3
- 67 Söll, Thomas: *Berechnungsverfahren zur Abschätzung anthropogener Temperaturanomalien im Grundwasser*, 1988, ISBN 3-921694-67-1
- 68 Dittrich, Andreas; Westrich, Bernd: *Bodenseeufererosion, Bestandsaufnahme und Bewertung*, 1988, ISBN 3-921694-68-X, vergriffen
- 69 Huwe, Bernd; van der Ploeg, Rienk R.: *Modelle zur Simulation des Stickstoffhaushaltes von Standorten mit unterschiedlicher landwirtschaftlicher Nutzung*, 1988, ISBN 3-921694-69-8, vergriffen
- 70 Stephan, Karl: *Integration elliptischer Funktionen*, 1988, ISBN 3-921694-70-1
- 71 Kobus, Helmut; Zilliox, Lothaire (Hrsg.): *Nitratbelastung des Grundwassers, Auswirkungen der Landwirtschaft auf die Grundwasser- und Rohwasserbeschaffenheit und Maßnahmen zum Schutz des Grundwassers*. Vorträge des deutsch-französischen Kolloquiums am 6. Oktober 1988, Universitäten Stuttgart und Louis Pasteur Strasbourg (Vorträge in deutsch oder französisch, Kurzfassungen zweisprachig), 1988, ISBN 3-921694-71-X
- 72 Soyeaux, Renald: *Unterströmung von Stauanlagen auf klüftigem Untergrund unter Berücksichtigung laminarer und turbulenter Fließzustände*, 1991, ISBN 3-921694-72-8
- 73 Kohane, Roberto: *Berechnungsmethoden für Hochwasserabfluß in Fließgewässern mit überströmten Vorländern*, 1991, ISBN 3-921694-73-6
- 74 Hassinger, Reinhard: *Beitrag zur Hydraulik und Bemessung von Blocksteinrampen in flexibler Bauweise*, 1991, ISBN 3-921694-74-4, vergriffen
- 75 Schäfer, Gerhard: *Einfluß von Schichtenstrukturen und lokalen Einlagerungen auf die Längsdispersion in Porengrundwasserleitern*, 1991, ISBN 3-921694-75-2
- 76 Giesecke, Jürgen: *Vorträge, Wasserwirtschaft in stark besiedelten Regionen; Umweltforschung mit Schwerpunkt Wasserwirtschaft*, 1991, ISBN 3-921694-76-0

- 77 Huwe, Bernd: *Deterministische und stochastische Ansätze zur Modellierung des Stickstoffhaushalts landwirtschaftlich genutzter Flächen auf unterschiedlichem Skalenniveau*, 1992, ISBN 3-921694-77-9, vergriffen
- 78 Rommel, Michael: *Verwendung von Kluftdaten zur realitätsnahen Generierung von Kluftnetzen mit anschließender laminar-turbulenter Strömungsberechnung*, 1993, ISBN 3-92 1694-78-7
- 79 Marschall, Paul: *Die Ermittlung lokaler Stofffrachten im Grundwasser mit Hilfe von Einbohrloch-Meßverfahren*, 1993, ISBN 3-921694-79-5, vergriffen
- 80 Ptak, Thomas: *Stofftransport in heterogenen Porenaquiferen: Felduntersuchungen und stochastische Modellierung*, 1993, ISBN 3-921694-80-9, vergriffen
- 81 Haakh, Frieder: *Transientes Strömungsverhalten in Wirbelkammern*, 1993, ISBN 3-921694-81-7
- 82 Kobus, Helmut; Cirpka, Olaf; Barczewski, Baldur; Koschitzky, Hans-Peter: *Versucheinrichtung zur Grundwasser und Altlastensanierung VEGAS, Konzeption und Programmrahmen*, 1993, ISBN 3-921694-82-5
- 83 Zang, Weidong: *Optimaler Echtzeit-Betrieb eines Speichers mit aktueller Abflußregenerierung*, 1994, ISBN 3-921694-83-3, vergriffen
- 84 Franke, Hans-Jörg: *Stochastische Modellierung eines flächenhaften Stoffeintrages und Transports in Grundwasser am Beispiel der Pflanzenschutzmittelproblematik*, 1995, ISBN 3-921694-84-1
- 85 Lang, Ulrich: *Simulation regionaler Strömungs- und Transportvorgänge in Karst-aquiferen mit Hilfe des Doppelkontinuum-Ansatzes: Methodenentwicklung und Parameteridentifikation*, 1995, ISBN 3-921694-85-X, vergriffen
- 86 Helmig, Rainer: *Einführung in die Numerischen Methoden der Hydromechanik*, 1996, ISBN 3-921694-86-8, vergriffen
- 87 Cirpka, Olaf: *CONTRACT: A Numerical Tool for Contaminant Transport and Chemical Transformations - Theory and Program Documentation -*, 1996, ISBN 3-921694-87-6
- 88 Haberlandt, Uwe: *Stochastische Synthese und Regionalisierung des Niederschlages für Schmutzfrachtberechnungen*, 1996, ISBN 3-921694-88-4
- 89 Croisé, Jean: *Extraktion von flüchtigen Chemikalien aus natürlichen Lockergesteinen mittels erzwungener Luftströmung*, 1996, ISBN 3-921694-89-2, vergriffen
- 90 Jorde, Klaus: *Ökologisch begründete, dynamische Mindestwasserregelungen bei Ausleitungskraftwerken*, 1997, ISBN 3-921694-90-6, vergriffen
- 91 Helmig, Rainer: *Gekoppelte Strömungs- und Transportprozesse im Untergrund - Ein Beitrag zur Hydrosystemmodellierung-*, 1998, ISBN 3-921694-91-4, vergriffen

- 92 Emmert, Martin: *Numerische Modellierung nichtisothermer Gas-Wasser Systeme in porösen Medien*, 1997, ISBN 3-921694-92-2
- 93 Kern, Ulrich: *Transport von Schweb- und Schadstoffen in staugeregelten Fließgewässern am Beispiel des Neckars*, 1997, ISBN 3-921694-93-0, vergriffen
- 94 Förster, Georg: *Druckstoßdämpfung durch große Luftblasen in Hochpunkten von Rohrleitungen* 1997, ISBN 3-921694-94-9
- 95 Cirpka, Olaf: *Numerische Methoden zur Simulation des reaktiven Mehrkomponententransports im Grundwasser*, 1997, ISBN 3-921694-95-7, vergriffen
- 96 Färber, Arne: *Wärmetransport in der ungesättigten Bodenzone: Entwicklung einer thermischen In-situ-Sanierungstechnologie*, 1997, ISBN 3-921694-96-5
- 97 Betz, Christoph: *Wasserdampfdestillation von Schadstoffen im porösen Medium: Entwicklung einer thermischen In-situ-Sanierungstechnologie*, 1998, ISBN 3-921694-97-3
- 98 Xu, Yichun: *Numerical Modeling of Suspended Sediment Transport in Rivers*, 1998, ISBN 3-921694-98-1, vergriffen
- 99 Wüst, Wolfgang: *Geochemische Untersuchungen zur Sanierung CKW-kontaminierter Aquifere mit Fe(0)-Reaktionswänden*, 2000, ISBN 3-933761-02-2
- 100 Sheta, Hussam: *Simulation von Mehrphasenvorgängen in porösen Medien unter Einbeziehung von Hysterese-Effekten*, 2000, ISBN 3-933761-03-4
- 101 Ayros, Edwin: *Regionalisierung extremer Abflüsse auf der Grundlage statistischer Verfahren*, 2000, ISBN 3-933761-04-2, vergriffen
- 102 Huber, Ralf: *Compositional Multiphase Flow and Transport in Heterogeneous Porous Media*, 2000, ISBN 3-933761-05-0
- 103 Braun, Christopherus: *Ein Upscaling-Verfahren für Mehrphasenströmungen in porösen Medien*, 2000, ISBN 3-933761-06-9
- 104 Hofmann, Bernd: *Entwicklung eines rechnergestützten Managementsystems zur Beurteilung von Grundwasserschadensfällen*, 2000, ISBN 3-933761-07-7
- 105 Class, Holger: *Theorie und numerische Modellierung nichtisothermer Mehrphasenprozesse in NAPL-kontaminierten porösen Medien*, 2001, ISBN 3-933761-08-5
- 106 Schmidt, Reinhard: *Wasserdampf- und Heißluftinjektion zur thermischen Sanierung kontaminierter Standorte*, 2001, ISBN 3-933761-09-3
- 107 Josef, Reinhold.: *Schadstoffextraktion mit hydraulischen Sanierungsverfahren unter Anwendung von grenzflächenaktiven Stoffen*, 2001, ISBN 3-933761-10-7

- 108 Schneider, Matthias: *Habitat- und Abflussmodellierung für Fließgewässer mit unscharfen Berechnungsansätzen*, 2001, ISBN 3-933761-11-5
- 109 Rathgeb, Andreas: *Hydrodynamische Bemessungsgrundlagen für Lockerdeckwerke an überströmbaren Erddämmen*, 2001, ISBN 3-933761-12-3
- 110 Lang, Stefan: *Parallele numerische Simulation instationärer Probleme mit adaptiven Methoden auf unstrukturierten Gittern*, 2001, ISBN 3-933761-13-1
- 111 Appt, Jochen; Stumpp Simone: *Die Bodensee-Messkampagne 2001, IWS/CWR Lake Constance Measurement Program 2001*, 2002, ISBN 3-933761-14-X
- 112 Heimerl, Stephan: *Systematische Beurteilung von Wasserkraftprojekten*, 2002, ISBN 3-933761-15-8, vergriffen
- 113 Iqbal, Amin: *On the Management and Salinity Control of Drip Irrigation*, 2002, ISBN 3-933761-16-6
- 114 Silberhorn-Hemminger, Annette: *Modellierung von Kluftaquifersystemen: Geostatistische Analyse und deterministisch-stochastische Kluftgenerierung*, 2002, ISBN 3-933761-17-4
- 115 Winkler, Angela: *Prozesse des Wärme- und Stofftransports bei der In-situ-Sanierung mit festen Wärmequellen*, 2003, ISBN 3-933761-18-2
- 116 Marx, Walter: *Wasserkraft, Bewässerung, Umwelt - Planungs- und Bewertungsschwerpunkte der Wasserbewirtschaftung*, 2003, ISBN 3-933761-19-0
- 117 Hinkelmann, Reinhard: *Efficient Numerical Methods and Information-Processing Techniques in Environment Water*, 2003, ISBN 3-933761-20-4
- 118 Samaniego-Eguiguren, Luis Eduardo: *Hydrological Consequences of Land Use / Land Cover and Climatic Changes in Mesoscale Catchments*, 2003, ISBN 3-933761-21-2
- 119 Neunhäuserer, Lina: *Diskretisierungsansätze zur Modellierung von Strömungs- und Transportprozessen in geklüftet-porösen Medien*, 2003, ISBN 3-933761-22-0
- 120 Paul, Maren: *Simulation of Two-Phase Flow in Heterogeneous Poros Media with Adaptive Methods*, 2003, ISBN 3-933761-23-9
- 121 Ehret, Uwe: *Rainfall and Flood Nowcasting in Small Catchments using Weather Radar*, 2003, ISBN 3-933761-24-7
- 122 Haag, Ingo: *Der Sauerstoffhaushalt staugeregelter Flüsse am Beispiel des Neckars - Analysen, Experimente, Simulationen -*, 2003, ISBN 3-933761-25-5
- 123 Appt, Jochen: *Analysis of Basin-Scale Internal Waves in Upper Lake Constance*, 2003, ISBN 3-933761-26-3

- 124 Hrsg.: Schrenk, Volker; Batereau, Katrin; Barczewski, Baldur; Weber, Karolin und Koschitzky, Hans-Peter: *Symposium Ressource Fläche und VEGAS - Statuskolloquium 2003, 30. September und 1. Oktober 2003*, 2003, ISBN 3-933761-27-1
- 125 Omar Khalil Ouda: *Optimisation of Agricultural Water Use: A Decision Support System for the Gaza Strip*, 2003, ISBN 3-933761-28-0
- 126 Batereau, Katrin: *Sensorbasierte Bodenluftmessung zur Vor-Ort-Erkundung von Schadensherden im Untergrund*, 2004, ISBN 3-933761-29-8
- 127 Witt, Oliver: *Erosionsstabilität von Gewässersedimenten mit Auswirkung auf den Stofftransport bei Hochwasser am Beispiel ausgewählter Stauhaltungen des Oberrheins*, 2004, ISBN 3-933761-30-1
- 128 Jakobs, Hartmut: *Simulation nicht-isothermer Gas-Wasser-Prozesse in komplexen Kluft-Matrix-Systemen*, 2004, ISBN 3-933761-31-X
- 129 Li, Chen-Chien: *Deterministisch-stochastisches Berechnungskonzept zur Beurteilung der Auswirkungen erosiver Hochwasserereignisse in Flusstauhaltungen*, 2004, ISBN 3-933761-32-8
- 130 Reichenberger, Volker; Helmig, Rainer; Jakobs, Hartmut; Bastian, Peter; Niessner, Jennifer: *Complex Gas-Water Processes in Discrete Fracture-Matrix Systems: Upscaling, Mass-Conservative Discretization and Efficient Multilevel Solution*, 2004, ISBN 3-933761-33-6
- 131 Hrsg.: Barczewski, Baldur; Koschitzky, Hans-Peter; Weber, Karolin; Wege, Ralf: *VEGAS - Statuskolloquium 2004*, Tagungsband zur Veranstaltung am 05. Oktober 2004 an der Universität Stuttgart, Campus Stuttgart-Vaihingen, 2004, ISBN 3-933761-34-4
- 132 Asie, Kemal Jabir: *Finite Volume Models for Multiphase Multicomponent Flow through Porous Media*. 2005, ISBN 3-933761-35-2
- 133 Jacoub, George: *Development of a 2-D Numerical Module for Particulate Contaminant Transport in Flood Retention Reservoirs and Impounded Rivers*, 2004, ISBN 3-933761-36-0
- 134 Nowak, Wolfgang: *Geostatistical Methods for the Identification of Flow and Transport Parameters in the Subsurface*, 2005, ISBN 3-933761-37-9
- 135 Süß, Mia: *Analysis of the influence of structures and boundaries on flow and transport processes in fractured porous media*, 2005, ISBN 3-933761-38-7
- 136 Jose, Surabhin Chackiath: *Experimental Investigations on Longitudinal Dispersive Mixing in Heterogeneous Aquifers*, 2005, ISBN: 3-933761-39-5
- 137 Filiz, Fulya: *Linking Large-Scale Meteorological Conditions to Floods in Mesoscale Catchments*, 2005, ISBN 3-933761-40-9

- 138 Qin, Minghao: *Wirklichkeitsnahe und recheneffiziente Ermittlung von Temperatur und Spannungen bei großen RCC-Staumauern*, 2005, ISBN 3-933761-41-7
- 139 Kobayashi, Kenichiro: *Optimization Methods for Multiphase Systems in the Sub-surface - Application to Methane Migration in Coal Mining Areas*, 2005, ISBN 3-933761-42-5
- 140 Rahman, Md. Arifur: *Experimental Investigations on Transverse Dispersive Mixing in Heterogeneous Porous Media*, 2005, ISBN 3-933761-43-3
- 141 Schrenk, Volker: *Ökobilanzen zur Bewertung von Altlastensanierungsmaßnahmen*, 2005, ISBN 3-933761-44-1
- 142 Hundecha, Hirpa Yeshewatersfa: *Regionalization of Parameters of a Conceptual Rainfall-Runoff Model*, 2005, ISBN: 3-933761-45-X
- 143 Wege, Ralf: *Untersuchungs- und Überwachungsmethoden für die Beurteilung natürlicher Selbstreinigungsprozesse im Grundwasser*, 2005, ISBN 3-933761-46-8
- 144 Breiting, Thomas: *Techniken und Methoden der Hydroinformatik - Modellierung von komplexen Hydrosystemen im Untergrund*, 2006, 3-933761-47-6
- 145 Hrsg.: Braun, Jürgen; Koschitzky, Hans-Peter; Müller, Martin: *Ressource Untergrund: 10 Jahre VEGAS: Forschung und Technologieentwicklung zum Schutz von Grundwasser und Boden*, Tagungsband zur Veranstaltung am 28. und 29. September 2005 an der Universität Stuttgart, Campus Stuttgart-Vaihingen, 2005, ISBN 3-933761-48-4
- 146 Rojanschi, Vlad: *Abflusskonzentration in mesoskaligen Einzugsgebieten unter Berücksichtigung des Sickerraumes*, 2006, ISBN 3-933761-49-2
- 147 Winkler, Nina Simone: *Optimierung der Steuerung von Hochwasserrückhaltebecken-systemen*, 2006, ISBN 3-933761-50-6
- 148 Wolf, Jens: *Räumlich differenzierte Modellierung der Grundwasserströmung alluvialer Aquifere für mesoskalige Einzugsgebiete*, 2006, ISBN: 3-933761-51-4
- 149 Kohler, Beate: *Externe Effekte der Laufwasserkraftnutzung*, 2006, ISBN 3-933761-52-2
- 150 Hrsg.: Braun, Jürgen; Koschitzky, Hans-Peter; Stuhmann, Matthias: *VEGAS-Statuskolloquium 2006*, Tagungsband zur Veranstaltung am 28. September 2006 an der Universität Stuttgart, Campus Stuttgart-Vaihingen, 2006, ISBN 3-933761-53-0
- 151 Niessner, Jennifer: *Multi-Scale Modeling of Multi-Phase - Multi-Component Processes in Heterogeneous Porous Media*, 2006, ISBN 3-933761-54-9
- 152 Fischer, Markus: *Beanspruchung eingeeerdeter Rohrleitungen infolge Austrocknung bindiger Böden*, 2006, ISBN 3-933761-55-7

- 153 Schneck, Alexander: *Optimierung der Grundwasserbewirtschaftung unter Berücksichtigung der Belange der Wasserversorgung, der Landwirtschaft und des Naturschutzes*, 2006, ISBN 3-933761-56-5
- 154 Das, Tapash: *The Impact of Spatial Variability of Precipitation on the Predictive Uncertainty of Hydrological Models*, 2006, ISBN 3-933761-57-3
- 155 Bielinski, Andreas: *Numerical Simulation of CO<sub>2</sub> sequestration in geological formations*, 2007, ISBN 3-933761-58-1
- 156 Mödinger, Jens: *Entwicklung eines Bewertungs- und Entscheidungsunterstützungssystems für eine nachhaltige regionale Grundwasserbewirtschaftung*, 2006, ISBN 3-933761-60-3
- 157 Manthey, Sabine: *Two-phase flow processes with dynamic effects in porous media - parameter estimation and simulation*, 2007, ISBN 3-933761-61-1
- 158 Pozos Estrada, Oscar: *Investigation on the Effects of Entrained Air in Pipelines*, 2007, ISBN 3-933761-62-X
- 159 Ochs, Steffen Oliver: *Steam injection into saturated porous media – process analysis including experimental and numerical investigations*, 2007, ISBN 3-933761-63-8
- 160 Marx, Andreas: *Einsatz gekoppelter Modelle und Wetterradar zur Abschätzung von Niederschlagsintensitäten und zur Abflussvorhersage*, 2007, ISBN 3-933761-64-6
- 161 Hartmann, Gabriele Maria: *Investigation of Evapotranspiration Concepts in Hydrological Modelling for Climate Change Impact Assessment*, 2007, ISBN 3-933761-65-4
- 162 Kebede Gurmessa, Tesfaye: *Numerical Investigation on Flow and Transport Characteristics to Improve Long-Term Simulation of Reservoir Sedimentation*, 2007, ISBN 3-933761-66-2
- 163 Trifković, Aleksandar: *Multi-objective and Risk-based Modelling Methodology for Planning, Design and Operation of Water Supply Systems*, 2007, ISBN 3-933761-67-0
- 164 Göttinger, Jens: *Distributed Conceptual Hydrological Modelling - Simulation of Climate, Land Use Change Impact and Uncertainty Analysis*, 2007, ISBN 3-933761-68-9
- 165 Hrsg.: Braun, Jürgen; Koschitzky, Hans-Peter; Stuhmann, Matthias: *VEGAS – Kolloquium 2007*, Tagungsband zur Veranstaltung am 26. September 2007 an der Universität Stuttgart, Campus Stuttgart-Vaihingen, 2007, ISBN 3-933761-69-7
- 166 Freeman, Beau: *Modernization Criteria Assessment for Water Resources Planning; Klamath Irrigation Project, U.S.*, 2008, ISBN 3-933761-70-0

- 167 Dreher, Thomas: *Selektive Sedimentation von Feinstschwebstoffen in Wechselwirkung mit wandnahen turbulenten Strömungsbedingungen*, 2008, ISBN 3-933761-71-9
- 168 Yang, Wei: *Discrete-Continuous Downscaling Model for Generating Daily Precipitation Time Series*, 2008, ISBN 3-933761-72-7
- 169 Kopecki, Ianina: *Calculational Approach to FST-Hemispheres for Multiparametrical Benthos Habitat Modelling*, 2008, ISBN 3-933761-73-5
- 170 Brommundt, Jürgen: *Stochastische Generierung räumlich zusammenhängender Niederschlagszeitreihen*, 2008, ISBN 3-933761-74-3
- 171 Papafotiou, Alexandros: *Numerical Investigations of the Role of Hysteresis in Heterogeneous Two-Phase Flow Systems*, 2008, ISBN 3-933761-75-1
- 172 He, Yi: *Application of a Non-Parametric Classification Scheme to Catchment Hydrology*, 2008, ISBN 978-3-933761-76-7
- 173 Wagner, Sven: *Water Balance in a Poorly Gauged Basin in West Africa Using Atmospheric Modelling and Remote Sensing Information*, 2008, ISBN 978-3-933761-77-4
- 174 Hrsg.: Braun, Jürgen; Koschitzky, Hans-Peter; Stuhmann, Matthias; Schrenk, Volker: *VEGAS-Kolloquium 2008 Ressource Fläche III*, Tagungsband zur Veranstaltung am 01. Oktober 2008 an der Universität Stuttgart, Campus Stuttgart-Vaihingen, 2008, ISBN 978-3-933761-78-1
- 175 Patil, Sachin: *Regionalization of an Event Based Nash Cascade Model for Flood Predictions in Ungauged Basins*, 2008, ISBN 978-3-933761-79-8
- 176 Assteerawatt, Anongnart: *Flow and Transport Modelling of Fractured Aquifers based on a Geostatistical Approach*, 2008, ISBN 978-3-933761-80-4
- 177 Karnahl, Joachim Alexander: *2D numerische Modellierung von multifraktionalem Schwebstoff- und Schadstofftransport in Flüssen*, 2008, ISBN 978-3-933761-81-1
- 178 Hiester, Uwe: *Technologieentwicklung zur In-situ-Sanierung der ungesättigten Bodenzone mit festen Wärmequellen*, 2009, ISBN 978-3-933761-82-8
- 179 Laux, Patrick: *Statistical Modeling of Precipitation for Agricultural Planning in the Volta Basin of West Africa*, 2009, ISBN 978-3-933761-83-5
- 180 Ehsan, Saqib: *Evaluation of Life Safety Risks Related to Severe Flooding*, 2009, ISBN 978-3-933761-84-2
- 181 Prohaska, Sandra: *Development and Application of a 1D Multi-Strip Fine Sediment Transport Model for Regulated Rivers*, 2009, ISBN 978-3-933761-85-9

- 182 Kopp, Andreas: *Evaluation of CO<sub>2</sub> Injection Processes in Geological Formations for Site Screening*, 2009, ISBN 978-3-933761-86-6
- 183 Ebigbo, Anozie: *Modelling of biofilm growth and its influence on CO<sub>2</sub> and water (two-phase) flow in porous media*, 2009, ISBN 978-3-933761-87-3
- 184 Freiboth, Sandra: *A phenomenological model for the numerical simulation of multiphase multicomponent processes considering structural alterations of porous media*, 2009, ISBN 978-3-933761-88-0
- 185 Zöllner, Frank: *Implementierung und Anwendung netzfreier Methoden im Konstruktiven Wasserbau und in der Hydromechanik*, 2009, ISBN 978-3-933761-89-7
- 186 Vasin, Milos: *Influence of the soil structure and property contrast on flow and transport in the unsaturated zone*, 2010, ISBN 978-3-933761-90-3
- 187 Li, Jing: *Application of Copulas as a New Geostatistical Tool*, 2010, ISBN 978-3-933761-91-0
- 188 AghaKouchak, Amir: *Simulation of Remotely Sensed Rainfall Fields Using Copulas*, 2010, ISBN 978-3-933761-92-7
- 189 Thapa, Pawan Kumar: *Physically-based spatially distributed rainfall runoff modeling for soil erosion estimation*, 2010, ISBN 978-3-933761-93-4
- 190 Wurms, Sven: *Numerische Modellierung der Sedimentationsprozesse in Retentionsanlagen zur Steuerung von Stoffströmen bei extremen Hochwasserabflussereignissen*, 2011, ISBN 978-3-933761-94-1
- 191 Merkel, Uwe: *Unsicherheitsanalyse hydraulischer Einwirkungen auf Hochwasserschutzdeiche und Steigerung der Leistungsfähigkeit durch adaptive Strömungsmodellierung*, 2011, ISBN 978-3-933761-95-8
- 192 Fritz, Jochen: *A Decoupled Model for Compositional Non-Isothermal Multiphase Flow in Porous Media and Multiphysics Approaches for Two-Phase Flow*, 2010, ISBN 978-3-933761-96-5
- 193 Weber, Karolin (Hrsg.): *12. Treffen junger WissenschaftlerInnen an Wasserbauinstituten*, 2010, ISBN 978-3-933761-97-2
- 194 Bliedernicht, Jan-Geert: *Probability Forecasts of Daily Areal Precipitation for Small River Basins*, 2011, ISBN 978-3-933761-98-9
- 195 Hrsg.: Koschitzky, Hans-Peter; Braun, Jürgen: *VEGAS-Kolloquium 2010 In-situ-Sanierung - Stand und Entwicklung Nano und ISCO -*, Tagungsband zur Veranstaltung am 07. Oktober 2010 an der Universität Stuttgart, Campus Stuttgart-Vaihingen, 2010, ISBN 978-3-933761-99-6

- 196 Gafurov, Abror: *Water Balance Modeling Using Remote Sensing Information - Focus on Central Asia*, 2010, ISBN 978-3-942036-00-9
- 197 Mackenberg, Sylvia: *Die Quellstärke in der Sickerwasserprognose: Möglichkeiten und Grenzen von Labor- und Freilanduntersuchungen*, 2010, ISBN 978-3-942036-01-6
- 198 Singh, Shailesh Kumar: *Robust Parameter Estimation in Gauged and Ungauged Basins*, 2010, ISBN 978-3-942036-02-3
- 199 Doğan, Mehmet Onur: *Coupling of porous media flow with pipe flow*, 2011, ISBN 978-3-942036-03-0
- 200 Liu, Min: *Study of Topographic Effects on Hydrological Patterns and the Implication on Hydrological Modeling and Data Interpolation*, 2011, ISBN 978-3-942036-04-7
- 201 Geleta, Habtamu Itefa: *Watershed Sediment Yield Modeling for Data Scarce Areas*, 2011, ISBN 978-3-942036-05-4
- 202 Franke, Jörg: *Einfluss der Überwachung auf die Versagenswahrscheinlichkeit von Staustufen*, 2011, ISBN 978-3-942036-06-1
- 203 Bakimchandra, Oinam: *Integrated Fuzzy-GIS approach for assessing regional soil erosion risks*, 2011, ISBN 978-3-942036-07-8
- 204 Alam, Muhammad Mahboob: *Statistical Downscaling of Extremes of Precipitation in Mesoscale Catchments from Different RCMs and Their Effects on Local Hydrology*, 2011, ISBN 978-3-942036-08-5
- 205 Hrsg.: Koschitzky, Hans-Peter; Braun, Jürgen: *VEGAS-Kolloquium 2011 Flache Geothermie - Perspektiven und Risiken*, Tagungsband zur Veranstaltung am 06. Oktober 2011 an der Universität Stuttgart, Campus Stuttgart-Vaihingen, 2011, ISBN 978-3-933761-09-2
- 206 Haslauer, Claus: *Analysis of Real-World Spatial Dependence of Subsurface Hydraulic Properties Using Copulas with a Focus on Solute Transport Behaviour*, 2011, ISBN 978-3-942036-10-8
- 207 Dung, Nguyen Viet: *Multi-objective automatic calibration of hydrodynamic models – development of the concept and an application in the Mekong Delta*, 2011, ISBN 978-3-942036-11-5
- 208 Hung, Nguyen Nghia: *Sediment dynamics in the floodplain of the Mekong Delta, Vietnam*, 2011, ISBN 978-3-942036-12-2
- 209 Kuhlmann, Anna: *Influence of soil structure and root water uptake on flow in the unsaturated zone*, 2012, ISBN 978-3-942036-13-9

- 210 Tuhtan, Jeffrey Andrew: *Including the Second Law Inequality in Aquatic Ecodynamics: A Modeling Approach for Alpine Rivers Impacted by Hydropeaking*, 2012, ISBN 978-3-942036-14-6
- 211 Tolossa, Habtamu: *Sediment Transport Computation Using a Data-Driven Adaptive Neuro-Fuzzy Modelling Approach*, 2012, ISBN 978-3-942036-15-3
- 212 Tatomir, Alexandru-Bodgan: *From Discrete to Continuum Concepts of Flow in Fractured Porous Media*, 2012, ISBN 978-3-942036-16-0
- 213 Erbertseder, Karin: *A Multi-Scale Model for Describing Cancer-Therapeutic Transport in the Human Lung*, 2012, ISBN 978-3-942036-17-7
- 214 Noack, Markus: *Modelling Approach for Interstitial Sediment Dynamics and Reproduction of Gravel Spawning Fish*, 2012, ISBN 978-3-942036-18-4
- 215 De Boer, Cjstmir Volkert: *Transport of Nano Sized Zero Valent Iron Colloids during Injection into the Subsurface*, 2012, ISBN 978-3-942036-19-1
- 216 Pfaff, Thomas: *Processing and Analysis of Weather Radar Data for Use in Hydrology*, 2013, ISBN 978-3-942036-20-7
- 217 Lebreuz, Hans-Henning: *Addressing the Input Uncertainty for Hydrological Modeling by a New Geostatistical Method*, 2013, ISBN 978-3-942036-21-4
- 218 Darcis, Melanie Yvonne: *Coupling Models of Different Complexity for the Simulation of CO<sub>2</sub> Storage in Deep Saline Aquifers*, 2013, ISBN 978-3-942036-22-1
- 219 Beck, Ferdinand: *Generation of Spatially Correlated Synthetic Rainfall Time Series in High Temporal Resolution - A Data Driven Approach*, 2013, ISBN 978-3-942036-23-8
- 220 Guthke, Philipp: *Non-multi-Gaussian spatial structures: Process-driven natural genesis, manifestation, modeling approaches, and influences on dependent processes*, 2013, ISBN 978-3-942036-24-5
- 221 Walter, Lena: *Uncertainty studies and risk assessment for CO<sub>2</sub> storage in geological formations*, 2013, ISBN 978-3-942036-25-2
- 222 Wolff, Markus: *Multi-scale modeling of two-phase flow in porous media including capillary pressure effects*, 2013, ISBN 978-3-942036-26-9
- 223 Mosthaf, Klaus Roland: *Modeling and analysis of coupled porous-medium and free flow with application to evaporation processes*, 2014, ISBN 978-3-942036-27-6
- 224 Leube, Philipp Christoph: *Methods for Physically-Based Model Reduction in Time: Analysis, Comparison of Methods and Application*, 2013, ISBN 978-3-942036-28-3
- 225 Rodríguez Fernández, Jhan Ignacio: *High Order Interactions among environmental variables: Diagnostics and initial steps towards modeling*, 2013, ISBN 978-3-942036-29-0

- 226 Eder, Maria Magdalena: *Climate Sensitivity of a Large Lake*, 2013, ISBN 978-3-942036-30-6
- 227 Greiner, Philipp: *Alkoholinjektion zur In-situ-Sanierung von CKW Schadensherden in Grundwasserleitern: Charakterisierung der relevanten Prozesse auf unterschiedlichen Skalen*, 2014, ISBN 978-3-942036-31-3
- 228 Lauser, Andreas: *Theory and Numerical Applications of Compositional Multi-Phase Flow in Porous Media*, 2014, ISBN 978-3-942036-32-0
- 229 Enzenhöfer, Rainer: *Risk Quantification and Management in Water Production and Supply Systems*, 2014, ISBN 978-3-942036-33-7
- 230 Faigle, Benjamin: *Adaptive modelling of compositional multi-phase flow with capillary pressure*, 2014, ISBN 978-3-942036-34-4
- 231 Oladyshkin, Sergey: *Efficient modeling of environmental systems in the face of complexity and uncertainty*, 2014, ISBN 978-3-942036-35-1
- 232 Sugimoto, Takayuki: *Copula based Stochastic Analysis of Discharge Time Series*, 2014, ISBN 978-3-942036-36-8
- 233 Koch, Jonas: *Simulation, Identification and Characterization of Contaminant Source Architectures in the Subsurface*, 2014, ISBN 978-3-942036-37-5
- 234 Zhang, Jin: *Investigations on Urban River Regulation and Ecological Rehabilitation Measures, Case of Shenzhen in China*, 2014, ISBN 978-3-942036-38-2
- 235 Siebel, Rüdiger: *Experimentelle Untersuchungen zur hydrodynamischen Belastung und Standsicherheit von Deckwerken an überströmbaren Erddämmen*, 2014, ISBN 978-3-942036-39-9
- 236 Baber, Katherina Inés: *Coupling free flow and flow in porous media in biological and technical applications: From a simple to a complex interface description*, 2014, ISBN 978-3-942036-40-5

Die Mitteilungshefte ab der Nr. 134 (Jg. 2005) stehen als pdf-Datei über die Homepage des Instituts: [www.iws.uni-stuttgart.de](http://www.iws.uni-stuttgart.de) zur Verfügung.